

1213

Bulletin 44

(Part 5 of 5 Parts)

ADD420189

THE SHOCK AND VIBRATION BULLETIN

Part 5
Isolation and Damping, Vibration Testing,
and Analysis

AUGUST 1974

A Publication of
THE SHOCK AND VIBRATION
INFORMATION CENTER
Naval Research Laboratory, Washington, D.C.



19960223 068

Office of
The Director of Defense
Research and Engineering

ETHIC QUALITY INSPECTED

Approved for public release; distribution unlimited.

PLASTIC
22720-
22724

SYMPOSIUM MANAGEMENT

THE SHOCK AND VIBRATION INFORMATION CENTER

Henry C. Pusey, Director
Edward H. Schell
Rudolph H. Volin
J. Gordan Showalter

Bulletin Production

Graphic Arts Branch, Technical Information Division,
Naval Research Laboratory

-- 5 OF 142

DTIC DOES NOT HAVE THIS ITEM

-- 1 - AD NUMBER: D420189
-- 3 - ENTRY CLASSIFICATION: UNCLASSIFIED
-- 5 - CORPORATE AUTHOR: NAVAL RESEARCH LAB WASHINGTON D C SHOCK AND
-- VIBRATION INFORMATION CENTER
-- 6 - UNCLASSIFIED TITLE: THE SHOCK AND VIBRATION BULLETIN.
-- 8 - TITLE CLASSIFICATION: UNCLASSIFIED
--11 - REPORT DATE: AUG , 1974
--12 - PAGINATION: 204P
--20 - REPORT CLASSIFICATION: UNCLASSIFIED
--21 - SUPPLEMENTARY NOTE: IN: SHOCK AND VIBRATION BULLETIN, BULL. 44,
-- PT. 5, AUG 74. CONTAINS PROCEEDINGS: 44TH SYMPOSIUM ON SHOCK AND
-- VIBRATION, 4-7 DEC 73, LYNDON B. JOHNSON SPACE CENTER, HOUSTON, TEX.
-- SPONSORED BY NASA. (SEE ALSO PL-22721 - PL-22724).
--22 - LIMITATIONS (ALPHA): APPROVED FOR PUBLIC RELEASE; DISTRIBUTION
-- UNLIMITED. AVAILABILITY: PUBLISHED IN: SHOCK AND VIBRATION BULLETIN,
-- BULL. 44, PT. 5, AUG 74.

Bulletin 44
(Part 5 of 5 Parts)

THE SHOCK AND VIBRATION BULLETIN

AUGUST 1974

**A Publication of
THE SHOCK AND VIBRATION
INFORMATION CENTER
Naval Research Laboratory, Washington, D.C.**

The 44th Symposium on Shock and Vibration was held at the Rice Hotel and Lyndon B. Johnson Space Center, Houston, Texas on 4-7 December 1973. The National Aeronautics and Space Administration was the host.

**Office of
The Director of Defense
Research and Engineering**

CONTENTS

PAPERS APPEARING IN PART 5

Isolation and Damping

- DESIGN OF CONSTRAINED LAYER TREATMENTS FOR BROAD TEMPERATURE DAMPING 1 ^{PL-} 22721
D.I.G. Jones, Air Force Materials Laboratory, Wright-Patterson AFB, Ohio
- REDUCTION OF INTERIOR CABIN NOISE LEVELS IN A HELICOPTER THROUGH ADDITIVE DAMPING 13
J.P. Henderson, Air Force Materials Laboratory, Wright-Patterson AFB, Ohio
and A.D. Nashif, University of Dayton, Dayton, Ohio
- VIBRATION DAMPING AND ISOLATION WITH ENERGY ABSORBING COMPOSITES 23 ^{PL-} 22722
J. Nunes, Brunswick Corporation, Skokie, Illinois
- SUPPRESSION OF TORSIONAL VIBRATION WITH ZERO TORSIONAL STIFFNESS COUPLINGS 43
J.M. Vance, University of Florida, Gainesville, Florida and R.A. Brown, E.I. du Pont de Nemours and Company, Inc., Wilmington, Delaware

Vibration Testing and Analysis

- DEVELOPMENT OF SAM-D MISSILE RANDOM VIBRATION RESPONSE LOADS . 55
P.G. Hahn, Martin Marietta Aerospace, Orlando, Florida
- EVALUATION OF BLOCKED ACOUSTIC PRESSURE ON STIFFENED CYLINDRICAL SHELLS 65
V.M. Conticelli, Aeritalia S.p.A., Naples, Italy, and G.C. Kao, Wyle Laboratories, Huntsville, Alabama
- REDUCTION OF HULL NOISE AND VIBRATION BY CENTER OF PERCUSSION ROADARM DESIGN 77
D.D. Ustick, U.S. Army Tank-Automotive Command, Warren, Michigan
- SYNCHRONIZATION AND PHASE ANGLE OF TWO UNBALANCED ROTORS .. 83
M. Paz, University of Louisville, Louisville, Kentucky, P.H. Schrader and R. Blackmon, Vibrating Equipment Division, Rexnord, Inc., Louisville, Kentucky
- EXPERIMENTAL INVESTIGATION OF THE DYNAMIC RESPONSE OF CANTILEVER ANTISOTROPIC PLATES 89 ^{PL-} 22723
R.L. Sierakowski, University of Florida, Gainesville, Florida and C.T. Sun, Iowa State University, Ames, Iowa

SPACECRAFT VIBRATION TEST LEVEL COST OPTIMIZATION STUDY	99
J.P. Young, NASA Goddard Space Flight Center, Greenbelt, Maryland	
FLIGHT QUALIFICATION OF SPECIAL EQUIPMENT	107
J. Pearson and R.E. Thaller, Air Force Flight Dynamics Laboratory, Wright-Patterson AFB, Ohio	
THE USE OF LISSAJOUS FIGURES IN VIBRATION TESTING	117
J.D. Ray, Memphis State University, Memphis, Tennessee and C.W. Bert, University of Oklahoma, Norman, Oklahoma	
STRUCTURAL DYNAMIC RESPONSE ANALYSIS OF ROCKET TEST SLEDS	129
T.N. Gardner, Mechanics Research Incorporated, Los Angeles, California	
CONSIDERATION OF THE RESPONSE OF A SLED BORNE MISSILE	141
A.R. Glaser, Rockwell International, Columbus, Ohio and L.C. Mixon, 6585th Test Group, Holloman AFB, New Mexico	
FLOW-INDUCED VIBRATIONS OF A GLASS-REINFORCED PLASTIC SONAR DOME	153
D.A. King, Rockwell International Corporation, Anaheim, California	
AERO-ACOUSTIC ENVIRONMENT OF A RECTANGULAR CAVITY WITH A LENGTH TO DEPTH RATIO OF FOUR	165
L.L. Shaw and D.L. Smith, Air Force Flight Dynamics Laboratory, Wright-Patterson AFB, Ohio	
RESPONSE OF LINEAR DYNAMICAL SYSTEMS UNDER NONSTATIONARY RANDOM EXCITATIONS	175
T.S. Sankar and D. Doan, Sir George Williams University, Montreal, Canada	
MEANS OF CONTROLLING THE DYNAMIC MOTION OF BOTTOM MOORED MINE CASES EXPOSED TO HIGH CURRENT	183
J.J. O'Neill, J. Berezow and J.E. Goeller, Naval Ordnance Laboratory, Silver Spring, Maryland	

PAPERS APPEARING IN PART 1

Summaries of Papers Presented at 44th Symposium

PAPERS APPEARING IN PART 2

Invited Papers

SPACE SHUTTLE DYNAMICS

Mr. Robert F. Thompson, Manager, Space Shuttle Program, Lyndon B. Johnson, Space Center, Houston, Texas

VIKING DYNAMICS — AN OVERVIEW

Dr. Richard E. Snyder, NASA Langley Research Center, Hampton, Virginia

VIKING ORBITER — DYNAMICS OVERVIEW

Mr. Ben K. Wada, Jet Propulsion Laboratory, Pasadena, California

VIKING LANDER DYNAMICS

Mr. Joseph C. Pohlen, Martin Marietta Aerospace, Denver, Colorado

Structural Dynamics

PERFORMANCE OF STATISTICAL ENERGY ANALYSIS

R.F. Davis and D.E. Hines, McDonnell Douglas Astronautics Company,
Huntington Beach, California

**PREDICTION OF SHOCK ENVIRONMENTS BY TRANSFER FUNCTION
MEASUREMENT TECHNIQUES**

G.C. Kao, J.M. Cantril, G.D. Shipway, Wyle Laboratories, Huntsville,
Alabama, and M.A. Boyd, U.S. Army Corps of Engineers, Huntsville, Alabama

**DETERMINATION OF GUIDEWAY ROUGHNESS FROM CONSTRUCTION
TOLERANCES**

B.J. Brock, Vought Systems Division LTV Aerospace Corporation,
Dallas, Texas

**SELECTED SYSTEM MODES USING THE DYNAMIC TRANSFORMATION WITH
MODAL SYNTHESIS**

E.J. Kuhar, General Electric Company, Philadelphia, Pennsylvania

**STRUCTURAL DYNAMICS COMPUTATIONS USING AN APPROXIMATE
TRANSFORMATION**

C.S. O'Hearne and J.W. Shipley, Martin Marietta Aerospace, Orlando, Florida

**LINEAR LUMPED-MASS MODELING TECHNIQUES FOR BLAST
LOADED STRUCTURES**

W.J. Liss, Jr. and N.J. DeCapua, Bell Laboratories, Whippany, New Jersey

**DEVELOPMENT AND CORRELATION: VIKING ORBITER ANALYTICAL
DYNAMIC MODEL WITH MODAL TEST**

B.K. Wada, J.A. Garba and J.C. Chen, Jet Propulsion Laboratory, Pasadena,
California

MODAL TEST RESULTS OF THE VIKING ORBITER

E.L. Leppert, B.K. Wada, Jet Propulsion Laboratory, Pasadena, California,
and R. Miyakawa, Martin-Marietta Aerospace, Denver, Colorado (assigned
to the Jet Propulsion Laboratory)

**IMPLEMENTATION OF INTERACTIVE GRAPHICS TO A TRANSIENT
RESPONSE RING CODE**

R.W. Buchanan, T.N. Vogel and P.G. Underwood, Lockheed Missiles and
Space Company, Sunnyvale, California

COMPUTER GENERATED DISPLAYS OF STRUCTURES IN VIBRATION

H.N. Christiansen, Brigham Young University, Provo, Utah

VIBRATION REDUCTION BY USING BOTH THE FINITE ELEMENT STRAIN
ENERGY DISTRIBUTION AND MOBILITY TECHNIQUES

J. J. Sciarra, Boeing Vertol Company, Philadelphia, Pennsylvania

INFLUENCE OF ELASTIC SUPPORTS ON NATURAL FREQUENCIES OF
CANTILEVER BEAMS

R.F. Solberg, Jr., Southwest Research Institute, San Antonio, Texas

PAPERS APPEARING IN PART 3

Shock Testing

DIGITALLY CONTROLLED TRANSIENT WAVEFORM TESTING —
ALTERNATE METHOD TO SLOW SINE SWEEP

B.K. Kim, Jet Propulsion Laboratory, Pasadena, California

COMPARISON OF SHOCK SPECTRUM TECHNIQUES AND THE METHOD
OF LEAST FAVORABLE RESPONSE

A.F. Witte and R.J. Wolf, Kaman Sciences Corporation, Colorado Springs,
Colorado

APPLICATION OF LEAST FAVORABLE RESPONSE TECHNIQUES INCORPO-
RATING FIELD DATA FOURIER TRANSFORM PHASE ANGLE

R.J. Wolf and A.F. Witte, Kaman Sciences Corporation, Colorado Springs,
Colorado

MATCHING SHOCK SPECTRA WITH SUMS OF DECAYING SINUSOIDS COMPEN-
SATED FOR SHAKER VELOCITY AND DISPLACEMENT LIMITATIONS

D.O. Smallwood and A.R. Nord, Sandia Laboratories, Albuquerque,
New Mexico

A CASE FOR DAMPED OSCILLATORY EXCITATION AS A NATURAL
PYROTECHNIC SHOCK SIMULATION

D.B. Nelson and P.H. Prasthofer, Sandia Laboratories, Livermore, California

DEVELOPMENT OF A PYROTECHNIC SHOCK TEST FACILITY

D.R. Powers, McDonnell Douglas Astronautics Company, Santa Monica,
California

STUDY OF AN EXPERIMENTAL TECHNIQUE FOR APPLICATION TO
STRUCTURAL DYNAMIC PROBLEMS

R.F. Snell, McDonnell Douglas Astronautics Company, Huntington Beach,
California

TIMESWISE OUTPUT OF PYROTECHNIC BOLTS

V.H. Neubert, The Pennsylvania State University, University Park, Pennsylvania
and R.P. Parker, Uniroyal Research Center, Middlebury, Connecticut

PYROTECHNIC SHOCK REDUCTION

S.N. Prescott, Jet Propulsion Laboratory, Pasadena, California

IMPACT TESTING WITH THE 35-FOOT CENTRIFUGE

J.V. Otts, Sandia Laboratories, Albuquerque, New Mexico

FRAGMENT VELOCITIES FROM EXPLODING LIQUID PROPELLANT TANKS

R.L. Bessey, Southwest Research Institute, San Antonio, Texas

Shock Analysis

PIPING DESIGN FOR HYDRAULIC TRANSIENT PRESSURE

C.C. Huang, R.J. Bradshaw, Jr., U.S. Army Engineer Division, Huntsville, Alabama and H.H. Yen, Sperry-Rand Corporation, Huntsville, Alabama

POPPING MOTOR DOME SHOCK DURING FIRST STAGE SEPARATION ON POSEIDON MISSILE FLIGHTS

L.R. Pendleton and R.L. Henrikson, Lockheed Missiles and Space Company, Sunnyvale, California

SCALING OF WATER IMPACT DATA FOR SPACE SHUTTLE SOLID ROCKET BOOSTER

R. Madden, H.A. Wright, Bolt Beranek and Newman, Inc., Cambridge, Massachusetts and D.A. Kross, NASA Marshall Space Flight Center, Huntsville, Alabama

IDENTIFICATION OF AN OPTIMUM SET OF TRANSIENT SWEEP PARAMETERS FOR GENERATING SPECIFIED RESPONSE SPECTRA

R.C. Rountree, The Aerospace Corporation, El Segundo, California and C.R. Freberg, University of Southern California, Los Angeles, California

ANALYSIS OF OPEN CELL POLYURETHANE FOAM UNDER IMPACT LOADING

V. Sepcenko, Boeing Aerospace Company, Seattle, Washington

MEASUREMENT OF PEAK PRESSURES PRODUCED AT THE GROUND SURFACE BY SHALLOW BURIED EXPLOSIVES

B.L. Morris, U.S. Army Mobility Equipment Research and Development Center, Fort Belvoir, Virginia

PAPERS APPEARING IN PART 4

Underwater Problems

APPLICATION OF MECHANICAL IMPEDANCE CONCEPTS TO THE COUPLING PROBLEM OF STRUCTURES IN SHOCK ENVIRONMENT

R. Aquilina and L. Gaudriot, Center D-Etudes et de Recherches Techniques Sous-Marines, Direction Des Constructions Et Armes Navales, Toulon, France

THE NAVY LARGE FLOATING SHOCK PLATFORM-PART I: PHYSICAL DESCRIPTION AND CAPABILITIES

C.G. Schrader, West Coast Shock Facility, San Francisco, California

THE NAVY LARGE FLOATING SHOCK PLATFORM-PART II: SHOCK
CHARACTERISTICS

E.W. Clements, Naval Research Laboratory, Washington, D.C.

THE EFFECT OF UNIFORM EXTERNAL PRESSURIZATION ON THE DYNAMIC
RESPONSE OF ISOTROPIC CYLINDRICAL SHELLS

F.J. Dzialo, University of Massachusetts, Amherst, Massachusetts

ON DEFINING TIME DOMAINS FOR RADIATION DAMPING AND ADDED MASS
EFFECTS IN FLUID-STRUCTURAL INTERACTION

A.V. Clark Jr., Naval Research Laboratory, Washington, D.C.

Environments and Measurements

HARPOON MISSILE FLIGHT ENVIRONMENTAL MEASUREMENT PROGRAM

V.S. Noonan, J.L. Gubser and R.D. Harmening, McDonnell Douglas Astro-
nautics Company, St. Louis, Missouri

NARROW BAND TIME HISTORY ANALYSIS OF TRANSPORT AIRCRAFT
VIBRATION DATA

R.E. Thaller and J. Pearson, Air Force Flight Dynamics Laboratory, Wright-
Patterson AFB, Ohio

PRELIMINARY MEASUREMENT AND ANALYSIS OF THE VIBRATION EN-
VIRONMENT OF COMMON MOTOR CARRIERS

W.N. Sharpe, T.J. Kusza, F.W. Sherman and J.W. Goff, School of Packaging,
Michigan State University, East Lansing, Michigan

THE DYNAMIC ENVIRONMENT OF LANDING CRAFT

M.B. Gens, Sandia Laboratories, Albuquerque, New Mexico

A RESONANCE-TYPE BACK-TO-BACK CALIBRATOR FOR ACCELEROMETERS

J.A. Macinante, N.H. Clark, B.H. Cresswell, CSIRO, Division of Applied
Physics, National Standards Laboratory, Sydney, Australia

A NEW TRANSVERSE CALIBRATOR FOR ACCELEROMETERS

J.A. Macinante, N.H. Clark, and B.H. Cresswell, CSIRO, Division of Applied
Physics, National Standards Laboratory, Sydney, Australia

ISOLATION AND DAMPING

DESIGN OF CONSTRAINED LAYER TREATMENTS FOR BROAD TEMPERATURE DAMPING

David I. G. Jones
Air Force Materials Laboratory
Wright-Patterson AFB, Ohio 45433

(U) The effect of multiple constrained layer damping treatments, with one or more viscoelastic adhesive materials and/or constraining layer materials, on the modal damping and resonant frequencies of stiffened plate structures is discussed from an experimental and analytical point of view. It is shown that very simple analytical techniques will often suffice and that proper choice of materials and the stacking sequence of the treatment can readily give a broad temperature range capability, as needed for vibration and noise control applications.

INTRODUCTION

(U) One of the most effective and versatile techniques for controlling vibrations in plate-like structures is the multiple constrained layer treatment illustrated in Fig. 1. This is because of the control one has over the adhesive and constraining layer dimensions and materials, in order to optimize the treatment for each given application. When properly designed, these treatments can be used over a wide temperature range, at both high and low frequencies and short and long bending wavelengths, with very little weight increase and be capable of withstanding even the most severe environmental conditions. Successful applications of these types of treatments have been made to solve a cavity resonance induced failure problem in a weapons dispenser [1, 2], and to reduce interior cabin noise levels in a military helicopter [3-5], and in several other instances. It is important, however, that it become more widely recognized that temperature is the dominant parameter controlling treatment behavior, being far more important than wavelength or frequency, even though these parameters must certainly be taken into account.

This paper is concerned with demonstrating the effect, on the modal damping of several simple types of structure, of various treatment parameters with particular emphasis on choice of adhesive materials and their dependence on temperature, and the effect of

various combinations of different adhesive materials. The approach is primarily experimental, accompanied by analysis for the simpler cases.

ANALYSIS OF STRUCTURES WITH MULTIPLE LAYER TREATMENTS

Multiple Constrained Layer System with Single Adhesive Material

When a multiple layer treatment consisting of several alternate layers of a single viscoelastic adhesive material and a single constraining layer material, as illustrated in Fig. 1, is applied to a structure, one can show [6, 7] that the treatment may be analyzed as if it were a uniform homogeneous free layer treatment having equivalent complex Young's modulus properties. The equivalent complex modulus properties are given by the empirically derived relationships [6]:

$$E_e/E_c = f(h_c/h_D, \phi_{nm}) \quad (1)$$

$$\eta_e/\eta_D = g(h_c/h_D, \phi_{nm}) \quad (2)$$

$$\text{where } \phi_{nm} = \frac{E_D (1 - \nu^2) \lambda_{nm}^2}{E_C (r^2 + 1) h_c h_D} \quad (3)$$

PL-22721
ADD 420190

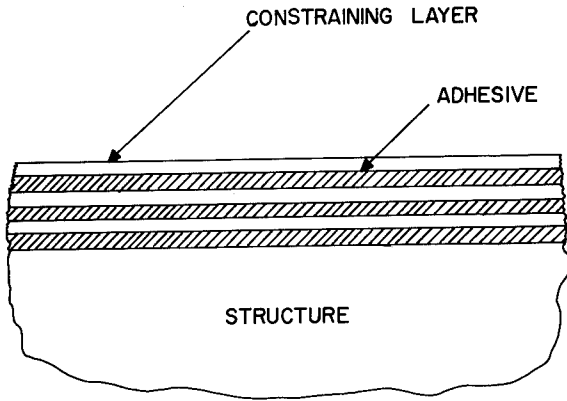


Fig. 1. Single adhesive material treatment

In these equations $E_D^* = E_D (1 + i\eta_D)$ is the complex Young's modulus of the adhesive material and $E_e^* = E_e (1 + i\eta_e)$ is the equivalent complex Young's modulus of the treatment. The functions f and g are illustrated in terms of h_c/h_D and ϕ_{nm} in Fig. 2.

Equations (1) to (3) give the equivalent free-layer properties of the treatment, which are readily calculated when E_D , η_D , h_c , h_D , λ_{nm} , E_c , r and ν are known. The next step, for the treatment applied uniformly to the surface of a stiffened structure, is to apply a generalized form of the equations derived by Oberst [8] for a beam or unstiffened plate. These equations are derived in reference [8] and are given by:

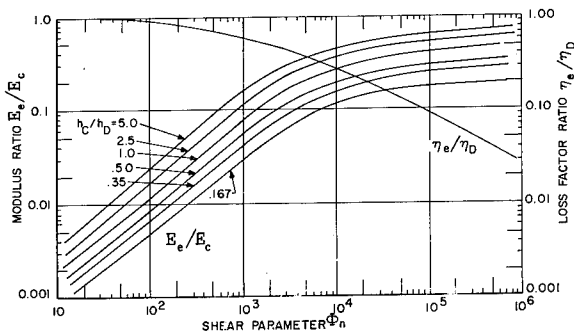


Fig. 2. Graphs of f and g versus ϕ_{nm} and h_c/h_d

$$\eta_s/\eta_e = [1 + (A - 2 + \beta_{nm})/Be]^{-1} \quad (4)$$

$$Z^2 = (1 + \rho_e h_e / \rho h) (f_{nm} / f_{onm})^2$$

$$= 1 + (A - 2 + Be) / \beta_{nm} \quad (5)$$

where

$$A = \{(1 - n^2 e)^3 + (1 + [2n + n^2]e)^3\} / (1 + ne)^3 \quad (6)$$

$$B = \{(2n + 1 + n^2 e)^3 - (1 - n^2 e)^3\} / (1 + ne)^3 \quad (7)$$

Equations (4) and (5) give the modal damping and stiffness parameter for the treatment applied to a structure, in terms of the equivalent complex modulus properties of the treatment derived from equations (1) to (3). The parameter β_{nm} , which is a measure of the effect of the stiffeners in the structure, can be derived from equation (6) if one has a detailed knowledge of the normal modes and their derivatives. Otherwise, this parameter may be determined experimentally from response tests on the structure using a known free layer treatment.

Multiple Constrained Layer Treatment with Two Adhesive Materials

If the treatment depicted in Fig. 3 is applied to the structure, a fairly simple analysis is applicable provided that the softer treatment is on the "outside". Otherwise, the "outer" treatment will act itself as a constraining layer for the "inner" treatment and complex shearing actions, qualitatively comparable to those occurring in a conventional constrained layer treatment, will take place. This will completely invalidate the assumption that the treatments may be regarded as equivalent free layer treatments. For the case when the softer treatment is on the "outside", however, no such problem occurs, because no such shearing actions occur.

It is shown in Appendix I that η_s and Z^2 are now given by:

$$\eta_s = \frac{\eta_1 B_1 e_1 + \eta_2 B_2 e_2}{B_1 e_1 + B_2 e_2 + A_1 - 2 + \beta_{nm}} \quad (9)$$

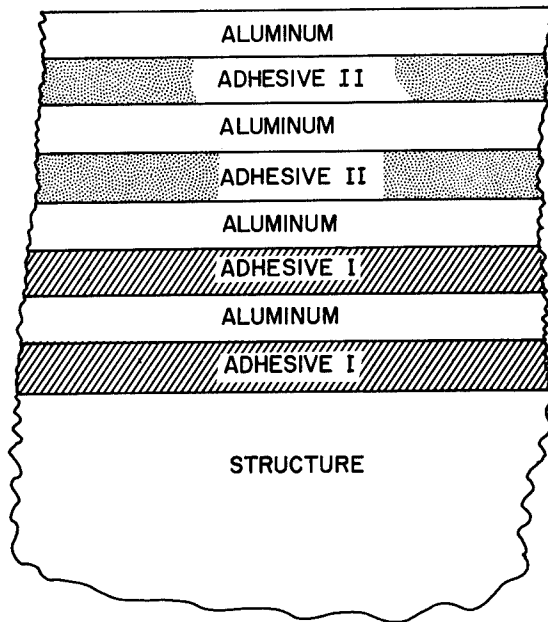


Fig. 3. Two-adhesive material treatment (System B)

$$Z^2 = \left(1 + \frac{\rho_e h_e}{\rho_h}\right) \left(\frac{f_{nm}}{f_{onm}}\right)^2$$

$$= 1 + \frac{A_1 - 2 + B_1 e_1 + B_2 e_2}{\beta_{nm}} \quad (10)$$

where:

$$A_1 = \left\{ [1 - n_1^2 e_1 - n_2^2 e_2 (2n_1 + n_2)]^3 + [1 + (2n_1 + n_1^2) e_1 + e_2 n_2 (2 + 2n_1 + n_2)]^3 \right\} / [1 + e_1 n_1 + e_2 n_2]^3 \quad (11)$$

$$B_1 = \left\{ [2n_1 + 1 + n_1^2 e_1 - n_2^2 e_2]^3 - [1 - n_1^2 e_1 - e_2 n_2 (2n_1 + n_2)]^3 \right\} / [1 + e_1 n_1 + e_2 n_2]^3 \quad (12)$$

$$B_2 = \left\{ [1 + 2(n_1 + n_2) + e_1 n_1^2 + e_2 n_2 (n_1 + n_2)]^3 - [1 + 2n_1 + n_1^2 e_1 - e_2 n_2]^3 \right\} / [1 + e_1 n_1 + e_2 n_2]^3 \quad (13)$$

These equations reduce to those used earlier (equations 4-6) when $\eta_2 \rightarrow 0$. It is emphasized here that these equations are approximate only and are applicable only to the type of treatment illustrated in Fig. 3, when the outer treatment is the "softest". Other damping treatment configurations are readily visualized, such as those illustrated in Fig. 4. However, these particular treatments are far more difficult to analyze and will be considered experimentally only in this paper.

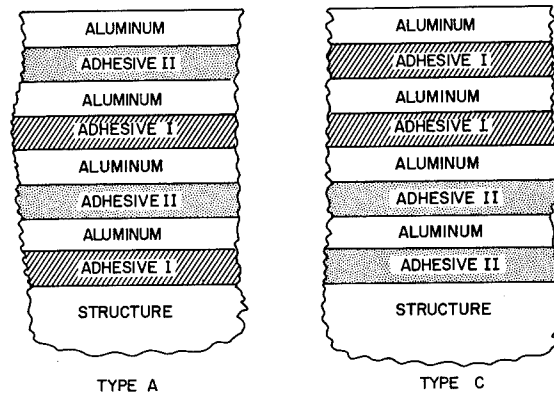


Fig. 4. Alternative two-adhesive system (System A and C)

EXPERIMENTAL INVESTIGATIONS OF MULTIPLE LAYER CONSTRAINED TREATMENTS ON CLAMPED-CLAMPED BEAMS

Single Adhesive/Constraining Layer Material System

Simple beams with classical boundary conditions fulfill many of the conditions needed for conducting successful vibration tests, including well spaced resonant frequencies and a wide range of wavelengths for the first few modes. While, therefore, such tests are not wholly representative of the behavior of more complex structures, the relative ease of testing does allow one to vary and control a large number of parameters. For example, on a clamped-clamped beam, tests have been conducted [6] using a single adhesive and a single constraining layer material in which the constraining layer thickness was varied from 0.0007 inches to 0.01 inches, the adhesive thickness was varied from 0.002 inches to 0.006 inches, the adhesive real Young's modulus was varied from under 50 lb/in² to over 10⁵ lb/in² and the loss factor from about 0.3

to 1.4, and the constraining layer modulus was varied from 10^7 lb/in² to 3×10^7 lb/in². The system is illustrated in Fig. 5. The purpose of those particular tests was to measure the equivalent complex modulus properties of a treatment comprising several alternate layers of a single viscoelastic adhesive material and a single constraining layer material as a function of the thickness of the constraining layers, the thickness of the adhesive layers, the modal semi-wavelength, the number of layer-pairs, the constraining layer Young's modulus, the real part of the adhesive complex Young's modulus, and the adhesive loss factor. The tests showed that the complex modulus of the equivalent free layer treatment was dependent only on four main parameters, namely the ratio h_c/h_D of constraining layer thickness to adhesive thickness, the modulus E_c of the constraining layer, the loss factor η_D of the adhesive and a "shear parameter" which involves the adhesive modulus E_D , the semi-wavelength λ_{nm} , the constraining layer modulus E_c , the constraining layer thickness h_c and the adhesive thickness h_D . These results are very important because a free-layer treatment is much easier to analyze than a multiple constrained layer treatment, particularly in the case of relatively complex structures, which we shall be considering presently.

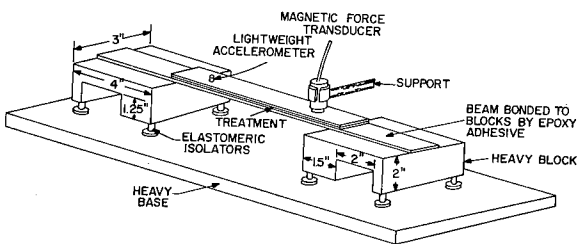


Fig. 5. Clamped-clamped beam system

This particular investigation led ultimately to equations (1) to (3). With E_e and η_e known from equations (1) and (2), it is then possible to use the appropriate equations (4) and (5) for the modal damping and resonant frequencies of a beam damped by a free layer treatment. For an unstiffened beam, $\beta_{nm}=2.0$. Calculations have been performed for many cases, including the case of a clamped-clamped aluminum beam seven inches long by 0.05 inches thick with a three layer-pair system

having $h_c = 0.005$ inches, $h_D = 0.002$ inches, $E_c = 10^7$ lb/in² and the adhesive (I) being a commercially available room temperature material [9], having complex modulus properties as shown in Fig. 6. Typical response spectra, consisting of graphs of acceleration at a point about 1/3 the length of the beam from one end versus frequency, for constant current into the exciting transducer, are shown in Fig. 7. Typical experimentally measured loss

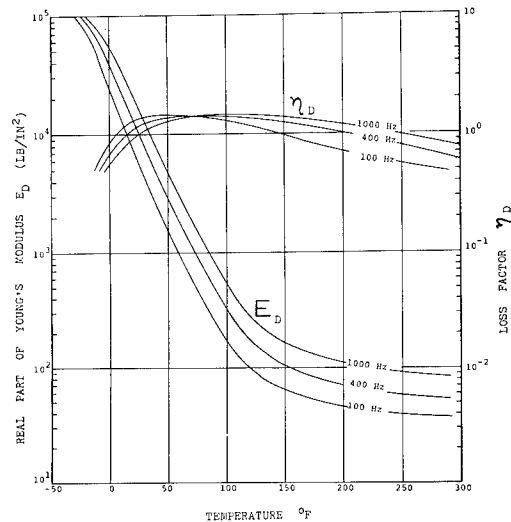


Fig. 6. Complex modulus properties of room temperature adhesive (Type I/3M-467)

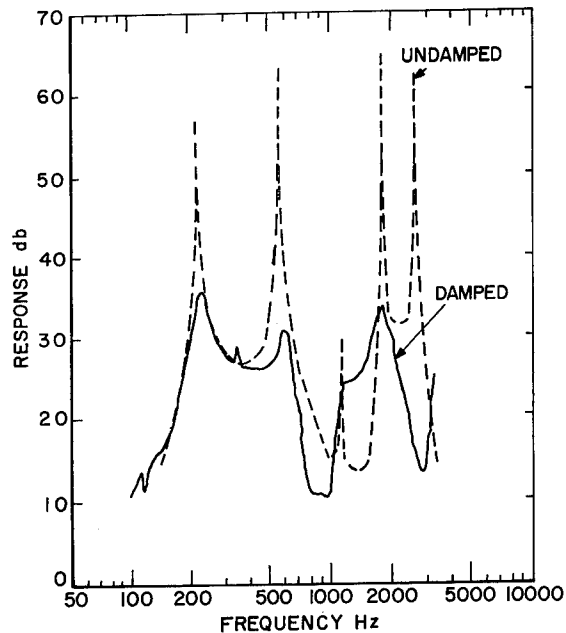


Fig. 7. Typical response spectra for clamped-clamped beam

factors for the first few modes are compared with analysis in Fig. 8. These results illustrate the secondary importance of wavelength as compared with temperature, as a parameter governing treatment behavior. Fig. 9 shows similar results for the first few modes of a low temperature adhesive/constraining layer system [10] having the same physical dimensions as before, but a different adhesive system (II) with complex modulus properties as shown in Fig. 10. The results again demonstrate the importance of temperature, and also the importance of selecting the appropriate material for a given problem.

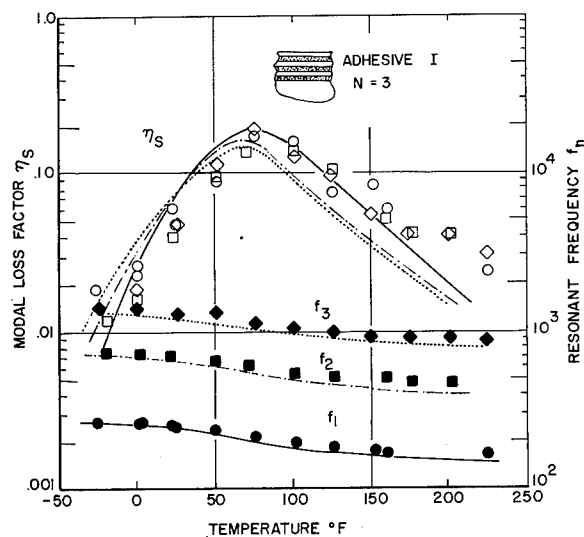


Fig. 8. Graphs of η_s and f_n versus temperature for single adhesive system on clamped-clamped beam ($h_c=0.005$ in., $h_D=0.002$ in.)

Double Adhesive/Single Constraining Layer Material System

If the physical dimensions of the aforementioned treatment remain unchanged, but one or more of the adhesive layers comprises a different adhesive from the others, then a very complex dynamical system results, which can be analyzed only with great difficulty. Experimental investigations are as readily conducted as for the single adhesive case, however. The three systems which have been investigated so far are illustrated in Figs. 3 and 4. System A consists of alternate layers of adhesive I and II separated by aluminum constraining layers 0.005 inches thick. System B consists of several layers of the treatment with adhesive I,

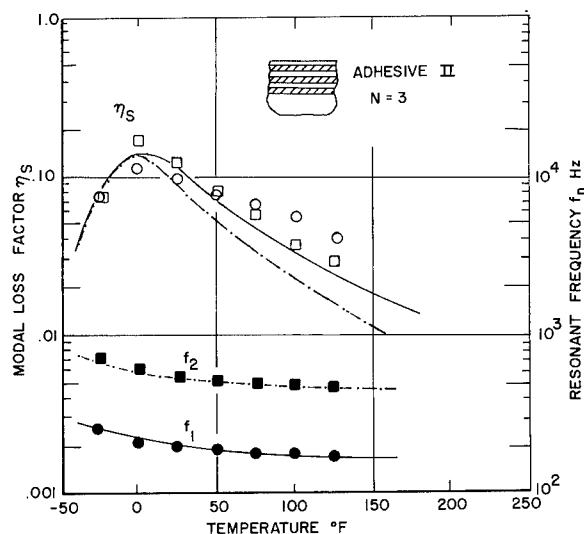


Fig. 9. Graphs of η_s and f_n versus temperature for single adhesive system on clamped-clamped beam ($h_c=0.005$ in., $h_D=0.002$ in.)

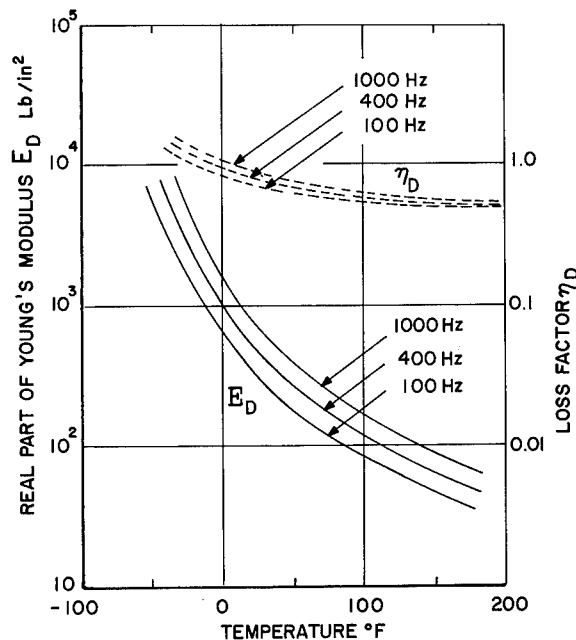


Fig. 10. Complex modulus properties of low temperature adhesive (Type II/3M-428).

with several layers of the treatment with adhesive II added on top. System C is the opposite of System B. Some test results for

System A are shown in Fig. 11, for System B in Fig. 12 and System C in Fig. 13. It is seen that the treatment geometry is an important parameter and, in particular, the order or sequence of the adhesive layers is very important. Systems A and B give the wide temperature capability desired, while treatment C is far less effective.

Systems A and C are difficult to analyze in any simple way, and no attempt to do so will be undertaken here. However, treatment B is more readily amenable to analysis. This is because the two subsystems each act as an equivalent free layer, with the stiffer "layer" adjacent to the structure, so that significant deviation of the treatment from classical free layer behavior is not expected. For treatment C, on the other hand, the softer "layer" is adjacent to the structure and will be subjected to shear rather than bending deformations as a result of the outer "layer" itself acting as a constraining layer. Equations (9) and (10) have been used to calculate η_s for treatment B and some of the results are illustrated in Fig. 12.

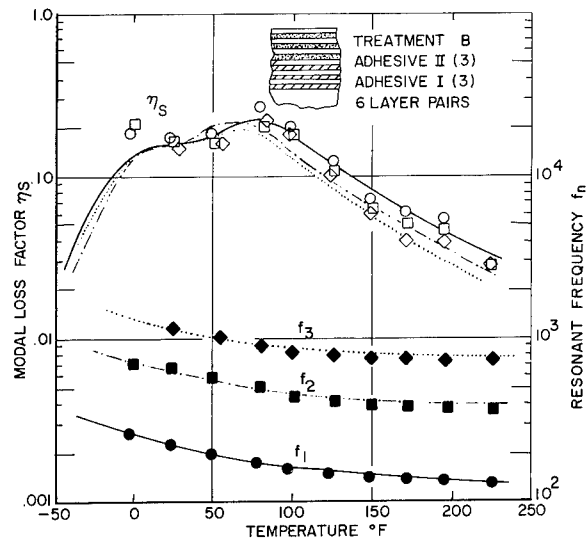


Fig. 12. Graphs of η_s and f_n versus temperature for damping treatment B on clamped-clamped beam ($h_c=0.005$ in., $h_D=0.002$ in.)

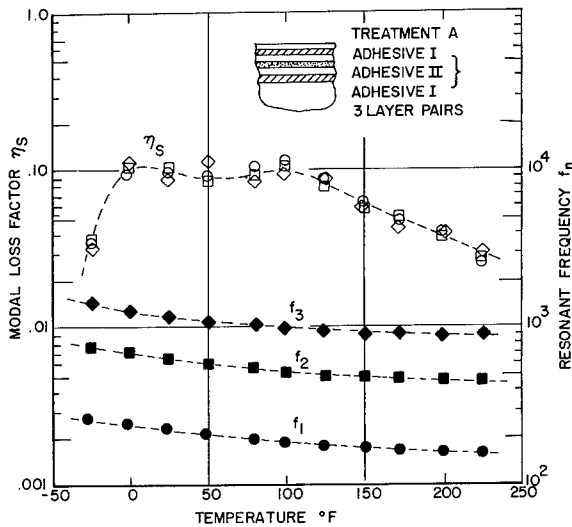


Fig. 11. Graphs of η_s and f_n versus temperature for damping treatment A on clamped-clamped beam ($h_c=0.005$ in., $h_D=0.002$ in.)

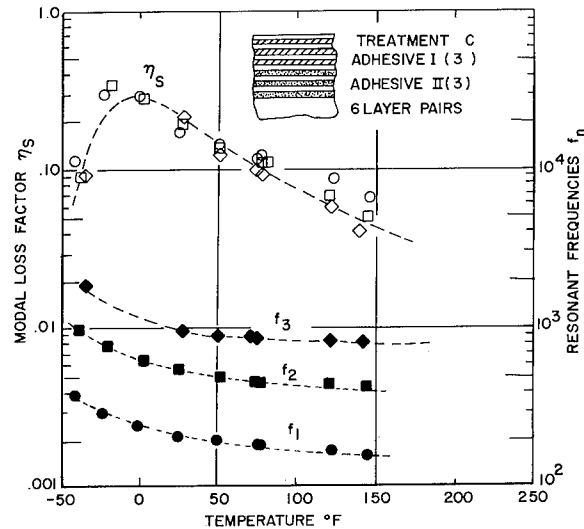


Fig. 13. Graphs of η_s and f_n versus temperature for damping treatment C on clamped-clamped beam ($h_c=0.005$ in., $h_D=0.002$ in.)

EXPERIMENTAL INVESTIGATION OF MULTIPLE LAYER CONSTRAINED TREATMENTS ON SKIN-STRINGER STRUCTURE

Single Adhesive/Constraining Layer Material System

When a free layer or equivalent free layer treatment is applied uniformly to the surface of a stiffened plate structure, the usual equations for a beam are replaced by the more general equations, (4) and (5). It has been shown [8] that for the particular structure investigated, illustrated in Figs. 14 and 15, $\beta_{nm}=8.0$. In the same way as before, therefore, we may estimate η_s and f_r as a function of temperature for the same treatments as used on the beam. Figure 16 shows typical undamped and damped response spectra consisting of graphs of acceleration versus frequency for excitation and pickup at the center. Figure 17 shows the measured and predicted modal damping for the single adhesive type of treatment on the structure, with adhesive system I.

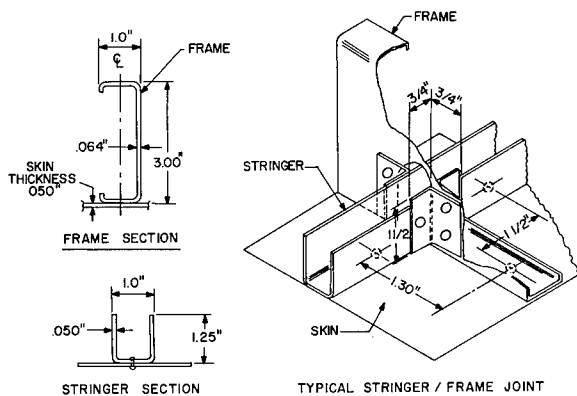


Fig. 14. Details of three-span skin-stringer structure

Two Adhesive Material/Single Constraining Layer Material System

Figure 18 shows the modal damping and resonant frequencies for the plate with a treatment of type B added, with adhesive system I in the first three layer pairs and adhesive system II in the outer three layer pairs. It is seen that analysis and experiment are in fair agreement and that the temperature range of useful damping is much broader than for the single adhesive system. Tests for systems C

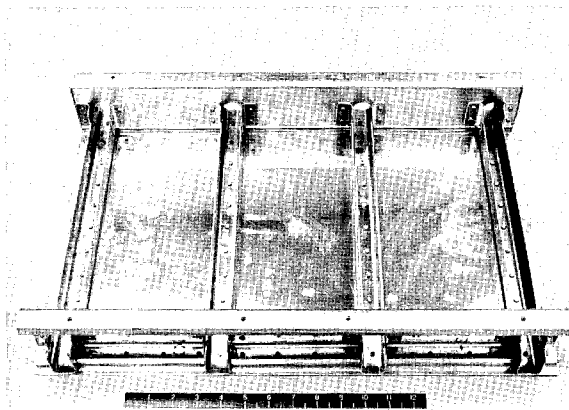


Fig. 15. Photograph of three-span skin-stringer structure

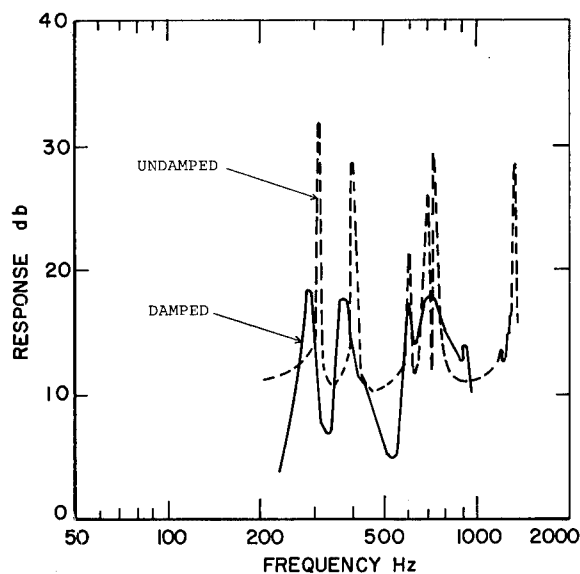


Fig. 16. Response spectra for three-span panel

and A have recently been completed, and the results were found to be qualitatively similar to those obtained for the clamped-clamped beam.

DISCUSSION AND CONCLUSIONS

It has been shown, on the basis of both experimental and analytical considerations, that multiple layer constrained damping treatments can be designed, using relatively simple analysis techniques, for broad temperature

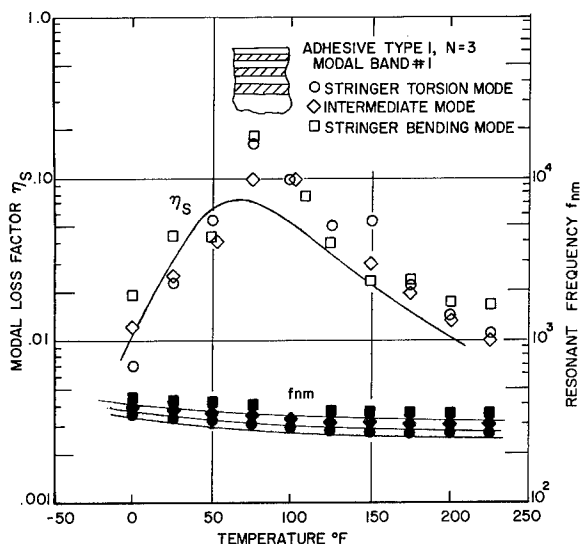


Fig. 17. Graphs of η_s and f_r versus temperature for single adhesive system (Type I) on three-span structure (3M-467)

range applications, given a knowledge of the complex modulus properties of the damping materials used and some structural parameters. Only a limited number of damping and constraining layer materials were considered in the paper but other materials may readily be evaluated using the analysis, including the use of epoxy-graphite composite materials in place of aluminum in the constraining layers, so as to increase damping and reduce weight, and the use of other damping adhesives as appropriate for other temperature ranges than those considered here. The relative simplicity of the analysis is most important because testing all possible damping treatment configurations is an immense task and the analysis will at least allow one to reduce the number of cases to be tested. Furthermore, although the parameter β_{nm} is difficult to predict for a given structural geometry, it is not difficult to measure. If β_{nm} is very large, say of the order of 10 or 20, then the modal damping is greatly reduced and the analysis again allows one to evaluate the effect of this parameter, simply by inserting several appropriate values in the equations. The procedure allows one to design treatments for specific applications with some degree of confidence, provided that the needed information is on hand.

ACKNOWLEDGMENTS

The work reported in this paper was conducted at the Air Force Materials Laboratory under Project No. 7351, Task No. 735106. Assistance in conducting the experiments by M. Parin and C. Porubchansky, in assisting with electronic instrumentation problems by S. Askins, in typing the manuscript by B. Dues and S. Lindsay and in preparing the figures by Mr. DeMarey is gratefully acknowledged.

REFERENCES

1. D. I. G. Jones and W. J. Trapp, "Influence of Additive Damping on Resonance Fatigue of Structure", *Journal of Sound and Vibration*, 17 (2), 157-185, 1971.
2. D. I. G. Jones, J. P. Henderson, and A. D. Nashif, "Reduction of Vibrations in Aerospace Structures by Additive Damping", *Shock and Vibration Bulletin* 40, Part 5, 1-18, 1969.
3. J. P. Henderson and A. D. Nashif, "Reduction of Interior Cabin Noise Levels in a Helicopter through Additive Damping", paper presented at 44th Shock and

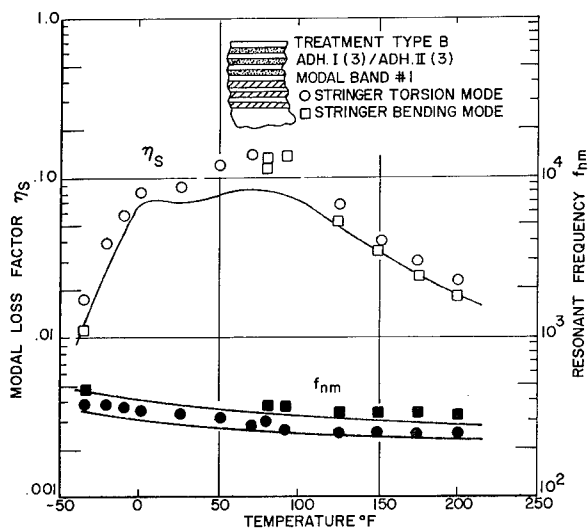


Fig. 18. Graphs of η_s and f_r versus temperature for damping treatment B on three-span structure

Vibration Symposium, Houston, Texas, December, 1973.	E_D	real part of Young's modulus of damping material
4. "Constrained Layer Treatments for Noise Control in a Helicopter", to be published as an Air Force Materials Laboratory technical report, 1974.	E_c	constraining layer modulus
	E_e	effective Young's modulus
	E_e^*	complex Young's modulus
5. "Test Report on HH-53 Helicopter; Effect of Multilayer damping Treatment on Vibratory and Interior Acoustic Environment", to be published as an Air Force Flight Dynamics Laboratory technical report.	E_1, E_2	Young's modulus for layer 1, 2
	e	E_D/E - modulus ratio
	e_1, e_2	modulus ratios
6. D. I. G. Jones, A. D. Nashif and M. L. Parin, "Parametric Study of Multiple-Layer Damping Treatments on Beams", Journal of Sound and Vibration, 29 (4), 423-434, 1973.	f	frequency (Hz); also function
	f_n	nth natural frequency
	f_{nm}	nmth resonant frequency
7. R. Plunkett and C. T. Lee, "Length Optimization for Constrained Viscoelastic Layer Damping", Journal of the Acoustical Society of America, 48, 150-161, 1970.	f_{onm}	nmth natural frequency
	f_r	resonant frequency of damped system
8. D. I. G. Jones, "Effect of Free Layer Damping on Response of Stiffened Plate Structures", Shock and Vibration Bulletin 41, Part 2, 105-120, 1970.	F	force
	g	function
9. Room temperature adhesive (3M-467) supplied by Minnesota Mining and Mfg. Co., Minneapolis, Minnesota. Same damping properties as ISD-112 material, same source.	h	thickness of plate or beam
	h_D	thickness of damping material
	h_c	thickness of constraining layer
	h_e	net thickness of damping layers
10. Damping tape system with low temperature viscoelastic adhesive (3M-428A) supplied by Minnesota Mining and Mfg. Co., Minneapolis, Minnesota. Adhesive has same damping properties as ISD-113 material, same source.	h_1, h_2	thickness of damping layer 1, 2
	$I, I_D, I_B, I_{D1}, I_{D2}$	second moments of area
	L	length of plate between stringers
	ℓ	breadth of plate
	m	measure of neutral axis position
	n	h_D/h - thickness ratio
	n_1, n_2	thickness ratios
	N	number of layer pairs
	N_1, N_2	number of layer pairs in treatments 1, 2
	P_{pq}	generalized force in pqth mode
SYMBOLS		
A, A_1	dimensionless constants	
B, B_1, B_2	dimensionless constants	
D	subscript denoting damping materials, flexural rigidity according to context	
D_e, D_o	flexural rigidities	
E	Young's modulus of elastic material	

r	ratio of λ_n to half wavelength of plate in direction parallel to stringers
S	area of plate skin
W	transverse vibration motion of plate
x, y	coordinates
Z	non-dimensional modal stiffness parameter
α_n	dimensionless constant
β_{nm}	dimensionless constant
γ_{nm}	non-dimensional parameter
δ	y/l
ϵ, ϵ_0	strains
Δ	x/L
η_D	loss factor in tension-compression
η_e	effective loss factor
η_s	modal loss factor of structure
η_1, η_2	loss factors of damping layers 1, 2
λ_n, λ_{nm}	modal half wavelengths
ν	Poisson's ratio
ξ_{nm}	nmth eigenvalue
ρ, ρ_e, ρ_D	densities
ρ_1, ρ_2	densities of damping layers 1, 2
σ	stress
ϕ_{nm}	nmth normal mode
Φ_{nm}	shear parameter
ω	frequency (rad/sec)

APPENDIX I

Multiple Free Layer Treatment on Stiffened Structure

Consider the treatment shown in Fig. 19. If the treatment shown behaves as a free layer treatment, the analysis closely parallels that shown in a prior paper [8]. We first

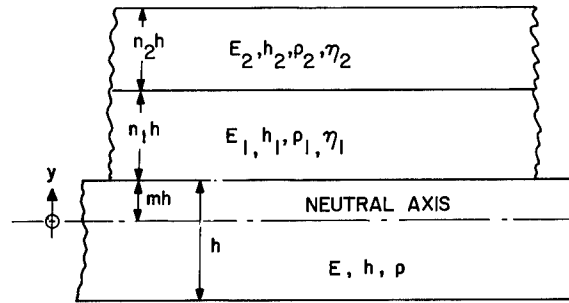


Fig. 19. Sketch of two-material free layer system

find the position of the neutral axis by making the net axial thrust as the plate bends equal to zero, i.e.:

$$F = \int \sigma dy = \sum_i \int E_i y (d^2W/dx^2) dy = 0 \quad (I.1)$$

$$\therefore \int_0^{mh} E y dy + \int_{mh}^{(m+n_1)h} E_1 y dy + \int_{(m+n_1)h}^{(m+n_1+n_2)h} E_2 y dy - \int_0^{(1-m)h} E y dy = 0 \quad (I.2)$$

This equation for the neutral axis position, given by m , eventually gives:

$$m = \frac{1 - e_1 n_1^2 - e_2 n_2 (2n_1 + n_2)}{2(1 + e_1 n_1 + e_2 n_2)} \quad (I.3)$$

The second moments of area of the beam, treatment 1 and treatment 2, are then given by:

$$I = \int_{-(1-m)h}^{mh} y^2 dy$$

$$= \frac{h^3}{24} A_1 \quad (I.4)$$

where A_1 is given by equation (I.1).

$$I_{D1} = \int_{mh}^{(m+n_1)h} y^2 dy$$

$$= \frac{h^3}{24} B_1 \quad (I.5)$$

$$I_{D2} = \int_{(m+n_1)h}^{(m+n_1+n_2)h} y^2 dy$$

$$= \frac{h^3}{24} B_2 \quad (I.6)$$

When A_1 , B_1 and B_2 are given by equations (I.1), (I.2), and (I.3). The net flexural modulus of the system is therefore given by:

$$D_e = D + D_D$$

$$= \frac{EI}{1-\nu^2} + \frac{E_1}{1-\nu^2} (1+i\eta_1) I_{D1}$$

$$+ \frac{E_2}{1-\nu^2} (1+i\eta_2) I_{D2}$$

$$= \frac{Eh^3}{24(1-\nu^2)} [A_1 + B_1 e_1 (1+i\eta_1)$$

$$+ B_2 e_2 (1+i\eta_2)] \quad (I.7)$$

The flexural rigidity D_o of the undamped system is given by

$$D_o = Eh^3/12 (1-\nu^2) \quad (I.8)$$

$$\therefore \frac{D_e - D_o}{D_o} = \frac{A_1}{2} - 1 + \frac{B_1 e_1}{2} + \frac{B_2 e_2}{2}$$

$$+ \frac{i}{2} [\eta_1 B_1 e_1 + \eta_2 B_2 e_2] \quad (I.9)$$

Thus far we have dealt with simple beam or plate theory. In reference [8], it is shown that for a free layer treatment applied to the surface of a stiffened structure, with full coverage by the treatment, the response is given by:

$$W = \sum_p \sum_q \frac{(P_{pq} L^4 / D_o) \phi_{pq}(x, y)}{\xi_{pq}^4 - \xi_e^4 \left(1 + \frac{\rho_e h_e}{\rho h}\right) + \frac{(D_e - D_o) 2 \xi_{pq}^4}{D_o \beta_{pq}}} \quad (I.10)$$

This is a fairly general analysis provided that the various assumptions implicit in the analysis are satisfied, and from it we may deduce the modal damping and stiffness because, if the plate were homogeneous and of loss factor η_s , the response would be:

$$W = \sum_p \sum_q \frac{(P_{pq} L^4 / D_o) \phi_{pq}(x, y)}{\xi_{pq}^4 (1+i\eta_s) - \xi_e^4 (1+\rho_e h_e / \rho h)} \quad (I.11)$$

The extra weight of the treatment is here accounted for in the term $1 + \rho_e h_e / \rho h$, and ξ_e^4 is a measure of the modal stiffness. Comparing equations (I.10) and (I.11) we see that:

$$\eta_s = \frac{\eta_1 B_1 e_1 + \eta_2 B_2 e_2}{\beta_{pq} + A_1 - 2 + B_1 e_1 + B_2 e_2} \quad (I.12)$$

$$Z^2 = (1 + \rho_e h_e / \rho h) (\xi_e / \xi_{pq})^4$$

$$= (1 + \rho_e h_e / \rho h) (f_r / f_{pq})^2$$

$$= 1 + \frac{A_1 - 2 + B_1 e_1 + B_2 e_2}{\beta_{pq}} \quad (I.13)$$

DISCUSSION

Mr. Carne (General Motors): What adhesives did you use?

Mr. Jones: They were commercially available adhesives. We purchased them on the open market. You can get these adhesives from any manufacturer the particular ones that we used were made by the 3M company. There are many others available, but you need to know the complex modulus properties of the adhesives that you use before you can do this or any other conditioning procedure and the problem is where to get the data.

Mr. Carne: Did 3M supply you with the complex modulus or did you do this yourself?

Mr. Jones: We did it ourselves, however you can obtain the data from 3M.

Mr. Carne: Did the results agree well with yours?

Mr. Jones: Yes.

Mr. Roberts: What is the major advantage in going from one layer of damping plus constraint to the multiple layer? What is the physical explanation of the gain in doing that?

Mr. Jones: Strictly speaking there is not necessarily any gain, you can certainly go to a single layer type treatment and gain more, but your problem very often does not lie there. If your prediction techniques are good enough you can come up with a single layer technique that will beat just about anything, but your problem is when you have a real structure that is vibrating excessively and you want to fix it immediately, you usually have to come up with something quick. There are two ways to look at this. You can use a multiple layer treatment to give you an idea whether damping is going to work at all, and this is something of concern to you; then you can go to those more refined analyses and come up with perhaps a single layer treatment that will do better than this. But that is a more difficult task and you have to give yourself time to do it especially for built up structures. As far as physical explanations, as I said, this is not necessarily a better treatment although as you can see from the results, it is a perfectly acceptable treatment, it gives you very good results. Up to about between 5 and 7 or 8 layers, or layer pairs, you do not get any great reduction in efficiency; if you start going to large number of layers, like 15-20, the law of diminishing returns sets in but that does not apply until you get a fairly large number of layers.

Mr. Ungar (Bolt Beranek & Newman): I noted that all of the analyses are really beam type analyses of multi layered treatments; then everybody goes ahead and applies these treatments and the analyses to two dimensional structures, such as plates, and it works. Why?

Dr. Jones: First of all it does not work unless you take into account the stiffness, and the curvature of your structure. For example, if you apply this type of treatment to a stiffened curved structure you will get qualitatively similar behavior but you will get a lot less damping, and in that respect, your prediction does not work unless you take into account some of the characteristics of the structure itself. In reality you are going back to the very fundamental approach to predicting damping; that is you calculate both the energy dissipated and the energy stored in the structure in a given mode, and the energy dissipated divided by 2 times the energy stored is the modal damping. As long as that kind of relationship is applicable and provided you can identify all of the sources of strain energy and energy dissipation, you are using the fundamental approach to the prediction of damping and that is why it works. But in the case of a curved stiffened structure the energy stored is a lot higher, for a given displacement in a given mode, than it is in a flat structure or a beam, and you get less damping and it is very important to be able to predict how much less.

Mr. Carne: Did you calculate the cost per square foot of the additive damping?

Dr. Jones: We know the cost per square foot of this particular treatment; the cost per square foot depends on the cost of the metal layers and the adhesive layers from the manufacturer and there are also the manufacturing cost themselves. If you are going to use this type of treatment on refrigerators you better count those costs very carefully because they are quite high, on the order of a few dollars per square foot. For aerospace applications that is not too crippling a price, because when you are solving a structural problem on a \$100,000 project two dollars is not going to worry you; this also applies to the problem of noise control in helicopters the cost is not high in view of what you are trying to solve, but you have got to bear in mind that these costs are calculable.

REDUCTION OF INTERIOR CABIN NOISE
LEVELS IN A HELICOPTER THROUGH ADDITIVE DAMPING

John P. Henderson
Air Force Materials Laboratory
Wright-Patterson AFB, Ohio

and

Ahid D. Nashir*
University of Dayton, Research Institute
Dayton, Ohio

INTRODUCTION

The task of reducing the noise generated by machinery to acceptable levels involves a very complex technology because of the multiplicity of noise sources and transmissibility paths, the latter including both airborne and structure-borne vibrations. Very frequently, an important part of the overall noise in a system is due to secondary noise radiation from resonating structural surfaces. In these particular instances, the noise control problem becomes identical with that of reducing structural vibrations. This type of problem can frequently be solved, in a cost-effective manner, by use of special energy dissipating materials which are applied to the system in a judicious manner so as to efficiently introduce vibration damping.

One particular problem falling into this category is that of reducing cabin noise in the HH-53 helicopter. In this case, specific structural resonant frequencies coincide with discrete excitations occurring at gear tooth-pass frequencies in the transmission. This paper is a discussion of an investigation of the application of layered damping treatments to the skin-stringer structure of the fuselage in order to reduce specific peaks in the noise spectrum caused by resonant vibrations of skin panels.

DESCRIPTION OF THE NOISE PROBLEM

The particular system investigated was an Air Force HH-53C helicopter, manufactured by Sikorsky Aircraft Company. The HH-53C is powered by 2 GE T-64-7 engines, with a 6-bladed main rotor. Its primary mission in the Air Force is Air Rescue, with transportation of personnel and equipment as a secondary function. Figure 1 shows a side-view of this system with fuselage station numbers and water line references. Acoustic data measured, prior to this investigation, in the middle of the cabin near station 342, showed high sound pressure levels at three frequency peaks as illustrated in Figure 2.

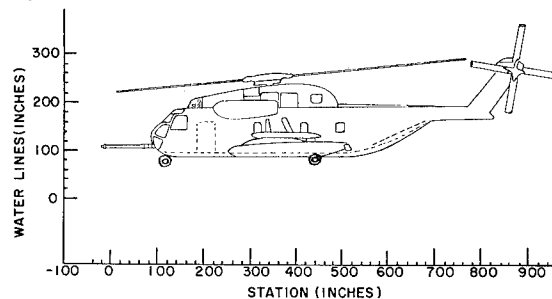


Figure 1 - Sideview of HH - 53 Helicopter

These frequencies were nominally 1370 Hz, corresponding to the first stage planetary gear clash, 2700 Hz corresponding to the main bevel and tail take-off gear clash, and 5400 Hz corresponding to the rail spur gear clash. It was estimated that a major noise source in the cabin was the resonant vibration of the

* Now at Structural Dynamics Research Corporation Cincinnati, Ohio

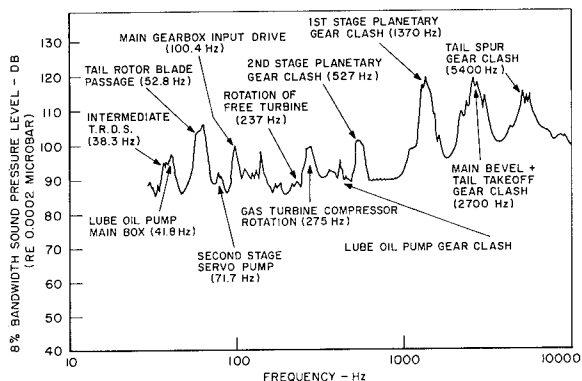


Figure 2 - Eight percent bandwidth Sound Pressure Level data.

fuselage skin which was excited by these gear clash vibrations of the transmission. If this was indeed the case, then damping of the skin would be an effective means of reducing cabin noise at these frequencies.

Standard-equipment acoustic blankets, consisting of a layer of fiberglass sandwiched between layers of heavy vinyl cloth can easily be attached to the inside of fuselage frames for the reduction of cabin noise, but are seldom used in the field. The objections to these standard acoustic treatments are that they interfere with maintenance and make rapid inspection and repair of battle damage in combat situations impossible. Therefore, the using command was interested in the layered damping treatments, which have the advantage of being attached directly to the skin out of the way of maintenance and inspection operations.

SCOPE OF THIS INVESTIGATION

The purpose of this investigation was, first of all, to obtain additional data on the nature of skin panel resonant vibrations and their contribution to the noise problem in the cabin. Secondly, it was desired to evaluate the reduction of these resonant responses through the application of a layered damping treatment known to be effective over the temperature range expected in these tests. No attempt was made to treat the entire aircraft, or test a material which would be suitable for the entire range of temperature of environments expected in world-wide USAF operations.

A small portion of the cabin structure near the transmission, between stations 322 and 362 and above water line 140, was chosen for detailed measurements and the application

of the damping material. Seventeen accelerometers were mounted at various locations on the transmission housing, on the heavy frames supporting the transmission, and on several skin panels in the area. Locations of some of the accelerometers are shown in Figures 3 and 4. Care was taken when choosing accelerometer sizes to avoid undue mass loading of the structure being measured.

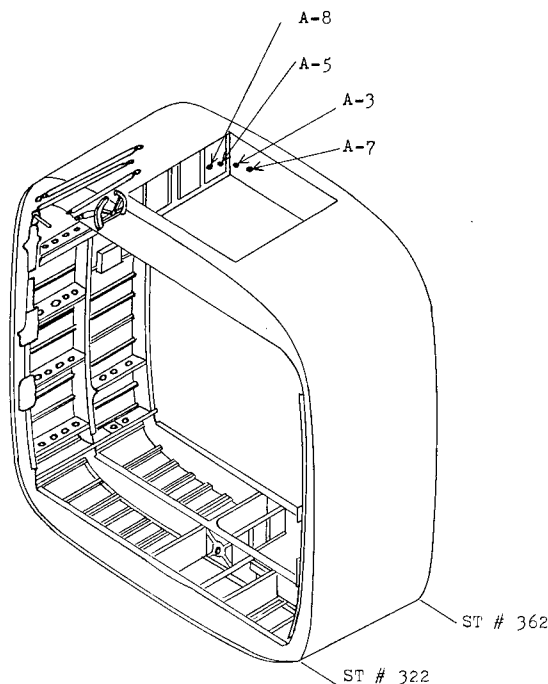


Figure 3 - Isometric view of center cabin structure where damping was applied

Five piezoelectric microphones were also located within this section of the cabin, as well as six thermocouples for monitoring structural temperatures. In-flight data recording equipment, calibration, and data reduction was provided by the Vehicle Dynamics Division, of the Air Force Flight Dynamics Laboratory. Since only a small portion of the aircraft was treated with damping materials, flanking paths for noise radiated from other sources were reduced by installing fiberglass blankets over the untreated panels and reducing the noise radiated through the transmission drip pan with alternate layers of fiberglass and lead-vinyl cloth. Photos of the treated area of fuselage skin are shown in Figures 5 and 6.

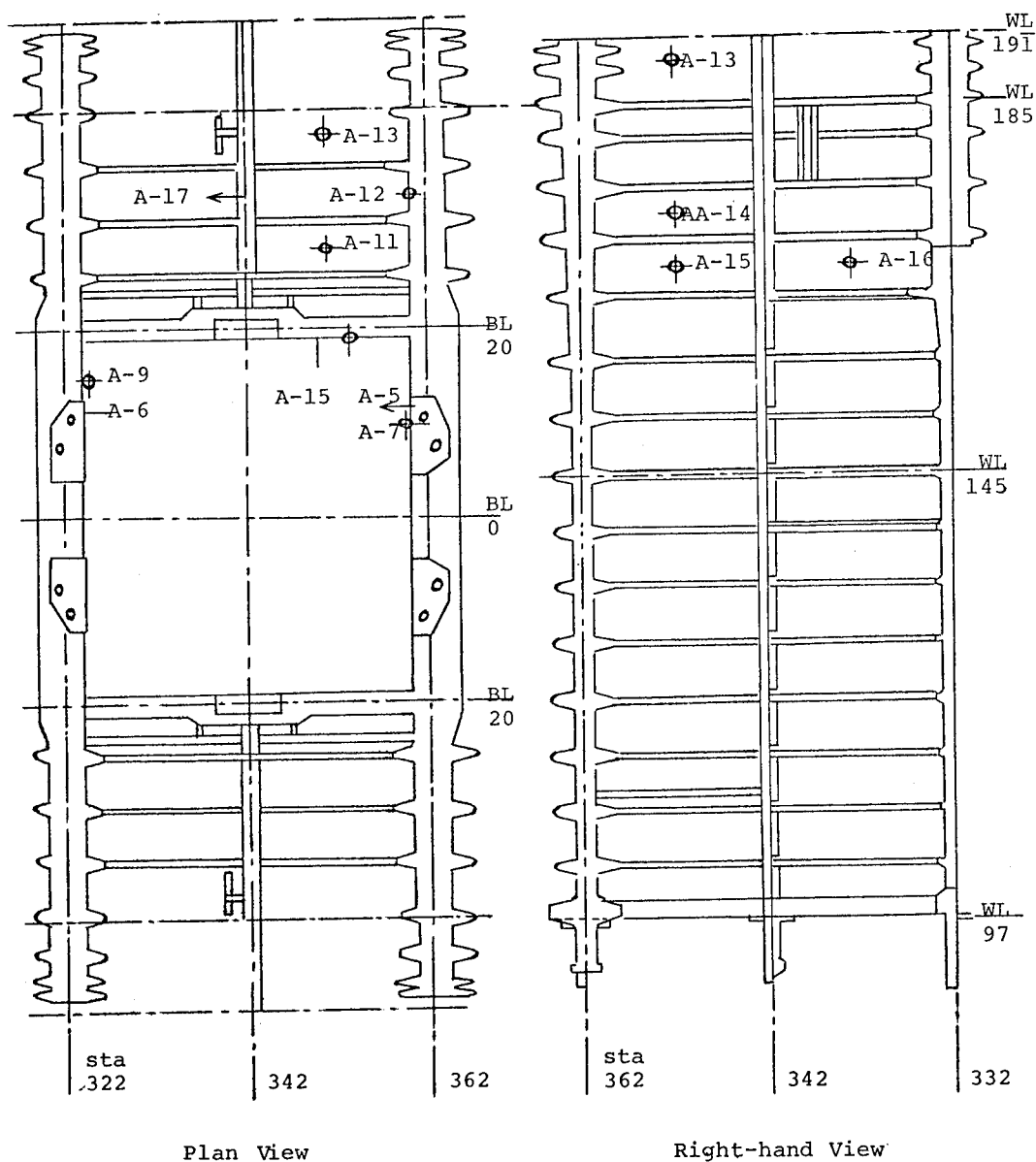


Figure 4 - Center cabin skin-stringer structure layout

Vibration and acoustic measurements were recorded during four flights of the helicopter to assess the effectiveness of the damping treatment. Several maneuvers were performed in each flight, to show the effects of the flight variables. Vibration measurements were also conducted on the ground utilizing harmonic excitation to compare dynamic response before and after adding the layered damping treatments.

DAMPING TREATMENT AND TEMPERATURE EFFECTS

Elastomeric damping materials can be very effective if applied in an appropriate geometry and utilized within their transition temperature region, to achieve optimum performance [1]*. Such materials reach their peak

* [] refer to listed references

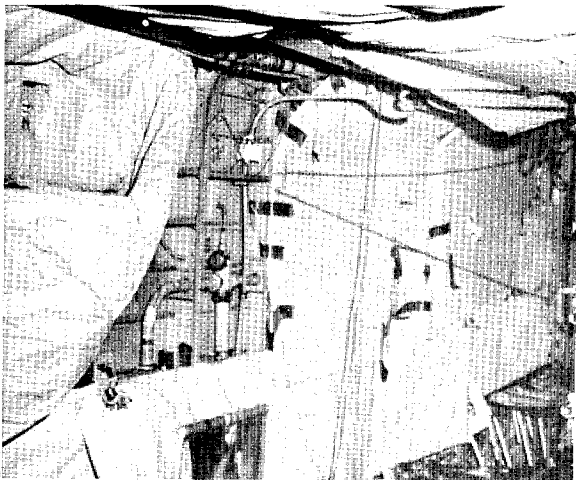


Figure 5 - Photograph of treated area

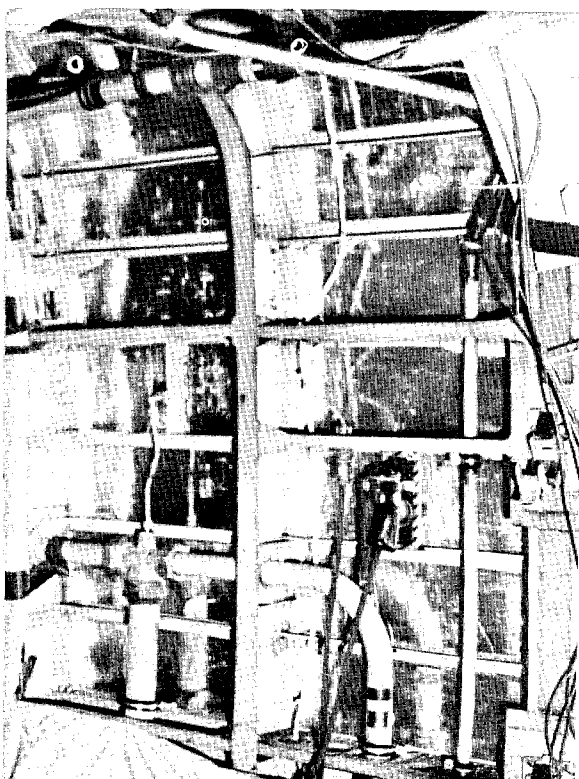


Figure 6 - Photograph of treated area

loss factor and optimum shear modulus in the transition temperature region between the glassy state at low temperature and the rubbery state at higher temperatures, as illustrated in Figure 7. The damping material applied in this investigation was a pressure

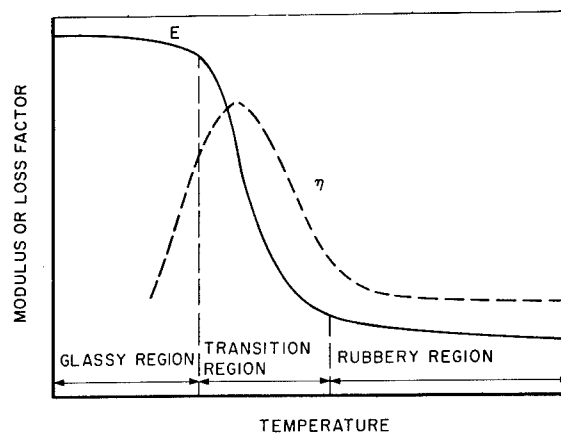


Figure 7 - Variation of the properties of a typical damping material with temperature

sensitive adhesive which has optimum damping near room temperature. The complex shear modulus properties of this material as a function of temperature are shown in Figures 8 and 9.⁺⁺

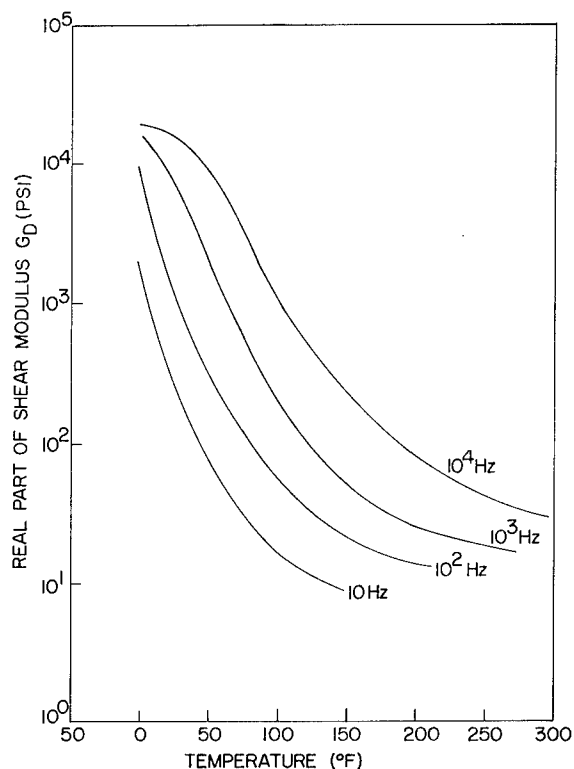


Figure 8 - Variations of the real part of shear modulus with temperature and frequency

⁺⁺ Minnesota Mining and Manufacturing Co., 467 adhesive (similar to current material designated ISD-112), measured at AFML [1]

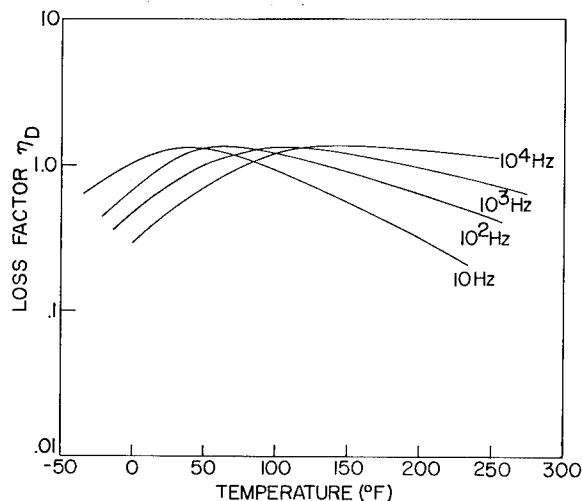


Figure 9 - Variations of the loss factor with temperature and frequency

The geometry of the layered damping treatment is illustrated in Figure 10, and consists of three (3) layers (0.002 in. thick each) of damping adhesive and three (3) alternate constraining layers (0.005 in. thick each). This treatment was selected because it would give high damping in the panels over the anticipated temperature range of the tests. However, for in-service applications, it may be necessary to cover a wider temperature range. This can be accomplished by combining different damping adhesives with different transition regions.

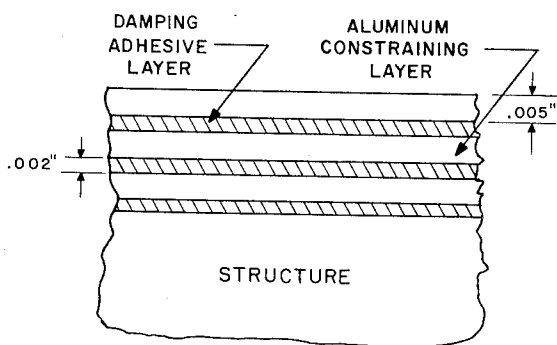


Figure 10 - Layered damping treatment

Figure 11 illustrates the effect of this procedure for a simple clamped-clamped beam with the same thickness and frequency as the panels considered in the helicopter tests [2]. It can be seen from the figure that high damping can be achieved, by the proper

selection of damping materials, over a wide temperature range from -25°F to +200°F.

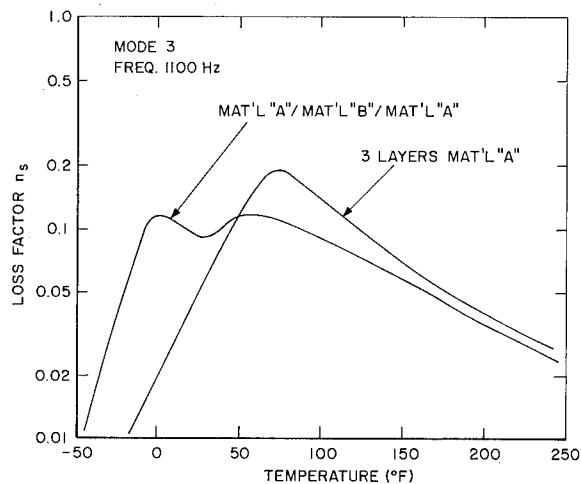


Figure 11 - System loss factor of a clamped-clamped beam with multiple layer damping treatments

TEST RESULTS

Flight Tests: Narrow band (50 Hz) analysis of a small portion of the flight test data [3] is presented in Figures 12-16 and summarized in the Table 1, for purposes of illustrating the effects of the damping treatment. Accelerometer A-14 was located on a skin panel at fuselage station 352, and water line 172. Microphone M-3 was located 5 inches below the transmission drip pan. Flight 1 was with an untreated aircraft and Flight 3 was with damping treatment installed.

It can be seen from these plots that the three gear clash frequencies correspond to peaks in the accelerations measured on the skin and in sound pressure levels measured in the cabin. Accelerations of the damped skin of the structure in the frequency band around 1370 Hz were generally reduced as much as 12 dB in the one-third octave band analysis and 14 dB in the narrow-band analysis, as compared with the undamped structure. There are indications that damping reduced the sound pressure levels at microphone M-3 near the skin and microphone M-5 under the transmission drip pan. Reductions in narrow band acceleration, and acoustic levels for the three frequency bands of interest, are shown in Table 1.

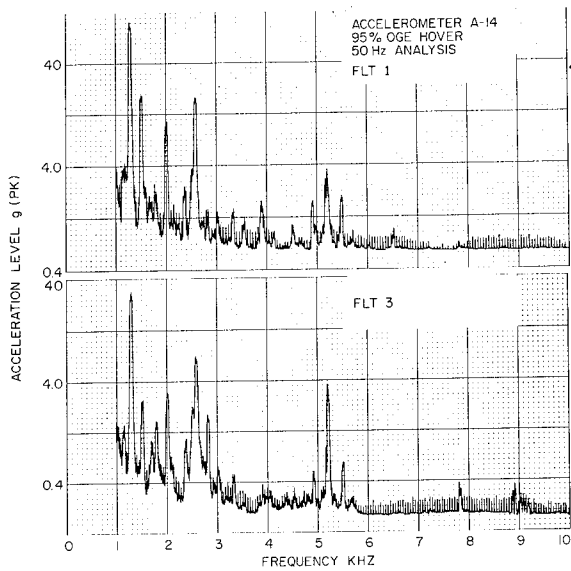


Figure 12 - Acceleration - 95% OGE hover

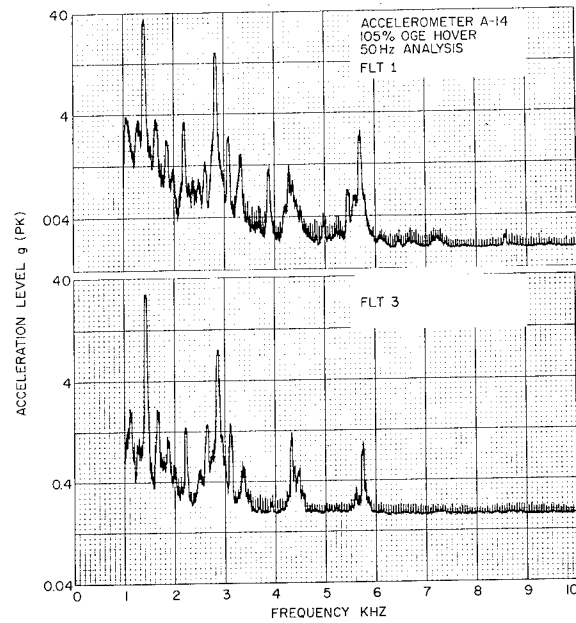


Figure 14 - Acceleration - 105% OGE hover

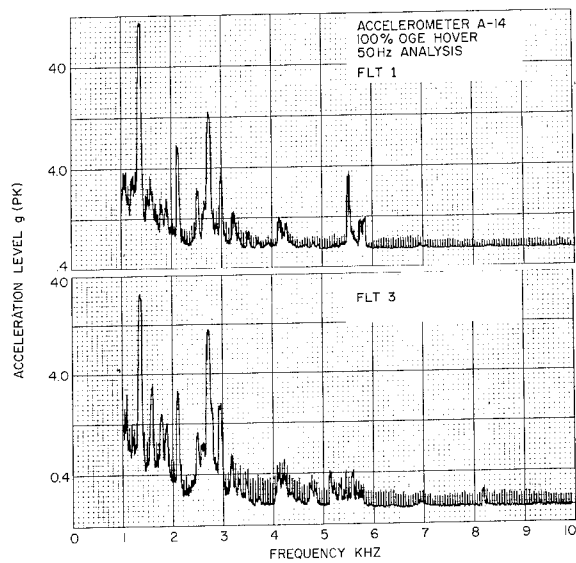


Figure 13 - Acceleration - 100% OGE hover

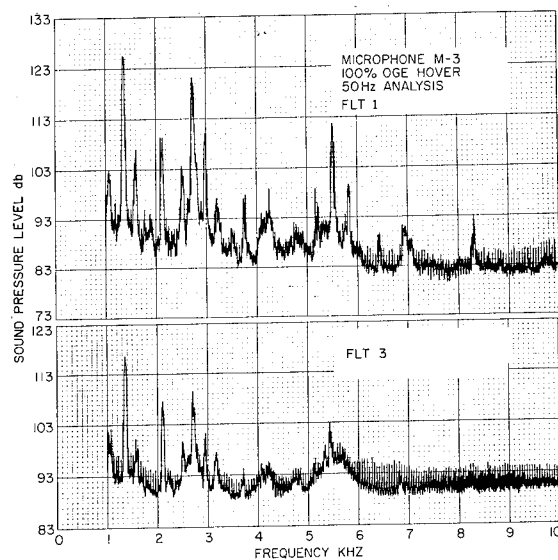


Figure 15 - Microphone M-3 data

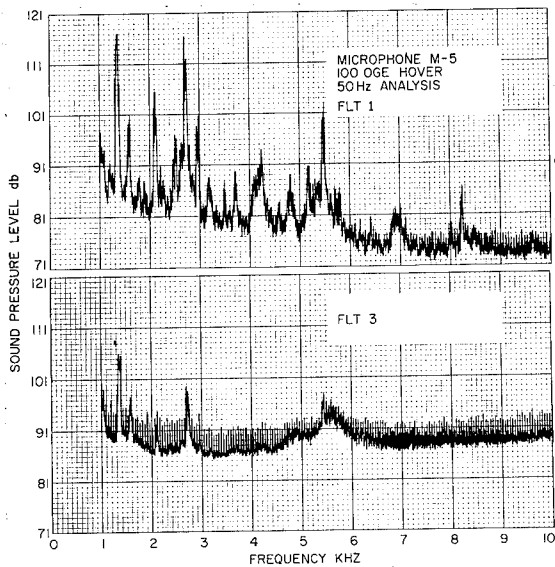


Figure 16 - Microphone M-5 data

TABLE 1

NARROW BAND ACCELERATION AND ACOUSTIC LEVELS OF FLIGHT 3 COMPARED WITH FLIGHT 1.

Acceleration (A-14): dB ref. flight 1			
	1370 Hz	2700 Hz	5400 Hz
O.G.E. Hover 95 %	-11 dB	-9 dB	0 dB
O.G.E. Hover 100 %	-13	-2	-10
O.G.E. Hover 105 %	-2	-5	-9
Sound Pressure Level -O.G.E. Hover 100 %:			
M-3	-10	-12	-9
M-5	-11	-17	-7

It must be remembered that large changes in acoustic levels due to damping were not anticipated because only a small portion of the structure was damped, noise radiating from other sources such as undamped skin and the transmission drip pan was not completely controlled, and the fact that cabin noise at these high frequencies (and hence short wave lengths) is not fully defined with measurements at a few microphone locations. In spite of these difficulties, there does appear to be a general trend in the data indicating a reduction of high frequency noise levels at microphones M-3 and M-5.

Ground Tests: Artificial excitation tests were conducted, with the helicopter on the ground, to establish the effectiveness of the

damping treatment in reducing the skin vibrational amplitudes. A harmonic force with constant amplitude was applied to the transmission supporting frame by means of an electromagnetic shaker, through an impedance head as illustrated in Figure 17. Frequency response spectra were obtained at the center of a panel by means of an accelerometer (A-14). Figure 18 represents the measured response spectra, a) without damping treatment, b) with damping treatment on the panel of interest only and c) with damping treatment on all panels; respectively. It can be seen from this figure that a considerable reduction, approximately 10 db, in amplitude was achieved in the peak near 1370 Hz, as anticipated.

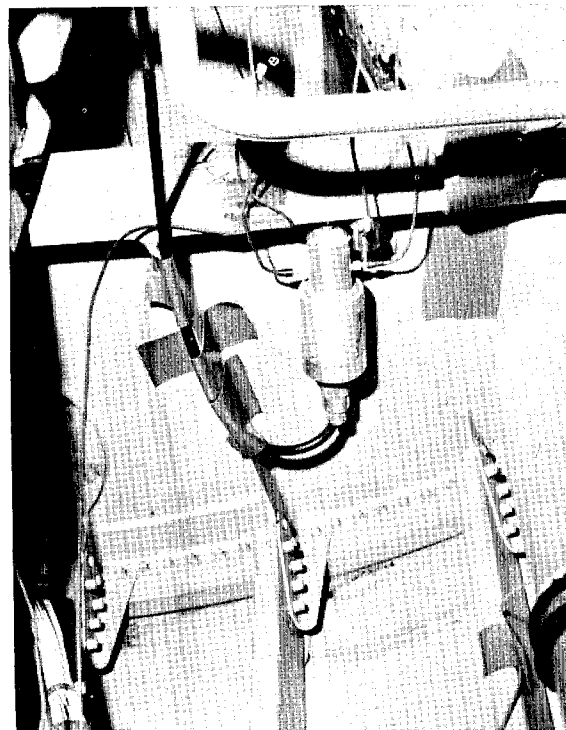


Figure 17 - Photo of impedance head and exciter

Mode shapes were measured by moving a very light accelerometer⁺⁺ along the panel while exciting a panel resonance. In general, for modes near 1370 Hz, it was found that node lines parallel to the stringers were spaced at intervals of about 1.5 inches, and that node lines parallel to the frames were spaced about 5 inches apart. Segments of panels on opposite sides of node lines were

⁺⁺(Endevco Model 22)

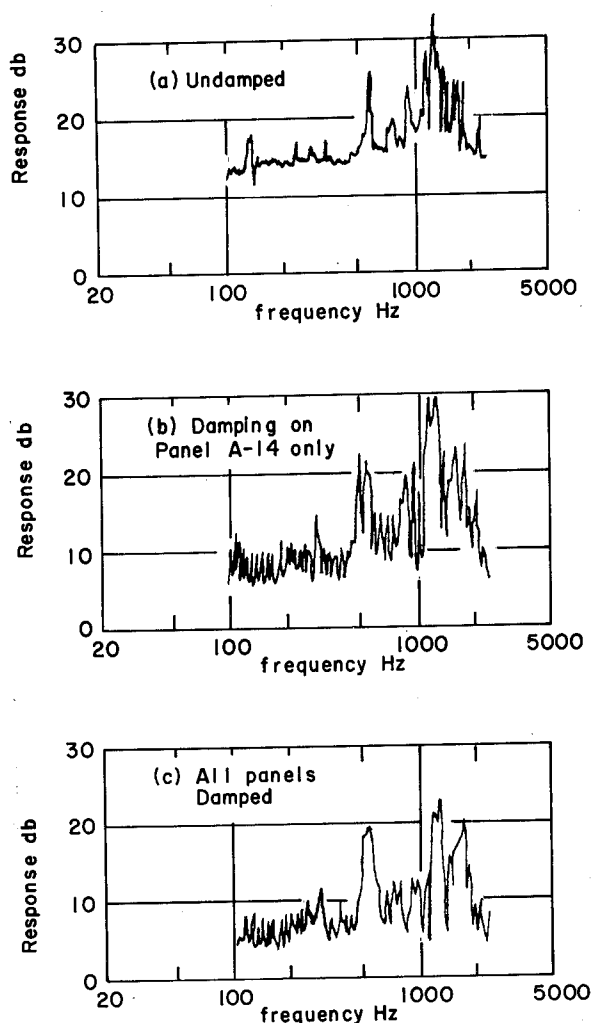


Figure 18 - Typical ground vibration test spectra

generally out of phase. There were several resonant frequencies of the skin near 1370 Hz so that slight changes in excitation frequency excited different modes in the skin stringer-structure. The higher frequency peaks near 2700 Hz and 5400 Hz correspond to resonances in the heavy supporting frame as well as in the skin-stringer structure.

SUMMARY AND CONCLUSIONS

Four flight tests plus additional ground tests were performed on an HH-53C helicopter for the purposes of evaluating the effectiveness of multiple layer damping treatments, applied to the skin, as a means of reducing high frequency cabin noise. Acceleration, acoustic, and temperature measurements were made on the aircraft at several locations and for

several flight conditions. Although only a small portion of the structure was covered with damping treatments, significant reductions (up to 12 db) in skin accelerations were noted at frequencies where the skin is a major noise source. Acoustic measurements indicated a reduction in high frequency noise levels in the cabin, of approximately 5-11 dB, although quantitative measurements were difficult to make because of the small area treated, the multiplicity of noise sources, and other variations in flight conditions.

The following conclusions may be drawn from the results of this investigation.

a. Cabin noise peaks that occur near 1370 Hz, 2600 Hz, and 5400 Hz correspond to specific gear clash frequencies. At these frequencies, the transmission causes the heavy supporting frame to vibrate. This in turn excites resonant frequencies in the skin-stringer structure. Much of the noise in the cabin is a result of the resonant response of the cabin structure.

b. The damping treatment applied in this test was shown to be effective, at the test temperatures, in reducing skin vibrations, particularly near the 1370 Hz peak, and thus reducing radiated noise in the cabin.

c. Although the feasibility of using damping treatments to control cabin noise has been demonstrated for one limited temperature range and for partial coverage of the cabin skin, different materials for broader temperature ranges and additional coverage would be required in a practical HH-53 modification.

d. The transmission drip pan is a major cabin noise source and should be modified to increase acoustic transmission loss in any future noise control efforts.

Subsequent to the completion of this investigation, damping treatments, similar to these, have been used as part of noise control treatments on some HH-53, VH-3, and SH-3H helicopters. In the Air Force HH-53 helicopters, approximately 150 ft² of coverage was used, with a total weight of about 37 pounds per aircraft. This treatment could be installed in the aircraft with about 24 manhours of labor. In each case the damping materials were chosen to provide maximum damping over the expected environmental temperature range, and additional acoustic absorption material was used to reduce cabin reverberation time.

ACKNOWLEDGMENTS

The authors wish to acknowledge the efforts of several individuals in this investigation. Particularly the tireless efforts of the AFFDL/FYS test crew consisting of Ed Hotz, Jim McIntosh, and Jim Willenborg, as well as George Buchalter of the University of Dayton Research Institute. The helicopter was provided by Military Airlift Command with Maj. Don Jenson as test pilot. Data analysis was conducted by John Ach and Lowell Vaughn (AFFDL/FYS). Manuscript was typed by Miss Becky Dues, and Miss Susan Hawkey.

REFERENCES

1. Nashif, A. D., "Materials for Vibration Control in Engineering" Shock and Vibration Bulletin, Bulletin 43, Part 4, PP-145-151, (June 1973).
2. Jones, D.I.G., "Design of Constrained Layer Treatments for Broad Temperature Damping" presented at the 44th Shock and Vibration Symposium.
3. "HH-53C Helicopter - Effect of Multi-layer Damping Treatment on Vibratory and Interior Acoustic Environment" Air Force Dynamics Laboratory Test Report (AFFDL/FYS) to be published.

DISCUSSION

Mr. Pakstys (General Dynamics/Electric Boat Div.): Why did you use the three layer treatment instead of a one layer treatment?

Mr. Henderson: Frequently in a multiple layer treatment you are trying to optimize a treatment so that the damping material is exposed to high strain. Generally speaking it is easier to do this in a multiple band treatment on a structure such as this. These materials can withstand tremendously high shear strains; there was one investigation several years ago where they took them to unity shear strain from millions of cycles, and if you want to simplify damping treatments you should induce high shear strains in the viscoelastic material. Frequently it is easier to do this in a multiple layered treatment where you have very thin layers of adhesive. You can develop equivalent single layer treatments but in order to do this you have to get very stiff constraining layers, and to get that very stiff constraining layer you either have to use exotic materials, such as graphite epoxy or some other form of very stiff constraining layer, or it costs you weight; frequently this turns out to be the most practical solution. You can design single layer treatments that perform as well as these but it is easier with conventional materials to do it with multilayer treatments.

Mr. McKee (IIT Research Institute): What noise level does the Air Force want in the cabin of a helicopter?

Mr. Henderson: The Air Force would like to get a noise level such that you could sit in that cabin without ear protection and not undergo chance of hearing loss damage; we are a long way from that in the HH-53. All of the levels that I showed were what we call narrowband analyses, 50 Hz analysis. If you look at the 1/3 octave band levels that were also measured you can see that we are measuring levels that are high enough so that if a man were in that bare aircraft for over eight hours, with the standard Air Force hard hat on for ear protection, he is still running the chance of hearing loss damage. It exceeds the appropriate Aeromedical Laboratory specifications on recommended noise in the back of the aircraft; it is a very serious problem if you are going to fly long missions, and some of the projected missions can get to be quite long since this bird can be refueled in the air. The Air Force would like to see noise levels down to the point where men could walk around with no ear protection and discuss things with his friends and be heard, but I don't think that they are going to get there.

Mr. Ungar (Bolt Beranek and Newman Incorporated): What noise levels did you measure?

Mr. Henderson: We measured third octave band levels of approximately 126 db at these frequencies. The OSHA type numbers are somewhere around 90 db and the Air Force has regulations out on levels between this, depending on the type of protective equipment that the personnel are wearing.

Mr. McKee: Is there any hope of achieving those levels by additive acoustical treatment?

Mr. Henderson: Yes, there is hope of achieving this and Sikorsky aircraft, who is the manufacturer of this particular helicopter, has done a lot for that. If you were to go to Sikorsky and buy an executive helicopter, and they are in the process of selling some for the presidential fleet, they would put damping treatments on the wall as a result of our test. But in addition to damping treatments, they have fiberglass blankets, lead vinyl blankets, and more treatment in the aircraft than would be acceptable to the military. Complete acoustical treatments within a helicopter can reduce the noise to acceptable levels, but it is a question of whether it is acceptable for other reasons for military use.

Mr. Ungar: I seem to recall that some time ago we were involved in a helicopter noiseiness study and it turns out that sitting in one of these helicopters, the only way you can tell if you are being shot at is to look for holes since you can't hear the bullets coming and that's the truth. As a matter of fact somebody developed a bullet passage detector, and this is not a joke; and somebody developed a detector that sensed the shockwaves left behind by a bullet and it gave the pilot an

indication that he was being shot at otherwise he can't tell until it is too late, and then the problem is relatively trivial. I doubt that one can get 50 db rate of noise reduction just by treating the cabin of the aircraft by damping, absorption, or otherwise. A redesign of the transmission is required and I understand that the Army is considering an extensive study along these lines. How does one design a helicopter transmission so that it makes less noise, that is a tough problem; at any rate I think Dr. Henderson pointed out very well that damping is only one way of noise and vibration reduction.

VIBRATION DAMPING AND ISOLATION WITH
ENERGY ABSORBING COMPOSITES

John Nunes
Brunswick Corporation
Skokie, Illinois

A simple model system was developed in order to describe and predict the behavior of an energy absorbing composite by taking into account the component materials mechanical properties and the relative volume fractions of metal needed to optimize damping. Damping is obtained by yielding and plastically deforming one of the metal components during cyclic deformation of the composite. From this analysis, experimental composites have been developed which exhibit damping capacities of up to 40 percent. Other significant developments and observations that were obtained are:

- (1) At 550°F, 25 percent of the input mechanical energy was damped in a copper clad niobium reinforced monel composite.
- (2) Up to 7.5 million fatigue life cycles have been obtained on composites which had 15 percent damping. At resonant frequency conditions, lives of 100,000 cycles were measured for a composite with 40 percent damping.
- (3) Helical spring isolators made with a stainless steel-copper composite have exhibited resonant frequency transmissibilities as low as 3 for a double amplitude input displacement of 0.1 inches.

Finally, some empirical relationships are presented for input displacement and the static damping coefficient as a function of the resonant frequency transmissibility.

INTRODUCTION

Damping caused by plastic deformation has long been recognized as an important metallic property (1,3) which can mitigate the effects of overstressing experienced, for example, in low cycle fatigue and shock loading.

This paper describes the use of this type of damping (also called hysteresic damping) for vibration control utilizing composite materials designed to convert mechanical energy into heat energy due to the plastic deformation of one of the composite's metallic components. (Other damping mechanisms; e.g., viscous and frictional as well as other types of material damping; e.g., viscoelastic and magnetoelastic are not covered here.)

A composite of aluminum reinforced with silica fibers was one of the first systems (4) reported to have significantly higher damping capacities than the conventional alloys such as cast iron, copper-manganese and nickel-titanium (5). Subsequent studies on composite damping have included the aluminum-stainless steel (6) and the aluminum-boron (7) systems.

A simple model for predicting damping behavior is described and experimentally confirmed for many other material combinations here. Some empirical relationships between the resonant frequency transmissibility and damping and the input amplitude of a simple spring-mass system are described.

PL- 221/22
R00420191

MODEL SYSTEM

An energy absorbing composite model has been developed that takes into account the component materials mechanical properties and the relative volume fractions needed to achieve damping. Damping is obtained by yielding and plastically deforming one of the metal components during cyclic deformation of the composite. This damping behavior is characterized by a hysteresis loop whose enclosed area is proportional to the amount of energy dissipated in the form of heat. Figure 1 schematically illustrates the individual components and the resultant composite stress-strain curves. The idealized composite consists of at least two elements. One displays purely elastic properties and the other exhibits damping. Some basic assumptions made are:

- (1) The composite experiences a uniform stress field.
- (2) The rule-of-mixtures applies for the composite elastic moduli and stresses.
- (3) The ductile plastic component has zero work hardening and an isotropic yield behavior.
- (4) The elastic component yields at a strain at least twice that of the plastic component.

The primary modulus defines the area where little or no damping occurs because both components deform elastically. The secondary modulus is reached once yielding occurs in the weaker component. A closed hysteresis loop develops in this region during cyclic deformation (U_c) due to plastic deformation of the lower yield strength component. The energy of the damping component U_p is directly proportional to the composite damping U_c and varies with the volume fraction as follows:

$$U_c = V_y U_p \quad (1)$$

Where:

V_y = volume fraction of the plastic component

Also:

$$U_p = 2\sigma_y \epsilon_p \quad (2)$$

Where:

σ_y = yield strength of the plastic component

ϵ_p = plastic strain experienced by the component

(The derivation of the preceding equation as well as equations 2 to 4 will be published elsewhere.)

Equations developed which related the energy stored, U_B and the energy damped, U_C to the volume fraction and mechanical properties are as follows (see figure 1):

$$U_B = 4U_y \{V_E B C^2 + V_y (2C-1)\} \quad (3)$$

Where:

V_E = volume fraction of the elastic component

$$U_y = \sigma_y^2 / 2E_y$$

U_y = elastic energy storage of the plastic component

E_y = elastic modulus of plastic component

B = ratio of elastic moduli of elastic to plastic component

$$C = 1 + \epsilon_p / 2\epsilon_y$$

ϵ_y = elastic yield strain of the plastic component.

The energy damped, U_C , shown in Equation 1 can also be rewritten as follows:

$$U_C = 8 U_y V_y (C-1) \quad (4)$$

The ratio of U_C to U_B is called the static damping coefficient, C_s , and can be readily determined in a simple tension test.

Finally there is an initial elastic prestrain, ϵ_{ps} , which develops during the first deformation cycle. It can be shown that this develops from the internal stress state needed to obtain a stable hysteresis loop and is related to the composite moduli and the ductile component's yield strength as follows:

$$\epsilon_{ps} = \left[\frac{E_1 - E_2}{E_2} \right] \epsilon_y \quad (5)$$

Because of the internal cumulative strain damage associated with the cyclic plastic deformation of the damping component interest has centered on describing fatigue behavior as well as damping behavior employing analysis (6,7) similar to that described here. Also a more complex analysis has been

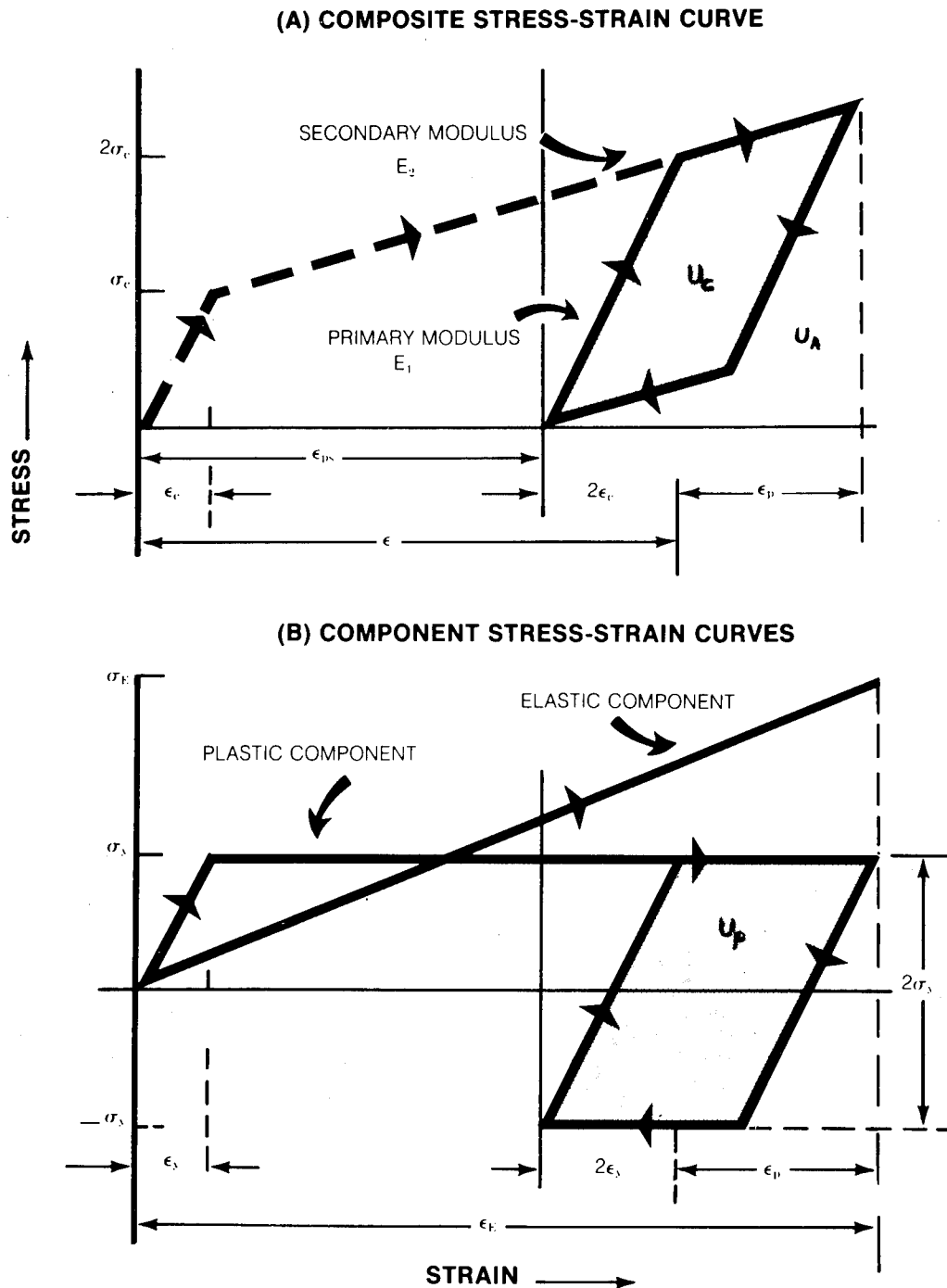


Figure 1. Idealized Stress - Strain Behavior for An Energy Absorbing Composite Under Static Loading Conditions.

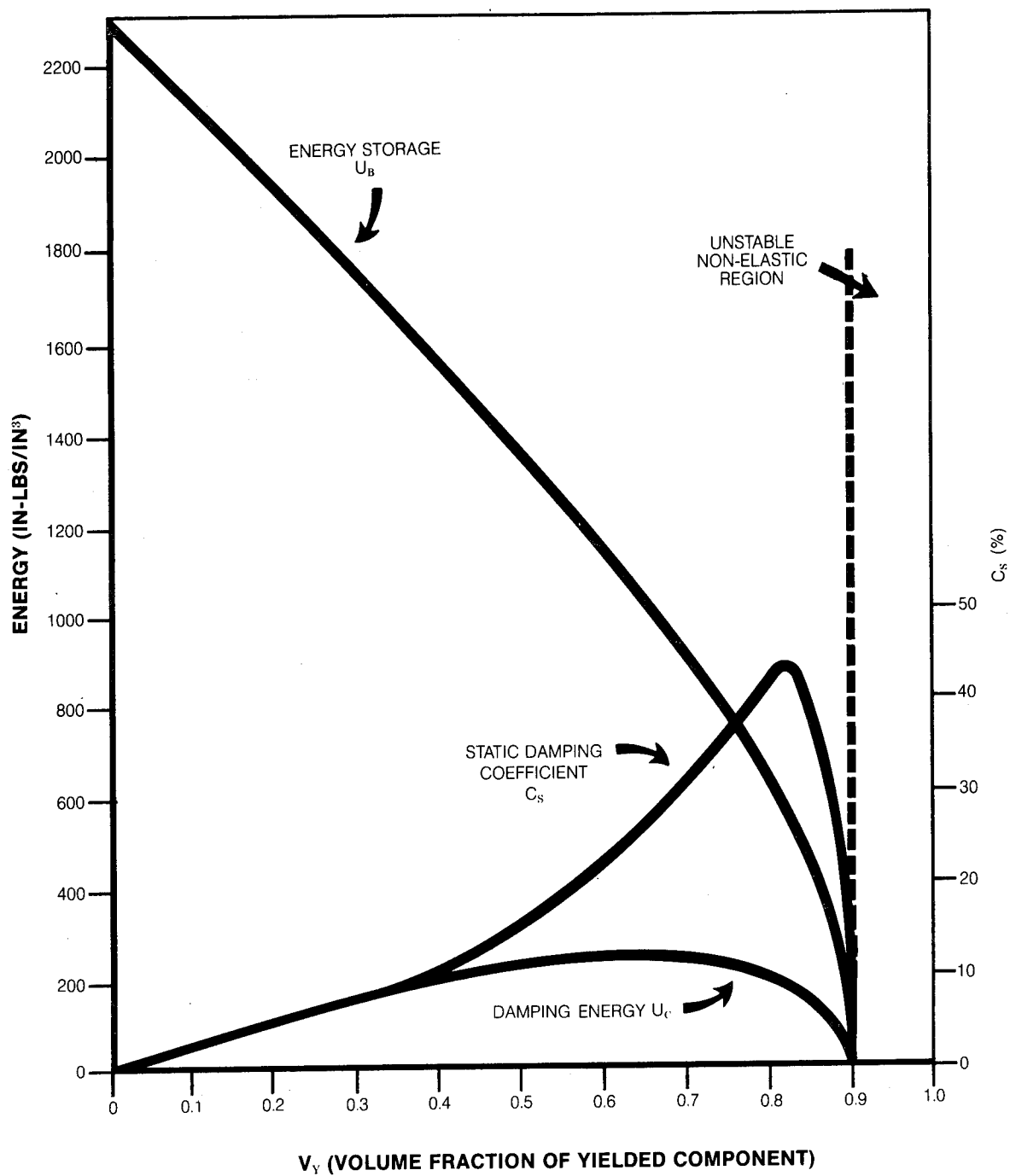


Figure 2. Effect of Volume Fraction of Yielded Plastic Component on Damping Energy, U_C , Storage Energy, U_B , and Static Damping Coefficient, C_S , (Zn/S.S. System).

described by Kelly and Bomford (8) for cases where the plastic component work hardens.

A typical theoretical analysis is graphically shown for high strength stainless steel as a function of volume fraction zinc in Figure 2. Optimization of material selection and synthesis into desirable energy absorbers is readily seen from this type of analysis. Damping or energy storage can be maximized depending upon the application requirements. For example, if a large amount of energy were to be damped per cycle, the absolute value of damping, U_c , would be selected. This would probably be done for requirements where the number of operating cycles was low. Conversely, to optimize damping efficiency, the damping coefficient would be used.

As with other forms of hysteretic material damping, the amount of damping is amplitude dependent. For the energy absorbing composites, this dependence is proportional to the plastic strain, ϵ_p . This relationship can be expressed in terms of a stress ratio (σ_E/σ_y) where the elastic operating stress is divided by the yield stress of the plastic component. Another factor controlling the amount of damping is the ratio of elastic moduli, B , of the elastic and plastic components (E_E/E_y).

Increasing the stress ratio or decreasing the modulus ratio, B , results in an increase in the static damping coefficient, C_s . For example, a composite system which has a modulus ratio of 0.82 and a volume fraction of 75 percent copper and 25 percent titanium at a stress ratio of 8 to 9 will give a damping coefficient of 53 percent. Naturally, a decrease in the volume fraction of the plastic copper component V_y results in lower maxima for C_s , which also occurs at lower stress ratios (see Equation 1).

With this background, several composite systems were evaluated to establish the validity of the model and the feasibility for obtaining practical material combinations. The results obtained generally confirmed the model system for which United States Patent Number 3,704,877 has been awarded, (9) which includes the use of these composites for shock and vibration control.

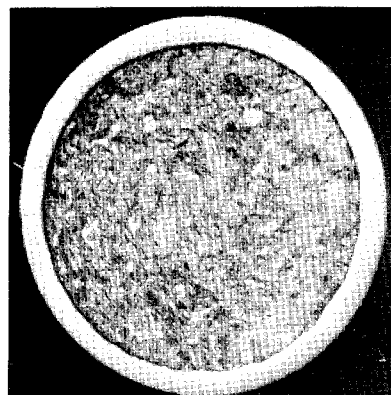


Figure 3a. Clad Composite (SS/Cu)

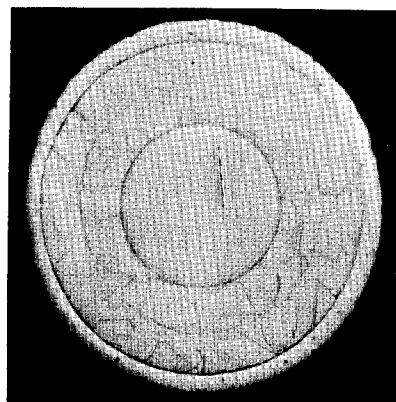


Figure 3b. Annular Composite (SS/Cu/SS)

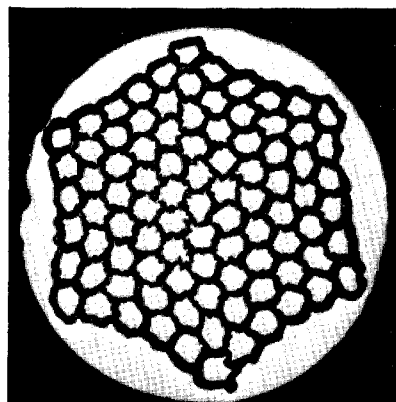


Figure 3c. Fiber Reinforced Composite (Cb/Monel/Cu)

EXPERIMENTAL RESULTS

Typical cross-sectional views illustrating the various internal composite configurations studied are shown in figure 3. The experimental tensile

strengths, elastic moduli and static damping coefficients, C_s , as well as the theoretically determined C_s values are listed in Table I. The theoretical C_s calculations were determined using typical values for modulus and yield

TABLE I

Experimental Tensile Strength (UTS), Primary Modulus (E_1) and Static Damping Coefficient (C_s) Values and Theoretical Calculated C_s Values

Composite System	Experimental Results				Theoretical Calculations		
	E_1 (10^6 psi)	UTS (ksi)	C_s (%)	σ (ksi)	σ_E/σ_y	B	C_s (%)
SS/Ti	15.6	204.1	4	150	1.53	1.67	0
4340/SS	23.1	212.6	10	200	2.20	0.83	6
Cb/Monel/Cu	16.8	155.6	11	152	4.86	1.24	9
Cb/Monel	20.7	180.3	5	178	1.12	0.54	0
Monel/SS	26.5	115.4	21	74	2.33	0.64	14
Cu/SS	19.2	79.1	37	59	27.5	1.47	28
			32	70			
SS/Cu/SS	19.4	138.1	19	99	27.5	1.47	19
			27	123			
SCS-14	-	83.9	40	67	14.0	1.06	30
Cu-2%Be/Cu	17.2	96.0	22	70	20.0	1.00	16

σ = Damping stress
 B = Elastic modulus ratio
 σ_E/σ_y = Ratio of elastic component's operating stress to the plastic component's yield stress.

strength. It can be seen in figure 4 that the experimental values obtained from a simple tension test are 30 percent greater than the predicted values.

The relatively high damping coefficients of up to 40 percent represent a significant accomplishment in metallic hysteresis damping which approaches the values obtained for elastomeric materials. A typical tensile stress-strain curve illustrating the magnitude of this hysteresis behavior is shown in figure 5. The composite shown here is a .036 inch diameter 304 stainless steel clad copper wire that was solution annealed at 1900°F for one minute prior to wire drawing to 92 percent cold work. It was then given a final heat treatment at 790°F for one hour. This final treatment accomplishes two things: 1) it stress relieves and ages the stainless to a higher strength level, and 2) it softens the copper so that maximum plastic deformation can occur. Naturally, this processing history would not necessarily

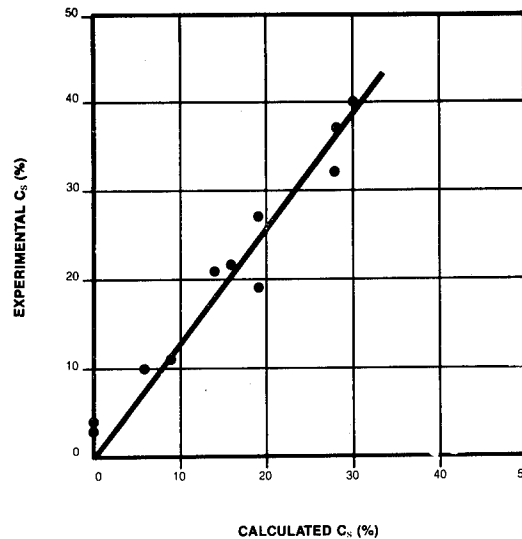


Figure 4. Comparison Between Experimental and Calculated Theoretical Static Damping Coefficients, C_s .

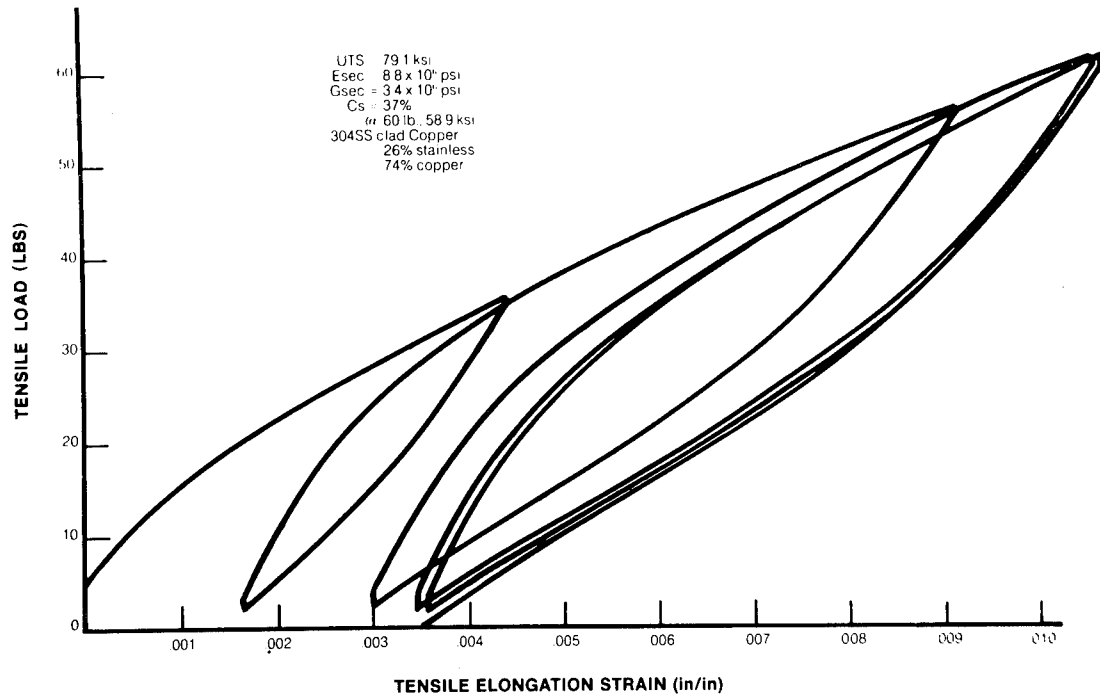


Figure 5. Typical Tensile Stress-Strain Curve and Hysteresis Behavior for an Energy Absorbing Composite.

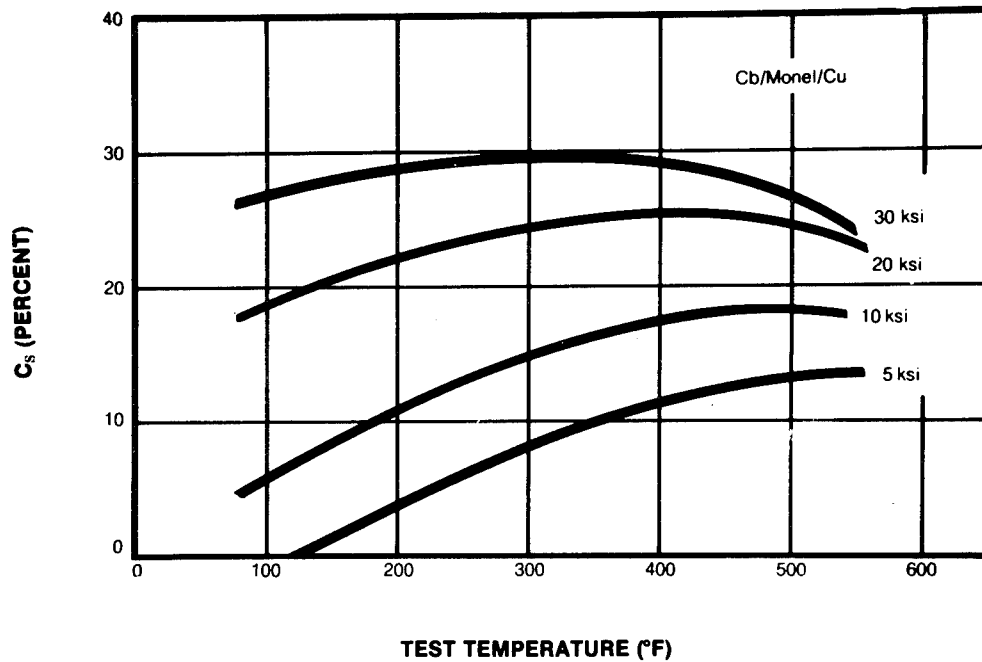


Figure 6. Effect of Test Temperature and Maximum Shear Stress on Torsional Damping.

TABLE II

Static Coefficient of Damping Results Obtained
on Spring Tests and Wire Torsion Tests

Composite System	Active Coils	Spring Dia. (in)	Wire Dia. (in)	$\tau_{\max.}$ (ksi)	C_s (%)
<u>Helical Extension Spring Data</u>					
SS/Ti	13	0.4	.032	72	4
4340/SS	13	0.4	.032	144	4
Cb/Monel/SS	13	0.5	.051	19	9
				68	14
				95	19
				114	25
<u>Helical Compression Spring Data</u>					
Cb/Monel/Cu	3	0.9	.051	79	10
Cb/Monel	3	0.85	.046	101	3
SS/Cu/SS	6	0.21	.029	20	8
				23	11
				30	14
				33	16
SS/Cu/SS	2	0.41	.029	15	20
				18	21
				24	25
				72	25
Cu/SS	6	0.45	.051	58	18
<u>Torsion Tests on Wire</u>					
Cb/Monel/Cu	-	-	.051	10	5
				20	17
				30	26
SS/Cu/SS	-	-	.051	34	18
				50	20
				69	21

be the same for other composites as the individual component's metallurgical properties must be taken into consideration. Ideally an optimum choice would be materials that are metallurgically compatible and capable of being thermomechanically processed or heat treated to the desired strength and damping properties.

For many applications where damping is needed the product involved is usually a helical spring or torsion bar. This is particularly true in shock absorption and vibration isolation. It is therefore important to translate the property data and concepts obtained from the uniform strain model to the more complex torsional (or bending), non-uniform strain case. Because material damping is strain or amplitude dependent, a material experiencing a strain gradient would be expected to ex-

hibit less damping during cyclic loading. (A rod of circular cross-section in torsion has a strain gradient that goes from zero at its center to a maximum at its surface.) However, as a first approximation, the uniform strain static damping coefficient will be considered equivalent to the non-uniform strain case.

The torsional damping for a Cb/Monel/Cu (columbium fibers embedded in a Monel matrix with an exterior cladding of copper) is shown in figure 6 as a function of testing temperature and maximum shear stress. This composite was cold worked by wire drawing to 75 percent reduction in area. Two significant effects can be seen in these data: 1) with increasing shear stress up to 30 ksi, which is the same as increasing the strain amplitude, the amount of damping increases up to a

maximum of 30 percent, and 2) the high damping coefficient remains reasonably stable over a broad range up to 550°F. This particular composite had 20 percent volume fraction of copper at its surface. Because of this, the softer copper component experienced the greatest strains resulting in the relatively large damping values.

Some disadvantages of a copper clad are that lower operating stresses and fatigue life can be anticipated. Also in time under cyclic loading, the appearance of the composite would be altered drastically as many surface cracks would have developed. The development of cracks in the copper would be expected as this

type of damping mechanism would lead to failure by low cycle fatigue. In order to circumvent some of these problems other configurations were designed to allow for higher operating shear stresses at the wire surface and improved fatigue life.

Listed in Table II are other torsional damping data obtained from helical spring tests and pure torsion tests on wire. The amplitude or stress dependence of the damping coefficient is evident in these data. In the case of a helical spring, it is clear that by altering the spring dimensions, larger stresses can be introduced to achieve improved damping. However, fatigue failure will occur in time, depending on the operating stress level.

TABLE III
Fatigue and Damping Behavior of Cb/Monel/Cu
Helical Extension Spring

Max. Shear Stress (ksi)	Cyclic Fatigue Life (no.)	Static Damping of Spring (%)
22	0 5 x 10 ⁶ 7.5 x 10 ⁶	8 11 Failed
39	0 5 x 10 ⁶	19 16
(75% CW, Spring Dia. = .4", Wire Dia. = 0.025" and Number of Active Coils = 13)		

It is, therefore, important to consider the low cycle fatigue characteristics of the composite material. Naturally, a device that requires continuous maximum damping would be shorter lived than one that requires maximum damping intermittently. Some typical fatigue curves are shown in figure 7 which illustrate the decrease in fatigue life at increased damping levels. It can be seen that relatively low plastic strains can be tolerated for fatigue life in excess of 10⁵ cycles. Although these data give a better understanding of the low cycle fatigue limitations, it should be noted that they are for bulk metals and may be on the conservative side when applied to composites.

The relatively good fatigue life of a composite, Cb/Monel/Cu, is shown in Table III.

Relatively high damping levels

were achieved with this composite without failure for up to 5 x 10⁶ cycles. In the one case where failure did occur, 7.5 x 10⁶ cycles were performed. It should be noted that the stresses shown are quite high for copper to sustain without failing even under static loading conditions. Because of this, the wire surface had to experience favorable residual stresses in order to tolerate these applied shear stresses.

Examination of the failed springs revealed that cracks developed in the spring wire at 40,000 cycles and extended well into the fiber reinforced Monel matrix at 80,000 cycles. This later fact indicates that the copper would have failed in this range of cycles if it were not for the composite core of columbium fiber reinforced Monel 400 matrix. This is an important factor to consider in the design of any energy absorbing composite where long life and high damping are desired.

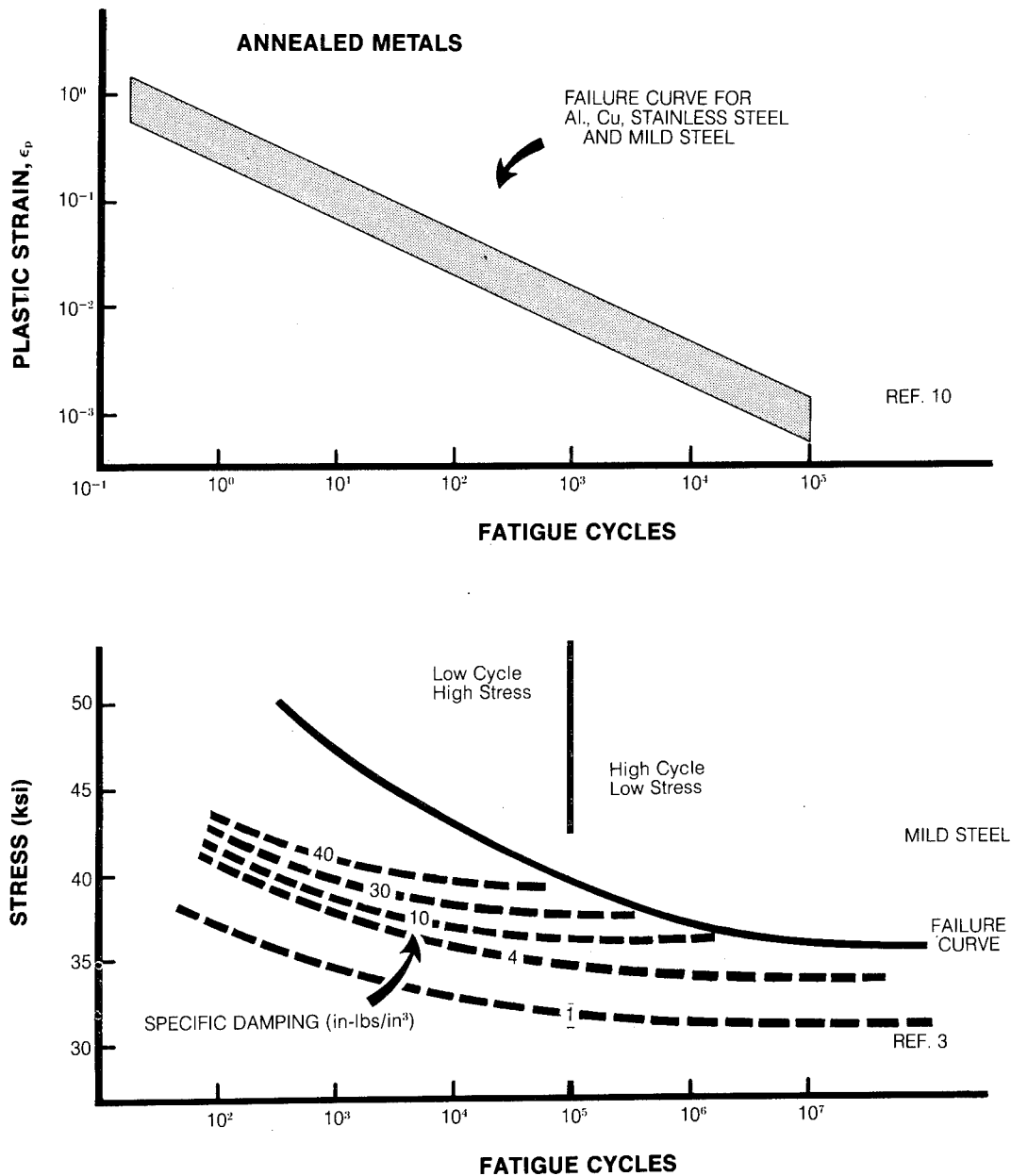


Figure 7. Typical Low Cycle Fatigue Behavior for Ductile Metals Illustrating Decreased Life with Increased Damping.

The fatigue life of composites appear to be primarily controlled by the elastic components, particularly when a ductile matrix material is present. This is borne out by other fatigue results on composites containing silver reinforced with tungsten or stainless steel (11) and aluminum reinforced with beryllium or boron (12). The controlling fatigue failure behavior of the elastic component may be either low cycle, high stress fatigue (less than 10^5 cycles), or high cycle, low stress fatigue (greater than 10^5 cycles), depending on the stresses ultimately experienced. For example, once the plastic component has failed and is no longer capable of carrying a load, the elastic component may yield causing it to immediately fail or to fail by low cycle fatigue. However, if it is properly designed to carry the increased load, it will remain elastic avoiding abrupt structural failure and fail by high cycle fatigue.

DAMPING RELATIONSHIPS

The static damping coefficient, C_s , is determined differently than other measures of damping referred to in the literature (2,13). Most other measures of damping are defined as a ratio of the energy dissipated per cycle to the maximum potential energy stored at the beginning of the cycle to the maximum potential energy stored at the beginning of the cycle and are dynamically measured on a forced or freely decaying vibrating system at resonance. Three of the most commonly used coefficients are as follows:

Specific Damping Capacity

$$\psi = D/U_{\text{pot}} \quad (6)$$

Where: D = energy dissipated per cycle

U_{pot} = maximum potential energy

Loss Factor

$$\eta = \frac{D}{2\pi U_{\text{pot}}} \quad (7)$$

(energy dissipated per radian)

Logarithmic Decrement

$$\delta = \frac{1}{N} \left(\ln \frac{A_0}{A_N} \right) \quad (8)$$

A_0 = Initial amplitude

A_N = Amplitude at the Nth cycle

N = Total no. of cycles

However, the static damping coefficient is defined, here, as the ratio of energy dissipated to the energy stored at a maximum strain amplitude obtained under static loading conditions. As shown earlier, the ratio of the energy damped, U_c , to the stored energy, U_B , is the static damping coefficient, C_s . The relationship between the static damping coefficient and the specific damping coefficient, ψ , can be easily obtained. Once this is done, all the other measures of damping may also be related to C_s .

The maximum potential energy, U_{pot} , may be related to the static energy storage as follows:

$$U_{\text{pot}} = \frac{U_B}{4} - \frac{U_c}{8} \quad (9)$$

Dividing through by U_c to obtain the damping coefficients results in the following relationship after rearranging terms.

$$\psi = 8C_s / (2 - C_s) \quad (10)$$

The more common damping coefficients that can be related to each other (13) can now also be related to C_s as follows:

$$\frac{4 C_s}{\pi(2 - C_s)} = \eta = \frac{\psi}{2\pi} = \frac{\delta}{\pi} = 2\zeta$$

Where: ζ = fraction of critical damping from ratio of viscous to critical damping coefficient.

Some of these terms will become more meaningful once damping at resonant frequencies is discussed. prior to doing this, however, it would be quite informative to compare representative materials and structures possessing high and low damping to that of the energy absorbing composites studied.

Listed in Table IV are some typical loss factors obtained from several sources for metallic and non-metallic systems and materials. No attempt has been made to identify the mechanisms associated with a given loss factor. However, several factors are immediately evident for these data on comparing energy absorbing composites.

TABLE IV

Typical Room Temperature Loss Factors for Various Materials

Material	η	Ref.	C_s
Hyd. Shock Absorber	.16 - .64	14	.22 - .67
Pneumatic Damping	.34	15	.42
SCS - 14	.32	EAC*	.40
Si base Elastomers	.30	15	.38
Cu/SS	.27	EAC*	.35
Metal Mesh	.24	15	.32
SS/Cu/SS	.19	EAC*	.26
Cu-2%Be/Cu	.16	EAC*	.22
Cork	.12	15	.17
Neoprene	.10	15	.14
Rubber	.08 - .10	14, 15	.12 - .14
Cb/Monel/Cu	.07	EAC*	.10
Cu-Mn	.07	5	.10
Bakelite	.05	14	.08
Lead	.05	14	.08
Ti-Ni (Nitalol)	.03	5	.05
Cast Iron	.03	5	.05
Lucite	.03	14	.05
Concrete	.02	14	.03
Spring Steel	.01 - .03	15	.02 - .05
Wood	.01	14	.02

η = Loss Factor, C_s = Static Damping Coefficient

* Energy Absorbing Composite (EAC) from this study.

1) No other metal system exhibits higher values of damping.

2) Shock absorbing or air damping systems appear to be one of the few systems possessing higher damping.

3) Most of the elastomers appear to be equivalent or less in their damping capacities.

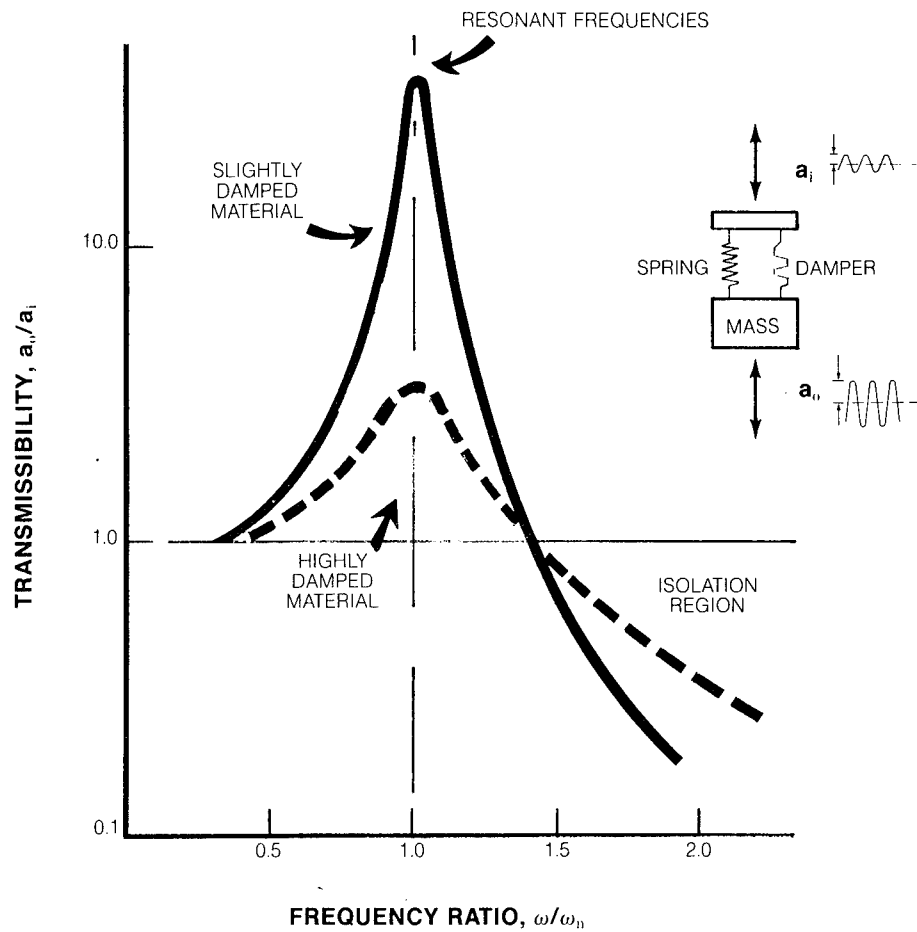
It can be seen that loss factors spanning equivalent C_s values of from 1 to 67 percent are represented in Table IV. (Loss factors, for C_s values of less than 1 percent, are not shown, included glasses and most cold rolled metals.) Assuming these data are reasonably accurate and representative, they forecast a rather promising future for an energy absorbing composite material, particularly when one considers their greater design flexibility for increased strength, temperature and environmental resistance.

CONTROLLING MECHANICAL VIBRATIONS

Figure 8 illustrates a highly damped and a slightly damped transmissibility curve for a simple linear system

having a single degree of freedom, excited by a force of constant magnitude and variable frequency. The mass, spring and damping components shown can be considered as elements of a unitary material as well as separate parts of a system. As the frequency increases and approaches resonance, it can be seen that the transmitted force and amplitude increase reaching maximum peak values at resonance. For example, values of up to 480 times the input force and deflection have been recorded at resonance on an airplane propellor (2). Beyond resonance, the transmitted forces and amplitudes decrease rapidly. One unique feature of composite energy absorbers and pure spring materials is that at these higher frequencies the transmitted forces are about the same. This is also illustrated in the figure. The physical meaning of the transmissibility curve is as follows:

- 1) At frequencies in the amplification region, the mass is deflected by a force equal to or greater than the static input deflection. At resonance, the amplitude can become infinitely larger.



ω_n = RESONANT FREQUENCY
 a_i = INPUT AMPLITUDE

Figure 8. Transmissibility Curves Illustrated Isolation and Amplification Effects on Slightly and Highly Damped Materials

- 2) At frequencies greater than resonance in the isolation region, the force moves so rapidly that the mass does not have time to follow and the resultant amplitude is small. (This usually occurs at frequency ratios greater than $\sqrt{2}$).

Some of the equations (13) describing transmissibility effects with and without damping are as follows.

Transmissibility (without damping)

$$T = 1 / [1 - (\omega/\omega_n)^2] \quad (11)$$

Where: T = Transmissibility, absolute ratio of output to input force or displacement.

ω = Forcing frequency

ω_n = Resonant frequency

Transmissibility (with hysteresic damping)

$$T = \left[\frac{1 + \eta^2}{(1 - \beta^2)^2 + \eta^2} \right]^{1/2} \quad (12)$$

Where: η = Loss factor

$\beta = \omega/\omega_n$

In equation 12, damping effects on the resonance transmissibility can be related to the static damping coefficient, C_s , by using the relationship shown earlier. Rearranging terms results in the following expression for C_s at resonance.

$$C_s = \frac{2\pi}{\pi + 4(T^2 - 1)^{1/2}} \quad (13)$$

Or in terms of transmissibility at resonance:

$$T = \left[1 + \frac{\pi^2}{16} \left(\frac{2 - C_s}{C_s} \right)^2 \right]^{1/2} \quad (14)$$

At frequencies beyond resonance, both equation 12 and 13 can be closely approximated by equation 11.

EXPERIMENTAL RESULTS FOR HELICAL SPRING ISOLATORS

Metal springs are most often used in the design of vibration isolation systems because they can be ideally fitted to a broad range of resonant frequencies simply by changing dimen-

sions and materials. In addition, metals also have the advantage of being most resistant to temperature changes and many deleterious environments as well as being capable of supporting heavy loads. Their greatest disadvantage is their lack of inherent damping sufficient to allow for operation at resonant frequencies for reasonable periods of time. Because of this lack of damping, it has always been necessary to incorporate some other component or system to give damping; such as wire mesh for frictional damping, rubber pads for hysteresic damping or a dash pot for viscous damping. Naturally energy absorbing composites would appear to be an ideal spring-isolator material.

To evaluate this, helical compression springs were made from various composite materials and tested as vibration isolators by determining their transmissibility as a function of frequency. In some cases the fatigue life at resonance was also determined.

Typical frequency versus transmissibility curves are shown in figures 9 and 10 for various composites and a bulk stainless steel spring material. In figure 9, transmissibility curves are shown for a constant input displacement of .01 inches double amplitude. Here a comparison is made with spring steel ($T = 38$) and some selected composites ($T = 23$ to 11).

Figure 10 illustrates the effect of increasing the input amplitude on lowering the resonant transmissibility due to the increased amount of hysteresic damping associated with the larger input strains. Fatigue cycles in excess of 100,000 cycles at resonance and transmissibilities as low as 3.0 were obtained for this spring.

A comparison of this experimental transmissibility data versus the theoretically predicted transmissibility as a function of the static damping coefficient is shown in figure 11. It can be seen that a good correlation between the predicted and measured values is obtained. In those cases where the data points didn't fit the theoretical curve, it can be shown that they were not being stressed to their maximum damping levels.

The experimental confirmation of the theoretical relationship is significant as it makes possible the design of a helical spring isolator using a relatively simple damping measurement obtained either in a static tension test or on a statically loaded spring.

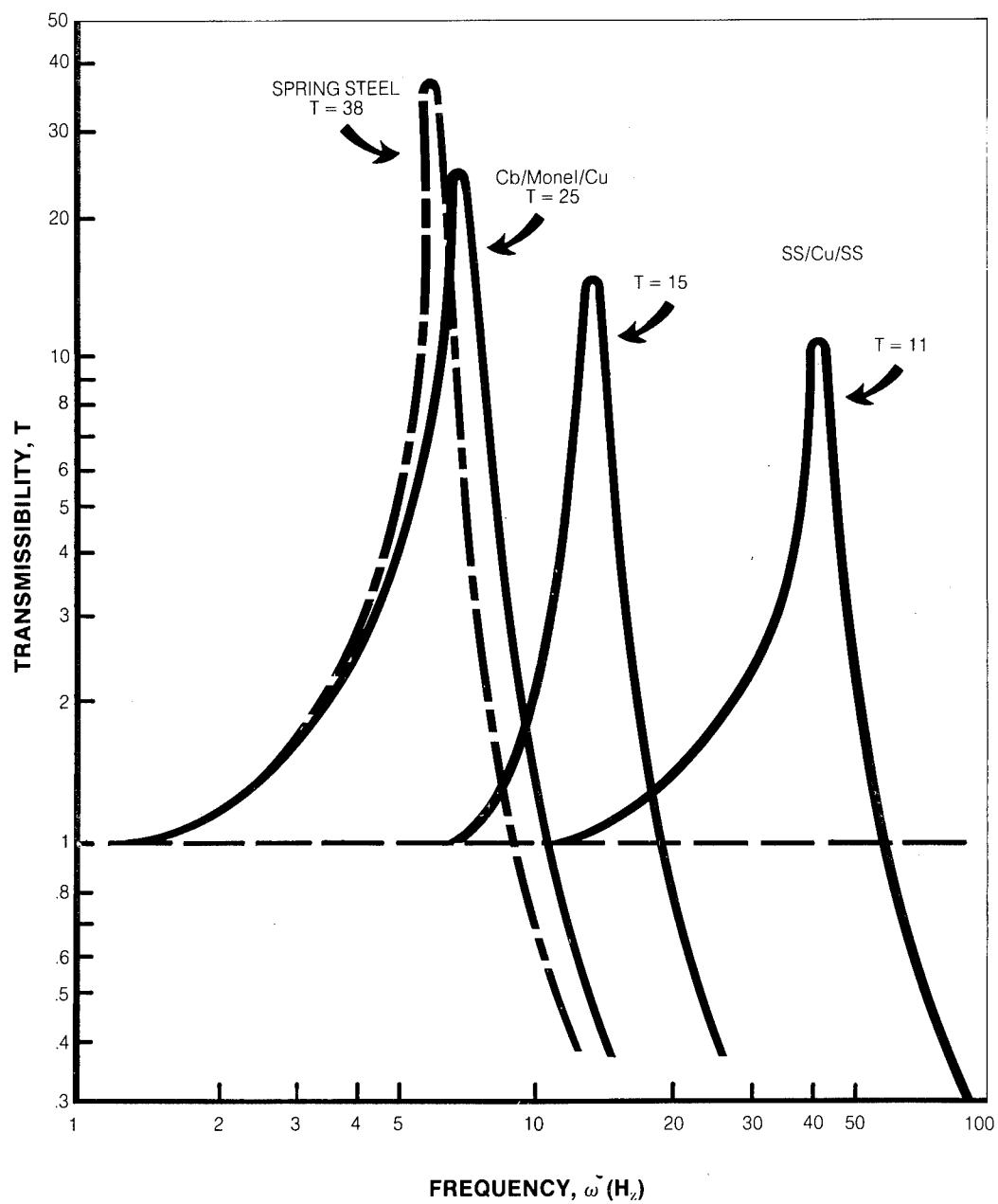


Figure 9. Typical Frequency Versus Transmissibility Curves of Various Materials for an Input Amplitude of .01 in. D. A.

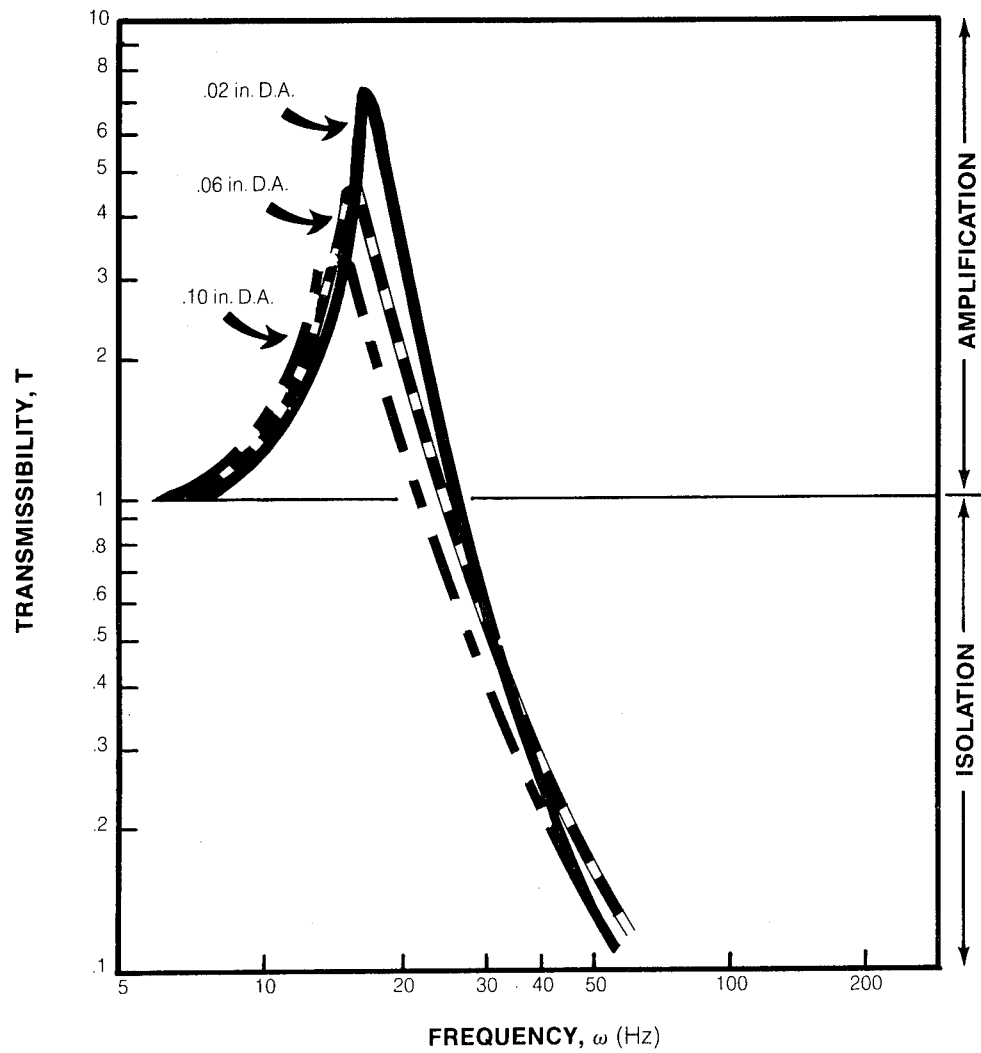


Figure 10. Typical Transmissibility Versus Frequency Curves for SS/Cu/SS Material for Various Input Amplitudes.

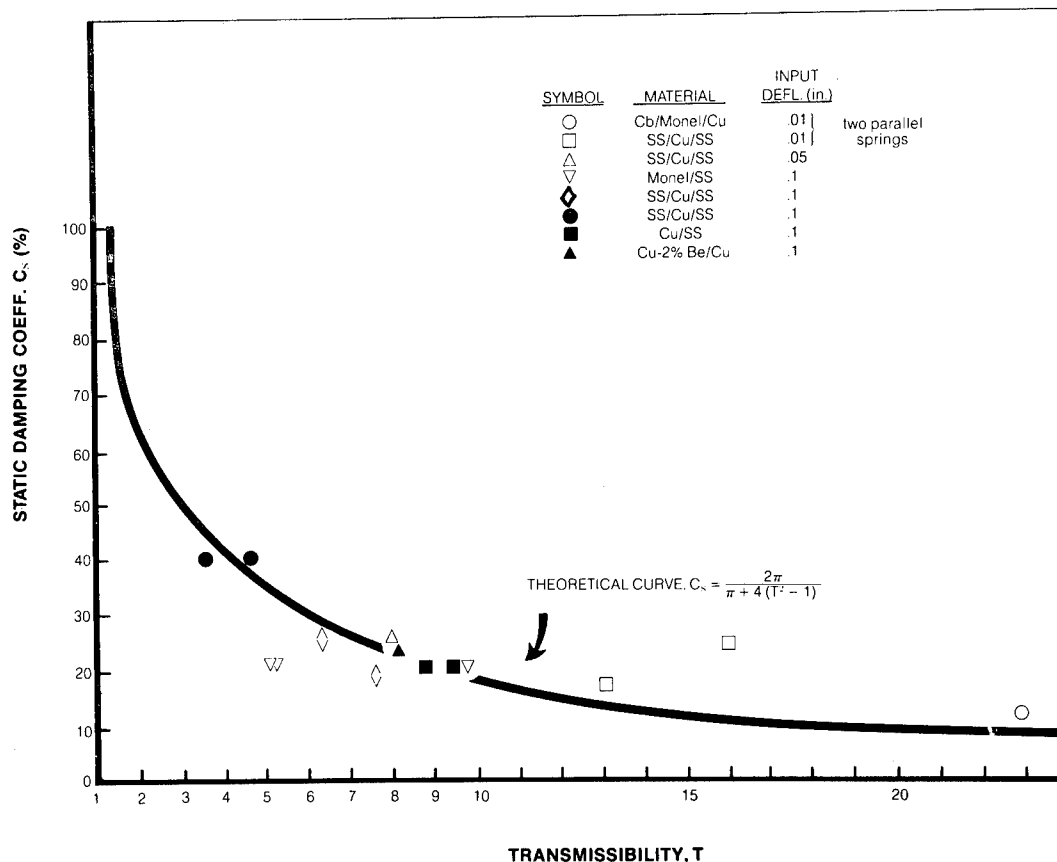


Figure 11. Comparison Between Theoretical and Experimental Transmissibilities for Some Composite Material Helical Spring Isolators Versus Their Static Damping Coefficients.

In either case, the measured static damping coefficient can be directly related to a given transmissibility. Also, because the static damping coefficient can be derived from the theoretical uniform stress model, it is possible to design a composite for a given transmissibility.

Because the amount of energy dissipated is a function of the softer component's plastic strain for a given composite there should be a relationship between the input amplitude and the measured resonant transmissibility. Although this relationship has not yet been analytically derived, an empirical relationship has been obtained which is illustrated in figure 12 for a SS/Cu/SS composite.

The effect of the input amplitude on the resonant transmissibility is

an exponential function that varies as the reciprocal square root of the amplitude. The relative effectiveness on lowering the resonant transmissibility is given by comparing the transmissibility at a double amplitude input of 1 inch. The empirical relationship is as follows:

$$T = T_1 a_1^{-1/2} \quad (15)$$

Although the end points of this relationship are not defined by the equation, they would appear to be controlled by the strains experienced by the damping component. For example, at the lower inputs, a strain will be reached where both components deform elastically resulting in little or no damping where the transmissibility would theoretically rise quite rapidly. At the larger amplitude, a maximum amount

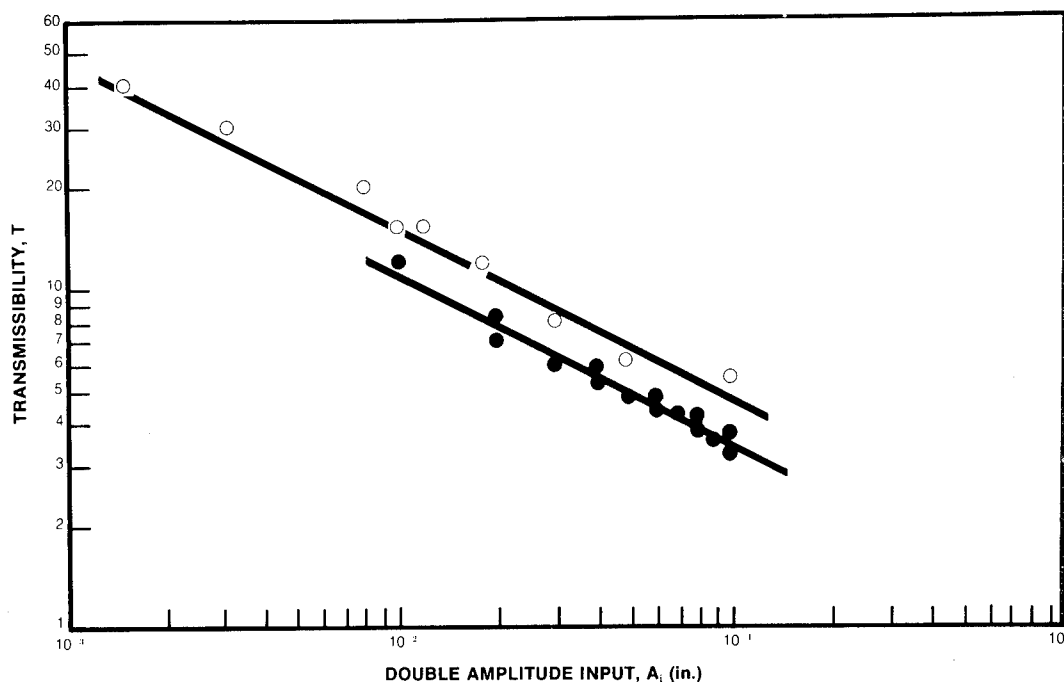


Figure 12. Effect of the Input Double Amplitude Displacement on Transmissibility for SS/Cu/SS Composite Helical Spring Isolators.

of energy dissipation would be experienced where further increases would either result in failure or no change in the transmissibility. Past experience has shown that failure of the component is the most likely thing to occur here.

From the preceding, it can be concluded that with our currently available composites relatively efficient helical springs can be designed and fabricated for vibration isolation applications.

SUMMARY

Some of the more significant developments and observations that have resulted from these and subsequent investigations into the design and behavior of energy absorbing composite material are as follows:

- (1) A uniformly stressed composite model system has been formulated to facilitate the design and analysis of potentially high high damping capacity combinations of materials. Using this type of analysis, composite

materials capable of damping up to 40 percent of input mechanical energy can be fabricated.

- (2) Superior damping characteristics have been retained for test temperatures up to 550°F. This coupled with the naturally high load bearing capacities of metallic composite materials makes them competitive with conventional elastomeric materials.
- (3) Fatigue lives of up to 7.5 million cycles have been measured where relatively low strains and damping (15 percent) capacities were experienced. At resonant frequencies (which is the most severe fatigue condition) cyclic lives of 100,000 cycles have been obtained with damping capacities up to 40 percent.
- (4) Composites for vibration isolation were developed by employing relationships that have been theoretically and experimentally established between

resonant frequency transmissibility, input displacement, static damping coefficient and various other mechanical properties.

- (5) Using these composites, helical spring isolators have been designed and developed with resonant frequency transmissibilities as low as 3 for an input displacement of 0.1 inches double amplitude.

REFERENCES

1. G. R. Brophy and E. R. Parker, "Damping Capacity - Its Variation and Relation To Other Physical Properties", Transactions of American Society for Metals, Vol. 24 (1936) pp. 919-931.
2. B. J. Lazan, "Fatigue Failure Under Resonant Vibration Conditions", Fatigue, American Society for Metals (1954) pp. 36-76.
3. B. J. Lazan, Damping of Materials and Members in Structural Mechanics, Pergamon Press, Great Britain (1968).
4. A. A. Baker and D. Cratchly, "Stress-Strain Behavior and Toughness of a Fibre-Reinforced Metal", Applied Material Research, Vol. 5 (1966) pp. 92-103.
5. Smithells Metals Reference, Vol. III (1967) p. 711.
6. A. A. Baker, "The Fatigue of Fibre-Reinforced Aluminum", Journal of Material Science, Vol. 3 (1968) pp. 412-423.
7. A. Varschavsky, "The Matrix Fatigue Behavior of Fibre Composites Subjected to Repeated Tensile Loads", Journal of Material Science, Vol. 7 (1972) pp. 159-167.
8. A. Kelly and M. J. Bomford, "Fatigue of the Matrix in a Fibre-Reinforced Composite", Physics of Strength and Plasticity, The M.I.T. Press, Cambridge, Mass. and London, England, Ali, S. Argon ed. (1969) pp. 339-350.
9. United States Patent Number 3,704, 877, dated December 5, 1972-"Means and Methods of Energy Storage and Damping", A. Geary, J. Roberts and J. Nunes, Brunswick Corporation.
10. Tavernelli, J. F. and Coffin, L. F. Jr., "A Compilation and Interpretation of Cyclic Strain Fatigue Tests on Metals", Transactions of American Society of Metals, Vol. 51, (1959) pp. 438-453.
11. Morris, A. W. H. and Steigerwald, E. A., "An Investigation of the Fatigue Behavior of Tungsten-Reinforced and Steel-Reinforced Silver Composites", Transactions of Metal Society of AIME, Vol. 239 (1967) pp. 730-739.
12. Hancock, J. R., "The Initiation and Growth of Fatigue Cracks in Filament-Reinforced Aluminum Alloys", AFML TR 71-82, Air Force Systems Command, Wright Patterson Air Force Base, Ohio, (March 1971).
13. Leo L. Beranek, editor, Noise and Vibration Control, McGraw Hill, New York (1971).
14. A. C. Wrotnowski, "Developing Composites for Torsional Damper-Spring Systems", ASME prepublication 71-DE-31 (July, 1971).
15. R. Erhart and C. M. Salerno, "Isolation Vibration", Machine Design, (July 1972) pp. 112-118.

DISCUSSION

Mr. Gertel (Kinetic Systems): In your curve of the static damping value versus transmissibility it would appear that if all those systems had the same weight you could make that kind of a comparison and get an effective damping to critical damping ratio for the vibrating system, but the mass of the system that was being vibrated seems to be missing. Were all those tests performed with the same weight systems?

Mr. Nunes: I think they were.

Mr. Gertel: In that case the curve that you presented was probable relatively appropriate if all of the masses of the system were essentially the same.

Mr. Nunes: I think in most cases they were. If you will notice most of the values reported had a double input amplitude of 0.1 inch and there were a few that had a double input of amplitude of 0.01 inch. I think most of those had the same mass.

Mr. Gertel: I should say stiffness as well as mass.

Mr. Nunes: That is true. We are changing stiffness since we have different composite systems. The purpose of that curve is really to show that we have an analytical tool for

predicting the transmissibility of a model metal system; that is we can design a metallic composite that will give a certain transmissibility that is the beauty of it.

Mr. Gertel: What is the long term vibration effect on the composite that is undergoing plastic deformation? Perhaps it has a relatively short life.

Mr. Nunes: We are taking advantage of a damage mechanism, low cycle fatigue, by plastically deforming our plastic component out to these relatively high strain amplitudes. We have a fairly good handle on the fatigue life of such a material. We know that if we cycle the material at a strain of .001, on the plastic component, that we would expect a fatigue life of 100,000 cycles and this is in bulk material. We think we can do something to even optimize a sort of negative aspect of this; we have measured fatigue life on the order of 7 1/2 million on a copper Columbian monel composite and, the copper, at those strain amplitudes, should have failed at 40 to 50 to 100,000 cycles, no more than that. The reason we were able to go to 7 1/2 million cycles was because the copper was not the stress bearing element, it was simply put there for damping; the other elements were put there to hold the composite together and to give it its structural integrity. The copper itself was severely cracked and deformed in that particular case but it did nothing to degrade the performance of the vibrating spring. It is a problem that you have to be aware of when you design the material, you have to design around those limitations, and it would depend on your application as well. You would trade off a damaging mechanism for a superiority in damping performance.

Mr. Eshleman (IIT Research Institute): I noticed that you dropped off at 50 Hz. Did you explore the damping at higher frequencies or were you at the surge wave frequency of the spring?

Mr. Nunes: No, do you mean forced vibration of the springs at 100, 200 or 300 Hz? Perhaps we have in that the fatigue tests may have been run at a faster rate.

Mr. Eshleman: That curve you showed is a simplistic curve because it doesn't come down to one.

Mr. Nunes: We may have cycled at higher frequencies in our fatigue tests but we never measured the transmissibilities at those higher frequencies.

SUPPRESSION OF TORSIONAL VIBRATION WITH ZERO TORSIONAL STIFFNESS COUPLINGS

J. M. Vance
Department of Mechanical Engineering
University of Florida
Gainesville, Florida

and

R. A. Brown
Dupont Engineering Development Lab
Wilmington, Delaware

A zero torsional stiffness coupling transmits torque which is nonlinearly dependent on the angle of twist across the coupling. The coupling can be designed so that the slope of the torque vs. twist angle curve is zero at a preselected condition of design speed and transmitted torque. A study was performed which showed the feasibility of designing a ZTS coupling to effectively suppress torsional resonance and vibration in a turboshaft powered helicopter drive train.

INTRODUCTION

Rotating machinery is inevitably subjected to exciting forces which set up torsional vibrations throughout the system. If a system is excited at or near its critical frequency, the system energy will increase with each successive cycle. The limiting factor for the energy build-up is internal or external damping which dissipates energy in the form of heat. Without sufficient damping it is of utmost importance that the exciting frequency be different from the critical frequency of the system.

Excitation at the critical frequency, of a system normally designed to operate away from the critical, can come about through:

- 1) Start up or shut down
- 2) Operation at other than design speeds
- 3) Unexpected exciting forces
- 4) Unexpected critical frequencies

Figure 1a is an example of an open-loop system where the torque input is independent of the system response. Open-loop systems of this type will not become torsionally divergent but can experience severe oscillation when externally excited at, or near, a critical frequency. For a closed-loop system (Figure 1b) where control action is dependent upon system response, instabilities can be caused by internal or external excitation. Turbo-powered machinery such as helicopters and electrical generators

are closed-loop systems where the operating speed is controlled by a governor. The speed governor causes a dependence between driving torque and output speed. Swick and Skarvan [1], Peczkowski [2], Canale and McCabe [3] and others describe governor systems for free turbine engines. This paper considers only the open-loop characteristics of torsional systems, such as free turbine helicopter systems, which are subjected to external excitation.

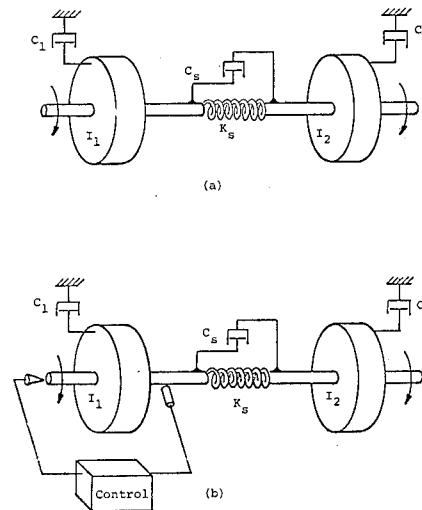


Fig. 1 - Torsional Systems

Removing critical speeds from the operating region in the open-loop system will generally improve closed-loop stability. In addition, fatigue failure due to cyclic torque variation from external excitation will be lessened.

DESIGN CONSIDERATIONS

Critical design parameters such as strength, weight, material and size often dictate the mass distribution of a system. It may be difficult to change the mass or inertia profile of a system without adversely affecting machine performance. Therefore, the designer may only be left with shaft stiffness and damping as free parameters with which to ensure safe operation at all expected operating speeds.

With proper damping, passage through critical frequencies during start-up or shut-down is usually not a problem. This is due to the short time duration that the machine is driven at a critical speed. However, large amounts of damping are needed when there is continuous excitation at or near a critical frequency. The damping will prevent the system from becoming divergent and magnifying the exciting force out of safe bounds. Unfortunately, this type of damping is generally hard to achieve and wasteful (heat dissipation). In addition, a highly damped system will transmit more exciting force than a lesser damped system when operation is above critical speed.

If the exciting frequency is known, it may be possible to design a shaft that has a stiffness which gives the system a critical frequency much higher or lower than the frequency of excitation. However, it may often be difficult to design a shaft with the desired stiffness and still have acceptable strength, weight and deflection characteristics.

NON-LINEAR COUPLINGS

A low stiffness shaft coupling may be used to solve the problem of excitation at a critical frequency. This is done by lowering the critical frequencies of a system to nearly zero, while at the same time transmitting the system torque requirements. Figures 2 and 3 show the characteristics of some linear and non-linear couplings. Figure 2 shows transmitted torque versus twist across the coupling, and the slope of the curve is the coupling stiffness. It is apparent from Figure 2 that a linear torsional spring with near zero stiffness would require large amounts of twist in order to transmit the design torque. The non-linear spring, however, can transmit design torque with zero stiffness at a small angle of twist. Present designs of non-linear couplings which have zero or low stiffness for certain operating conditions are described below.

For linear systems the resonant frequencies are inherent to the system and are not functions

of the exciting forces. The resonant frequencies of non-linear systems are functions of the amplitude and period of the exciting force, as well as the system state when excitation occurs. As can be seen in Figure 3, if the twist is varied over a large range, the non-linear spring stiffness increases on either side of the low stiffness operating region. In order to obtain an "average" stiffness over a cycle, consideration must be given to the time variation of the torque.

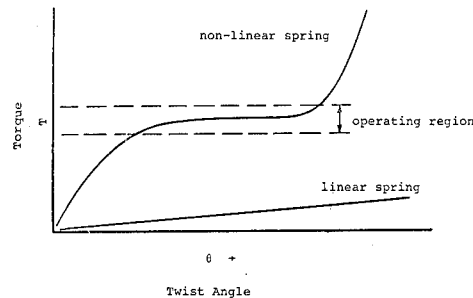


Fig. 2 - Coupling characteristics

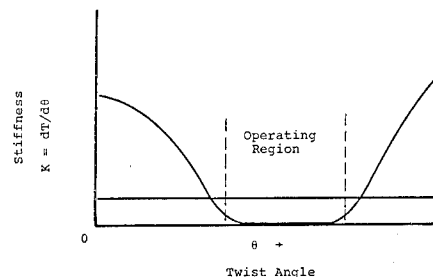


Fig. 3 - Coupling stiffness

THE HELICOPTER PROBLEM

A feasibility investigation was made for the U.S. Army (USAAMRDL - Eustis Directorate, Propulsion Division) to determine if a zero torsional stiffness (henceforth "ZTS") coupling could be designed for a turboshaft powered helicopter drive train, and if it would effectively suppress torsional vibration and instability. It was found that the typical operating speeds and torques found in modern helicopter drive trains make the ZTS coupling ideal for this application, especially from the standpoint of minimizing coupling weight. The design analysis, detail design, and design optimization of the various types of ZTS couplings is an extensive subject which will be covered in another paper at a later date. A descriptive summary of the various types of couplings found suitable for helicopter applications is given in a section below.

The values used to represent the dynamic characteristics of the helicopter drive train were obtained from a helicopter stability analysis by Swick and Skarvan [1]. Figure 4 shows

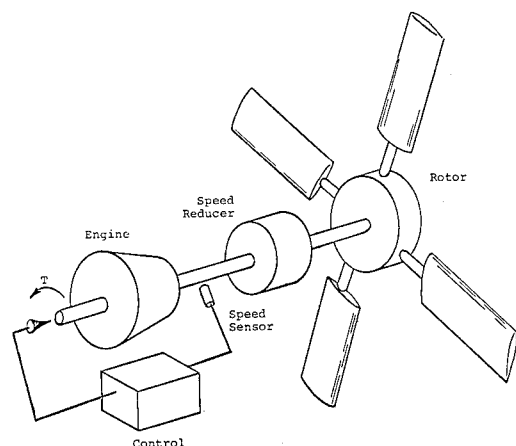


Fig. 4 - Closed-loop helicopter drive train

the basic helicopter drive system.

It has been found in past helicopter designs that the closed-loop system (system with an automatic speed governor) can become unstable in certain flight configurations. When this happens, self-excitation from a small perturbation can quickly cause destructive vibrations. The major incentive for the Army-supported study originally was provided by a desire to suppress these instabilities without resort to a compromise of fuel control characteristics.

The problem of fatigue failure of elastic members can also be reduced by lowering the amplitude and frequency of self-excited vibrations as well as the amplitude of vibration caused by external excitation. The major external sources or torsional excitation are:

- 1) Pilot excitation of control parameters
 - a) collective pitch
 - b) engine speed setting
- 2) Aerodynamic excitation of rotor blades

As helicopter ground speeds increase the whip effect from aerodynamic excitation of the rotor blades can be expected to increase. This is due to the changing relative air velocities the rotor blade sees as it enters and leaves the direction of flight. Figure 5 shows that the maximum velocity the rotor blades see during each revolution is

$$V_{\max} = V_H + r\omega$$

and the minimum velocity is

$$V_{\min} = V_H - r\omega$$

This effect combined with the cyclic variation of the rotor blades to achieve forward motion causes substantial torque variations on the rotor and drive train.

An added incentive for the development of a

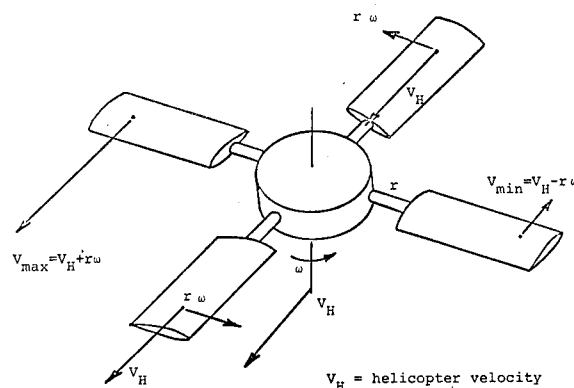


Fig. 5 - Rotor blade velocities

versatile coupling for helicopters comes from the nature of helicopter design and development. Nearly every major component of a helicopter drive train is made by a different company. It is usually the responsibility of the air frame manufacturer to couple all the drive train components together. Thus it is very possible, unless there is exceptional coordination during the component design state, that the assembled system will have critical frequencies which are unacceptable.

ZERO TORSIONAL STIFFNESS COUPLINGS

ZTS couplings can employ rigid or elastic linkages, as well as a variety of torsional and linear springs. Centrifugal force caused by the rotating links plays an important role in determining the stiffness characteristics of many of the couplings.

The geometry of the coupling (arrangement of components) is the dominant factor in determining the torque resulting from either the centrifugal force of the links or the force due to the elastic deformation of the links or springs.

This section briefly describes various coupling designs which, for certain operating conditions, have zero, or very low, torsional stiffness and the capability of transmitting high torque.

Elastic Link Designs

The elastic materials used in coupling designs range from rubber to steel. For systems with low torque requirements, a rubber or elastomeric material may be used successfully to achieve low stiffness. For the more common high torque systems, steel links have been employed to achieve low torsional stiffness.

The most notable of the high torque elastic link designs is the half moon "H.M." coupling developed by C. W. Chapman [14]. Figure 6 is a diagram of the H.M. coupling showing the elastic (steel) links. Pins X_1 and X_2 are equally spaced about 0 and connected to the driving flange.

Pins Y_1 and Y_2 are also equally spaced about 0 but are connected to the driven flange. When one flange is rotated relative to the other about point 0, torque can be transmitted across the coupling through the mechanism of elastic deformation of the steel links. The zero speed torque-deflection curve of the H.M. coupling is shown in Figure 7. At other than zero speed, the centrifugal force of the links enables additional torque to be transmitted across the coupling. The additional torque is proportional to the square of the coupling speed. Figure 6 shows that the center of gravity of each link moves toward 0 as the twist angle, θ , of the coupling is increased. As a result of the path of the center of gravity, the amount of additional torque transmitted across the coupling resulting from centrifugal force is reduced with increasing twist angle. If, at a given speed, the decrease in torque resulting from centrifugal force is larger in magnitude than the increase in torque resulting from elastic link deformation, a negative torsional stiffness will result. Chapman overcomes the negative stiffness problem and the resulting instability for operation up to a maximum design speed, by including some torsional rigidity in the bushings at pins X_1 , X_2 , Y_1 and Y_2 . The H.M. coupling has been quite successful in low speed-high power applications.

A modified arrangement of the elastic links in the coupling is shown in Figure 8, where the pins X_1 , X_2 , Y_1 and Y_2 are not necessarily colinear in the unstrained position. The X and Y pins are the same distance from 0, as opposed to Chapman's staggered pin design.

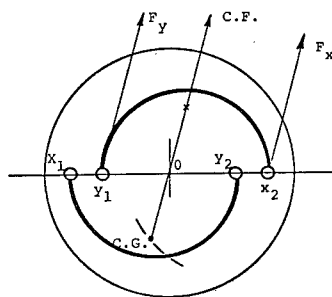


Fig. 6 - Half-moon coupling [4]

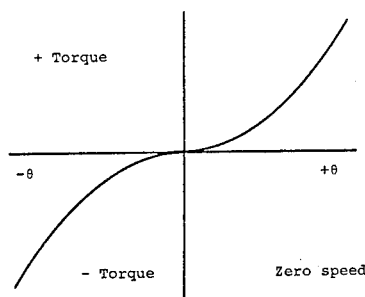


Fig. 7 - Stiffness Characteristic of H.M. coupling [4]

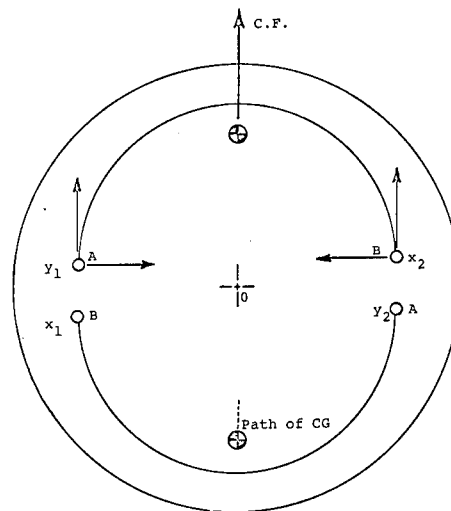


Fig. 8 - Elastic link coupling

Pinned Link Designs

Two pinned link coupling designs are known to have been developed. One is the toggle link or "T.L." coupling designed by C. W. Chapman [4]. The other is a design of Russian origin [5]. An illustration of the "T.L." coupling is shown in Figure 9. The torsional stiffness of this coupling is effectively zero at zero speed but increases as the speed increases. Chapman has been able to produce "T.L." couplings with torsional stiffness to mean torque ratios of 4 or less for low speed, high power applications. This ratio is a measure of relative stiffness which Chapman uses as criteria for effectively eliminating torsional vibrations. The "T.L." coupling like the "H.M." coupling has some torsional rigidity in the bushings to overcome negative stiffness at operating speed. The Russian pinned link design, shown in Figure 10, consists of a mass connected by two links, one

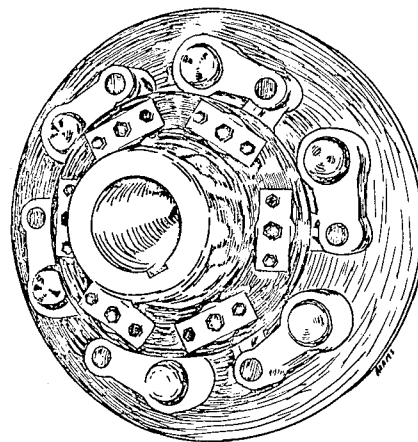


Fig. 9 - T.L. Coupling

Low stiffness couplings up to now have been designed for low speed operation (500-3,000 RPM) as would be found in diesel engine systems. For turbine engine applications, such as found in many helicopter drive trains, drive shaft speeds of 10,000 to 20,000 RPM are not uncommon.

Figure 11 shows the stiffness characteristics of this coupling for several different values of a geometry parameter which can be chosen by the designer. It can be seen that the stiffness is practically zero over a range of at least ten degrees of twist. For a given amount of twist, the transmitted torque is proportional to the square of the shaft speed. If the load is also proportional to the square of the shaft speed (approximately true for helicopters), then the zero stiffness characteristic of the coupling is independent of the shaft speed.

47

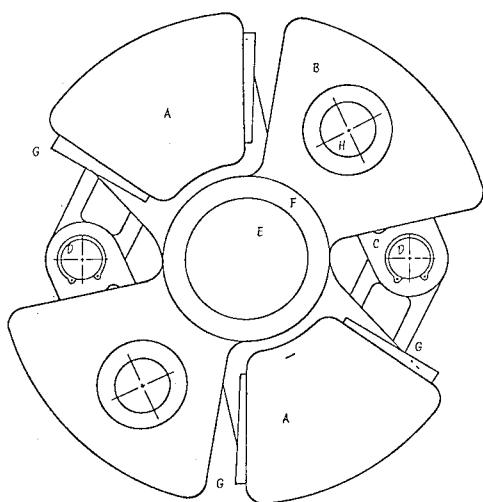


Fig. 14 - ZTS coupling (back)

The various components of the coupling are:

A	driving flange	F	connecting tubes
B	driven flange	G	deformable stops
C	link	H	link pin and fastener
D	connecting pin		
E	alignment shaft	I	torsion bar (not shown)

The connecting tubes are part of the flanges and are designed to fit inside the drive shaft of the helicopter. A free running alignment shaft is used to prevent lateral motion of the flanges. A soft torsion bar is inserted through the center of the alignment shaft which closes the coupling against the stops during initial startup. The stiffness of the torsion bar is easily compensated for by adjustment of the β parameter in Figure 11.

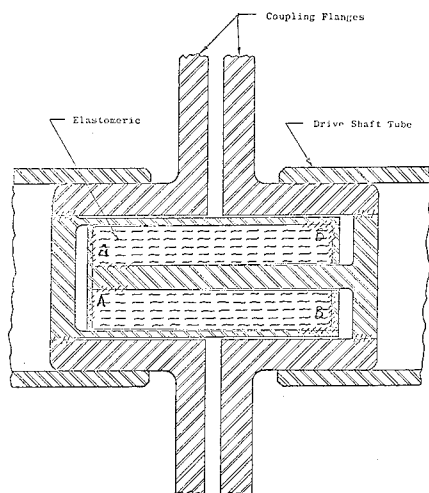


Fig. 15 - View of proposed ZTS coupling dampener configuration

Additionally, the torsion bar has been specially designed with an annular sleeve of elastomeric material to dissipate energy for damping. An important feature of this design is the sliding friction induced at both the inner and outer surfaces of the elastomeric material, as shown in Figures 15 and 16.

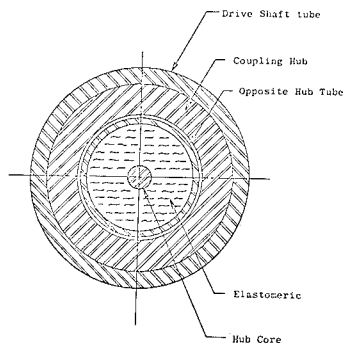


Fig. 16 - Section view of proposed ZTS coupling dampener configuration

COMPUTER SIMULATION OF DRIVE TRAIN DYNAMICS

The helicopter drive train shown in Figure 4, but without the feedback speed control, can be modeled with the following parameters:

Rotor inertia	I_R
Engine inertia	I_e
Speed reducer inertia	I_G
Mast shaft stiffness	K_S
Drive shaft stiffness	K_t
Rotor damping	C_L
Engine damping	C_e
Mast shaft damping	C_s
(see Figure 17)	

For systems with speed reducers it is common practice to reference all springs and inertias to one side of the gear box. For this analysis the engine side will be used.

Numerical values for the above inertias and spring constants taken from Swick and Skarvan [1] are:

$I_R = 3.888$	slug-ft ²
$I_e = 0.500$	slug-ft ²
$I_G = 0.144$	slug-ft ²
$K_S = 212.1$	ft-lb/rad
$K_t = 21,417$	ft-lb/rad
(all values references to engine side of gear box)	

It will be assumed that the aerodynamic rotor drag and engine drag are proportional to angular velocity squared [1]. Nearly all of the shaft horsepower of the engine is dissipated in the aerodynamic drag of the rotor, where

$$T_{\text{DRAG}} = C_L \dot{\theta}_R^2$$

For steady state operation with $T = 2004 \text{ ft-lb}$ and $\dot{\theta}_R = \dot{\theta}_e = 1447 \text{ rad/sec}$

$$C_L = 9.564 \times 10^{-4} \text{ ft-lb-sec}^2$$

A value for the engine damping coefficient C_e is determined by assuming a 25-30% total power loss due to turbine drag, thus total Hp = 7400 Hp.

An engine drag torque of about 800 ft-lb is calculated, giving

$$C_e \dot{\theta}_e^2 = 800 \text{ ft-lb}$$

or

$$C_e = 3.82 \times 10^{-4} \text{ ft-lb-sec}^2$$

The speed reducer inertia is small compared to the engine inertia and the drive shaft stiffness is much larger than the mast shaft stiffness which is effectively reduced by the speed reduction ratio.

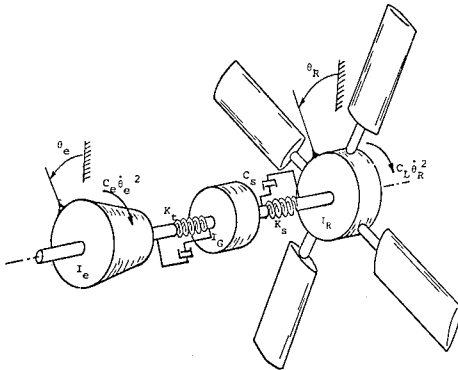


Fig. 17 - Helicopter drive train parameters

Since the investigation of torsional vibrations is not directly concerned with very high frequency vibrations, the drive shaft can be assumed to be rigid, allowing the speed reducer inertia to be combined with the engine inertia giving a new value I'_e :

$$I'_e = I_e + I_G$$

The model for the helicopter drive train with $K_t \rightarrow \infty$ and $I'_e = I_e + I_G$ reduces to the two degree of freedom system as shown in Figure 18 (System 1).

The mast shaft damping is assumed to be 10% of critical damping.

$$C_s = \frac{1}{10} (2 K_s I_{eff}) = 2.24$$

where

$$I_{eff} = \frac{I'_e I_R}{I'_e + I_R}$$

The drive train model of Figure 18, with the zero torsional stiffness coupling installed in the drive shaft, has an additional degree of freedom. The inertia of the driving flange of the coupling is combined with the engine inertia since K_t is assumed to be infinite, giving $I'_e = I_e + I_{fe}$. The driven flange of the coupling is combined with the speed reducer inertia to give $I'_{fr} = I_G + I_{fr}$. Coupling damping is not included in the simulation.

Figure 19 shows the resulting three degree of freedom system with the coupling (System 2).

The open-loop helicopter drive train model without a zero-torsional stiffness coupling can be dynamically described by the following two differential equations of motion:

$$\Sigma T_e = I'_e \ddot{\theta}_e \quad \Sigma T_R = I_R \ddot{\theta}_R \quad (1)$$

or by inspection

$$I'_e \ddot{\theta}_e = -K_s (\theta_e - \theta_R) - C_e \dot{\theta}_e^2 - C_s (\dot{\theta}_e - \dot{\theta}_R) + T(t)$$

$$I_R \ddot{\theta}_R = K_s (\theta_e - \theta_R) - C_L (t) \dot{\theta}_R^2 + C_s (\dot{\theta}_e - \dot{\theta}_R)$$

The equations of motion for the helicopter drive train with a zero torsional stiffness coupling are much more complex than the above. They can be derived from Lagrange's equation, but this involves some extremely lengthy expressions from the time derivative and requires numerical re-integration of these derivatives for a solution. Both of these disadvantages are circumvented by the use of the method of references [6] and [7]. Derivation of the equations of motion by this method, and their solution, are described in Appendix A.

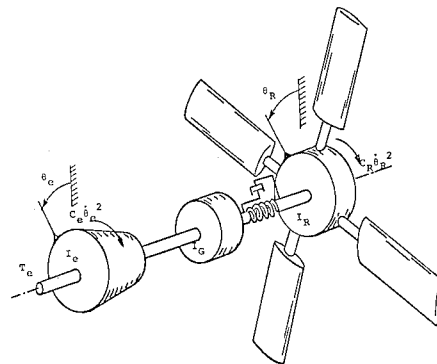


Fig. 18 - System 1 - Helicopter drive train (no coupling)

Modes of Excitation

System 1 (Figure 18) and System 2 (Figure 19) were subjected to the following external excitation in the computer simulation:

Test 1--Variation of C_L

This test models the cyclic change of the aerodynamic rotor drag caused by the rotor blades entering and leaving the direction of flight as well as cyclic variations caused by pilot excitation of collective pitch. The lift coefficient of the rotor, C_L , is sinusoidally varied $\pm 10\%$ about its average value.

$$C_L(t) = C_L(1 + 0.1 \sin \omega t)$$

$$\omega = 2.5 \rightarrow 10 \text{ Hz}$$

Test 2--Variation of T_e

Pilot adjustment of engine speed as well as possible feedback excitation is represented by sinusoidally varying the engine torque $\pm 10\%$ about normal operating input torque, T_e (2804 ft-lb).

$$T_e(t) = T_e(1 + 0.1 \sin \omega t)$$

$$\omega = 2.5 - 10 \text{ Hz}$$

Test 3-- $T_e(t)$

System start-up is modeled by increasing engine torque parabolically from 0 to 2800 ft-lb in 3 seconds. System shut-down is modeled by cutting the engine torque to zero when system is operating at steady state.

$$\begin{aligned} T_e(t) &= 1/3t T_e(2-t/3) & 0 < t < 3 \text{ sec} \\ T_e(t) &= T_e & 3 < t < 20 \text{ sec} \\ T_e(t) &= 0 & t \geq 20 \text{ sec} \end{aligned}$$

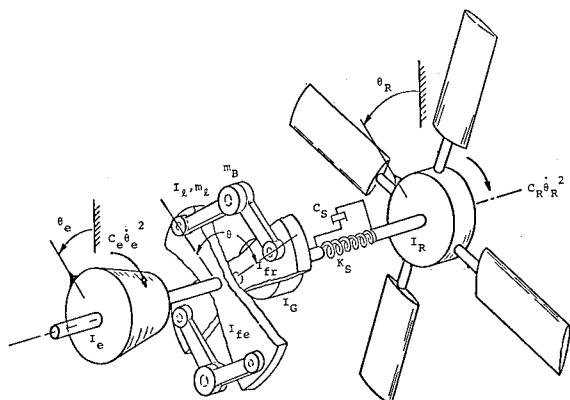


Fig. 19 - System 2 - Helicopter drive train (with coupling)

Measuring System Response

A helicopter control system compares the engine speed with a desired speed and alters the various engine torque producing parameters accordingly. If external excitations cause large variations of the engine speed, controlling system stability may prove to be difficult. A beneficial effect of the ZTS coupling is to effectively isolate the engine inertia from the rest of

the system, resulting in a reduction of the engine speed variation due to external excitation. The first measure of system response is $\Delta \dot{\theta}_e$, the engine speed variation about the normal operating speed (1447 rad/sec). The second measure of system response is ΔT_s , the variation of the torque transmitted by the mast shaft about the normal operating torque (2004 ft-lb). The quantity ΔT_s indicates the torque overload experienced by the mast shaft, gearbox, engine turbine, and rotor.

The speed variation, $\Delta \dot{\theta}_e$, has units of rad/sec and the torque overload, ΔT_s , is in percentage of operating torque.

System Response

The results of Test 1 given in Figure 20 shows the engine speed variation, $\Delta \dot{\theta}_e$, and mass torque variation, ΔT_s , as a function of the exciting frequency ω . Above 5 Hz, $\Delta \dot{\theta}_e$ and ΔT_s are virtually unaffected by the exciting force. At slightly above 3 Hz, System 1 experiences a critical frequency. System 2 has a critical region below 2.5 Hz where the coupling hits against the stops during each cycle of excitation, with no coupling damper acting.

It should be noted that the "critical frequencies" referred to here are actually the speeds at which maximum response is observed for the non-linear system. These critical frequencies are therefore amplitude dependent. In fact, the systems with ZTS couplings would show no vibratory response at all for very small amplitudes of excitation or from a linear analysis.

Due to the non-linearity of the coupling in System 2 the values of $\Delta \dot{\theta}_e$ and ΔT_s depend not only on the exciting frequency but on the state (position and velocity) the system is in when excitation occurs. If either System 1 or 2 is excited at very low frequencies $\omega < .5$ Hz then the values of $\dot{\theta}_e$ and $\dot{\theta}_R$ will be nearly the same. For this type of excitation the coupling in System 2 may close against the stops causing the system to assume the stiffness of the mast shaft, K_S .

Figure 21 shows the results from Test 2. The engine inertia is directly excited in this test causing severe oscillations of engine speed and mast shaft torque when excitation occurs at or near the critical frequency.

A time response curve of $\dot{\theta}_e$ and $\dot{\theta}_R$ during start-up and shut-down is shown in Figure 22. $\dot{\theta}_e$ and $\dot{\theta}_R$ of System 1 and System 2 closely follow curve 1 for the first 20 seconds (start-up and steady state). During initial start-up $\dot{\theta}_e$ leads $\dot{\theta}_R$ while the mast shaft "winds up" and then small oscillations of $\dot{\theta}_e$ and $\dot{\theta}_R$ about curve 1 slowly dampen out. After 20 seconds, when T_e is set to zero, $\dot{\theta}_e$ and $\dot{\theta}_R$ of System 1 closely follow curve 2. Small oscillations again occur as the mast shaft unwinds. $\dot{\theta}_R$ in System 2 closely follows curve 2 but $\dot{\theta}_e$ experiences severe oscillations for the first one-half second when the

system is shut down. This is due to the coupling mass traveling radially outward causing the coupling to quickly close against the reverse stops.

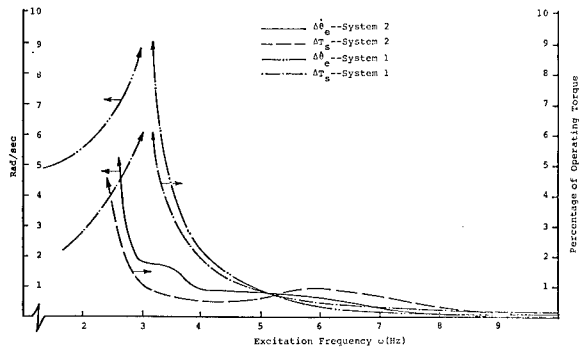


Fig. 20 - Variation of C_L

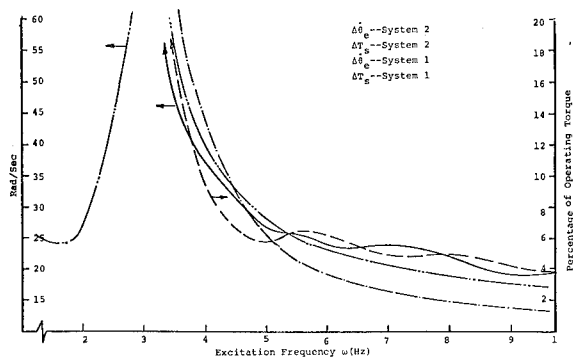


Fig. 21 - Variation of T_e

Other Systems

Swick and Skarvan [1] point out that the difference in the natural frequencies of helicopter drive trains depends primarily on mast shaft stiffness. A common range for the natural frequencies is 2-6 Hz. The basic helicopter design presented thus far has a critical frequency slightly above 3 Hz. Increasing the mast shaft stiffness of the helicopter design by a factor of four gives the system a natural frequency of approximately 6 Hz. Figure 23 shows the response of Systems 1 and 2 with increased mast shaft stiffness to the excitation of Test 1. At the critical frequency of System 1 (6 Hz) the torque variation is over 22% while the speed variation is over 11 rad/sec. With the use of a

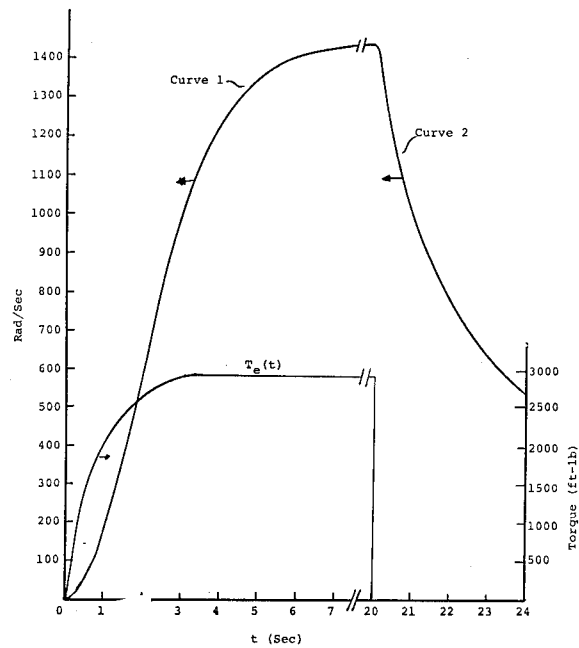


Fig. 22 - Time response of helicopter drive train

ZTS coupling (System 2) the critical frequency of the system is shifted below 4 Hz.

The time response of $\dot{\theta}_e$, $\dot{\theta}_R$ and mast shaft torque to a 6 Hz excitation of the system of Figure 23 is shown in Figure 24. The zero reference speed in Figure 24 is 1447 rad/sec and the zero reference torque is 2004 ft-lb.

The rotor speed varies +2.2 rad/sec for System 1 and +1.3 rad/sec for System 2. The engine varies +12 rad/sec for System 1 while the engine

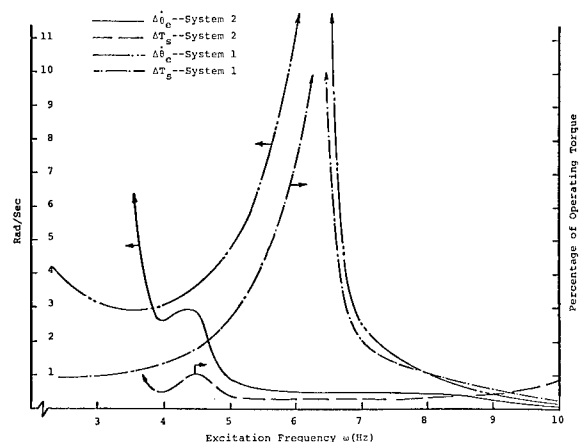


Fig. 23 - Variation of C_L

variation for System 2 is less than +0.5 rad/sec. Variation of the mast shaft torque is +23% for System 1 and less than 1% for System 2.

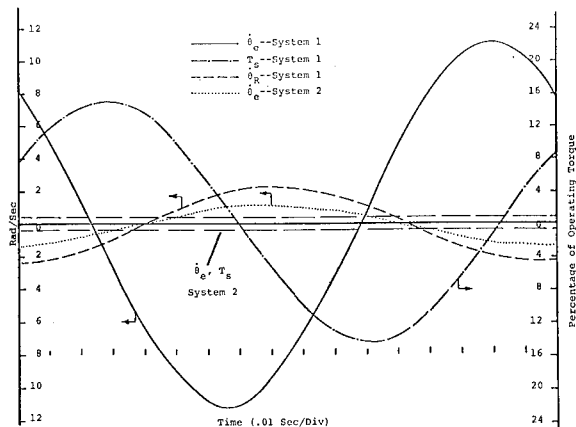


Fig. 24 - System time response to excitation

Systems which have higher shaft stiffness may represent other turbine applications such as pump or generator systems. The final investigation of system response to external excitation is with mast shaft stiffness eight times that of the original helicopter design. Figure 25 shows the system response from Test 1. The critical frequency of System 1 is slightly under 7.5 Hz. Using a ZTS coupling shifts the critical frequency of the system below 4 Hz.

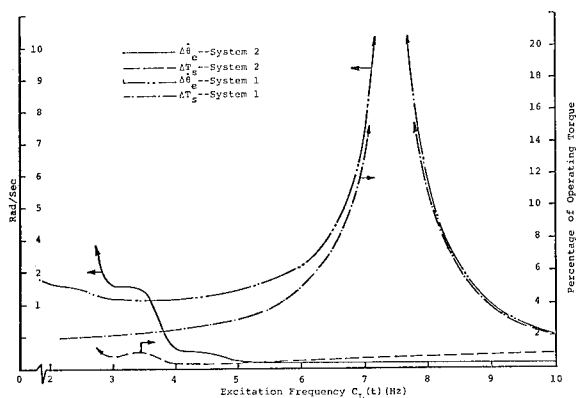


Fig. 25 - Variation of C_L

CONCLUSIONS

1. Torsional vibrations can be reduced or eliminated with a ZTS coupling. The factors which can limit coupling effectiveness are:

- very low frequency excitation

- very large torque variations
- new critical frequencies in the range of excitation.

2. ZTS couplings can be designed for high-speed turbo-powered machinery, and are ideally suited for the drive shaft speeds found in modern helicopters.

3. For systems where the drag torque is proportional to the angular velocity squared (helicopter system) the ZTS coupling becomes speed independent (see Figure 11).

4. Since the coupling damper of Figures 15 and 16 was not included in the simulations, the responses obtained can be considered to be "worst case", and were controlled entirely by the low stiffness characteristics of the coupling.

5. Since a ZTS coupling can twist through relatively large angles without failure, the possibility exists to dissipate large amounts of energy in an integral damper, thus further improving (reducing) the response to vibratory excitation. Actual damping coefficients must be determined by testing.

ACKNOWLEDGEMENT

The work described in this paper was supported by a contract with the U.S. Army Air Mobility Laboratory, Eustis Directorate, Propulsion Division, Ft. Eustis, Virginia. The Army Project Engineer was Mr. James Gomez. The support of the Laboratory and Mr. Gomez is gratefully acknowledged.

APPENDIX A: EQUATIONS OF MOTION FOR SYSTEM 2

The generalized coordinates are θ_e , θ and θ_R . In order to find an expression for the Lagrangian of the three degree of freedom system, the linear and angular velocities of each mass and inertia must be determined. For the engine and rotor inertias I_e' and I_R , the angular velocities are $\dot{\theta}_e$ and $\dot{\theta}_R$ respectively. The velocities of the coupling links are functions of $\dot{\theta}_e$ and $\dot{\theta}$ as well as θ_e and θ . Referring to Figure A-I the kinetic and potential energies are:

$$T = \frac{1}{2} I_e' \dot{\theta}_e^2 + \frac{1}{2} I_R \dot{\theta}_R^2 + \frac{1}{2} I_{FR} (\dot{\theta}_e - \dot{\theta})^2 + \frac{1}{2} N m_B v_B^2 + \frac{1}{2} N m_\ell (v_{\ell 1}^2 + v_{\ell 2}^2) + \frac{1}{2} N I_\ell (\omega_{\ell 1}^2 + \omega_{\ell 2}^2)$$

$$V = \frac{1}{2} K_S (\theta_e - \theta - \theta_R)^2$$

where

- N = number of link pairs
- $v_{\ell 1}$ = linear velocity of C.G. of link 1.
- $\omega_{\ell 1}$ = angular velocity of link 1.
- $v_{\ell 2}$ = linear velocity of C.G. of link 2.
- $\omega_{\ell 2}$ = angular velocity of link 2.
- (see Figure A-I)

For the static analysis of the coupling it was shown that m_ℓ and m_B can be combined, but

when $\dot{\theta}$ is not constant the mass distribution of the links will have some effect on the system response. A significant effect would only be expected when the links are massive (low speed-high power) but will be left in the analysis for generality.

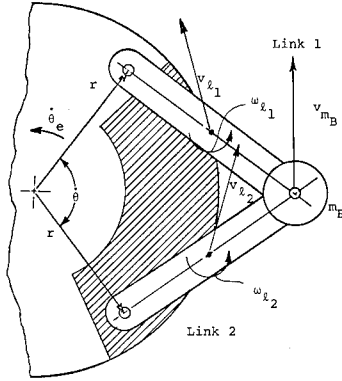


Fig. A-I - Coupling velocities

The expressions for the v's and ω 's in the kinetic energy equation are given below.

$$\begin{aligned} v_B^2 &= \dot{R}^2 + R^2(\dot{\theta}_e - \dot{\theta}/2)^2 \\ v_L^2 &= v_{L1}^2 + v_{L2}^2 = \frac{1}{2}\{r^2(\dot{\theta}_e^2 - \dot{\theta}_e\dot{\theta} + \dot{\theta}^2/2) \\ &\quad - r\dot{R}\dot{\theta}(\sin\theta/2) + \dot{R}^2 + 2rR(\dot{\theta}_e - \dot{\theta}/2)^2\cos\theta/2 \\ &\quad + R^2(\dot{\theta}_e - \dot{\theta}/2)^2\} \quad (A-2) \\ \omega_L^2 &= \omega_{L1}^2 + \omega_{L2}^2 = \frac{2}{\ell^2}\{r^2(\dot{\theta}_e^2 - \dot{\theta}_e\dot{\theta} + \dot{\theta}^2/2) \\ &\quad + r\dot{R}\dot{\theta}(\sin\theta/2) + \dot{R}^2 - 2rR(\dot{\theta}_e - \dot{\theta}/2)^2\cos\theta/2 \\ &\quad + R^2(\dot{\theta}_e - \dot{\theta}/2)^2\} \end{aligned}$$

where \dot{R} is the time derivative of R in

$$\dot{R} = -\frac{1}{2}\dot{\theta}\left[r(\sin\theta/2) + \frac{r^2\sin\theta}{2\sqrt{\ell^2 - r^2}(\sin\theta/2)}\right] \quad (A-3)$$

The Lagrangian can now be written in terms of the generalized coordinates as

$$\begin{aligned} L &= \frac{1}{2}I_R\dot{R}^2 + \frac{1}{2}I_e\dot{\theta}_e^2 + \frac{1}{2}I_{FR}(\dot{\theta}_e - \dot{\theta})^2 \\ &\quad + \frac{1}{2}NM_1[\dot{R}^2 + R^2(\dot{\theta}_e - \dot{\theta}/2)^2] - \frac{1}{2}NM_2[r\dot{R}\dot{\theta}(\frac{\sin\theta}{2}) \\ &\quad - 2rR(\dot{\theta}_e - \dot{\theta}/2)^2\cos\theta/2] \\ &\quad + \frac{1}{2}NM_3[r^2(\dot{\theta}_e^2 - \dot{\theta}_e\dot{\theta} + \dot{\theta}^2/2)] - K_S(\theta_e - \theta - \theta_R)^2 \end{aligned} \quad (A-4)$$

where

$$\begin{aligned} M_1 &= m_B + m_L/2 + 2I_L/\ell^2 \\ M_2 &= m_L/2 - 2I_L/\ell^2 \\ M_3 &= m_L/2 + 2I_L/\ell^2 \end{aligned}$$

The potential forces, $\partial L/\partial q_i$, are:

$$\begin{aligned} \frac{\partial L}{\partial \theta} &= \frac{1}{2}NM_1[2\dot{R}\frac{\partial \dot{R}}{\partial \theta} + 2R\frac{\partial R}{\partial \theta}(\dot{\theta}_e - \dot{\theta}/2)^2] \\ &\quad - \frac{1}{2}NM_2[r\dot{\theta}\frac{\partial \dot{R}}{\partial \theta}(\sin\theta/2) + \frac{1}{2}r\dot{R}\dot{\theta}(\cos\theta/2) \\ &\quad - 2r\frac{\partial R}{\partial \theta}(\dot{\theta}_e - \dot{\theta}/2)^2\cos\theta/2 + rR(\dot{\theta}_e - \dot{\theta}/2)^2\sin\theta/2] \\ &\quad + K_2(\theta_e - \theta - \theta_R) \quad \text{for } \theta \\ \frac{\partial L}{\partial \theta_e} &= -K_S(\theta_e - \theta - \theta_R) \quad \text{for } \theta_e \\ \frac{\partial L}{\partial \theta_R} &= K_S(\theta_e - \theta - \theta_R) \quad \text{for } \theta_R \end{aligned} \quad (A-5)$$

The momenta, P_i , are:

$$\begin{aligned} P_T &= \frac{\partial L}{\partial \dot{\theta}} = I_{FR}(\dot{\theta}_e - \dot{\theta}) + \frac{1}{2}NM_1[2\dot{R}\frac{\partial \dot{R}}{\partial \dot{\theta}} - R(\dot{\theta}_e - \dot{\theta}/2)] \\ &\quad - \frac{1}{2}NM_2[r\dot{\theta}\frac{\partial \dot{R}}{\partial \dot{\theta}}(\sin\theta/2) + r\dot{R}(\sin\theta/2) \\ &\quad + 2rR(\dot{\theta}_e - \dot{\theta}/2)\cos\theta/2] + \frac{1}{2}NM_3r^2(\dot{\theta}_e - \dot{\theta}) \quad \text{for } \theta \\ P_e &= \frac{\partial L}{\partial \dot{\theta}_e} = I_e\dot{\theta}_e + I_{FR}(\dot{\theta}_e - \dot{\theta}) + \frac{1}{2}NM_1[2R^2(\dot{\theta}_e - \dot{\theta}/2)] \\ &\quad + \frac{1}{2}NM_2[4rR(\dot{\theta}_e - \dot{\theta}/2)\cos\theta/2] \\ &\quad + \frac{1}{2}NM_3[2r^2(\dot{\theta}_e - \dot{\theta}/2)] \quad \text{for } \theta_e \\ P_R &= \frac{\partial L}{\partial \dot{\theta}_R} = I_R\dot{\theta}_R \quad \text{for } \theta_R \end{aligned} \quad (A-5)$$

The expressions for the partial derivatives of R and \dot{R} used in equations (A-5) in terms of the generalized coordinate are:

$$\begin{aligned} \frac{\partial R}{\partial \theta} &= -\frac{1}{2}[r(\sin\theta/2) + \frac{r^2\sin\theta}{2\sqrt{\ell^2 - r^2}(\sin^2\theta/2)}] \\ \frac{\partial \dot{R}}{\partial \theta} &= -\frac{1}{4}\dot{\theta}[r(\cos\theta/2) + \frac{r^2\cos\theta}{\sqrt{\ell^2 - r^2}(\sin^2\theta/2)} \\ &\quad + \frac{r^4\sin^2\theta}{4[\ell^2 - r^2(\sin^2\theta/2)]^{3/2}}] \\ \frac{\partial \dot{R}}{\partial \dot{\theta}} &= \frac{\partial R}{\partial \dot{\theta}} \end{aligned}$$

The generalized forces F_i determined from the principle of virtual work are:

$$\begin{aligned} \delta W_e &= F_e\delta\theta_e \\ F_e &= T_e(t) - C_S(\dot{\theta}_e - \dot{\theta} - \dot{\theta}_R) - C_e\dot{\theta}_e|\dot{\theta}_e| \quad \text{for } \theta_e \end{aligned}$$

where $T_e(t)$ is any time function of the input torque.

$$\begin{aligned} \delta W_R &= F_R\delta\theta_R \\ F_R &= C_S(\dot{\theta}_e - \dot{\theta} - \dot{\theta}_R) - C_L(t)\dot{\theta}_R|\dot{\theta}_R| \quad \text{for } \theta_R \end{aligned}$$

where $C_L(t)$ is any time function of the rotor lift coefficient.

$$\begin{aligned} \delta W_T &= F_T\delta\theta \\ F_T &= C_S(\dot{\theta}_e - \dot{\theta} - \dot{\theta}_R) - C_D\dot{\theta} - K_{fk}(\theta) \quad \text{for } \theta \end{aligned} \quad (A-8)$$

where C_D is viscous hinge friction in the coupling and $K_{FK}(\theta)$ represents any additional springs that might be added to the coupling. C_s and C_e are the shaft and engine damping coefficients respectively.

Using equations (A-5) and (A-8), Lagrange's equations can be expressed in canonical form, which eliminates the necessity to take time derivatives of equations (A-6):

$$\begin{aligned}\dot{P}_e &= \frac{\partial L}{\partial \dot{\theta}_e} + F_e \\ \dot{P}_T &= \frac{\partial L}{\partial \dot{\theta}} + F_T \\ \dot{P}_R &= \frac{\partial L}{\partial \dot{\theta}_R} + F_R\end{aligned}\quad (A-9)$$

From equation (A-5):

$$\begin{Bmatrix} \dot{P}_T \\ \dot{P}_e \end{Bmatrix} = [A] \begin{Bmatrix} \dot{\theta} \\ \dot{\theta}_e \end{Bmatrix}\quad (A-10)$$

$$P_R = I_R \dot{\theta}_R$$

where the elements of the A matrix are:

$$\begin{aligned}a_{11} &= \frac{1}{2}N\{M_1(2\bar{R}\frac{\partial \dot{R}}{\partial \dot{\theta}} + \frac{1}{2}R^2) + M_2(-r\frac{\partial \dot{R}}{\partial \dot{\theta}}(\sin\theta/2) \\ &\quad - r\dot{R}(\sin\theta/2) + rR(\cos\theta/2) + M_3r^2) + I'_{FR}\} \\ a_{12} &= -\frac{1}{2}N(M_1R^2 + 2M_2rR(\cos\theta/2) + M_3r^2) - I'_{FR} \\ a_{21} &= a_{12} \\ a_{22} &= I'_e - I'_{FR} - 2a_{12}\end{aligned}$$

and

$$\bar{R} - \dot{R}/\dot{\theta} = \frac{\partial R}{\partial \dot{\theta}}$$

Upon inversion of equations (A-10) the following expressions for the three generalized velocities result:

$$\begin{aligned}\dot{\theta} &= (a_{22}P_R - a_{12}P_e)/(a_{11}a_{22} - a_{21}a_{12}) \\ \dot{\theta}_e &= (a_{11}P_R - a_{21}P_e)/(a_{11}a_{22} - a_{21}a_{12}) \\ \dot{\theta}_R &= P_R/I_R\end{aligned}\quad (A-11)$$

Equations (A-9) and (A-11) form a set of six first-order differential equations in coordinates:

$$\begin{aligned}P_e \\ P_T \\ P_R \\ \theta_e \\ \theta \\ \theta_R\end{aligned}$$

These equations can be numerically solved by

- 1) specifying initial conditions for P_T , P_{e0} , P_{R0} , θ_{e0} , θ_0 and θ_{R0} (initial conditions for $\dot{\theta}_{e0}$, $\dot{\theta}_0$, and $\dot{\theta}_{R0}$ can be used

with equations (A-10) to produce P_{e0} , P_{T0} , and P_{R0})

- 2) finding values for $\dot{\theta}_e$, $\dot{\theta}$ and $\dot{\theta}_R$ from equations (A-11)
- 3) finding values for \dot{P}_e , \dot{P}_T and \dot{P}_R from equations (A-9)
- 4) numerically integrating \dot{P}_e , \dot{P}_T , \dot{P}_R , $\dot{\theta}_e$, $\dot{\theta}$, $\dot{\theta}_R$.

Using Euler integration

$$\begin{aligned}\theta_{e,n+1} &= \theta_{e,n} + \dot{\theta}_{e,n} \Delta t \\ \theta_{n+1} &= \theta_n + \dot{\theta}_n \Delta t \\ \theta_{R,n+1} &= \theta_{R,n} + \dot{\theta}_{R,n} \Delta t \\ P_{e,n+1} &= P_{e,n} + \dot{P}_{e,n} \Delta t \\ P_{T,n+1} &= P_{T,n} + \dot{P}_{T,n} \Delta t \\ P_{R,n+1} &= P_{R,n} + \dot{P}_{R,n} \Delta t \\ t_{n+1} &= t_n + \Delta t\end{aligned}$$

- 5) Using the n+1 values from step 4, return to step 2 and repeat procedure for desired length of time.

REFERENCES

- a. R.M. Swick and C.A. Skarvan, "Investigation of Coordinated Free Turbine Engine Control Systems for Multi-Engine Helicopters," USAAVLABS Technical Report 67-73, Dec. 1967.
- b. J. L. Peczkowski, "Automatic Control of Free Turbine Engines," ASME Paper No. 73-WA-159, Aug. 1973.
- c. R. P. Canale and P. R. McCabe, "The Fuel Flow Reset Approach to Gas Turbine Governing," SAE Paper No. 650530, May 1965.
- d. C. W. Chapman, "Zero (Or Low) Torsional Stiffness Couplings," J. Mech. Engr. Sci., Vol. II, No. 1, 1969.
- e. M.F. Balzhi and G.D. Esin, "Flexible Metallic Couplings with Dynamic Links," The Engrs. Digest, Apr. 1960.
- f. J.M. Vance and A.Sitchin, "Numerical Solution of Dynamical Systems by Direct Application of Hamilton's Principle," Int. J. Numer. Meth. Eng., Vol. 4, 207-216, 1972.
- g. J.M. Vance and A.Sitchin, "Derivation of First-Order Difference Equations for Dynamical Systems by Direct Application of Hamilton's Principle," J. App. Mech., June 1970, 276-278.

VIBRATION TESTING AND ANALYSIS

DEVELOPMENT OF SAM-D MISSILE RANDOM VIBRATION RESPONSE LOADS

Paul G. Hahn
Martin Marietta Aerospace
Orlando, Florida 32805

An investigation was performed to obtain the random vibration response loads for inclusion in the design of the SAM-D Engineering Development (ED) flight vehicle. The response loads are assumed to be the summation of the individual responses of the lightly damped lateral bending vibration modes of the vehicle when subjected to the excitation of the random aerodynamic pressures generated in flight.

I. SUMMARY

The characteristic lateral bending vibration modes are a function of the flight vehicle structural stiffness and mass distribution. The higher lateral response accelerations occur for the lighter mass condition; hence, the burnout condition was assumed for the principal investigation. The eleven modes having characteristic frequencies up to 500 Hz were included in the evaluation of the random loads.

The excitation force associated with the random aerodynamic pressure distribution acting on the external surface of the vehicle in flight was evaluated from data obtained during flight tests of the SAM-D Control Test Vehicle, (CTV) which are described in references 1 to 3. This external force spectral density was assumed to have an amplitude-versus-frequency distribution similar and proportional to measurement distributions obtained from several accelerometers on each flight test vehicle. The energy contained in the measured lateral acceleration frequency band of 0-2000 Hz was assumed to be effective within a reduced frequency band of 0-1000 Hz, thereby developing a conservative magnitude for this external force input to determine the random response of the structural modes.

Using the flight vehicle characteristic and aerodynamic force data described above, the random response loads acting in the vehicle structure were obtained. These design data are the lateral bending moment, shear force, and lateral acceleration distributions along the length of the vehicle.

II. INTRODUCTION

Design loads acting within the primary structure of the SAM-D flight vehicle are a function of the vehicle translational load factors and angular accelerations, plus the

loads resulting from transient excitation of the vehicle by fluctuating aerodynamic pressure generated by vehicle boundary layer, base and cross flow, and control surface motion.

The vehicle loads generated are limited to the lateral bending moment and shear force distributions resulting in the vehicle in response to random loading of the vehicle by the fluctuating aerodynamic pressures. The effect of aerodynamic control surface motion is included by assuming the vehicle to have an airload distribution including a control surface rotation consistent with the maximum angle of attack obtainable by the vehicle in its burnout flight configuration. The associated random vibration lateral acceleration distribution is also generated.

III. RANDOM LOADS IN STRUCTURE

A number of approaches to the evaluation of the random loads acting on and within structure are considered in reference 7 and 8. The approach selected for evaluation of the SAM-D ED flight vehicle random vibration response loads is based upon the displacement of a linear structure being expressed in terms of the principal modes of motion as

$$y(X,t) = \sum_n q_n(t) h_n(X) \quad (1)$$

where the structure is considered a beam, symmetric about the X, y plane, extending in length along the longitudinal X axis, and deflecting laterally in the y direction; $q_n(t)$ is the generalized lateral bending coordinate in the n^{th} normal mode; $h_n(X)$ is the associated n^{th} normal mode lateral bending deflection mode shape; t is, as usual, the independent variable, time.

Assuming the existence of the positive structural damping that is in phase with the modal velocity and proportional to the general-

ized displacement of each mode, the Lagrangian equations of motion have the following form:

$$\ddot{Q}_n(t) + (1 + i g_d) \omega_n^2 Q_n(t) = \frac{Q_n(t)}{M_n} \quad (2)$$

where ω_n is the n^{th} mode frequency; $Q_n(t)$ is the generalized force; and M_n the generalized mass associated with the n^{th} mode. $Q_n(t)$ and M_n are evaluated as follows:

$$Q_n(t) = \int_{x=0}^{x=l} f(X,t) h_n(X) dX \quad (3)$$

$$M_n = \int_{x=0}^{x=l} h_n^2(X) M(X) dX \quad (4)$$

In the above, $f(X,t)$ is the applied force, which can be assumed harmonic, or

$$f(X,t) = F(X) e^{i\omega t} \quad (5)$$

where ω is the force excitation frequency. Substituting equation (5) in equation (3) yields an expression for the generalized force

$$Q_n(t) = e^{i\omega t} \int_{x=0}^{x=l} F(X) h_n(X) dX \quad (6)$$

which can be rewritten

$$Q_n(t) = e^{i\omega t} W_o W_n \quad (7)$$

where

$$W_o = \int_{x=0}^{x=l} F(X) dX = \text{amplitude of total applied force on structure} \quad (8)$$

$$W_n = \frac{\int_{x=0}^{x=l} F(X) h_n(X) dX}{W_o} = \text{mode participation of load.} \quad (9)$$

Now let the mean squared response be defined by

$$\bar{Y}^2(X) = \frac{1}{T} \int_{t=0}^{t=T} Y^2(X,t) dt. \quad (10)$$

Assuming a spectrum of excitation frequencies, we can define a power spectral density, $f(\omega)$, of the excitation force such that its mean square value is given by

$$\bar{F}^2 = \frac{W_o^2}{2} = \int_{\omega=0}^{\omega=\infty} f(\omega) d\omega. \quad (11)$$

Substitution of the steady-state solution for each q_n of equation (2) into equation (1) yields the corresponding displacement, $y(x,t)$.

Substitution of both the displacement function and the mean square value of the excitation force from equation (11) into equation

(10) yields, upon integration over the characteristic time T of the applied force, the following expression for the mean square response in terms of the power spectral density of the excitation:

$$\bar{Y}^2(X) = \sum_n \int_{\omega=0}^{\omega=\infty} h_n^2(X) \frac{f(\omega)}{|Z(\omega)|^2} d\omega \quad (12)$$

where

$$\frac{1}{|Z(\omega)|^2} = \frac{1}{M_n^2 \omega_n^4} \left[\left(1 - \frac{\omega^2}{\omega_n^2} \right)^2 + g_d^2 \right]^{-1} \quad (13)$$

For small damping, g_d , all the contributions to the response are small except near resonance, and the generalized impedance of the structure, $Z(\omega)$, will undergo a large change near the resonant frequency, ω_n . If the variation of the power spectral density, $f(\omega)$, is of lesser extent in proximity to ω_n (see Figure 1.), equation (12) can be reasonably approximated by the following:

$$\bar{Y}^2(X) = \sum_n h_n^2(X) f(\omega_n) \int_{\omega_n - \Delta\omega_n}^{\omega_n + \Delta\omega_n} \frac{d\omega}{|Z(\omega)|^2} = \quad (14)$$

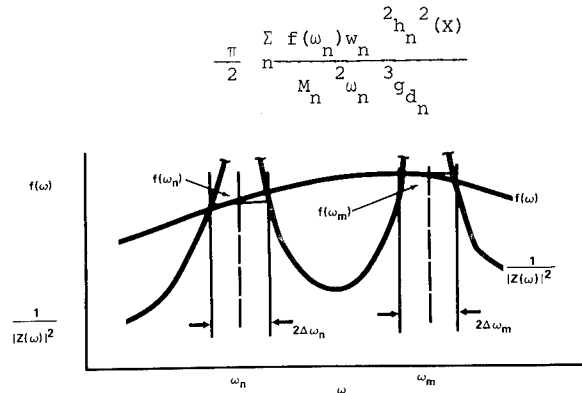


Figure 1. Mean Squared Response Evaluation

From equation (11) it is seen that the contribution to the mean square value of excitation in the range $\Delta\omega$ is

$$\Delta \bar{F}^2 = f(\omega) \Delta\omega \quad (15)$$

Now if \bar{F} consists of spectral frequency content of $\Delta\omega = W_c - 0$, then

$$f(\omega_n) = \frac{\bar{F}^2}{W_c} = \frac{F}{2\pi f_c} = \frac{1}{2\pi} f(f_n) \quad (16)$$

$$\text{where } f(f_n) = \frac{\bar{F}^2}{f_c} \text{ and } \omega_n = 2\pi f_c \quad (17)$$

Now, letting λ be any random variable such as lateral displacement, bending moment, or shear force in the beam structure and η its corresponding variable modal displacement, modal bending moment, or modal shear force, equation (14) can be rewritten, with (16) and (17) as follows:

$$\bar{\lambda}^2(X) = \frac{1}{32\pi^3} \sum_n \frac{W_n^2 \eta_n^2(X) f(f_n)}{M_n^2 f_n^3 g_{dn}}, \quad (18)$$

which expresses the mean square of the random variable in terms of the spectral density of the excitation and the principal modes of the structure.

Since both the excitation force and the structural response have been assumed to be harmonic, we have, from the steady-state solution of equation (2), $\ddot{q}_n = -\omega_n^2 q_n$, and hence from equation (1) the lateral acceleration of the structure is

$$\ddot{y}(X,t) = -\sum_n \omega_n^2 q_n(t) h_n(X). \quad (19)$$

Letting ξ be any random variable acceleration and η again its corresponding variable modal displacement, it can be shown in a similar manner that

$$\bar{\xi}^2(X) = \frac{\pi}{2} \sum_n \frac{W_n^2 \eta_n^2(X) f_n^2 f(f_n)}{M_n^2 g_{dn}}. \quad (20)$$

In order to bolster confidence in the validity of these expressions for application to design of the SAM-D ED flight vehicle, data from ground test of the SAM-D AD control test vehicle shown in Figure 2 were obtained from

reference 5 and analyzed by means of these expressions. Data were obtained for the case of missile lateral vibration excited by an electrodynamic shaker attached at the control surface shaft with a lateral random force of 148 pounds rms. The force gage installation is shown in Figure 3. The spectral content of this force is illustrated in Figure 4. This force was applied at missile station 19. An accelerometer mounted externally to the missile to measure lateral acceleration at station 7 indicated 0.95g rms response to this force. Pertinent data measured on and calculated for the CTV missile are shown in Table I. Nine lateral bending modes were considered in the evaluation. These included all modes up to 250 Hz.

An estimate of the effective rms force acting on the missile structure was made by utilizing equation (15) in which Δf_n was evaluated at each modal half-power point. Thus, we have the following:

$$\bar{F} = \left[\Delta \bar{F}^2 \right]^{1/2} = \left[\sum_n f(f_n) \Delta f_n \right]^{1/2} = \left[\sum_n f(f_n) f_n g_{dn} \right]^{1/2} \quad (21)$$

from which we see that the effective force driving the bending modes is $\bar{F} = 52.1$ pounds rms, which is about 35 percent of the shaker input force of 148 pounds rms. The remainder of the force goes into overcoming structural joint damping and exciting shell, support structure and equipment responses. Substitution of data from Table I into equation (20) yields a value of lateral response acceleration of 1.19g rms at station 7 which is about 25 percent greater than the corresponding measured value of 0.95g rms.

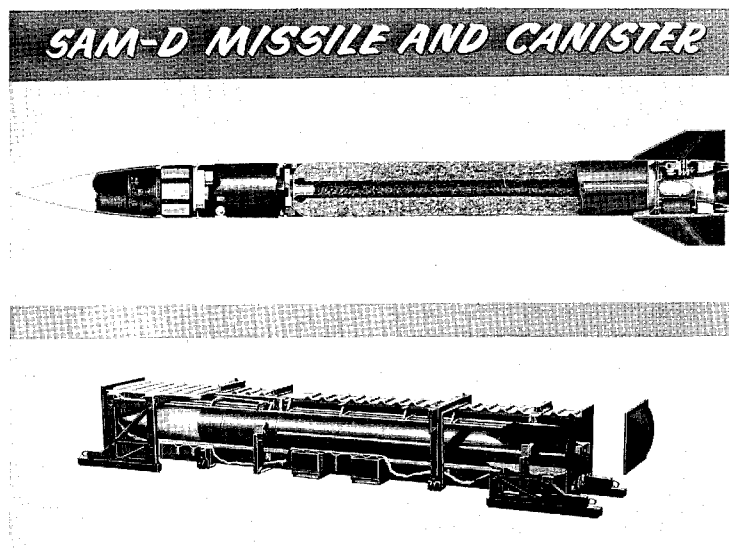


Figure 2. SAM-D Missile and Canister

SAM-D WITH LATERAL FORCE GAUGE

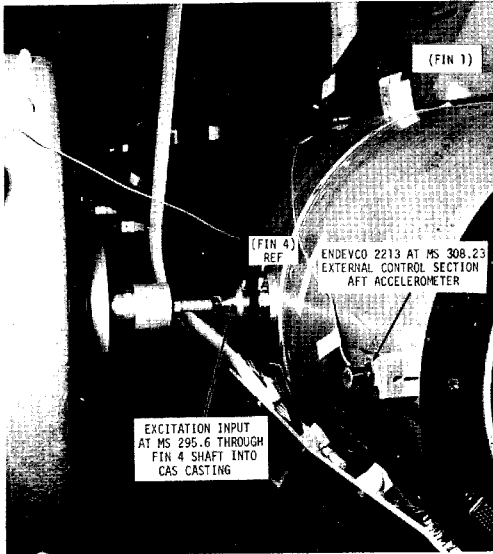


Figure 3. SAM-D With Lateral Force Gauge

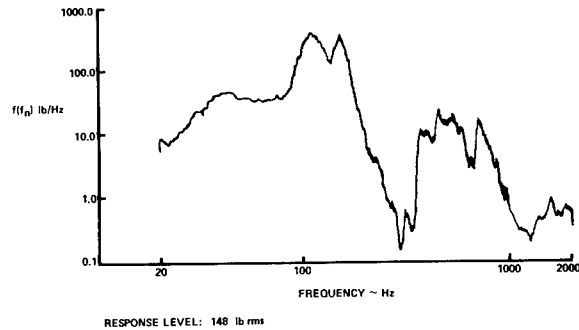


Figure 4. Lateral Force Spectral Density for SAM-D Burnout Missile

TABLE I

SAM-D CTV DATA

n, Mode	f_n , HZ	M_n , $\frac{\text{lb-sec}^2}{\text{in.}}$	$ W_n $, $\frac{\text{in.}}{\text{in.}}$	h_n , $\frac{\text{in.}}{\text{in.}}$	$g_{d_n}^{\text{non}}$	$f(f_n)$, $\frac{\text{lb}^2}{\text{HZ}}$
1	50.1	0.14495	0.165	0.335	0.022	34.0
2	83.6	0.11218	0.025	0.500	0.006	44.0
3	115.8	0.18065	0.140	0.160	0.019	350.0
4	133.2	0.10658	0.040	0	0.025	140.0
5	152.0	0.60881	0.045	0.010	0.020	315.0
6	168.9	0.08598	0.265	0.065	0.016	104.0
7	187.8	0.23803	0.180	0.485	0.022	34.0
8	208.1	-	0.235	0.120	0.024	6.3
9	249.5	0.31570	0.364	0.250	0.026	1.05

IV. ED FLIGHT VEHICLE LATERAL BENDING VIBRATION ANALYSIS

The ED flight vehicle was analyzed to determine its lateral bending dynamic characteristics. The lengthwise distributed mass and lateral bending stiffness properties were input into digital program W-59, currently in the library of Orlando Division of Martin Marietta Aerospace to obtain the fundamental series of lateral bending frequencies and associated modal deflections. One feature of this program is the allowance for inclusion of the elastic attachment of large discrete mass items in both relative translation and rotation in the plane of bending. The solution of this program was performed by the IBM 360/65 digital computer. The results computed for the burnout configuration of the flight vehicle are obtained from reference 4. The first three lateral bending mode displacements are illustrated in Figure 5. Typical modal data for the first of 11 fundamental modes are shown in Table II. These data are the

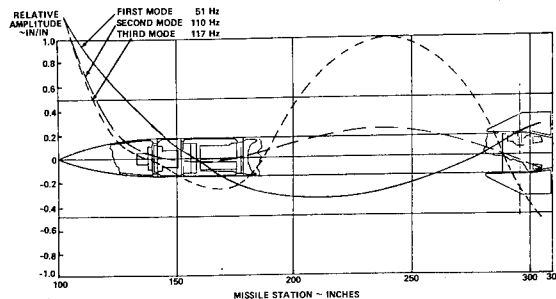


Figure 5. Computed SAM-D ED Bending Modes at Burnout

modal lateral normalized displacement, h in/in; bending slope angle, ϕ rad/in; bending moment, M in-lb/in; and lateral shear force, S lb/in; for each station of the primary structure indicated. For the four discrete cantilevered mass items considered at stations 4, 5, 7 and 20, similar deflection data are shown in Table III. The equivalent spring rates and sprung item moment arms are as follows:

TABLE II

ED Flight Vehicle First Bending Mode Data

1 BENDING MODE FREQUENCY = 51.051 CPS

STA	DISP	SLOPE	MOMENT	SHEAR
1.000	1.0000000	-0.027647276	0.26382D 02	0.17358D 04
2.000	0.6362837	-0.020312178	0.26057D 05	0.50489D 04
3.000	0.3672699	-0.016322664	0.10147D 06	0.82363D 04
4.000	0.2520017	-0.015702592	0.15517D 06	0.15040D 05
5.000	0.0713454	-0.014663572	0.32275D 06	0.15503D 05
6.000	-0.1114213	-0.012525975	0.52276D 06	0.14598D 05
7.000	-0.2412224	-0.008110927	0.62407D 06	0.30881D 04
8.000	-0.2894027	-0.005350599	0.64721D 06	0.51968D 03
9.000	-0.3365693	-0.003189833	0.65334D 06	-0.88836D 03
10.000	-0.3583258	-0.001233453	0.64466D 06	-0.23874D 04
11.000	-0.3603924	0.000674254	0.62080D 06	-0.38951D 04
12.000	-0.3434797	0.002487382	0.58167D 06	-0.53321D 04
13.000	-0.3087746	0.004160995	0.52802D 06	-0.66238D 04
14.000	-0.2579173	0.005653456	0.46130D 06	-0.77028D 04
15.000	-0.1929559	0.006928574	0.38367D 06	-0.85101D 04
16.000	-0.1162798	0.007957519	0.29785D 06	-0.89965D 04
17.000	-0.0305358	0.008720455	0.20710D 06	-0.91243D 04
18.000	0.0614720	0.009207854	0.11106D 06	-0.80474D 04
19.000	0.1620578	0.009424992	0.14639D 05	-0.17424D 04
20.000	0.2446726	0.009448615	-0.10544D-05	-0.11031D-07

TABLE III

ED Cantilevered Mass Modal Deflection Data

BENDING MODE/STA	4C	5C	7C	20C
Displacement				
1	.2664112	.0715593	-.2492535	.2608517
2	-.0507115	-.0180083	.0052505	-.1752760
3	.1543123	-.1894167	-.3192940	-.7934515
4	-.1908481	-.0802425	.0522461	.0805572
5	.0265485	.0120407	.0200239	1.0
6	.1901998	.3109173	.3962824	-.8483407
7	.4403296	-.1191182	-.0433514	.0369284
8	-.2075007	.6335782	-.1013015	.0612099
9	-.2387571	1.0	.2231806	-.0693570
10	-.1982759	1.0	-.4411623	.1671393
11	.0297708	-.0908317	.2427368	1.0
Slope				
1	-.0149284	-.0149694	-.0074986	.0093022
2	-.0580482	-.0033288	.0046477	-.0076105
3	.1257542	-.0076159	.0325590	-.0330026
4	.0312643	.0035978	-.0020407	.0023180
5	-.0033354	.0024768	.0091895	-.0145308
6	-.0248345	.1222160	.0945152	.1044287
7	-.0421655	.0494687	-.0077972	-.0127030
8	.0171710	1.0	-.0072559	-.0241646
9	.0166345	-.1979521	.0443066	-.1216919
10	.0148797	-.1103484	-.0458553	.1138917
11	-.0025143	.0053451	.0274145	.4980790

Station	Spring Rate $\times 10^{-6}$		Moment Arm, in.
	Lateral, lb/in.	Rotational, in-lb/rad	
4C	0.4555	7.010	3.04
5C	0.1319	2.108	1.76
7C	2.587	115.040	-7.75
20C	0.07037	0.8061	-1.71

V. ED FLIGHT VEHICLE RANDOM AERODYNAMIC FORCES

The estimation of the random aerodynamic excitation force must be made with three aspects of the force in mind. As shown in Section III, an evaluation of the maximum amplitude of the applied force, W_0 , is required as well as the frequency spectrum distribution of the applied force spectral density, $f(f_n)$. The portion of the total load that acts to drive each of the normal lateral bending modes is evaluated through the mode participation factor, W_n .

An evaluation was made to determine the airload distribution that would tend to maximize the excitation of the structural modes. Since normal modes were utilized in the evaluation of the structural dynamic characteristics of the flight vehicle, the integrated lateral forces and moments over the length of the vehicle are zero for each mode. A simple beam of uniform mass and bending stiffness is assumed for illustration. A lateral bending deflection function, $y = \cos 2\pi x/L$, satisfied the condition of zero integrated lateral shear force,

$\int_{x=0}^{x=L} y dm = 0$ for the illustrative beam with constant mass distribution. In the above, y is the lateral deflection at any station x on the beam of length, L . Similarly, a uniform normal airload distribution, $\partial C_N / \partial x$, results in a zero integrated lateral shear force. The lateral airload distribution per length of missile body shown in Figure 6 includes the distribution due to maximum nominal angle of attack, 30 degrees, and control vane rotational deflection including carryover distributions between body and vanes. It is noted that a peak value of C_{N_x} occurs at the nose due to angle of attack, and at the tail due to vane rotation. Hence, the simple model was checked for a uniform distribution over the total vehicle length plus a superposed additional uniform distribution of the same magnitude over both the first and last quarters of beam length. The integrated lateral force for this case,

$$\int_{x=0}^{x=L} y C_{N_x} dx, \text{ is found to be } C_{N_x} L / \pi. \text{ Thus,}$$

the airload distribution associated with an angle of attack and appropriate vane rotation will result in the maximum excitation of the normal lateral bending modes of the vehicle. The same result can also be shown from the beam bending moment considerations.

The modal participation factor associated with each of n modes can be evaluated with the airload distribution data of Figure 6 and the lateral deflection data of Table II, as follows:

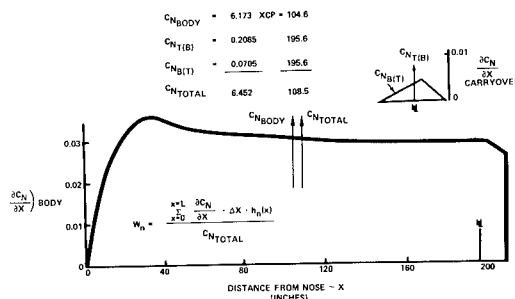


Figure 6. Normal ED Airload Coefficient Distribution

$$W_n = \frac{\sum_{x=0}^{x=L} C_{N_x} \Delta x h_n(x)}{C_{N \text{ total}}} \quad (22)$$

which yields the values shown in Table IV for each of the n bending modes.

TABLE IV
Mode Participation Factors

n	W_n
1	0.007794
2	0.122375
3	0.273250
4	-0.000164
5	0.012260
6	0.089376
7	-0.101553
8	0.007785
9	0.049960
10	0.105380
11	-0.002938

The maximum value of the applied aerodynamic force, W_0 , is found from the product of either the vehicle weight times lateral load factor or of the normal airload coefficient times the flight dynamic pressure times the vehicle reference area. The value of F , the root mean square force driving the vehicle lateral bending modes, is found as a proportional portion of W_0 . This proportionality factor is the ratio of the general root mean square lateral vibration acceleration in g units to the total lateral load factor. From the data obtained on lateral accelerometer No. 10204, shown in References 1 to 3, the maximum root mean square acceleration was found to be in g units; grms = 0.32 for the maximum dynamic pressure flight, grms = 0.30 for the maximum Mach number flight,

and grms = 0.30 for the maximum angle of attack flight. The spectral distribution of these data are shown in Figure 7. Hence, a value of grms = 0.30 was used to determine \bar{F} to be 264.78 pounds force. These root mean square lateral acceleration values were obtained by integrating the acceleration spectral densities over the full instrumentation range of frequency from 0 to 2000 Hz. The frequency distribution of this acceleration spectral density data was essentially the same shape for the three flight conditions and, hence, assumed to be the same for the airload spectral density as well. An additional conservatism was introduced by assuming that the full root mean square force, \bar{F} , would be effective within the reduced frequency band of 0 to 1000 Hz within which the 11 bending mode frequencies are located. Assuming the airload force spectral density, $f(f_n)$ lbs²/HZ, to have the same linear distribution of $f(f_n) = 0$ at zero Hz to $f(f_n) = \bar{F}$ at 1000 Hz, the following relation was derived to obtain the force spectral density components within the half-power bandwidth at the bending mode frequencies, n , which are shown in Table V below:

$$f(f_n) = 2\bar{F}^2 f_n 10^{-6} = 0.140217 f_n \text{ lbs}^2/\text{HZ} \quad (23)$$

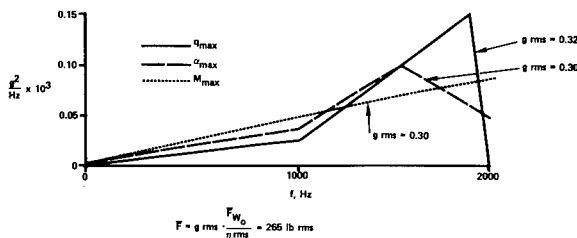


Figure 7. Nose Accelerometer, Radial Acceleration Spectral Density, Burnout

TABLE V
Force Spectral Density

n	f_n , HZ	$f(f_n)$, lbs ² /HZ
1	51.08	7.162
2	109.9	15.410
3	117.3	16.447
4	152.0	21.313
5	200.4	28.099
6	250.5	35.124
7	288.7	40.481
8	293.3	41.126
9	371.6	52.105
10	433.7	60.812
11	510.8	71.623

VI. ED FLIGHT VEHICLE RANDOM VIBRATION RESPONSE LOADS

The appropriate equations of Section III were programmed for solution on a Wang model 370 desk-top calculator. Appropriate input data were obtained from those presented for the lateral vibration modes in Section IV, and for the

random aerodynamic excitation forces in Section V. In addition, the required equivalent modal structural damping coefficients, g_{dn} , assumed for this study are essentially those developed from experimental data obtained during the ground vibration survey of the CTV flight vehicle described in reference 5. Values for the higher modes were assumed the same as for the sixth mode. These coefficients are shown in Table VI for each mode n .

The aerodynamic force magnitude was not extrapolated beyond that associated with the maximum dynamic pressure flight of the CTV. For flight at higher dynamic pressure conditions, the frequency content of the random force excitation would shift upwards such that much more of the energy would appear at frequencies above 2000 Hz and hence would be less effective in the generation of primary structural bending moments, shear forces, and modal accelerations. This higher-frequency content would affect such things as insulation bond and joint fatigue life, which is not a product of this random loads analysis.

TABLE VI
Modal Structural Damping Coefficients

n	g_{dn}
1	0.022
2	0.019
3	0.025
4	0.022
5	0.024
6	0.026
7	0.026
8	0.026
9	0.026
10	0.026
11	0.026

Consideration was also given to the possibility of higher random loadings occurring coincident with the maximum lateral loading during the flight vehicle boost phase. At this time, the vehicle weight (W_B) would be about twice that at burnout (W_{Bo}), and hence the modal root mean square lateral acceleration (g_B) would be anticipated to be one-half that at burnout (g_{Bo}). The flight dynamic pressure (q_B) would be about 4/3 that of the condition analyzed above (q_{Bo}). For flight condition 401 of reference 6, the total normal airload coefficient $C_{NB} = 9.286$, or about 3/2 that of the condition analyzed above (C_{NBo}). To evaluate the lateral load factor for boost (η_B) with respect to burnout (η_{Bo}), we have the following:

$$\frac{\eta_B}{\eta_{Bo}} = \frac{C_{NB}}{C_{NBo}} \frac{q_B}{q_{Bo}} \frac{g_B}{g_{Bo}} = \frac{3}{2} \frac{4}{3} \frac{1}{2} = 1 \quad (24)$$

Hence, the random vibration loads estimated in this analysis for the flight vehicle burnout condition can be considered the maximum attained

throughout the ED flight vehicle operational range. Computations were performed to yield the root mean square magnitudes of the response loads acting in the vehicle primary structure. These magnitudes were then multiplied by a factor of three to obtain the expected peak magnitudes presented in Table VII and shown in Figures 8, 9, and 10. These loads are incremental loads and are to be added to the basic structural design loads.

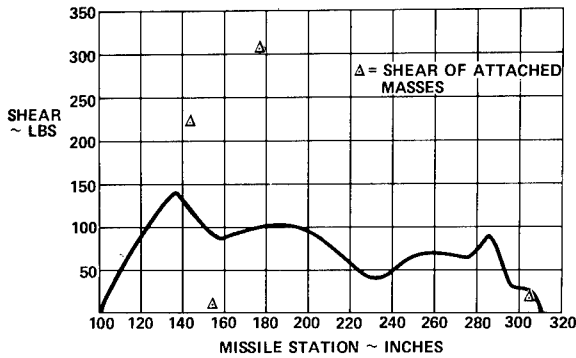


Figure 8. Lateral Shear Force

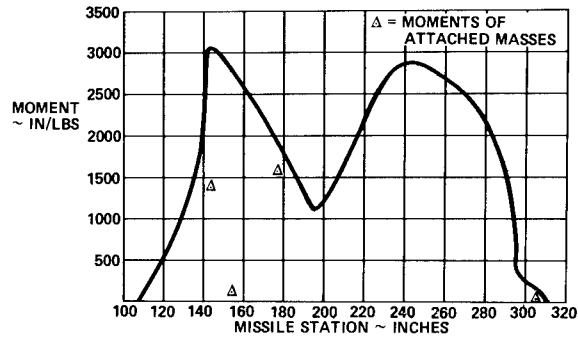


Figure 9. Lateral Bending Moments

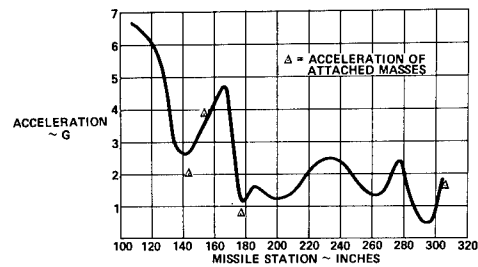


Figure 10. Lateral Acceleration

TABLE VII
Peak Random Vibration Loads

Station (in.)	Shear Force (lbs)		Bending Moment (in-lbs)		Lateral Acceleration (g)	
	Body	Item	Body	Item	Body	Item
107.113	43.6		4.4		6.69	
121.340	95.6		588.1		5.96	
135.567	140.6		1485.9		2.84	
142.680	117.7	220.6	3088.2	1357.1	2.65	1.98
153.620	95.8	9.0	2781.7	82.5	3.53	3.83
166.310	95.2		2342.8		4.72	
178.000	100.9	306.3	1874.6	1562.6	1.18	0.75
185.000	103.0		1550.0		1.60	
195.979	100.7		1114.7		1.29	
205.937	88.7		1395.6		1.32	
215.895	67.0		2017.9		1.89	
225.853	45.7		2545.9		2.40	
235.811	45.1		2827.5		2.46	
245.769	59.6		2859.5		2.05	
255.727	69.0		2729.5		1.52	
265.685	69.5		2535.1		1.41	
275.643	66.5		2306.4		2.41	
285.080	86.6		1880.6		1.16	
295.600	31.8		384.7		0.46	
304.300	27.9	21.7	178.8	18.1	1.81	1.59

VII. REFERENCES

1. OR 11002-2, "SAM-D Control Test Vehicle Flight Two Interim Test Report, Missile S/N 0005," Martin Marietta Corporation, April 1971, Unclassified.
2. OR 11002-3, "SAM-D Control Test Vehicle Flight Three Interim Test Report, Missile S/N 0006," Martin Marietta Corporation, April 1971, Unclassified.
3. OR 11002-4, "SAM-D Control Test Vehicle Flight Four Interim Test Report, Missile S/N 0007," Martin Marietta Corporation, May 1971, Unclassified.
4. ANA 10721729-002, "Vibration Analysis of SAM-D Missile," Martin Marietta Aerospace, Unclassified.
5. OR 10847, "Final Report for SAM-D CTV Ground Vibration Survey Tests," Volume III, GVS Tests (Airframe Structure), Pages 4-10 to 4-19, August 1970, Unclassified.
6. ANA 10000000-004, Rev. A, "SAM-D ED Missile Body and Control Fin Air-Load Distributions," Martin Marietta Aerospace, Unclassified.
7. Lin, Y. K., Probabilistic Theory of Structural Dynamics, McGraw-Hill 1967.
8. Crandall, Stephen H., William D. Mark, "Random Vibration in Mechanical Systems," Academic Press, New York and London, 1963.

EVALUATION OF BLOCKED ACOUSTIC PRESSURE ON STIFFENED CYLINDRICAL SHELLS

V. M. Conticelli
Aeritalia S.p.A.
Naples, Italy

and

G. C. Kao
Wyle Laboratories
Huntsville, Alabama

Integrity and performance of critical component packages mounted inside rocket vehicles must be assured for the entire flight mission. These packages, which are subjected to dynamic loads caused by random acoustic excitations and transmitted by the external shroud through the connecting structural members, must therefore be tested on the ground with simulated in-flight environments.

Recently a new technique has been developed to determine interaction forces between a component and its support structure, and then the component is tested under the force controlled environments. The interaction forces (force spectrum) are predicted by a one-dimensional equation which utilizes four types of data measured at equipment mounting locations. These data consist of: input impedance of support structure; acoustic mobility of support structure; input impedance of component package; and blocked pressure spectrum.

Analytical methods are described in this paper for computing blocked pressure spectra of cylindrical structures. These methods can be used when the far-field pressure or the pressure on the surface of a flexible structure is known.

Also, an experimental program which was used to assess the accuracy of the analytical methods is discussed in this paper. During these experiments, a stiffened aluminum cylinder with the dimensions of 3 ft (diameter) x 3 ft (height) x 0.02 in (skin thickness) and a rigid dummy concrete cylinder with the same diameter were employed. The aluminum cylinder was used in acquiring input impedances and acoustic mobilities and the concrete cylinder was used for measuring the blocked pressure spectra.

Comparisons between theory and experiments indicate that, for the structure considered in this study, the maximum deviation in data is within 1 dB. A comparison is also made between pressure measurements obtained with flush-mounted and external-mounted microphones. No significant differences are detected between these two types of measurements and this leads to the conclusion that both mounting configurations are acceptable.

INTRODUCTION

A new approach to predict localized vibratory environments of space vehicles subjected to broad-band random acoustic excitations has been recently reported in Reference 1. This approach allows vibratory environments at component mounting locations being specified in terms of either a force spectrum representing interaction force between the component and the primary support structure or a response spectrum of the loaded primary structure. The force-spectrum method is briefly described below.

A structural system (component and support structure) can be represented by a one-dimensional impedance model as shown in Figure 1. In this figure, the basic unloaded structure is replaced by an equivalent structural "black box"; external loads are applied at Terminals 1, 2 and component packages which are treated as load impedances, $Z_L(\omega)$, are attached to Terminals 3, 4. The corresponding velocities and interaction forces at the attachment points are

indicated by $V_L(\omega)$ and $\Phi_L(\omega)$, respectively. The dynamic characteristics of the attachment points (Terminals 3, 4) are represented by $Z_s(\omega)$ which is defined as the support-structure impedance, or source impedance, i.e., the impedance looking back to the left of Terminals 3, 4 without any loads attached.

The component-structure interaction force spectra, $\Phi_L(\omega)$, can be expressed by the following equation:

$$\Phi_L(\omega) = \Phi_{\text{block}}(\omega) \cdot [\alpha(\omega)]^2 \cdot \left[\frac{Z_s Z_L}{Z_s + Z_L} \right]^2 \quad (1)$$

where

$\Phi_{\text{block}}(\omega)$ = Power spectral density (PSD) of blocked sound pressure which is assumed to be constant over the surface of the component attachment locations.

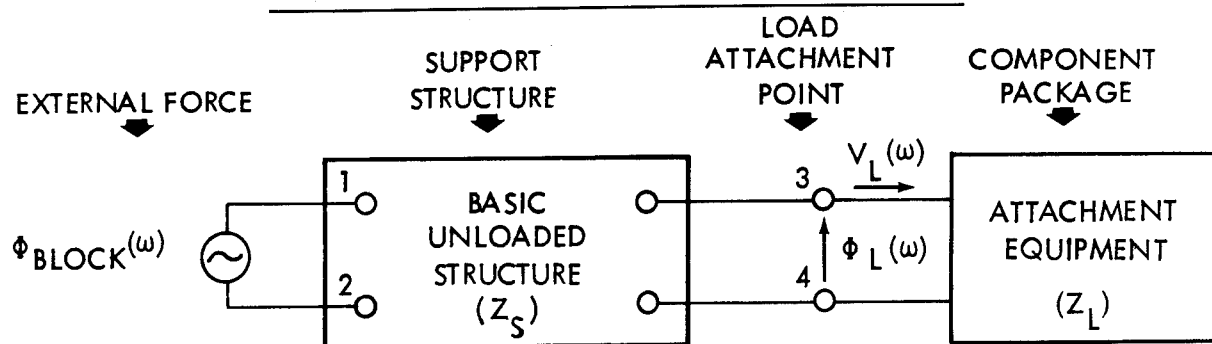


Figure 1: ONE-DIMENSIONAL IMPEDANCE MODEL OF A STRUCTURAL SYSTEM

$[\alpha(\omega)]^2$ = Acoustic mobility at component mounting locations, and is defined by the ratio of the rms velocity response of a support structure and its corresponding rms sound pressure.

The accuracy of the interaction force spectrum computed in the above manner depends on the ability of assessing accurately the blocked pressure spectra which is used in Equation (1). In the program described in Reference 1, a concrete pipe was used to determine the spectra of the blocked acoustic pressure.

The work presented in this paper had the following objectives: (i) to assess the validity of using a concrete pipe as a rigid dummy to measure the blocked pressure spectrum which is required to compute the force spectra relative to any flexible shell of the same size; (ii) to develop a method for converting sound pressure levels measured on flexible structures into blocked pressure spectra; (iii) to determine the difference between sound pressure levels measured on the surface of a cylinder when using two different microphone mounting configurations, such as flush mounting and external mounting at a small distance from the shell wall. The data obtained from two sets of experiments, referred to as alpha and gamma runs, were used to perform this study. A brief description of the entire experimental program is also presented for clarity and completeness purposes.

EXPERIMENTAL PROGRAM

Three groups of experiments were conducted during the entire force-spectrum experimental program whose principal characteristics and objectives are here briefly described.

ALPHA RUNS: These experiments consisted of exposing an aluminum stiffened cylindrical shell (36 in. long, 36 in. diameter, 0.02 in. thick) and a concrete pipe of the same diameter to a reverberant acoustic field in Wyle Laboratories' 100,000 cu. ft. reverberation room (Figure 2). Measurements of the acoustic field were taken far from the test specimens (far-field sound pressure level) and at the surface of the two cylinders. For the latter measurements, the microphones were mounted on a fixture and held at about 0.25 inches from the shell wall. Also, the acceleration response of the aluminum shell was measured at different locations such as skin, stringer and ring locations. During these experiments three different overall sound pressure levels (OASPL) were used and a classification of the experiments according to these OASPL and to the measurement locations is presented in Table 1. The purpose of these experiments was to determine experimentally the acoustic mobility of the stiffened shell at points with different local structural characteristics.

Table 1: CLASSIFICATION OF
α- EXPERIMENTS

TEST SERIES	OASPL - dB	MEASUREMENT LOCATION
α 11	133.3	Skin
α 12	136.8	Skin
α 21	136.8	Ring
α 22	142.4	Ring
α 31	136.4	Stringer
α 32	142.8	Stringer

BETA RUNS: During these experiments, a component (plate supported by four springs) was mounted on the aluminum shell through four load cells and the whole structure was subjected to a reverberant acoustic field. The purpose of these tests was to measure the component-shell interaction loads and compare them with those determined analytically by using the acoustic mobility values obtained from the alpha runs.

GAMMA RUNS: These experiments are similar to the alpha runs except for the mounting of the microphones which, in this case, were flush-mounted microphones of 0.5 inches in diameter. The purpose of the gamma experiments was to

determine the variation of the pressure level at the surface of the shell wall for two different mounting configurations of the microphones.

Data were acquired on-line by digital computer and stored permanently on magnetic tapes. A thorough discussion of these experiments on the alpha and beta series and presentation of experimental data is found in Reference 1.

For the purpose of this study, only data from the alpha and gamma runs were used in the manner that is described in the following sections.

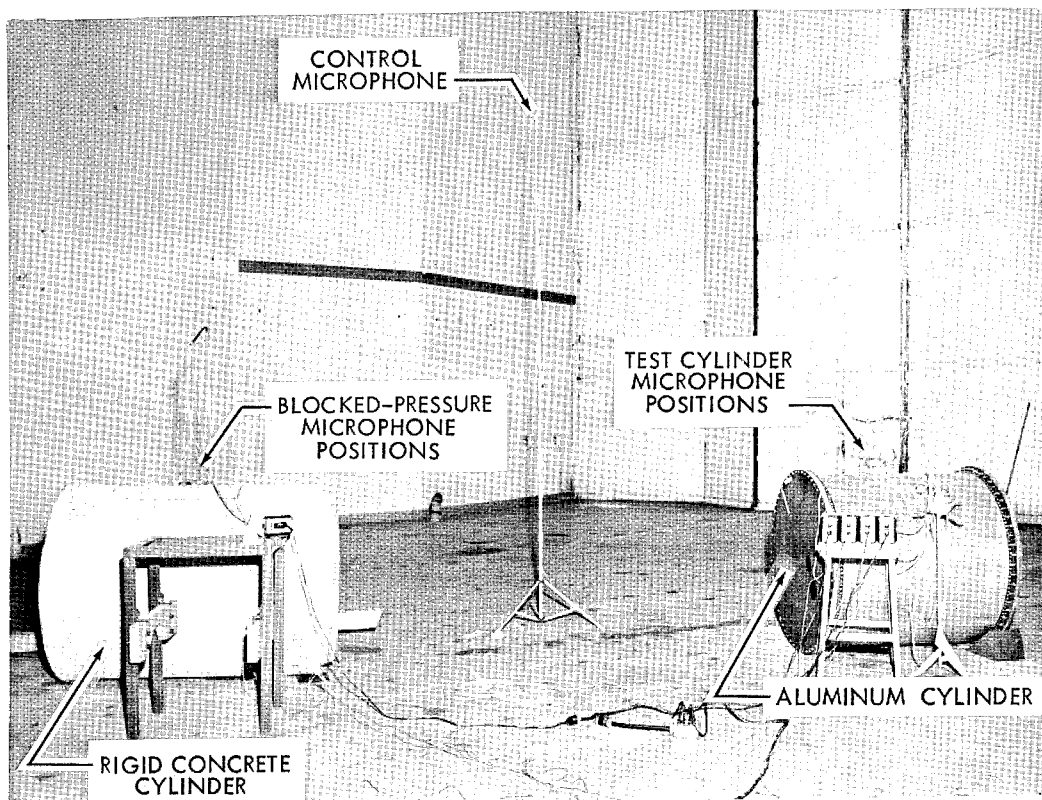


Figure 2: POSITIONAL CONFIGURATION OF ALUMINUM AND CONCRETE CYLINDERS INSIDE WYLE LABORATORIES' 100,000 CU.FT. REVERBERATION ROOM DURING VIBRO-ACOUSTIC EXPERIMENTS

EVALUATION OF BLOCKED PRESSURE MEASUREMENTS

A concrete pipe of the same diameter as the aluminum shell was used to measure the blocked pressure to be used to compute the force spectra relative to the flexible cylinder. The concrete pipe was chosen on the assumption that it was rigid enough to be employed as the rigid dummy of the aluminum cylinder. It is the purpose of this study to assess the validity of this assumption and determine the magnitude of the errors that might have been introduced in the final computations.

Toward this end, the sound pressure spectra measured at the surface of the concrete cylinder (P_{concrete}) during the α -runs were, first, normalized by far-field pressure measured by the control microphone (P_{control}). This ratio was then compared with the theoretical value as derived in Reference 2. As to P_{concrete} , four microphones were employed for each α -experiment to make a total of 24 measurements, whose normalized spectra fall within the band shown in Figure 3. This figure contains also the theoretical curve for the mean squared pressure on the surface of a rigid cylinder in a reverberant sound field divided by the mean squared pressure existing in the far field.

Figure 3 indicates that the agreement between the theoretical blocked pressure spectrum and the pressure spectrum measured on the "dummy" cylinder is quite satisfactory for frequencies above 100 Hz. Discrepancies below this frequency are probably due to the lack of perfect diffuseness of acoustic field which affects the measurements of the only control microphone used for the experiments.

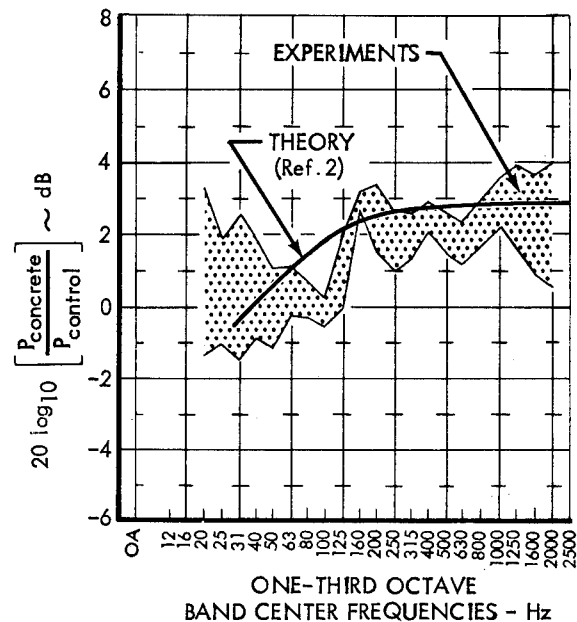


Figure 3: AVERAGE NORMALIZED PRESSURE MEASURED ON CONCRETE PIPE DURING α - RUNS AND THEORETICAL BLOCKED PRESSURE SPECTRUM

THEORETICAL EVALUATION OF BLOCKED PRESSURE

The exact blocked pressure, which is the true acoustic pressure load acting on a flexible structure, can be determined most accurately only by using a rigid dummy structure. However, in many cases, the construction of the rigid dummy is not practical and it is desirable to determine the blocked pressure from the pressure measured at the surface of the flexible structure.

An approximate formula for converting sound pressure levels measured on flexible structures into blocked sound pressure levels can be obtained as shown below. Consider an incident sound wave to impinge on a flat flexible panel at any angle, θ , relative to a normal to the panel. Reference 3 shows that:

$$\frac{P_{flex}(x, \theta)}{P_{block}} = \frac{(z_w + z_t) \cos \theta \cos \left(\frac{2\pi x}{\lambda} \cos \theta \right) + j\rho c \sin \left(\frac{2\pi x}{\lambda} \cos \theta \right)}{(z_w + z_t) \cos \theta + \rho c} \quad (2)$$

where:

z_w = specific transmission impedance of wall (mechanical impedance per unit area)

z_t = specific acoustic impedance of transmitted sound wave

x = distance normal to panel on the source side where $x = 0$ is the panel surface

θ = angle of incident wave relative to normal to panel

λ = acoustic wavelength of incident wave

$P_{flex}(x, \theta)$ = rms value of pressure at a distance x

P_{block} = rms value of pressure at the surface of a rigid panel

At the surface ($x = 0$) of a flexible panel, Equation (2) becomes:

$$\frac{P_{flex}(\theta)}{P_{block}} = \frac{(z_w + z_t) \cos \theta}{(z_w + z_t) \cos \theta + \rho c} \quad (3)$$

A similar expression can be obtained for the case of reverberant acoustic field impinging on a flat flexible panel. This is obtained by averaging Equation (3) over a hemispherical surface. The hemispherical average is given by:

$$\left\langle \frac{P_{flex}}{P_{block}} \right\rangle_{hemisphere} = \frac{1}{2\pi} \oint \frac{(z_w + z_t) \cos \theta}{(z_w + z_t) \cos \theta + \rho c} dw \quad (4)$$

where: dw = solid angle

The integral of expression (4) gives:

$$\frac{P_{flex}}{P_{block}} = \int_0^{\pi/2} \frac{(z_w + z_t) \cos \theta \sin \theta}{(z_w + z_t) \cos \theta + \rho c} d\theta = 1 + \frac{\rho c}{z_w + z_t} \log_e \left[\frac{\rho c}{\rho c + z_w + z_t} \right] \quad (5)$$

The sum $\rho c + z_w + z_t$ is the total impedance equal to the inverse of the acoustic mobility, α . Also, the acoustic impedance, ρc , is usually much smaller than the structural impedance and Equation (5) can, therefore, be written as:

$$\frac{P_{flex}}{P_{block}} = 1 + \rho c \alpha \log_e (\rho c \alpha) \quad (6)$$

or:

$$P_{block} = \frac{P_{flex}}{1 + \rho c \alpha \log_e (\rho c \alpha)} \quad (7)$$

Expression (6) has been derived for an infinite flat panel and does not account for diffraction effects that occur

when the structure is not infinite or planar. However, above certain frequencies this expression should give an accurate estimate of the blocked pressure for finite panels and other structures such as cylinders.

To determine the accuracy of expression (6) the values of the ratio P_{flex}/P_{block} were evaluated by using this expression and the values of the acoustic mobilities that were obtained from the α -experiments. The values of these acoustic mobilities and the theoretically evaluated P_{flex}/P_{block} are listed in Table II. A comparison of these theoretical, P_{flex}/P_{block} , based on expression (6), with the measured values of the same ratio is illustrated in Figures 4, 5 and 6 for skin, ring and stringer locations, respectively.

Table II: VALUES OF MEASURED ACOUSTIC MOBILITY
AND THEORETICAL P_{flex}/P_{block}

FREQUENCY Hz	α -ACOUSTIC MOBILITY - IN ³ /LB SEC			$1 + \rho c \alpha \log_e (\rho c \alpha) = \frac{P_{flex}}{P_{block}}$		
	MEASUREMENT LOCATION			MEASUREMENT LOCATION		
	PANEL	RING	STRINGER	PANEL	RING	STRINGER
31	14.5	17.0	14.5	0.917	0.907	0.917
40	16.7	18.3	14.8	0.908	0.902	0.916
50	13.4	13.4	14.0	0.922	0.922	0.919
63	12.5	12.1	12.8	0.926	0.928	0.924
80	11.7	11.0	11.5	0.929	0.933	0.930
100	10.5	10.5	10.0	0.935	0.935	0.937
125	8.5	8.9	8.9	0.945	0.943	0.943
160	10.0	9.4	9.1	0.937	0.940	0.942
200	9.7	9.5	9.5	0.938	0.939	0.939
250	13.4	12.1	13.8	0.922	0.928	0.920
315	12.2	14.5	14.5	0.927	0.917	0.917
400	17.9	22.4	25.5	0.903	0.886	0.876
500	36.7	17.6	21.7	0.841	0.904	0.889
630	38.7	16.9	22.4	0.836	0.906	0.886
800	27.7	17.9	36.1	0.868	0.903	0.842
1000	29.5	22.1	35.4	0.863	0.887	0.844
1250	33.2	22.4	35.4	0.851	0.886	0.844
1600	28.3	24.5	26.3	0.866	0.879	0.873
2000	15.8	22.8	21.9	0.912	0.885	0.888

* $\rho c = 0.0015 \text{ LB SEC/IN}^3$

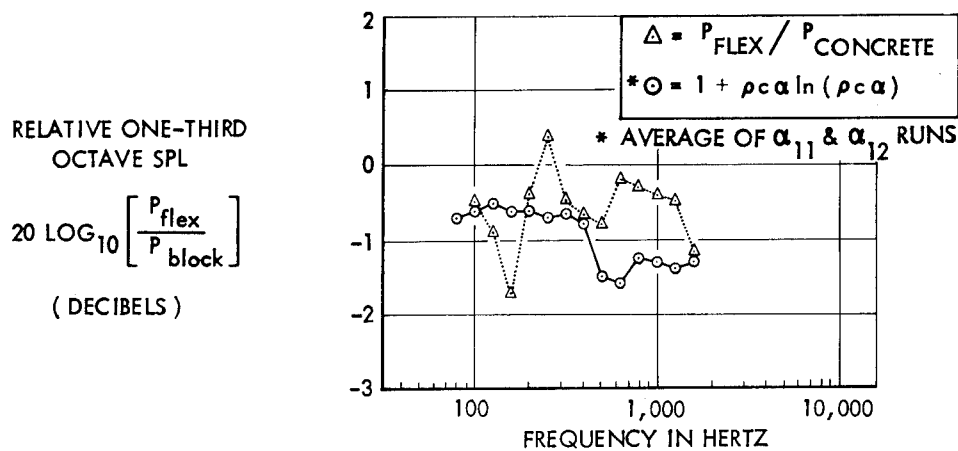


Figure 4: MEASURED AND EXPERIMENTALLY EVALUATED BLOCKED ACOUSTIC PRESSURE AT PANEL LOCATION

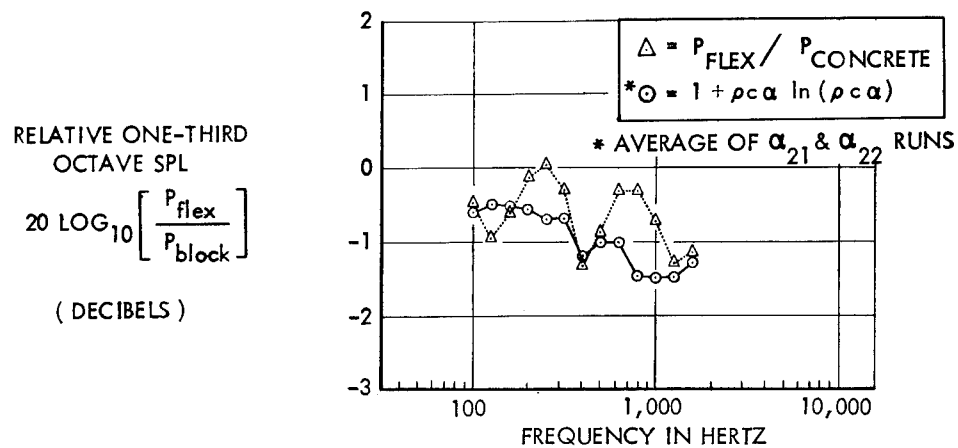


Figure 5: MEASURED AND EXPERIMENTALLY EVALUATED BLOCKED ACOUSTIC PRESSURE AT STRINGER LOCATION

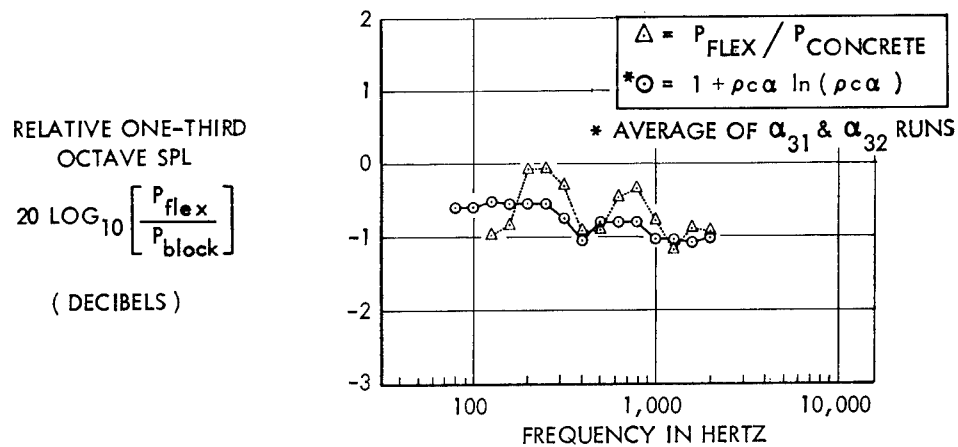


Figure 6: MEASURED AND EXPERIMENTALLY EVALUATED BLOCKED ACOUSTIC PRESSURE AT RING LOCATION

Figure 4 shows that theoretical ratio is significantly lower than the measured values which, for one band center frequency, are higher than 1.0(0 dB). This leads to questioning of the experimental data because theoretically the pressure on a flexible surface is never expected to be higher than the pressure on a rigid surface.

Figures 5 and 6 also show experimental data higher than the theory but at a lesser degree than the case of the panel location. It must be noted, however, that discrepancies between theory and experiments are only of the order of 10 percent or ≤ 1 dB. Furthermore, since the theoretical ratio P_{flex}/P_{block} is lower than the experimental values, the use of Equation (7) will produce values of blocked pressure higher than the actual levels thus leading to conservative estimates of the force spectra.

COMPARISON OF DATA FOR DIFFERENT MICROPHONE MOUNTING CONFIGURATIONS

During the α -experiments, microphones were mounted at a distance of about 0.25 inches from the surface of the aluminum and concrete cylinders. This type of microphone set-up could introduce errors in the pressure measurements because of the possible presence of standing waves between the microphone and the wall of the test specimen.

To determine whether errors were introduced in the α -runs and to assess their magnitude, another set of experiments, referred to as γ -runs, were conducted. During these experiments, the microphones were flush-mounted so that they measured exactly the total pressure existing at the surface of the cylinders.

In order to make a comparison between the data of the α -runs and those of the γ -runs, the third octave pressure levels were normalized by the pressure levels measured by the control microphone ($P_{control}$) located far from the test specimens and compared graphically as shown in Figure 7.

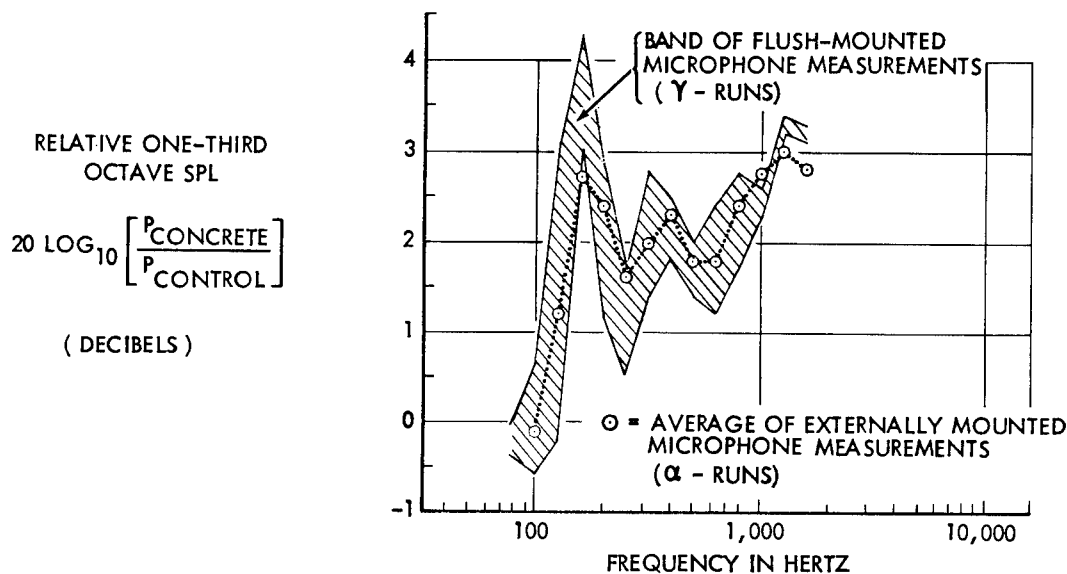


Figure 7: COMPARISON BETWEEN PRESSURE MEASUREMENTS TAKEN ON CONCRETE CYLINDER WITH FLUSH MOUNTED AND EXTERNALLY MOUNTED MICROPHONES

In this figure data relative to the concrete cylinder are presented; namely, the average of all the pressure levels measured during the α -experiments (average of band shown in Figure 3) and a band within which the pressure data from γ -runs fall. This figure clearly indicates that no significant difference exists between the experimental data of the two series of experiments, that is the α - and the γ -experiments. Therefore, it can be concluded that the distance between the surface of the cylinders and the microphones employed during the α -experiments was sufficiently small so that no standing wave conditions affected the experimental data within the frequency range of testing.

CONCLUSIONS

The most significant conclusions, which can be drawn as a result of this study are:

- The concrete cylinder used to measure the blocked pressure represents a good rigid "dummy" structure. This means that the pressure measured at the surface of this cylinder can be considered, with good approximation, as the blocked pressure relative to any flexible cylindrical structure with the same diameter.
- A purely theoretical prediction of the blocked pressure can be made by using the theory developed in Reference 2.
- To convert measured sound pressure levels on flexible structures into blocked sound pressure levels, Equation (7) can be used. The factor within parentheses depends on the flexibility, α , of the structure. For

common aerospace structures this factor is of the order of 0.9 and consequently the rms blocked pressure is approximately 10 percent higher than the pressure measured on these structures. The data obtained during the experiments reported in this paper indicate that the error which might be introduced by using this formula is in the order of 1 dB and generally leads to conservative estimates of the force spectrum.

- When measuring sound pressure levels on flight hardware for the purpose of predicting the blocked acoustic pressure, good data also can be obtained by mounting the microphones externally to avoid drilling holes in the structure. It is, however, required that the distance between structure and microphones be sufficiently small to avoid the formation of standing waves which could alter the data.

ACKNOWLEDGMENT

The program was supported by the National Aeronautic and Space Administration, George C. Marshall Space Flight Center, under Contract No. NAS8-25811.

REFERENCES

- 1) Kao, G. C., "Prediction of Force Spectra by Mechanical Impedance and Acoustic Mobility Measurement Techniques," Wyle Laboratories Research Staff Report WR 71-16, September 1971.
 - 2) Waterhouse, R.V., "Diffraction Effects in a Random Sound Field," J. Acous. Soc. Am., Vol. 35, pp. 1610-1620, October 1963.
 - 3) Eldred, K. M. and Sutherland, L.C., "Acoustic Facility Utilization" from Lecture Notes for Training Course in Acoustic Environments and Structural Response - Session 14, Wyle Laboratories - El Segundo Research Staff, April 1970.
-
-

REDUCTION OF HULL NOISE AND VIBRATION BY CENTER
OF PERCUSSION ROADARM DESIGN

Daniel D. Ustick
U. S. Army Tank-Automotive Command
Warren, Michigan 48090

The study investigates a method for reducing roadwheel noise and shock loads into the vehicle hull of a track-laying vehicle. This reduction is theoretically possible by designing the center of percussion of the roadarm to coincide with the roadwheel spindle axis. In this manner dynamic forces applied at the spindle, normal to the roadarm length, will not be transmitted as shock to the center of arm rotation, i. e., the point of assembly to the vehicle hull.

The design constraint is given as a function for application in the design of future roadwheel and roadarm assemblies. It is modified for application of design changes to existing assemblies. A brief discussion about the potential magnitude of impulse energy input is followed by an application of design principle to the M551, Sheridan.

It is concluded that by application of the "center-of-percussion principle to the design of roadwheel and roadarm assemblies, components of impulse normal to the roadarm length will transmit energy into the vehicle suspension system rather than directly to the vehicle hull.

Future design implications are briefly discussed.

INTRODUCTION

A variety of highly sophisticated systems designed for target surveillance, target acquisition and ranging, communications, and various servo drives are housed in today's military tracked vehicles; like most precision equipment, they are sensitive to shock and vibration. Shock, vibration, and noise are not only detrimental to equipment, but also induce fatigue to the crew.

Operation of a vehicle over any given terrain and track profile will generate an impulse function acting on the vehicle. The impulse which the vehicle suspension system does not absorb is transmitted directly to the vehicle hull; the energy of this impulse is dissipated as hull noise and vibration.

DISCUSSION

For any suspended body free to swing, the point at which an impulsive force must be applied in order that no impulse be transmitted to the axis of rotation is called the center-of-percussion relative to the center of rotation. To take advantage of this principle, the combined roadwheel and roadarm assembly should be designed such that the roadarm spindle is

located at the center-of-percussion.

Application of this principle imposes a design constraint on any new roadarm assembly design. The design constraint is not so restricting that it cannot be used to modify existing assembly design by adding or subtracting mass from the roadarm or adding mass to the roadwheel.

The "roadarm" is meant an assembly of component masses. These include the arm itself, the spindle, half the mass of the torsion bar, a fraction of the bearing assemblies which rotate with the arm (as determined by the ratio of its angular displacement to the angular displacement for a given arm rotation), and all other components rigidly attached to the arm and rotating with it with the exception of the roadwheel. The "roadwheel" is understood to include the assembly and the fraction of bearing mass which rotates with the roadwheel.

To arrive at the correct equation of design constraint, we must find the total moment of inertia about the roadarm center of rotation (the roadarm axis of suspension to the vehicle hull). This includes all components of roadarm and roadwheel assemblies as given above.

The roadwheel mass, although carried with the arm, is not subject to rigid rotation with it. For this reason the roadwheel can be assumed to act only as a point mass in contributing to the total moment of inertia.

The equations which follow are presented to develop the design constraint which would take advantage of the "center-of-percussion

principle". For this discussion, the origin of the coordinate system is placed at the center of roadarm rotation on the vehicle hull. For simplicity, all points identified, including the center of mass location for roadarm and roadwheel assemblies, are assumed to be on the line joining centers of rotation and percussion. Refer to Figure 1.

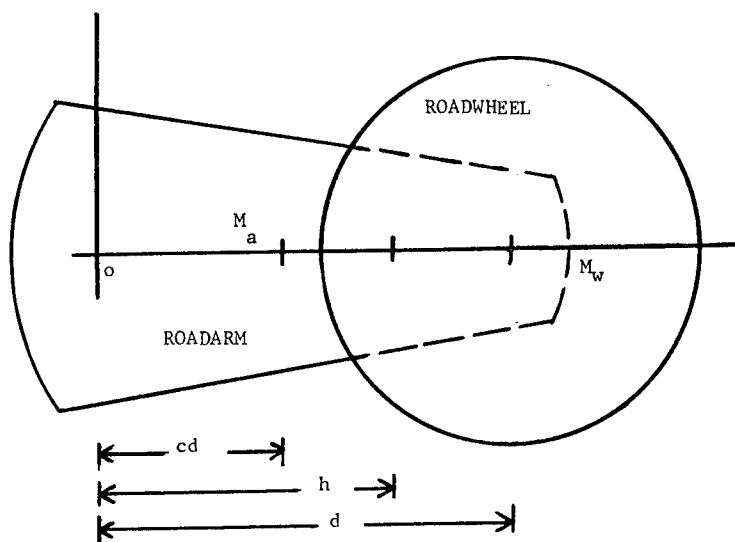


FIGURE 1

- d = the distance from the axis of roadarm rotation to the roadwheel axis and center of mass.
- c = multiplication factor which locates the roadarm center of mass in terms of the length d .
- cd = the distance from the axis of roadarm rotation to the roadarm center of mass.
- I_a = moment of inertia for the roadarm about an axis thru its center of mass parallel to the roadarm axis of rotation.

- I_o = moment of inertia about the roadarm axis of rotation.
- M_a = mass of roadarm.
- M_w = mass of roadwheel.
- h = the distance from the roadarm axis of rotation to the roadarm - roadwheel assembly - center of mass.

The location of the roadarm - roadwheel assembly center of mass is:

$$h = \frac{M_a c d + M_w d}{M_a + M_w}$$

The moment of inertia about the roadarm axis of rotation, the origin, is:

$$I_o = I_a + M_a (cd)^2 + M_w d^2$$

From theory, we are given that the center-of-percussion relative to the center of rotation must satisfy the following condition:

$$d = \frac{I_o}{(M_a + M_w) \left(\frac{M_a c d + M_w d}{M_a + M_w} \right)}$$

Substituting for I_o , combining and factoring like terms yields:

$$(1) \quad M_a d^2 (c-c^2) = I_a$$

Equation (1) is the design constraint for new roadarm designs. It will be found not to hold true for present roadarm designs where the equation was not considered as one of the design axioms. To modify an existing design, one solution is to find an additional mass, M_x , and its moment of inertia about an axis thru its center of mass, I_x , and attaching this body at the known center of mass for the roadarm. This will increase the total roadarm mass and its moment of inertia about the axis of arm suspension so that equation (1) is satisfied. This develops as follows.

The inertial mass is introduced with appropriate proportionality constants to simplify mathematical operations which follow. Let $I_a = k M_a d^2$, where k is the proportionality constant; and $I_x = a M_x d^2$, where a is the proportionality constant.

Equation (1) is now modified by adding and subtracting terms as follows:

$$(M_a + M_x) d^2 (c-c^2) = (k M_a + a M_x) d^2$$

Rearranging terms,

$$(2) \quad M_x = \frac{M_a (k-c+c^2)}{(c-c^2-a)}$$

The terms k , c , M_a are determined from examination of the designed parts; M_x and a are chosen for convenience.

An examination of equation (2) and the variables M_x and a reveals that the added mass and its moment of inertia can be either positive or negative. That is, one can add or subtract from the total roadarm mass and its moment of inertia to satisfy the design constraint, equa-

tion (1) above.

Equation (2) can be modified to add the unknown mass, M_x and its inertia, I_x , at the roadwheel axis. This is accomplished by changing the multiplication factor, c , which locates the roadarm center of mass in terms of the length d . The new factor for c is:

$$\frac{M_a c + M_x}{M_a + M_x}$$

Substituting the new factor in equation (2) and solving for M_x yields the new equation:

$$(3) \quad M_x = M_a \frac{(1-k-c-a) = (a+k+c-1)^2 - 4a(k-c+c^2)^{\frac{1}{2}}}{2a}$$

The magnitude of shock transmission that takes place by not taking full advantage of the center-of-percussion principle is given by the equation*.

$$(4) \quad \left(\frac{hd}{k_o^2} - 1 \right) J' = J$$

h = distance from the roadarm center of rotation to the center of the roadarm - roadwheel assembly mass

d = distance between centers of rotation and percussion

k_o = radius of gyration for the roadarm - roadwheel assembly moment of inertia about the roadarm center of rotation

k_m = radius of gyration for the roadarm - roadwheel assembly moment of inertia about its center of mass

J' = impulse delivered at the center-of-percussion

J = impulse delivered at the roadarm center of rotation

It follows that:

$$(5) \quad k_o^2 = k_m^2 + h^2$$

Equation (5) defines the relationship between k_o , k_m , and h . It can be obtained using the parallel axis theorem for computing moments of inertia.

Combining equation (4) and (5) above we obtain,

$$(6) \quad \left(\frac{hd}{k_m^2 + h^2} - 1 \right) J' = J$$

We now investigate the condition for minimum impulse transmission as a function of the location of the roadarm - roadwheel assembly center of mass. By differentiating terms with respect to h , and solving for h equal to zero,

*K. Symon, Mechanics, ;. 214.

in equation (6), we find that a minimum condition exists when the distance from the roadarm center of rotation to the assembly center of mass equals the radius of gyration for the mass moment of inertia about the assembly center of mass.

$$h = k_m$$

The radius of gyration, k_m , for a typical M551 roadarm - roadwheel assembly is 6.5 inches. If we assume the above minima condition exists, then the minimum transmission to the hull of force components normal to the roadarm of the M551 is 7.7 percent. (Values quoted for physical parameters of the M551 were obtained or computed from assembly drawings.)

From the wheel load vs. deflection curves for the M551, it is seen that a maximum potential energy of about 8,000 foot pounds can be stored by the suspension system before the wheel hits the bump stop. Considering the unsprung mass of the roadwheel, roadarm, and torsion bar assembly, the impulse required to deliver this energy is 765 pounds-second. For an estimated impulse duration of about 100 milliseconds, a peak force of 16,000 pounds could be expected. The magnitude of peak force transmission that takes place is, therefore, 1200 pounds.

Vertical force inputs like that due to the wheels rolling over track pads have components of force normal to the arm and along the arm. The normal component of a vertical force is found to be the vertical force magnitude multiplied by the cosine of the angle between the roadarm and hull. For the M551 this factor is .84 under static conditions. At least a portion of this normal force will be transmitted to the vehicle hull if the assembly design does not take into account the center-of-percussion principle.

As previously stated, for the M551, a calculated radius of gyration for the roadarm - roadwheel assembly is 6.5 inches. Assume also that this is the distance from the center of rotation to the center of mass, a minima for shock transmission. The length between centers of rotation and percussive is designed to be 12 inches. Therefore, $k = .292$, $c = .542$, $c^2 = .292$. Substituting these values into equation (3) yields:

$$(7) \quad M_x = M_a \frac{(.166-a) + (a^2 - .5a + .0278)^{\frac{1}{2}}}{2a}$$

If the mass, M_x , is added to the roadwheel, then the inertia about its center of mass, I_x , can be ignored because it contributes only as a point mass to the total inertia about the roadarm center of rotation. This condition is expressed for $a = 0$. Therefore,

$$M_x = .25M_a$$

Twenty-five percent of the roadarm assembly

mass added concentrically to the roadwheel will satisfy the constraint equation for the present design. This weight is approximately 38 pounds for one of the assemblies. (These values were computed for discussion purposes only and are not to be regarded as design information. Design data should be obtained directly from hardware or from a detailed analysis of each assembly design.)

FINDINGS

An ideal suspension system is one that isolates the hull body from all external terrain and track loads. The component of impulse that the suspension system does not absorb must be absorbed by the vehicle hull. This energy is converted into hull noise and vibration. As a minimum, 7.7 percent of impulse forces is not absorbed by the M551 suspension system. If this 7.7 percent is a major contributor to the total energy absorbed by the vehicle hull; then, reducing its source would substantially reduce the amount of hull vibration and noise experienced inside this vehicle.

CONCLUSION

Application of the percussive principle can minimize the transmission into the vehicle hull of force components normal to the roadarm.

IMPLICATIONS

To reduce to a minimum the vehicle noise and vibration transmitted to the hull from track and terrain profiles, it might be desirable to incorporate a mechanism that would insure that at least most of the forces are normal to the roadarm. The suspension system would have the capacity to adjust itself, changing the angle between roadarm and hull, to an optimum value of minimum force transmission.

Although not specifically addressed in the discussion, another source of noise and vibration is the idler wheel for the track assembly. It is caused by a phenomenon commonly called "chordal action" to those familiar with track laying vehicles. Possibly a pendulum idler wheel designed using the center-of-percussion principle could reduce this source of noise and vibration, as well.

ACKNOWLEDGEMENTS

The author wishes to express thanks to the numerous individuals at TACOM without whose critique and encouragement this paper would not have been written. Special thanks is acknowledged Messrs. W. L. Luptowski, T. H. Puuri and D. J. Hackenbruch.

REFERENCES

K. Symon, Mechanics

DISCUSSION

Mr. Forkois (Naval Research Laboratory): I think the center of percussion is another term for the location of the distance of the radius of gyration.

Mr. Ustick: Yes.

Mr. Forkois: That goes way back to the mechanics I had in 1932, I believe.

Mr. Balke (Bell Helicopter): I think you are to be congratulated for moving so quickly from experience into application. Sometimes we tend to lag in bringing our ideas forth. We have used similar techniques in the helicopter to isolate rotor forces from the fuselage using the center percussion technique and found it very successful. However there we are dealing primarily with a single sinusoid of essentially fixed frequency. You have quite another task in the road terrain. We find a requirement for a spring about the point of rotation for static requirements. I suspect that you would find a similar requirement. When we apply this spring to the system, the effective point of rotation moves as a function of frequency of application. Considering the random vibrations from the road, I think you might have quite a problem in optimizing is this correct? Do you have a requirement for spring restraint?

Mr. Ustick: I really haven't analyzed that problem at all, and I thank you bringing it up. I can consider it.

Mr. Askin: Has anything been done at your agency to implement this idea?

Mr. Ustick: I submitted the idea to our track and suspension laboratory. They reviewed it and like the idea. However, at the time they said there just weren't sufficient funds to do any development work on it.

SYNCHRONIZATION AND PHASE ANGLE
OF TWO UNBALANCED ROTORS

Mario Paz
University of Louisville
Louisville, Kentucky

and

P. H. Schrader and R. L. Blackmon
Vibrating Equipment Div., Rexnord Inc.
Louisville, Kentucky

The problem of predicting the phase angle of two-synchronized unbalanced rotors is presented. It is shown that the use of Hamilton's Principle permits the determination of the magnitude of this angle as well as the necessary condition for a stable solution. The theoretical results for self-synchronization of two unbalanced rotors are applied to a system for the whole range of the pertinent parameters. The conclusions of this analysis are corroborated by experiments conducted on a test unit in the study of this problem.

INTRODUCTION

Rectilinear vibration required in some types of mechanical equipment such as vibrating feeders and conveyors may be produced by two synchronized motors having eccentric weights rotating in opposite directions. The condition for self-synchronization, as well as the phase angle maintained by the rotors, has been investigated for simplified cases by Blekham¹ for one directional motion and by Paz² for two directional motion. These developments gave solutions prescribing the conditions for self-synchronization but did not analytically predict the stable phase angle or the resultant direction of motion.

The purpose of this paper is to extend the scope of the previous work to include the general case of plane motion of any mechanical system subjected to the driving action of two unbalanced rotors. With this extension it is possible to predict analytically the stable phase angle and the direction of the resultant force of any two rotors with parallel axes of rotation. Development of the general solution for plane motion of two

unbalanced rotors permits further extension of the scope of the theory to incorporate the following factors: (1) systems with more than two unbalanced rotors, (2) systems with rotors in any orientation in space, (3) effect of dissipative forces (damping) in the synchronization of rotors and stability of the phase angle.

These extensions have applications in mechanical vibrators which are used for packing, screening, and conveying materials and in similar operations. Ability to determine analytically the conditions for self-synchronization of large mechanical systems would produce more efficient designs. Furthermore, the possibilities for extensions of rotors to military craft, such as torpedos, constructed with two or more rotors are subjected to the principle of self-synchronization. When built, rotating parts of these crafts contain small imperfections which produce mass eccentricity and cause these parts to act as unbalanced rotors.

EQUATIONS OF MOTION

The method presented herein is general and may be applied to any mechanical system driven by the unbalanced rotors. However, for clarification it is expedient to refer the explanation to a specific example. Figure 1 shows the diagram of a rigid body of mass M , and moment of inertia I constrained to plane motion and mounted on resilient elements. As shown by Thomson (3), the two unbalanced rotors rotating in opposite directions produce forces of magnitude equal to

$$F_0 = m' e \omega^2$$

where m' is the unbalanced mass, e the eccentricity, and ω the angular velocity of the rotors.

The problem is first, to demonstrate that the rotors maintain a constant phase angle, and secondly, to predict the value of this angle. The equations of motion for the system shown in Fig. 1 are obtained by applying Newton's law of motion in terms of the coordinates X , Y of the mass center and the angle of rotation α and are given in matrix notation by Eq. (1).

$$[M] \{\ddot{X}\} + [K] \{X\} = \{Q\} \quad (1)$$

where

$$\{Q\} = [F] \{T\} \quad (2)$$

$$M = \begin{bmatrix} M & 0 & 0 \\ 0 & M & 0 \\ 0 & 0 & I \end{bmatrix} \quad (3)$$

$$[K] = \begin{bmatrix} K_1 + K_2 & 0 & K_1 d_1 + K_2 d_2 \\ 0 & K_3 + K_4 & K_4 C_2 - K_3 C_1 \\ K_1 d_1 + K_2 d_2 & K_4 C_2 - K_3 C_1 & K_1 d_1^2 + K_2 d_2^2 + K_3 C_1^2 + K_4 C_2^2 \end{bmatrix} \quad (4)$$

$$[F] = \begin{bmatrix} 0 & F_0 & 0 & F_0 \\ -F_0 & 0 & F_0 & 0 \\ -b F_0 & -a_1 F_0 & b_2 F_0 & -a_2 F_0 \end{bmatrix} \quad (5)$$

$$\{T\} = \begin{bmatrix} \sin \omega t \\ \cos \omega t \\ \sin (\omega t + \theta) \\ \cos (\omega t + \theta) \end{bmatrix} \quad (6)$$

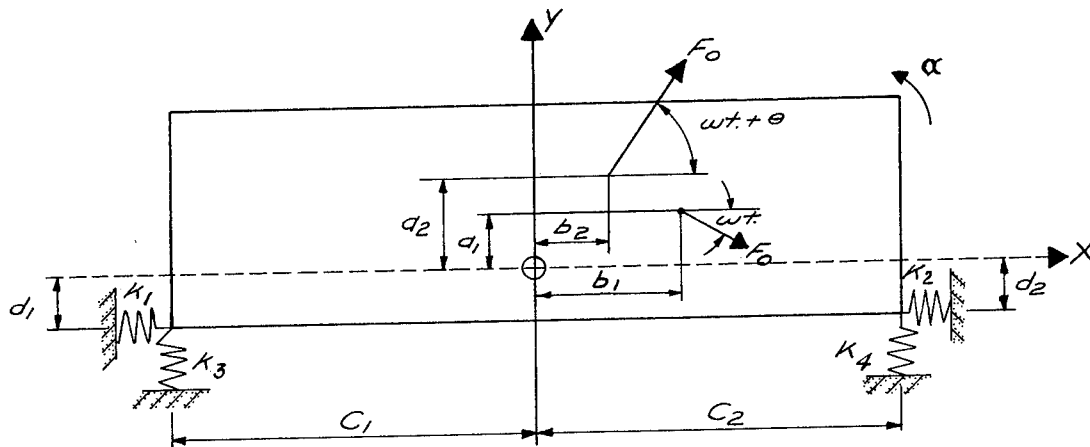


Fig. 1. Model of a rigid body mounted on resilient elements and acted upon by two eccentric rotors.

$$\begin{matrix} & X \\ \{X\} = & Y \\ & \alpha \end{matrix} \quad (7)$$

and $\{\ddot{X}\}$ the corresponding acceleration vector.

PRINCIPAL COORDINATES

It is advantageous to transform the generalized coordinates in Eq. (1) to principal coordinates. It is well known that when presented in terms of the latter coordinates the equations of motion are uncoupled; that is, each equation contains only one of the dependent variables. The procedure is to set the second member in Eq. (1) equal to zero and to solve the resulting eigenvalue problem. The eigenvalues are then equal to the square of the natural frequencies ω_1^2 , ω_2^2 and ω_3^2 . The corresponding eigenvectors may be arranged in the columns of the modal matrix as

$$[\phi] = \begin{bmatrix} \phi_{11} & \phi_{12} & \phi_{13} \\ \phi_{21} & \phi_{22} & \phi_{23} \\ \phi_{31} & \phi_{32} & \phi_{33} \end{bmatrix} \quad (8)$$

The eigenvalues and eigenvectors are then used in computing the modal masses, spring constants, and forces as:

$$M_n = \sum_r M_r \phi_{rn} \quad (9)$$

$$K_n = M_n \omega_n^2 \quad (10)$$

and

$$P_n = \sum_r Q_r \phi_{rn} \quad (11)$$

(for $n = 1, 2, 3$)

The substitution of Q from Eqs. (2) (5), and (6) into Eq. (11) results in the following expression for modal forces

$$\begin{bmatrix} P_1 \\ P_2 \\ P_3 \end{bmatrix} = \begin{bmatrix} P_{11} & P_{12} & P_{13} & P_{14} \\ P_{21} & P_{22} & P_{23} & P_{24} \\ P_{31} & P_{32} & P_{33} & P_{34} \end{bmatrix} \begin{bmatrix} \sin \omega t \\ \cos \omega t \\ \sin(\omega t + \theta) \\ \cos(\omega t + \theta) \end{bmatrix} \quad (12)$$

where

$$P_{ij} = \sum_r F_{rj} \phi_{ri} \quad (13)$$

In Eq. (13) F_{rj} designates the elements of the matrix given by Eq. (5). The modal differential equation is written as

$$M_n \ddot{Y}_n + K_n Y_n = P_n \quad (14)$$

The steady-state solution of Eq. (14) is given by

$$Y_n = \frac{1}{K_n - M_n \omega^2} [P_{n1} \sin \omega t + P_{n2} \cos \omega t + P_{n3} \sin(\omega t + \theta) + P_{n4} \cos(\omega t + \theta)] \quad (15)$$

Equation (15) presupposes the existence of a constant phase angle between the rotors. In order to determine the value of this angle as well as to ascertain its stable condition, use is made of Hamilton's principle. This principle states that a conservative system moves from time t_1 to time t_2 in such a way that the integral of the Lagrangian function

$$I = \int_{t_1}^{t_2} L dt \quad (16)$$

has a stationary value which is a minimum for a stable condition. This condition is expressed mathematically as the variation of the integral in Eq. (16) equated to zero; that is,

$$\delta I = \int_{t_1}^{t_2} \delta L dt = 0 \quad (17)$$

The Lagrangian function in terms of the principal coordinates is,

$$L = \sum_{n=1}^3 \frac{1}{2} M_n \dot{Y}_n^2 - \sum_{n=1}^3 \frac{1}{2} K_n Y_n^2 \quad (18)$$

Substituting the Lagrangian function from Eq. (18) into Eq. (17) and taking the variation during a cycle ($\omega t = 2\pi$) with respect to the parameter θ results in

$$\delta I = \int_0^{2\pi} \left(\sum_{n=1}^3 M_n \dot{Y}_n \frac{\partial \dot{Y}_n}{\partial \theta} - \sum_{n=1}^3 K_n Y_n \frac{\partial Y_n}{\partial \theta} \right) d\theta \quad (19)$$

Finally, the substitution of Y_n and its derivative \dot{Y}_n from Eq. (15) into Eq. (19) and performing the integrations will simplify to the following expression

$$\frac{\partial I}{\partial \theta} = \frac{\pi}{\omega} \left\{ \sum_n \frac{P_{n1}P_{n3} + P_{n2}P_{n4}}{K_n - M_n \omega^2} \sin \theta - \sum_n \frac{P_{n2}P_{n3} - P_{n1}P_{n4}}{K_n - M_n \omega^2} \cos \theta \right\} = 0 \quad (20)$$

From Eq. (20) the phase angle θ is given by

$$\tan \theta = \frac{\sum_{n=1}^3 \frac{P_{n2}P_{n3} - P_{n1}P_{n4}}{K_n - M_n \omega^2}}{\sum_{n=1}^3 \frac{P_{n1}P_{n3} + P_{n2}P_{n4}}{K_n - M_n \omega^2}} \quad (21)$$

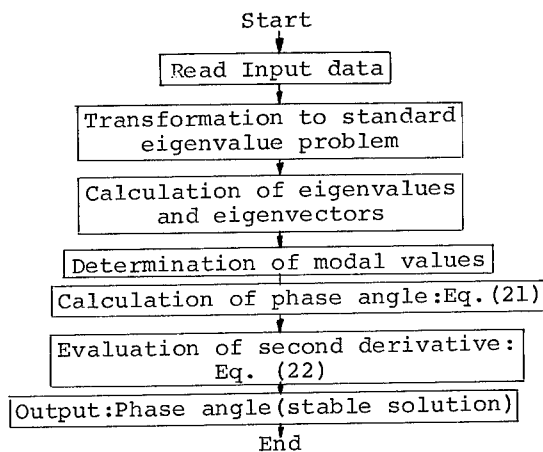
Equation (21) provides two solutions for the phase angle of synchronization θ . To ascertain which of these solutions minimizes the integral I in Eq. (17) it is necessary to examine the second derivative, namely,

$$\frac{\partial^2 I}{\partial \theta^2} = \frac{\pi}{\omega} \left\{ \sum_n \frac{P_{n1}P_{n3} + P_{n2}P_{n4}}{K_n - M_n \omega^2} \cos \theta + \sum_n \frac{P_{n2}P_{n3} - P_{n1}P_{n4}}{K_n - M_n \omega^2} \sin \theta \right\} \quad (22)$$

A positive result for the second derivative, evaluated for a root of Eq. (21), indicates a minimum value of the integral I in Eq. (17). This condition yields a stable solution for the system under consideration.

COMPUTER PROGRAM

The flow diagram of a computer program developed to calculate the phase angle of two unbalanced rotors mounted on an elastic system is as follows:



EXPERIMENTAL INVESTIGATION OF SELF-SYNCHRONIZATION

Experiments on self-synchronization were conducted by Paz [2] on a system consisting of a frame supporting two electric motors with their axes horizontally aligned. The frame itself, which has a parallelopiped external shape, is mounted to a rigid foundation through airbag springs located at all four sides and parallel to the axes of the two motors. Equal eccentric masses are attached to the axes of the two motors which are connected electrically to run in opposite directions. The system constructed conforms to the model represented in Fig. 1, except that the two motors have their axes aligned as shown in Fig. 2. This arrangement avoids the development of a couple when the rotor phase produces a horizontal motion.

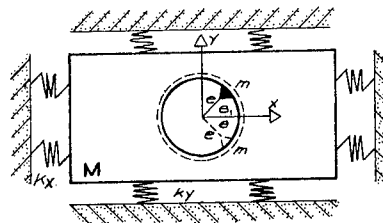


Fig. 2. Experimental system driven by two self-synchronized rotors.

By changing the air pressure of the airbag springs at the top and bottom (K_y) or at the sides of the frame (K_x) it is possible to tune the system to frequencies below or above the resonant condition in either of the two directions.

The system constructed has the following characteristics: weight of supporting frame and motors ($M_g = 407 \text{ #}$), eccentricity of rotors ($m_g e = 2.4 \text{ #-in}$), airbag springs of the air mount type, having a total spring constant for a pair of opposite springs given by

$$K = 2 (100.P + 960.) \text{ #/in} \quad (23)$$

where P = pressure of the airbags (p.s.i.), electric motors are 1 HP inductive type.

The natural frequencies of the system, in radians per second, in the X or Y directions are given by the following relations:

$$\omega_x = \sqrt{\frac{K_x}{M}} \quad \text{and} \quad \omega_y = \sqrt{\frac{K_y}{M}} \quad (24)$$

Setting the natural frequency equal to the nominal frequency of the motors (900 RPM) and solving Eq. (24) for the spring constant result in $k = 9300 \text{ \#/in.}$ which, when replaced in Eq. (23), gives a value of the resonant pressure $P_r = 41.70 \text{ psi.}$

A series of experiments have been run at different pressures in the horizontal and vertical airbag springs, and the directions of the motion of mass M were recorded. It was observed that the rotors maintain a definite synchronization, producing either a vertical or horizontal motion, and that the direction depends on the relative values of the pressures P_x , P_y and the resonant pressure $P_r = 41.7 \text{ psi.}$ The experimental observations are summarized in Table I.

TABLE I.

OBSERVED SELF-SYNCHRONIZATION
FOR SYSTEM IN FIG. 2

Case	Relative Values for Pressures in the Airbags and Resonant Pressure	Observed Motion
1	$P_x < P_y < P_r$	Horizontal
2	$P_y < P_x < P_r$	Vertical
3	$P_y < P_r < P_x$	Horizontal
4	$P_x < P_r < P_y$	Vertical
5	$P_r < P_x < P_y$	Horizontal
6	$P_r < P_y < P_x$	Vertical

From Eqs. (23) and (24) it is seen that pressures P_x , P_y and P_r in the inequalities of Table I could be replaced by corresponding inequalities in the natural frequencies ω_x , ω_y and by the resonant frequency $\omega = 94 \text{ rad/sec.}$ In Table II these inequalities are shown after dividing the expressions by the resonant frequency ω .

TABLE II

SELF-SYNCHRONIZATION FOR THE SYSTEM IN
FIG. (2) IN TERMS OF
RELATIVE FREQUENCIES

Case	Frequency Relations	Observed Motion
1	$\omega_x/\omega < \omega_y/\omega < 1$	Horizontal
2	$\omega_y/\omega < \omega_x/\omega < 1$	Vertical
3	$\omega_y/\omega < 1 < \omega_x/\omega$	Horizontal
4	$\omega_x/\omega < 1 < \omega_y/\omega$	Vertical
5	$1 < \omega_x/\omega < \omega_y/\omega$	Horizontal
6	$1 < \omega_y/\omega < \omega_x/\omega$	Vertical

The observed motion of mass M , as a function of the frequency ratios ω_x/ω and ω_y/ω , is shown graphically in Fig. 3 where the corresponding values of the phase angle θ are also indicated.

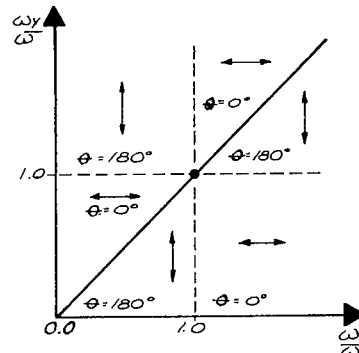


Fig. 3. Pictorial representation of the phase angle between rotors for the system in Figure 2. (Horizontal and vertical arrows indicate direction of resultant motion.)

These experimental results agree entirely with the theory presented. The system shown in Fig. 2 has two natural frequencies given by Eq. (24) and has corresponding eigenvectors $(1, 0)$ and $(0, 1)$. In this case the modal forces are

$$\begin{bmatrix} P_1 \\ P_2 \end{bmatrix} = \begin{bmatrix} 0 & F_0 & 0 & F_0 \\ -F_0 & 0 & F_0 & 0 \end{bmatrix} \begin{bmatrix} \sin \omega t \\ \cos \omega t \\ \sin(\omega t + \theta) \\ \cos(\omega t + \theta) \end{bmatrix} \quad (25)$$

When the appropriate substitutions are made in Eq. (21), it is found that $\theta_1 = 0^\circ$ and $\theta_2 = 180^\circ$ are the roots of this equation. For this example, the second derivative, Eq. (22), reduces to the following expression

$$\frac{\partial^2 I}{\partial \theta^2} = \frac{\pi}{\omega} F_O^2 \frac{\omega_Y^2 - \omega_X^2}{(\omega_X^2 - \omega^2)(\omega_Y^2 - \omega^2)} \cos \theta \quad (26)$$

since for the root $\theta_1 = 0^\circ$ the cosine is positive, it follows that for a stable phase angle the other factor in Eq. (26) should also be positive; that is

$$\frac{\omega_Y^2 - \omega_X^2}{(\omega_X^2 - \omega^2)(\omega_Y^2 - \omega^2)} > 0 \quad (27)$$

For the second root, $\theta_2 = 180^\circ$, the cosine is negative and consequently a stable condition requires

$$\frac{\omega_Y^2 - \omega_X^2}{(\omega_X^2 - \omega^2)(\omega_Y^2 - \omega^2)} < 0 \quad (28)$$

It can be seen that conditions stated by Eqs. (27) and (28) for a stable phase angle of 0° or 180° are corroborated by the results observed in the experiments and are shown pictorially in Fig. 3.

CONCLUSIONS

The general case of self-synchronization of two unbalanced rotors has been presented. It has been shown that the application of Hamilton's principle to this problem permits determination of the value of the phase angle and the stability condition for synchronization. Theoretical results have been verified by experimental work conducted on a simplified experimental model. Further investigation both theoretical and experimental is required to extend the scope of the work presented to include more general cases of self-synchronization of unbalanced rotors.

NOMENCLATURE

Symbols are defined where they are first introduced in the text and are also defined here for convenience.

e = Eccentricity of rotors

g = Acceleration of gravity

K_i = Spring constants

K_x = Spring constant in the x direction

K_y = Spring constant in the y direction

I = Mass moment of inertia

L = Lagrangian's function

m' = Mass of a rotor

M = Mass of body in Fig. 2

t = Time

ω = Angular velocity rotors

ω_x = Natural frequency in x direction

ω_y = Natural frequency in y direction

X = Horizontal displacement center of mass

Y = Vertical displacement center of mass

θ = Phase angle

α = Angular displacement of M

ϕ_{ij} = Modal displacement

REFERENCES

1. Blekhman, I. I., "Rotation of an Unbalanced Rotor Produced by Harmonic Oscillation of the Axis". Bulletin of Academy of Sciences, USSR, Division of Technical Sciences No. 8, 1954.
2. Paz, Mario, "Self-Synchronization of Two Eccentric Rotors on in Plane Motion." The Shock and Vibration Bulletin, Bulletin 41, Naval Research Laboratory, Washington, D.C., Dec. 1970.
3. Thomson, T. William, Vibration Theory and Applications, p. 59, Prentice-Hall, Inc., 1965.

EXPERIMENTAL INVESTIGATION OF THE DYNAMIC RESPONSE
OF CANTILEVER ANISOTROPIC PLATES

R. L. Sierakowski
Department of Engineering Science, Mechanics
and Aerospace Engineering
University of Florida
Gainesville, Florida

and

C. T. Sun
Department of Engineering Science, Mechanics
and Engineering Research Institute
Iowa State University
Ames, Iowa

An experimental study of the natural frequencies and mode shapes of glass-epoxy composite plates tested in a cantilever configuration is presented. The experimental data has been compared with an existing analytical computer solution for anisotropic plates considering such variable geometrical parameters as aspect ratio, angle ply orientation, and ply thickness. In the experimental program thirty composite material plates consisting of 4, 8, and 16 plies of glass epoxy material have been tested. Natural frequencies and corresponding mode shapes have been determined for each of the plates. Excellent agreement was found between experiment and analytical predictions within a controlled frequency range.

INTRODUCTION

The continued widespread use of filamentary composite materials as structural subsystems and components has required an understanding of the response characteristics of such materials to a wide spectrum of loading conditions. One technologically important area being considered for introduction of such types of laminated structural composites is in the inlet fan stages of air breathing propulsion systems. In order to establish guidelines for examining the vibratory response of composite fan blades, information dealing with the influence of various geometrical and material parameters such as angle ply orientation, variable aspect ratio, and moduli mismatch on resultant dynamic characterization are necessary.

Some previously reported studies on the dynamic response of anisotropic plates have been discussed in References [1] through [5]. In Reference [1], an analytical model for predicting the uncoupled dynamic response of laminated composite plates based upon the Ritz energy formulation was developed. The usual assumptions of classical thin plate theory considering small deflections were used. The analytical model was

compared with experimental data obtained using a mechanical shaker for square cantilever plates fabricated from Scotchply^(R) 1002 tape. This analytical model was also used by the authors in References [2-3] to examine the frequencies and mode shapes of plates of different material combinations and for different boundary conditions. Experimental data was obtained for the free vibration case of a fully clamped edge configuration and good agreement between theory and experiment was observed. In Reference [4] the Ritz method was extended to include the effects of coupling, and an analytical solution for the case of a fully-clamped edge plate presented. Experimental data was obtained for glass-epoxy composite plates using a mechanical shaker and good agreement was noted between theory and experiment. Most recently an analytical model based upon Galerkins method has been used in Reference [5] to study the characteristic frequencies and mode shapes of anisotropic plates for the case of varying edge fixities. The analytical development appears to omit some terms for the case of certain boundary conditions.

PL-22723
ADD 420192

In the present study an experimental investigation of the natural frequencies and mode shapes of thirty cantilever composite plates with varying geometry is reported on. The plates have been tested over a frequency range of 30 to 1000 Hertz using an electro-mechanical shaker. Plates considered in the current investigation were fabricated at the Air Force Materials Laboratory and consisted of laminated plies of Scotchply(R) 1002 tape material with varying thickness and aspect ratios. Since the principal axis of the individual plies were not geometrically parallel to the plate edges, the plates were anisotropic in varying degrees. Analytical data on the characteristic frequencies and mode shapes in the present investigation was obtained from General Dynamics using an updated version of a previously reported algorithm based upon the Ritz method presented in References [1-3]. The boundary conditions used in the present tests are those of a clamped free plate which analytically represents the most severe test for numerical representation.

The natural frequencies and mode shapes were calculated for each of the plates tested using lamina properties determined from specification sheets furnished by the fiberglass manufacturer and verified by experimental data obtained for controlled material samples at the Air Force Materials Laboratory. In general, good agreement between the analytical predictions and experimental results were observed over a finite frequency range as limited by linear plate response with increasing excitation.

EXPERIMENTAL INVESTIGATION

Thirty panels were tested with each panel having a different combination of lamina orientations, individual thicknesses and varying aspect ratios. The configurations tested are indicated in Table I and plate geometry data presented in Table II. Since the density of Scotchply(R) 1002 is about 0.086 lb per cubic inch, we find from Table II that the mass per unit area for 4-ply laminate, 8-ply laminate, and 16-ply laminate are respectively 8.540×10^{-5} , 1.708×10^{-4} and 3.416×10^{-4} slug per square inch.

The panels were fabricated of Scotchply(R) type 1002 tape manufactured by Minnesota Mining and Manufacturing. Since the individual plate lamina were symmetrically arranged with respect to the plate center, extensional-bending coupling was eliminated. The particular geometrical configurations constructed, however, allowed for combined bending-twisting interaction.

Each panel was clamped into a rigid frame fixture which was attached to a twelve hundred pound dynamic shaker manufactured by MB Electronics. An overview of the test equipment is shown in Fig. 1 and a schematic diagram of the equipment used in Fig. 2. The holding frame consisted of two 1-inch-square by 9-inch-long clamping bars fastened at three points with 3/8-inch bolts on centers, with a center bolt

TABLE I
Configurations of Tested Plates

Panel Aspect Ratios	Ply Orientations *	Total Number of Plies
1, 3/4, 1/4	0°	8
	± 15°	4, 8, 16
	± 30°	4, 8, 16
	± 45°	4, 8, 16

* The angle of ply orientation as shown in Table I is the angle between the direction of fiber orientation with respect to a line perpendicular to the clamped edge.

TABLE II
Plate Geometry Data

Aspect Ratio	Panel Dimensions
1	7.75" x 7.75" x .032", .064", .128"
3/4	7.75" x 5.82" x .032", .064", .128"
1/4	7.75" x 1.93" x .032", .064", .128"

passing through the clamped edge of the composite panel. This attachment configuration reduced the unsupported span of the panels to a square configuration of 7-3/4 inches for the case of panels having an aspect ratio of one.

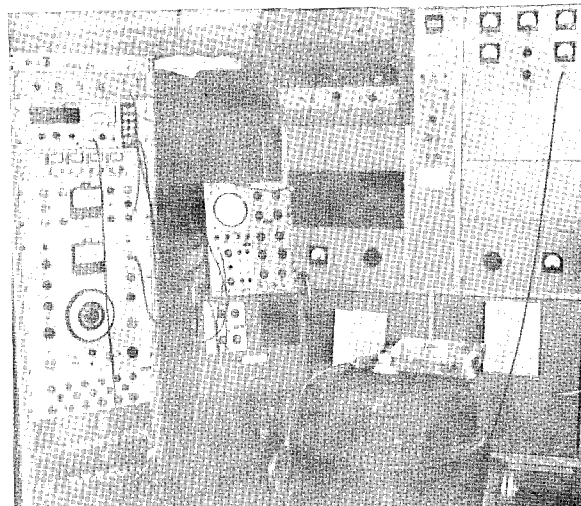


Figure 1 An overview of the test equipment

Plate excitation was generated using a controlled sweep oscillator with signal amplification; and response was monitored on an adjacent oscilloscope. Frequency response was separately checked using a graphic level recorder synchronized with the sweep oscillator. A miniaturized accelerometer was positioned on each of the plate specimens, usually at the free end of the plate, to locate nodes and antinodes for the various mode shapes recorded.

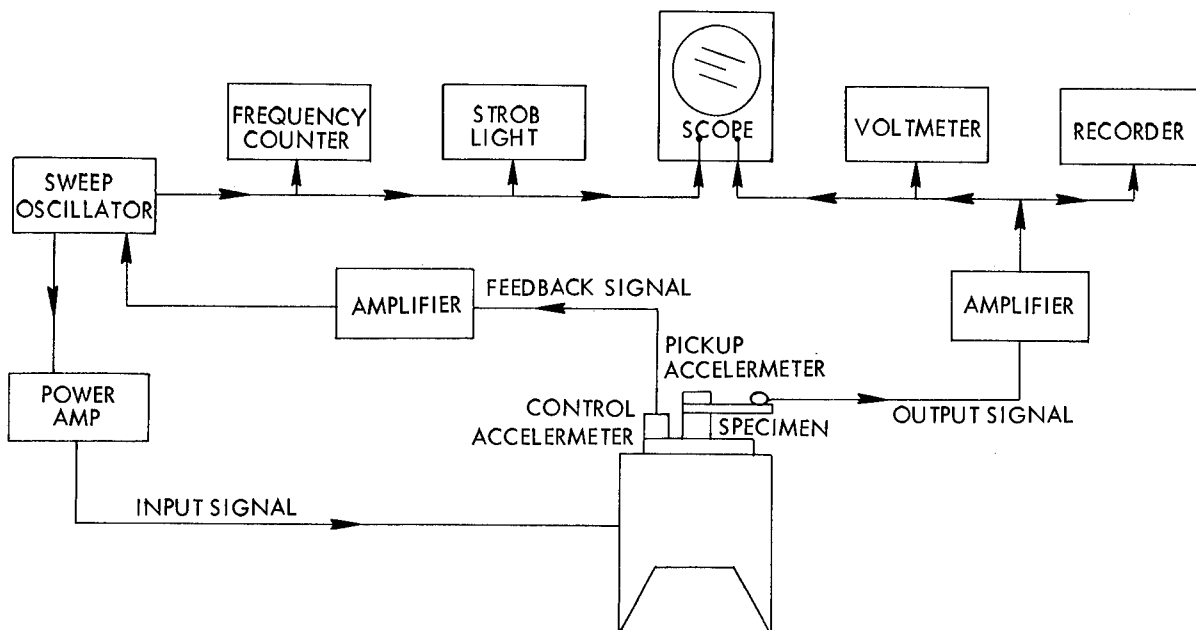


Figure 2 A schematic diagram of the test equipment

When the plates were excited at a resonant frequency, the panels vibrated in a characteristic mode shape. This shape was visually identified using limestone ballast granules sprinkled on the surface of the individual panels. The granular material bounced off the moving areas of the panels and identified points where relatively little and where excessive motion could be easily observed. At resonant frequencies, stationary node lines were formed along specific geometric patterns. The granules used were selected for their visual characteristics against the plate background and for their weight and resiliency. When a resonant frequency was approached having been identified by monitoring the oscilloscope, the granules were sprinkled on the surface of the plate, the power was then cut off and the resultant mode shape photographed. The frequency sweep was then advanced until the next frequency was observed and the procedure repeated. In some cases difficulties in identifying some of the bending-twisting mode shapes were noted due to clamping stiffness of the plate in the vicinity of the root attachment area. This can be observed in Figure 5 where a greater accumulation of granules was noted near the attached end of the plate.

DISCUSSIONS AND RESULTS

The experimental tests reported on here were conducted in order to obtain information on the dynamic response characterization of composite plates with controlled geometrical parameters for use in conjunction with ongoing plate impact tests at the Air Force Materials Laboratory. Studies based on the above results are planned to obtain dynamic data on plates having non-uniform stiffness properties, thickness variations, and varying aspect ratios.

For the current test program, a fixed longitudinal to transverse modulus ratio with varying aspect ratios, ply thicknesses, and angle ply orientations was tested. The reason for selecting a variable ply thickness was as a screening procedure for use in examining the extent to which a meaningful response characterization might be obtained using the shaker assembly previously described. Some previously reported experimental data, indicated in References [1-3], have generally been taken on eight ply plate configurations. Based upon present test data such plate thicknesses appear to be most suitable for mechanical shaker type equipment. This appears due to the input limitations for which an essentially linear response, over the frequency range of interest, may be obtained. For example, consider the following non-dimensional parameter used in quantifying plate response data of the form $\rho h b^4 \omega^2 / D$, where ω is the response frequency, D the plate flexural rigidity, ρ the material density, and h , b represent the plate thickness and width, respectively, Reference [3]. If we now consider two identical plates of similar material properties with only a thickness variation and examine the non-dimensional parameter ratios with respect to input-output levels, we note that the recorded response levels are proportional to the square of the plate thickness. This indeed has been observed experimentally since ply thicknesses of $m = 4$ were found to be extremely flexible and difficult to obtain experimental data on, due to the large deflections occurring at or near a resonant condition. In addition, the influence of inplane membrane forces and of any added weight to the plate configuration such as the granular media used to identify the mode shapes

and the miniaturized accelerometer used for locating nodes and antinodes appear to influence response data considerably. On the other hand, plates having ply thickness of $m = 16$ are extremely stiff and require considerable input to drive at a resonant condition. In order to do this, one must overdrive these systems necessitating the introduction of secondary effects such as root clamping influences and frame resonances detrimental to obtaining satisfactory mode frequencies and identifying mode shapes. Therefore, data collected in the present test program has been based upon an eight ply plate configuration. It should be noted that the non-dimensional plate parameter previously introduced indicates that the actual frequency varies linearly with plate thickness and this has been shown to be in agreement with experimental observations and theoretical predictions.

The selection of the variable angle ply geometry was considered to examine the coupling influence of D_{16} , D_{26} terms on plate response. Physically the presence of the terms D_{16} and D_{26} will couple twisting curvature to normal moment resultants of the plate [6]. The bending stiffness, D_{ij} , is related to the reduced stiffness, Q_{ij} , by the following relation

$$D_{ij} = \int_{-h/2}^{h/2} Q_{ij}^{(k)} z^2 dz \quad (1)$$

where the superscript, k , indicates the Q_{ij} of the k^{th} layer of the laminate.

The values of Q_{ij} for 0 degree fiber orientation are given below

$$[Q_{ij}] = \begin{bmatrix} 5.63 & 0.512 & 0 \\ 0.512 & 2.05 & 0 \\ 0 & 0 & 0.8 \end{bmatrix} \times 10^6 \text{ psi}$$

The values of Q_{ij} for the cases when the angle of fiber orientation is different from zero degree can be obtained by the well-known transformation formula [7]. The values of the corresponding bending stiffness D_{ij} can then be obtained from Eq. (1).

For a 0° plate, $D_{16} = D_{26} = 0$; for a $\pm \theta^\circ$ plate, $D_{16} \neq D_{26} \neq 0$, and for a $\pm 45^\circ$, $D_{16} = D_{26}$. The selection of variable aspect ratios was considered to examine the importance of plate geometrical shape in changing frequencies and mode shapes for dynamic response calculations. A tabulated summary of results for the first five frequencies excluding the fundamental bending mode and considering varying aspect ratio and angle ply orientation are included in Table III - V with typical experimental data for the corresponding mode shapes for the $m = 8$, $\pm 45^\circ$ case shown in Figures 3-7. It should be noted that experimental data has been included for the $m = 8$ ply configuration only since for this case consistently reproducible data was collected as previously discussed. Also, Table III includes a comparison between the analytically predicted

frequencies for the anisotropic and specially orthotropic plate configurations. The latter are obtained by taking D_{16} , D_{26} as identically zero for all angle ply configurations. It was observed that for calculated frequencies up to the first ten values, for any angle ply configuration and plate thickness, the upper bound error admitted by suppressing D_{16} , D_{26} was less than two percent.

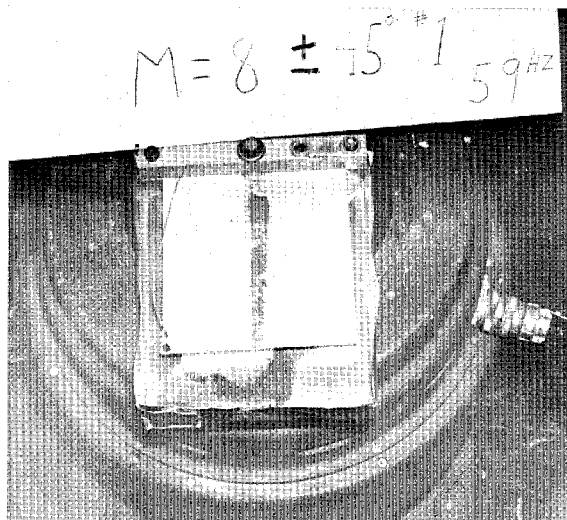


Figure 3 Experimental result of mode shape and natural frequency of the second mode for $m = 8$ and $\pm 45^\circ$ symmetric angle ply square plate

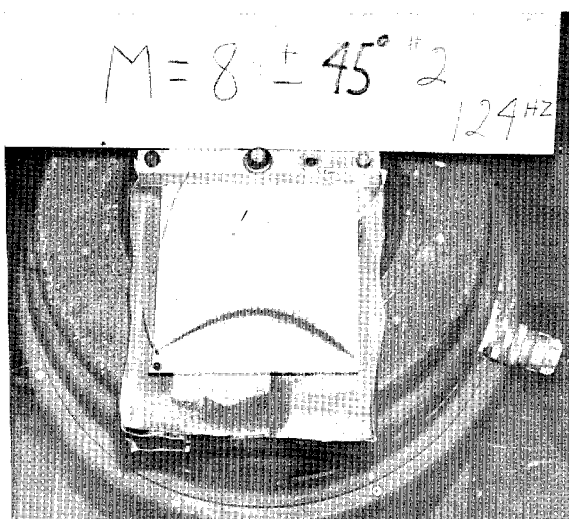


Figure 4 Experimental result of mode shape and natural frequency of the third mode for $m = 8$ and $\pm 45^\circ$ symmetric angle ply square plate

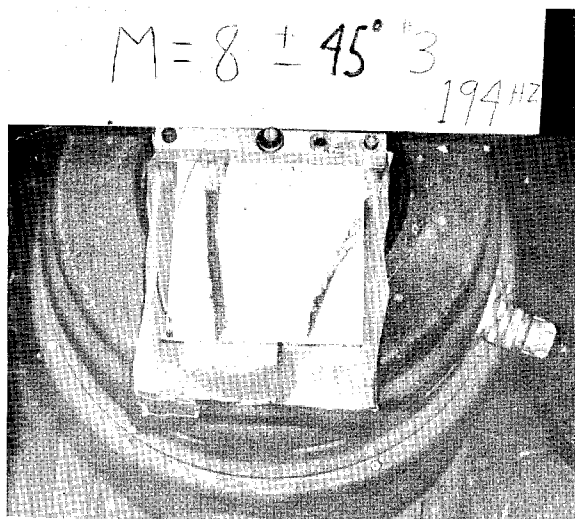


Figure 5 Experimental result of mode shape and natural frequency of the fourth mode for $m = 8$ and $\pm 45^\circ$ symmetric angle ply square plate

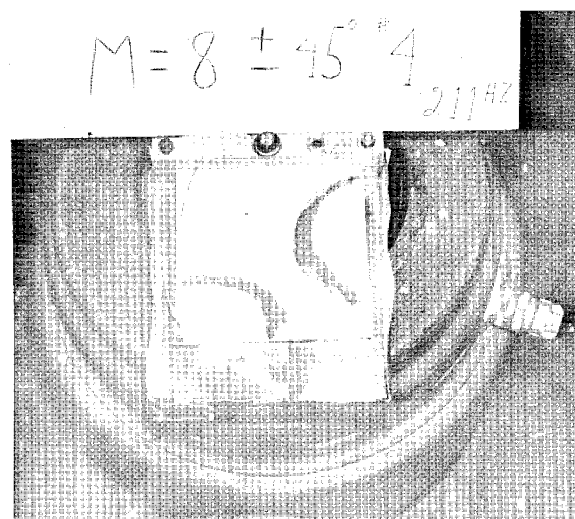


Figure 6 Experimental result of mode shape and natural frequency of the fifth mode for $m = 8$ and $\pm 45^\circ$ symmetric angle ply square plate.

Typical plots of mode shape change as obtained from analytical predictions for the $m = 8$, $\pm 45^\circ$ case with varying aspect ratios are shown in Figure 8 for the first six frequencies excluding the fundamental mode. For an aspect ratio of one, these results can be compared with the experimental data shown in Figures 3-7. Also included for comparison in these data are results obtained when D_{16} , D_{26} coupling are suppressed. Note that aspect ratio scaling has not been preserved in Figure 8; however, the mode shapes have been drawn to scale. It can be ob-

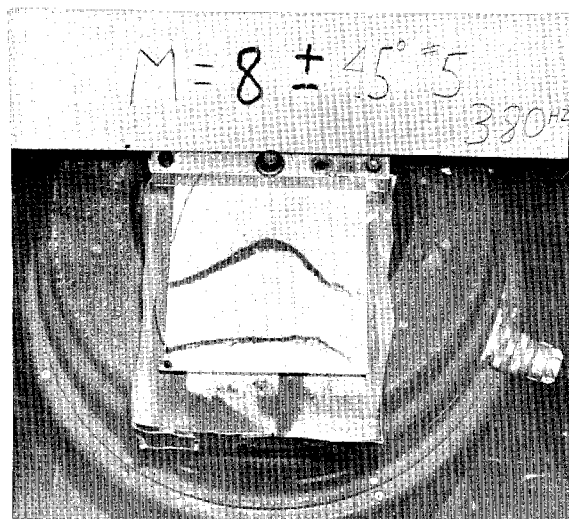


Figure 7 Experimental result of mode shape and natural frequency of the sixth mode for $m = 8$ and $\pm 45^\circ$ symmetric angle ply square plate

served that in the fundamental mode (See Table III-V) the influence of change in aspect ratio has little effect. For the higher modes shown in Figure 8 the frequency increases; however, no general rule as to the rate of increase can be formulated. Also, there is a considerable difference in corresponding mode shape change with aspect ratio as the frequency is increased. This is also observed for the other angle ply cases considered. The suppression of the D_{16} , D_{26} coupling terms appears to have little influence on the corresponding frequencies but as can be observed considerable influence on the resultant mode shapes. This trend has also been noted for the other angle ply laminate considered.

As a separate graphical illustration, results are shown for a typical variation of ply orientation for a fixed aspect ratio and ply thickness, ($AR = 1$, $m = 8$) with data for the suppressed case of D_{16} , D_{26} coupling included. These data are shown in Figure 9 again for the case of the first six frequencies. There appears to be no discernible change in natural frequency with change in angle ply orientation; however, there are considerable changes in mode shapes. The most significant changes in mode shape occur for the higher modes between the cases where $D_{16} \neq D_{26}$ and $D_{16} = D_{26}$, for each change in aspect ratio.

CONCLUDING REMARKS

On the basis of results obtained here the following concluding remarks are made:

- Experimental limitation of electro-mechanical shakers for determining frequencies response to be ~ 30 -500 Hz.
- Plates of ply thickness $m = 8$ appear most suitable for test purposes.

- (c) The influence of orthotropy, that is, suppression of D_{16} , D_{26} , appears negligible in so far as determining characteristic frequencies but influence mode shapes.
- (d) Both frequency and mode shape change with aspect ratio, with aspect ratio change particularly important for the higher modes.
- (e) For a fixed aspect ratio, the influence of ply orientation appears important for determining corresponding frequency and mode shapes. This is particularly important at higher frequencies for the cases where $D_{16} \neq D_{26}$.

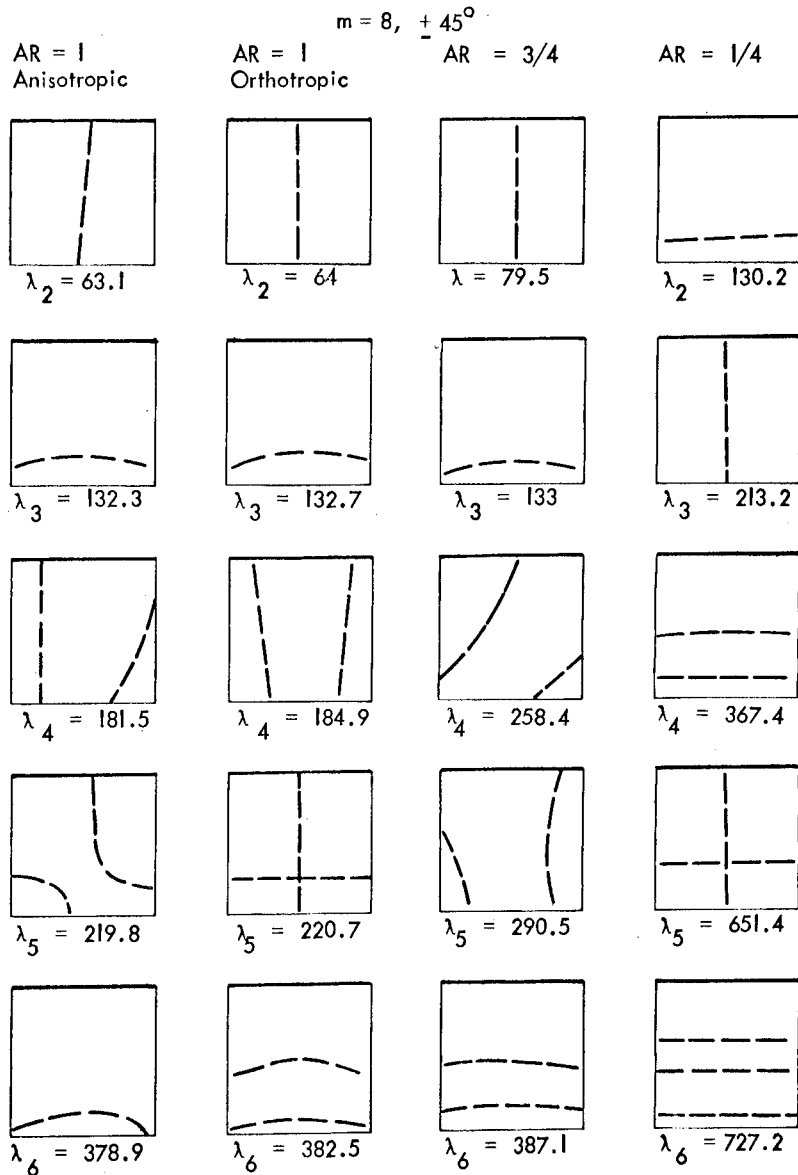


Figure 8 Theoretical plots of mode shapes and natural frequencies for the second through sixth modes for $m = 8$ and $\pm 45^\circ$ with varying aspect ratios

$m = 8, AR = 1$

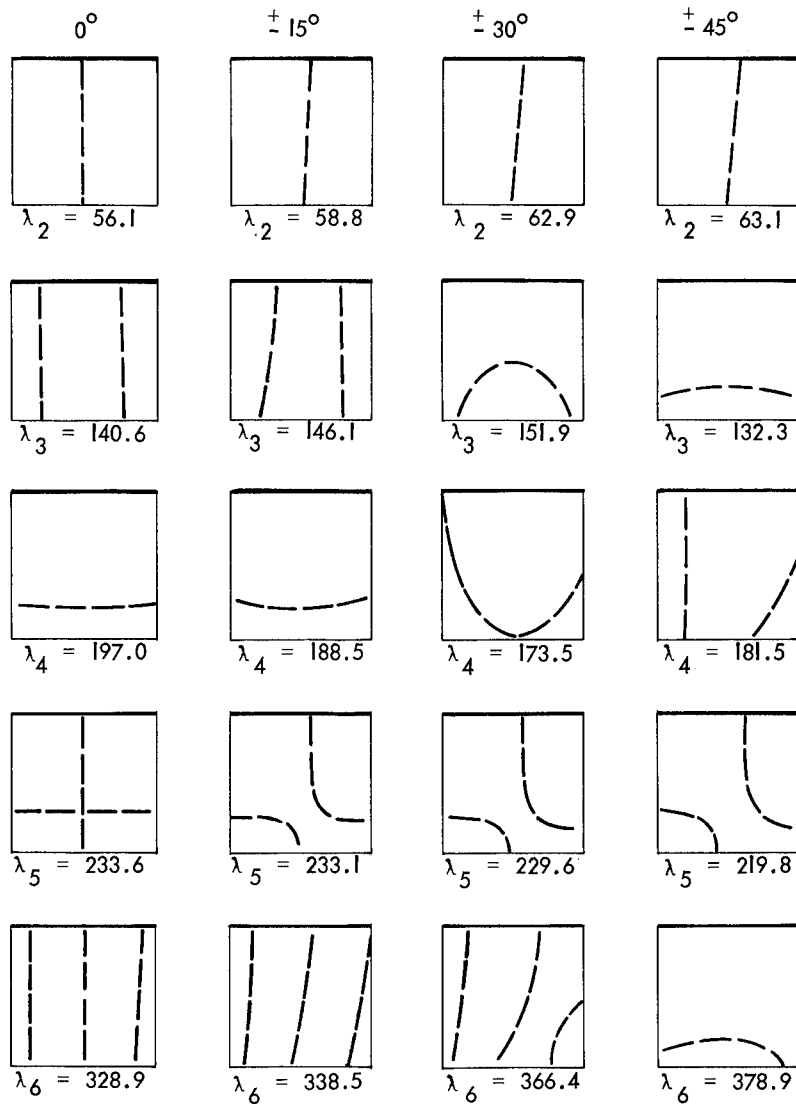


Figure 9 Theoretical plots of mode shapes and natural frequencies for the second through sixth modes for $m = 8$ and $AR = 1$ with varying ply orientation

Table III
Theoretical and Experimental Results for the Case of AR = 1

	0°		± 15°		± 30°			± 45°		
	m = 8	m = 4	m = 8	m = 16	m = 4	m = 8	m = 16	m = 4	m = 8	m = 16
$\lambda_1(a)$	31.3	14.8	29.9	60.0	12.8	26.1	52.5	10.6	21.7	43.6
$\lambda_1(o)$	31.3	15.0	30.0	60.0	13.2	26.3	52.6	10.9	21.8	43.7
$\lambda_1(e)$	32.0	15.8	31.1	60.0	12.1	24	48.1	11.0	22	44.1
$\lambda_2(a)$	56.1	29.0	58.8	118.0	30.3	62.9	126.9	30.1	63.1	127.6
$\lambda_2(o)$	56.1	29.5	59.1	118.1	31.8	63.6	127.2	32.0	64.0	128.0
$\lambda_2(e)$	48.0	29.7	60	119.2	28.2	57	114.1	29.3	59	118.0
$\lambda_3(a)$	140.6	72.4	146.1	292.8	74.7	151.9	304.9	65.4	132.3	265.3
$\lambda_3(o)$	140.6	73.3	146.5	293.0	76.3	152.6	305.3	66.4	132.7	265.5
$\lambda_3(e)$	143.7	82.0	163	326.5	67.5	134	270.5	62.4	124	249.0
$\lambda_4(a)$	197.0	93.5	188.5	377.7	84.1	173.5	349.4	85.4	181.5	368.2
$\lambda_4(o)$	197.0	94.5	189.0	377.9	87.6	175.1	350.3	92.5	184.9	369.9
$\lambda_4(e)$	205	101.2	202	405.0	96.2	192	385.0	97.2	194	389.2
$\lambda_5(a)$	233.6	115.4	233.1	467.3	112.2	229.6	461.8	108.4	219.8	441.0
$\lambda_5(o)$	233.6	116.9	233.8	467.6	115.6	231.3	462.6	110.3	220.7	441.4
$\lambda_5(e)$	231	122.0	243	487.2	106.4	211	422.5	105.3	210	421.7

$\lambda_i = \omega_i / 2\pi$ Unit in Hertz

(a) Anisotropic

(o) Orthotropic

(e) Experimental

Table IV
Theoretical and Experimental Results for the Case of AR = 3/4

	0°	± 15°			± 30°			± 45°		
		m = 4	m = 8	m = 16	m = 4	m = 8	m = 16	m = 4	m = 8	m = 16
$\lambda_1(a)$	31.3	14.9	29.8	59.6	13.0	25.9	51.9	10.8	21.5	43.1
$\lambda_1(e)$	32.9	15.8	31.6	63.4	11.9	23.6	47.3	10.6	21.3	42.7
$\lambda_2(a)$	68.2	36.0	72.2	144.7	39.4	78.4	157.0	39.7	79.5	160.1
$\lambda_2(e)$	63.4	35.5	71.1	142.5	39.2	78.4	157.2	41.0	81.8	163.0
$\lambda_3(a)$	194.5	92.7	185.0	371.2	80.6	160.6	321.5	66.7	133.0	267.0
$\lambda_3(e)$	205.6	98.2	195.9	392.1	76.1	150.5	301.5	65.4	130.6	262.0
$\lambda_4(a)$	223.4	116.2	231.5	463.5	125.8	251.3	503.2	129.7	258.4	517.2
$\lambda_4(e)$	257.0	120.5	240.2	481.7	130.5	260.1	521.7	132.9	265.3	531.7
$\lambda_5(a)$	259.7	133.0	264.6	529.7	137.0	273.2	547.2	146.0	290.5	582.1
$\lambda_5(e)$	271.2	140.9	281.7	564.7	145.9	290.6	583.0	155.9	310.7	622.5

$\lambda_i = \omega_i / 2\pi$ Unit in Hertz

(a) Anisotropic

(e) Experimental

TABLE V

Theoretical and Experimental Results for the Case of AR = 1/4

	0°	± 15°			± 30°			± 45°		
		m = 4	m = 8	m = 16	m = 4	m = 8	m = 16	m = 4	m = 8	m = 16
$\lambda_1(a)$	31.2	14.7	29.5	59.7	12.6	25.3	50.6	10.6	20.9	41.9
$\lambda_1(e)$	32.1	14.9	29.8	59.9	12.8	25.5	51.0	10.6	21.2	42.0
$\lambda_2(a)$	164.8	88.3	176.2	352.7	89.1	157.8	316.0	65.2	130.2	260.9
$\lambda_2(e)$	167.0	88.7	177.6	353.2	79.9	159.8	320.1	66.4	132.9	265.0
$\lambda_3(a)$	195.6	93.2	188.2	376.9	102.7	205.0	410.2	106.7	213.2	426.5
$\lambda_3(e)$	200.7	97.4	195.2	390.0	105.4	210.6	422.0	116.7	223.2	446.0
$\lambda_4(a)$	524.4	256.7	512.0	1030.7	221.7	444.3	889.7	184.0	367.4	735.0
$\lambda_4(e)$	535.7	263.7	527.0	1055.0	230.7	460.4	921.0	190.2	380.4	761.0
$\lambda_5(a)$	548.1	286.0	570.9	1143.0	317.0	632.4	1249.7	322.0	651.4	1304.0
$\lambda_5(e)$	567.1	281.0	590.9	1181.0	328.7	657.2	1320.1	336.1	679.1	1360.2

$\lambda_i = \omega_i / 2\pi$ Unit in Hertz

(a) Anisotropic

(e) Experimental

ACKNOWLEDGMENT

This research work was conducted while both authors held National Research Council Air Force Systems Command Senior Resident Research Associateships at Wright-Patterson Air Force Base, Ohio.

The analytical data were obtained using a computer program developed at General Dynamics, Fort Worth. The program was made available through the courtesy of Dr. D. Read.

The design of the experiments conducted and the fabrication of the specimens used were under the direct supervision of the authors. However, the authors wish to acknowledge the technical assistance of Mr. C. Browning and Mr. T. Harkness of the Air Force Materials Laboratory, and of Mr. M. Parin of the University of Dayton Research Institute.

This work was partially supported by the Engineering Research Institute, Iowa State University, Ames, Iowa.

REFERENCES

- [1] Ashton, J. E. and Waddoups, M. E., "Analysis of Anisotropic Plates," J. of Composite Materials, Vol. 3, p. 148, 1969.
- [2] Ashton, J. E. and Anderson, J. D., "The Natural Modes of Vibration of Boron-Epoxy Plates," Shock and Vibration Bulletin, Vol. 39, Part 4, pp. 81-91, 1969.
- [3] Ashton, J. E., "Natural Modes of Free-Free Anisotropic Plates," Shock and Vibration Bulletin, Vol. 39, Part 4, pp. 93-97, 1969.
- [4] Bert, C. W. and Mayberry, B. L., "Free Vibrations of Unsymmetrical Laminated Anisotropic Plates with Clamped Edges," J. of Composite Materials, Vol. 3, pp. 282-293, 1969.
- [5] Mohan, D. and Kingsbury, H. B., "Free Vibrations of Generally Orthotropic Plates," Journal of Acoustical Society of America, Vol. 50, pp. 266-269, 1971.
- [6] Ashton, J. E. and Whitney, J. M., "Theory of Laminated Plates," pp. 77, Progress in Materials Science Series, Vol. IV, Technomic Publishing Co., Stamford, Conn., 1970.
- [7] J. E. Ashton, J. C. Halpin and P. H. Petit, "Primer On Composite Materials; Analysis," p. 21, Technomic Publishing Co., Stamford, Conn., 1969.

SPACECRAFT VIBRATION TEST LEVEL COST
OPTIMIZATION STUDY

Joseph P. Young
National Aeronautics and Space Administration
Goddard Space Flight Center
Greenbelt, Maryland

A consideration common to all nondestructive testing of hardware to provide the necessary confidence in the design is the question regarding the proper magnitude of the test level. The objective of this investigation was to study the possibility of establishing "optimum" vibration test levels consistent with minimizing dollar cost. This investigation was based on studying the influence of test level on a cost of error cost model that reflects the adverse effects of "undertesting" and "overtesting." For the assumed conditions of normal distribution for the random variables and a protoflight spacecraft case, the results indicated that the limits for an optimum vibration test factor can range between slightly more than 1.0 to slightly less than 1.5.

INTRODUCTION

When performing any "not to destruction" test designed to demonstrate the acceptability of flight design hardware, a common question arises regarding the proper magnitude of the test level. This question is prompted by the desire to set the test level at a point that is high enough to provide a high level of confidence in the strength of the design but not too high so as to cause unreasonable test failures. Due to the complex statistical nature of the problem and the unique characteristics associated with each testing situation, little progress has been made toward defining a universal "optimum" test level. Therefore, the objective of this investigation was to study the possibility of establishing optimum vibration test levels that would be compatible with reducing the dollar cost of environmental testing.

The basis for this investigation was a cost model and test level optimization study done by Piersol & Maurer

(Ref. 1). Most specifically, this effort has dealt only with the cost model and test level optimization results from Reference 1 that pertain directly to the proto-flight program case. A proto-flight program by definition is a program where a specific spacecraft article will serve both as a prototype and a flight model. In addition, all the random variables were assumed to be normally distributed.

The cost model from Reference 1 is derived from the cost of error viewpoint. That is, the model is the sum of the expected cost resulting from an overtest and the expected cost resulting from an undertest. This cost model is

$$C = P_1 C_{RT} + P_2 C_F \quad (1)$$

where,

C = total expected cost for both
overtesting and undertesting

C_{RT} = cost resulting from a test failure

C_F = cost resulting from a service failure

P_1 = probability of experiencing an overttest

P_2 = probability of experiencing a service failure (undertest)

In Reference 1, the above cost model was minimized with respect to the test level. This resulted in an optimum test level expressed in terms of the percentile of the environment statistical distribution. The general expression for the optimum test level percentile was derived to be

$$X_0 = \frac{100}{1 + C_{RT}/C_F} \quad (2)$$

Figure 1 shown below presents a plot of Equation (2).

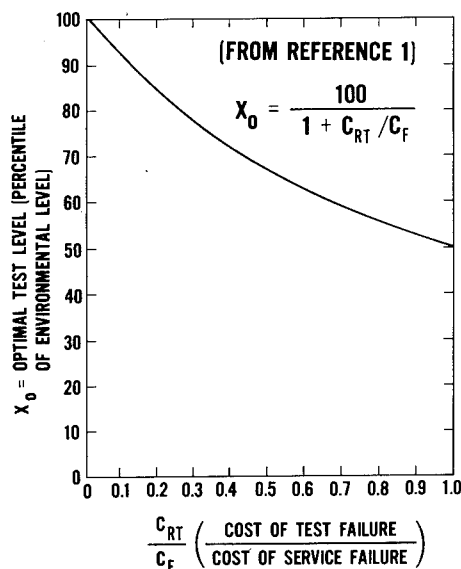


Fig. 1 - Optimal Test Level vs. Cost Ratio

It is to be noted that, although the expected cost expression in Equation (1) is a function of both the strength and environment distributions and the relative spread between the two, the derived optimal test level is a function of only the environment distribution. The individual minimized overttest and undertest cost relations are functions of both distributions and their separation, but when added, the strength distribution is a common term that is eliminated.

Several other observations should be noted about the approach used in Reference 1 which in turn applies to this study. First, the results are valid for any type of environmental loading condition where the load level is the only essential environment variable and where it can be expressed in terms of a statistical distribution with known parameters. Time of loading application is not considered as a variable due to assuming that either time is not significant or that the actual service exposure duration is being simulated in real time.

Since the practice for establishing qualification environmental test levels is often to multiply the maximum expected flight levels by a test factor, the need was felt to study the optimum test level in terms of this test factor procedure. Additionally, it was considered to be of value to investigate the sensitivity of the optimum test level and the expected cost to parameter variations. The remainder of this report presents the details of how this study was performed and a discussion of the results.

FORMULATION OF COST MODEL STUDY

The mathematical relationship studied was the cost model in Equation (1) rewritten slightly as follows:

$$C/C_F = P_1 \left(\frac{C_{RT}}{C_F} \right) + P_2 \quad (3)$$

The investigation considered the effects of changes in the parameters P_1 (probability of overttest), P_2 (probability of flight failure), and C_{RT}/C_F (cost ratio) on the normalized

expected cost of error. The probabilities P_1 and P_2 are defined as,

$$P_1 = \int_0^L F_E(s) f_S(s) ds$$

$$P_2 = \int_L^\infty [1 - F_E(s)] f_S(s) ds$$

where,

$$F_E(s) = \int_0^s f_E(e) de = P[E \leq s]$$

$f_E(e)$ = probability density function of the flight environment

$f_S(s)$ = probability density function of the spacecraft strength

L = test level.

Dealing with the normalized cost expression in Equation (3) is particularly attractive because knowledge of absolute costs is not required. Only the ratio of retest cost to flight failure cost is required information.

As stated earlier, this study assumed the environment and strength random variables to be normally distributed. With this assumption, the statistical variables can be pictured as shown below.

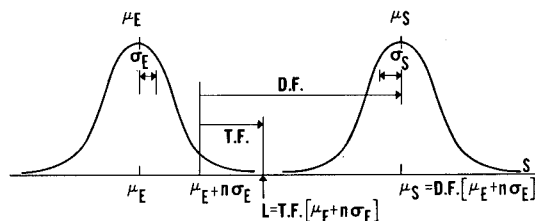


Fig. 2 - Statistical Model

where,

μ_E = service environment mean

σ_E = service environment standard deviation

μ_S = specimen strength mean

σ_S = specimen strength standard deviation

n = factor that establishes the flight loads probability level

D.F. = design factor that multiplies the flight loads to establish the specimen strength mean

T.F. = test factor that multiplies the flight loads to establish the qualification test level (L).

As shown, the relationship between the test level, L , and the test factor, T.F., is

$$L = T.F. [\mu_E + n\sigma_E]. \quad (4)$$

Based on an assumed normal distribution for the random variables, the solution for the normalized expected cost of error in Equation (3) will be a function of the following nondimensional terms:

μ_E/σ_E , μ_S/σ_S , n , T.F., D.F., and C_{RT}/C_F .

As stated earlier, Reference 1 derived an optimum test level percentile, X_o , that produces a minimum normalized expected cost $C/C_F = (C/C_o)$. To actually compute (C/C_o) the value of X_o , which is in terms of percentile of the environmental load distribution (F_E), must be converted into the equivalent number of standard deviations, k_o . The optimum test level can then be expressed as $L = \mu_E + k_o \sigma_E$. The value of (C/C_o) can then be computed as indicated in the preceding paragraphs.

One can now form the ratio, $(C/C_F) = (C/C_o)$, as a function of

T.F., C_{RT}/C_F , μ_E/σ_E , μ_S/σ_S , n , and D.F. This ratio (C/C_o) , represents a measure of the deviation of the cost of error from the minimum for specific values of the nondimensional parameters. In addition, the quantities P_1 (probability of overtest) and P_2 (probability of flight failure) and the normalized forms $\frac{P_1}{(P_1)_{1.5}}$ and $\frac{P_2}{(P_2)_{1.5}}$ can be studied.

The terms $(P_1)_{1.5}$ and $(P_2)_{1.5}$ are the respective probabilities corresponding to a test factor, T.F., of 1.5.

PARAMETRIC STUDY RESULTS

The results obtained emphasize both the effects of variation in the test factor, T.F., from the nominal 1.5 value and the magnitude of the optimized test factor, $(T.F.)_o$, as a function of the cost ratio, C_{RT}/C_F , and the other pertinent variables. Figures 3 - 7 present plots of cost of error deviation, (C/C_o) , vs. test factor, T.F., as a function of the nondimensional variables μ_E/σ_E , μ_S/σ_S , C_{RT}/C_F , n , and D.F. Figures 3 - 5 illustrate the sensitivity of the optimum test factor, $(T.F.)_o$, occurring at the minimum points on the curves, to variations in C_{RT}/C_F (Figure 3), μ_E/σ_E (Figure 4), and n (Figure 5). Figures 6 and 7 illustrate the total insensitivity of $(T.F.)_o$ to changes in μ_S/σ_S and D.F. This insensitivity is not at all unexpected as can be seen by inspecting Equations (1) and (2). In fact, from those equations, the following expression for $(T.F.)_o$ can be derived,

$$(T.F.)_o = \frac{1 + k_o \sigma_E / \mu_E}{1 + n \sigma_E / \mu_E} \quad (5)$$

Figures 3 - 7 also serve the purpose of providing a picture of the penalty paid when "off optimum" testing is performed. For example, Figure 3 shows that, for the $C_{RT}/C_F = .0001$ case, a test performed with T.F. = 1.2 instead of $(T.F.)_o = 1.4$ will result in an excessive cost factor of 4.

To further investigate the optimum test factor, Equation (5) was plotted,

as shown in Figure 8 for bounding values of the pertinent parameters. For clarification, the k_o factor is directly related to C_{RT}/C_F and hence, Figure 8 is a family of plots of $(T.F.)_o$ vs. C_{RT}/C_F . If one accepts the values of the plotted parameters as bounding values, the most obvious feature of this figure is that a $(T.F.)_o = 1.5$ lies at an upper corner of the bounded area. It is recognized that a test factor of 1.5 has been used quite commonly in the development of unmanned spacecraft.

Additional insight into the degree of reality and ultimate value of the results produced by this total cost of error model can possibly be gained by studying the separate behavior of the two probability terms that contribute to the total cost model. Figure 9 presents a plot of a normalized probability of service failure vs. test factor. The probability of service failure at a test factor of 1.5 was used as the normalizing term as a means for illustrating the effect of deviating from the use of the nominal test factor of 1.5. This plot shows two distinct characteristics. One feature is the distinct influence of the strength parameter, μ_S/σ_S , on the probability term. As would be expected, a smaller variance in the strength distribution produces a lower service failure probability. The second feature is, that for a small strength variance, e.g., $\mu_S/\sigma_S = 10$, the service failure probability very rapidly approaches a constant level as the test factor is reduced below 1.5.

A plot of the corresponding normalized probability of test failure vs. test factor is presented in Figure 10. No unusual trends are observed in this data. A smaller variance in the strength distribution produces a lower probability of test failure, and as the test factor increases, the test failure probability shows a continual increase.

CONCLUSIONS

From the results of this study, the following observations were made:

- (1) The optimum test factor, $(T.F.)_o$, is a function of only C_{RT}/C_F , μ_E/σ_E , and n .

- (2) As the cost ratio C_{RT}/C_F is increased, $(T.F.)_0$ decreases.
- (3) As the environment flight level percentile parameter, n , is increased, $(T.F.)_0$ decreases.
- (4) For cost ratios ≤ 0.01 and $n \leq 2$, these being conditions that will encompass the majority of situations, an increase in μ_E/σ_E will produce a decrease in $(T.F.)_0$. If C_{RT}/C_F is large (i.e., > 0.1) in conjunction with a large n (> 2), $(T.F.)_0$ will increase as μ_E/σ_E increases.
- (5) It is suggested that cost ratios, C_{RT}/C_F , of 0.1 and 0.00001 probably represent the extreme bounds with values of 0.01 to 0.0001 being the most likely range. Based on this assumption, it is concluded that the realistic limits for an optimum vibration test factor appear to be 1.1 to 1.4.

As a reminder, the results of this investigation and the preceding observations have as their basis the assumptions of a normal distribution for the random variables and a proto-flight test condition. Application of these results to other conditions is not recommended. In addition, two very practical considerations are to be satisfied before absolute use can be made of the information presented here. First, possible deficiencies in test simulation of the service environment could influence selection of "optimized" test levels. Second, and most importantly, the input cost ratio and statistical descriptors of the environment and hardware strength are not data that can be easily specified. Although the title of this report and the preceding discussion makes reference to applying the technique only to the optimization of vibration test levels, the results are valid for other conditions where the service environment and hardware strength are describable as normal distributions.

ACKNOWLEDGMENT

Appreciation is expressed to K. Bulow for computer programming of all the

computations and the valuable assistance provided in performing the computer runs.

REFERENCES

1. A. G. Piersol and J. R. Maurer, "Investigation of Statistical Techniques to Select Optimal Test Levels for Spacecraft Vibration Tests," Digitek Corporation Report 10909801-FC, NASA CR-115778, May 1971.

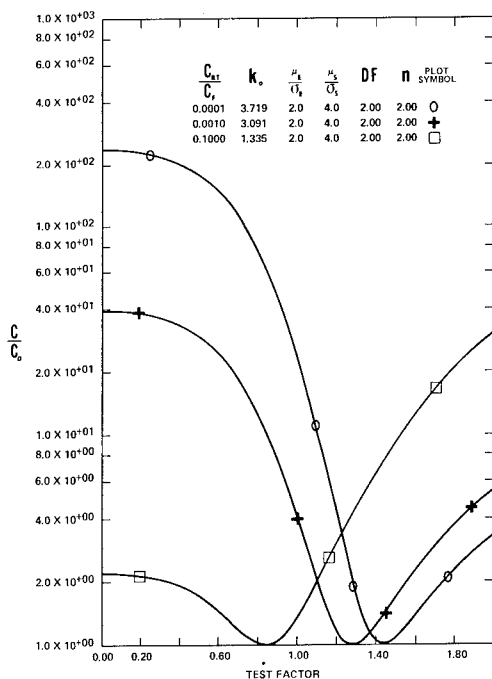


Fig. 3 - Normalized Expected Cost Ratio Vs. Test Factor (Variable C_{RT}/C_F)

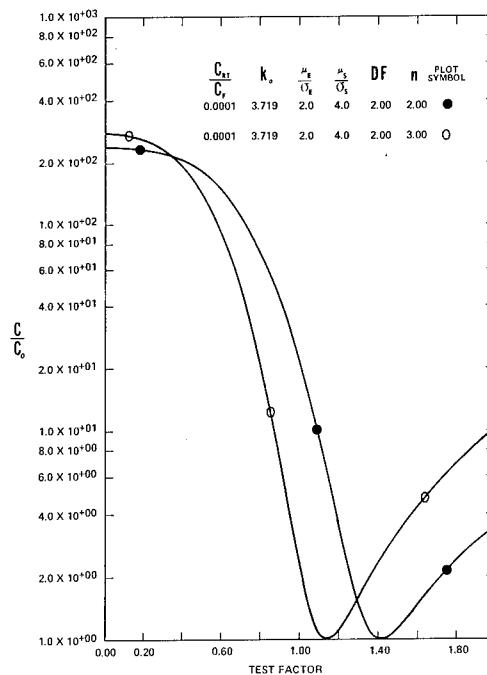


Fig. 5 - Normalized Expected Cost Ratio Vs. Test Factor (Variable n)

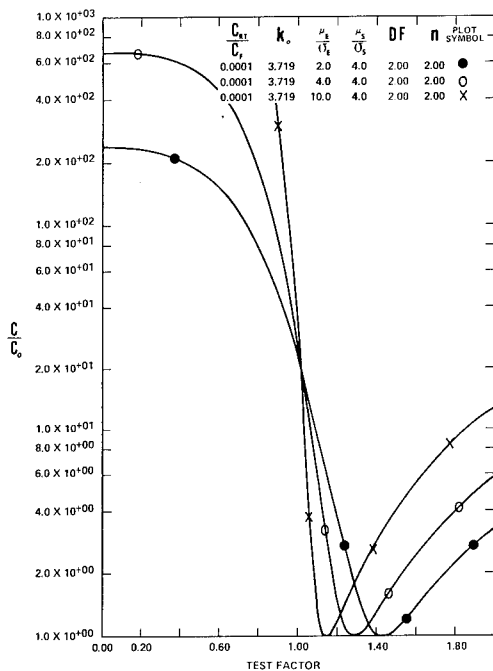


Fig. 4 - Normalized Expected Cost Ratio Vs. Test Factor (Variable μ_E/σ_E)

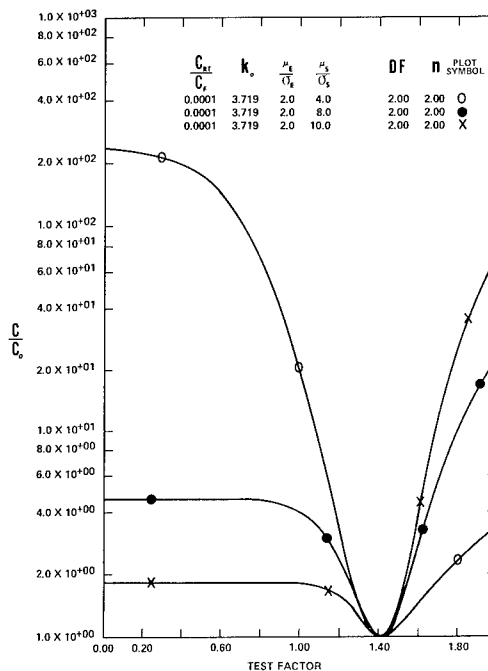


Fig. 6 - Normalized Expected Cost Ratio Vs. Test Factor (Variable μ_S/σ_S)

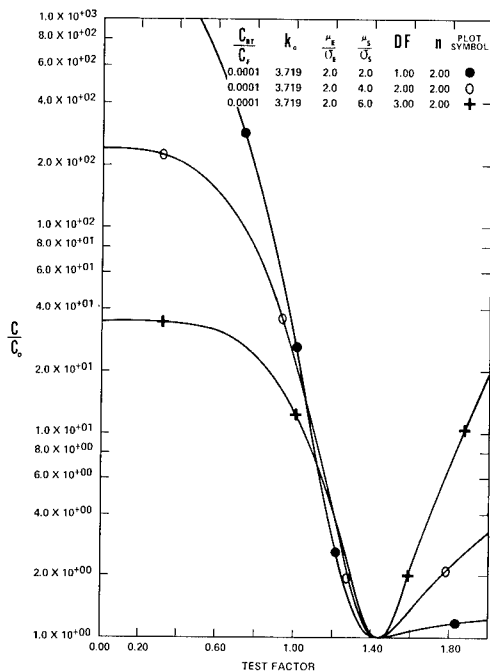


Fig. 7 - Normalized Expected Cost Ratio Vs. Test Factor (Variable D.F.)

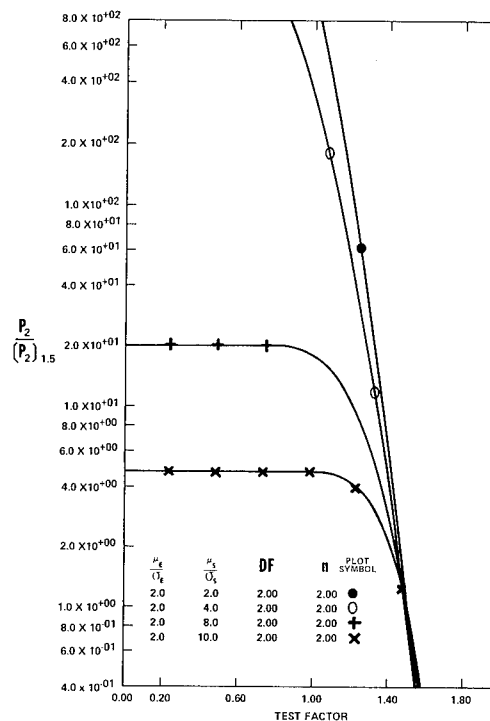


Fig. 9 - Normalized Flight Failure Probability Vs. Test Factor

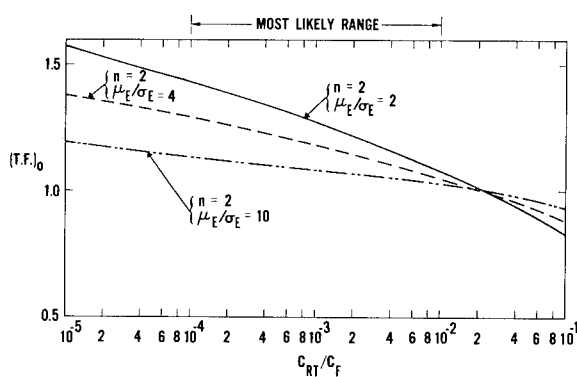


Fig. 8 - Optimal Test Factor Vs. Cost Ratio

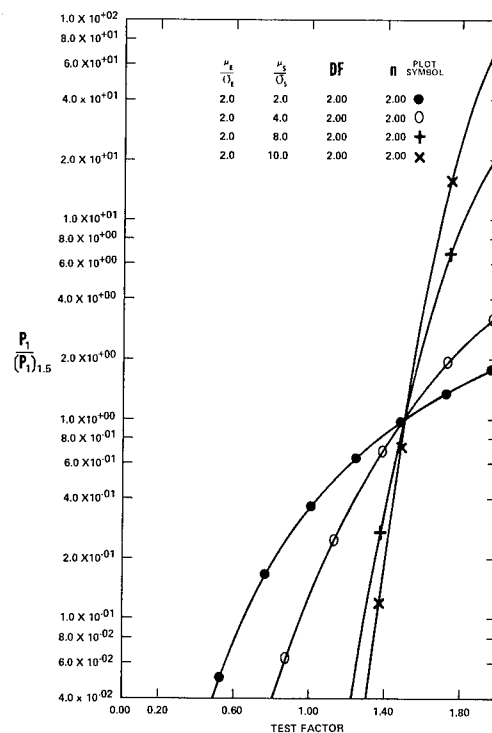


Fig. 10 - Normalized Test Failure Probability Vs. Test Factor

FLIGHT QUALIFICATION OF SPECIAL EQUIPMENT

Jerome Pearson and Roger E. Thaller
Air Force Flight Dynamics Laboratory
Wright-Patterson AFB, Ohio 45433

The flight vibration testing of special equipment to be flown aboard a modified C-135B is described, and the test results are compared with those of a finite-element modal analysis and a laboratory vibration survey. A newly-developed airborne data recording package was used for the flight tests. The vibration qualification test curves resulting from these quick-reaction flight tests showed lower vibration levels than predicted, confirming the adequacy of the equipment mount and averting a costly redesign. These results also emphasized that the interaction of equipment mass with the aircraft structure may have a significant effect on the aircraft vibration response and must be seriously considered in future analyses of airborne systems.

INTRODUCTION

The general procedure in qualifying a new payload for its expected aircraft flight vibration environment is to analyze the design to predict the structural vibration modes and frequencies, to vibrate the completed prototype with shakers to define the actual modes, and finally, to fly the payload on the aircraft to measure flight vibrations. The flight vibration test is thus the crucial proof of the design. The results of the flight vibration test may also point out deficiencies in the design or analysis and show unexpected dynamic effects. This paper describes such a flight vibration test and compares the results with the analytical predictions and the laboratory vibration survey. This particular program involved the flight qualification of special equipment to be flown aboard a C-135B for the Space & Missiles Systems Organization (SAMSO) of the U. S. Air Force. The "B" designation indicates turbofan engines. Although the vibration characteristics of the various models of the C-135 were in general well known [Ref. 1,2], the particular aircraft had been extensively modified for the installation of the special equipment, and therefore the existing data were not totally applicable.

ANALYSIS AND LABORATORY VIBRATION SURVEY

The special equipment was designed for SAMSO under contract and was to be located in the forward right section of the C-135B fuselage, indicated by the shaded area of Figure 1. The equipment was intended to be exposed to the atmosphere during operation, which required a modification of the fuselage structure in this area in order to allow the section to remain unpressurized during flight.

A generalized schematic of the equipment mount is shown in Figure 2. The mount was designed to allow motion longitudinally with respect to the aircraft fuselage and also at right angles to this direction. In designing the mount to allow for these desired motions, long jackscrews were used. In such mechanical systems some backlash is inevitable; the result is a decreased correlation between the linear analysis and the vibration survey.

In order to assess the dynamic response of the mounted equipment, a finite-element analysis of the complete structural system of the equipment, mount, and modified cargo deck was performed under contract. The dynamic model was composed of several substructures to allow

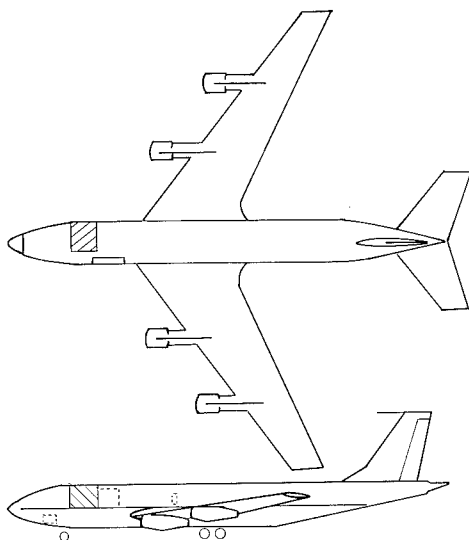


Fig. 1 - C-135B Aircraft With Equipment Location Shaded.

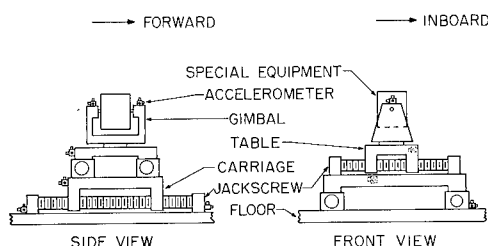


Fig. 2 - Generalized Schematic of Equipment Mount.

for design changes. The five substructures were the equipment package, the gimbal, the table, the carriage, and the jackscrew and floor. These substructure models included 161 degrees of freedom. The response of this structural system to the operational random vibration environment was determined by a modal approach. Two rigid body modes and eighteen elastic modes were included in the analysis. The frequencies determined for these elastic modes are shown in the second column of Table I. The first column gives the major direction of each mode. The detailed modeshapes for these modes were also determined, but for the purpose of this paper the frequency and the predominant direction of each major resonance are sufficient.

Mode	Direction	Analysis	Vibration Survey	Flight Test
1	Vert, Lat	45.3 Hz	23 Hz	23 Hz
2	Vert		36	36
3	Long		52	
4	Lat	60.6		
5	Lat			70
6	Long		75	76
7	Vert, Lat		80	80
8	Lat		85	95
9	Vert	115.7	95	100
10	Vert	173.6	95	100
11	Long		120	140
12	Long			160
13	Lat	179.3		
14	Long, Vert			200
15	Vert			220
16	Lat	224.2		

Table I. Resonant Frequencies Compared From The Analysis, Vibration Survey, and Flight Test.

A laboratory vibration survey was performed by a different contractor on the mount and dummy equipment, which was a mass and moment-of-inertia model of the flight article. Two 100-pound force electrodynamic shakers were used, both in-phase and out-of-phase, in order to excite each mode occurring in the frequency range of 10 to 250 Hz. The resonances observed are summarized in the third column of Table I.

These observed frequencies are considerably lower than those predicted by the finite-element analysis. The vibration test showed the first major resonance at 23 Hz; the analysis had predicted 45.3 Hz. One reason called upon to explain the discrepancy is the lack of allowance in the analysis for mechanical backlash in the jackscrews. The analysis had also shown two minor resonances in the 50-60 Hz range, and the equipment was known to be particularly sensitive in this frequency range. The laboratory vibration survey showed, however, that these resonances were much lower in frequency and were not likely to cause problems. The fact that each major resonance was observed to occur at only 50 to 70% of the predicted frequency was cause for some concern over the accuracy of the stiffnesses used in the finite-element analysis.

A second cause of concern was the lack of knowledge about the flight vibration responses of the modified cargo deck. The modifications added a large mass to the aircraft structure, which was expected to significantly alter the vibration responses near the equipment. It had been theorized that the added system mass would significantly lower the vibration levels of the KC-135A data, due to the limited ability of the aircraft structure to generate vibrational energy sufficient to excite a large mass forward of the aircraft center of gravity. It was difficult, however, to predict the actual flight vibration levels. Because of these uncertainties, a timely flight vibration test was needed to confirm the adequacy of the design.

FLIGHT VIBRATION TEST

The Air Force Flight Dynamics Laboratory (AFFDL) was contacted by SAMS0 and requested to perform an in-flight vibration survey of the modified portion of the fuselage and of strategic points on the equipment mount. The Flight Dynamics Laboratory's Dynamics Test Group decided to use an airborne measuring and recording package designed especially for this kind of quick-reaction flight test. The package, shown in Figure 3, contained 12 amplifiers which were compatible with a variety of sensors such as accelerometers, strain gages, and microphones. A tape recorder was included which recorded up to 15 minutes of data at a tape speed of 30 inches per second. Power supplies for all components used 400 Hz aircraft power. The entire package weighed just 75 pounds and was mounted on a 24" square aluminum plate; it occupied a total volume of 4 cubic feet. In order to eliminate the need for a calibration flight or knowing in advance what signal levels would occur in flight, the amplifiers were equipped with automatic gain controls which monitored the signal levels and selected the proper 10dB gain step over a range of 70dB. The change in gain was nearly instantaneous and was triggered when the average signal level remained out of the range for 0.4 seconds or more. The gain settings were recorded on a separate tape recorder channel.

Four test flights were made for this program, encompassing the expected aircraft operating altitudes and airspeeds and other possible flight conditions. After the flights, the recorded tapes were flown to the AFFDL for analysis. The data were analyzed in third-octave frequency bands, which were considered adequate for this test, and for each band the accelerations in g rms and the acceleration spectral densities in g^2/Hz were computed. An automatic digital plotter used these calculated values to produce report-form plots directly.

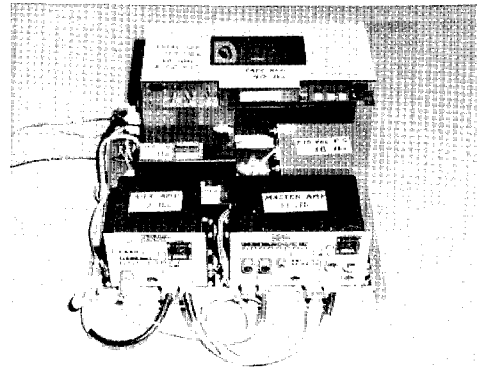


Fig. 3 - Flight Data Measuring and Recording Package.

RESULTS

Three flight conditions summarize those under which the equipment will operate. The equipment mounting point responses during the operating condition at 35,000 feet altitude and 220 knots indicated air speed are shown in Figure 4. The responses are shown as acceleration spectral densities versus third-octave frequency band. Figure 5 shows the mounting point responses at 35,000 feet and the maximum operating speed of 262 knots. Figure 6 shows the responses at the highest dynamic pressure expected in the operating regime, 26,500 feet and 320 knots. The maximum responses in the vertical, lateral, and longitudinal directions for these three flight conditions are summarized in Figure 7, which thus represents the most severe environment in which the equipment would be required to operate. From these data, the vibration test envelope for the operating conditions was drawn as shown, allowing a factor of safety to account for the short testing times [3]. A

constant test spectrum of $4 \times 10^{-4} g^2/Hz$ would be adequate except for the high responses observed in the 80-100 Hz range and in the 1250-1600 Hz range.

Three other flight conditions summarize those under which the equipment will not be operating; it must simply withstand these conditions without failing. Figure 8 shows the mounting point responses during takeoff. Figure 9 shows these responses at 26,500 feet and 373 knots, and Figure 10 shows the responses during a 2.2g pullup from a dive. Figure 11 summarizes the highest measured responses of the equipment mounting points in the vertical, lateral, and longitudinal directions during these non-operating conditions. From the data of Figure 11, the vibration test envelope for the non-operating

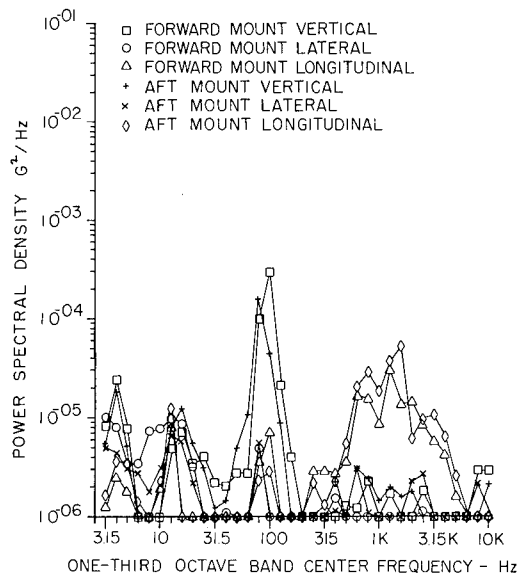


Fig. 4 - Equipment Mounting Point Responses at 35,000 Feet Altitude and 220 Knots.

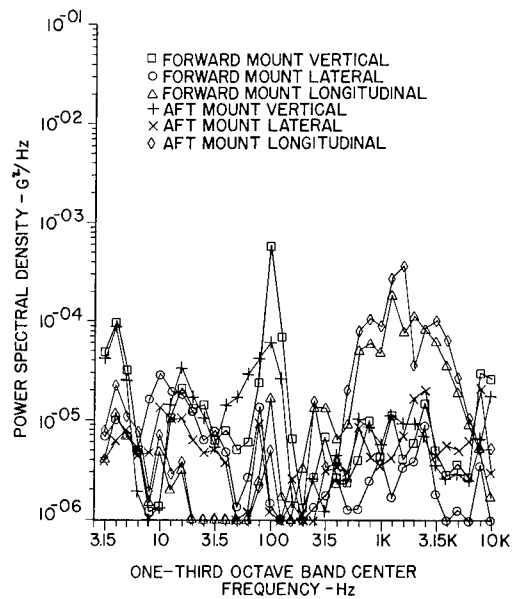


Fig. 6 - Equipment Mounting Point Responses at 26,500 Feet Altitude and 320 Knots.

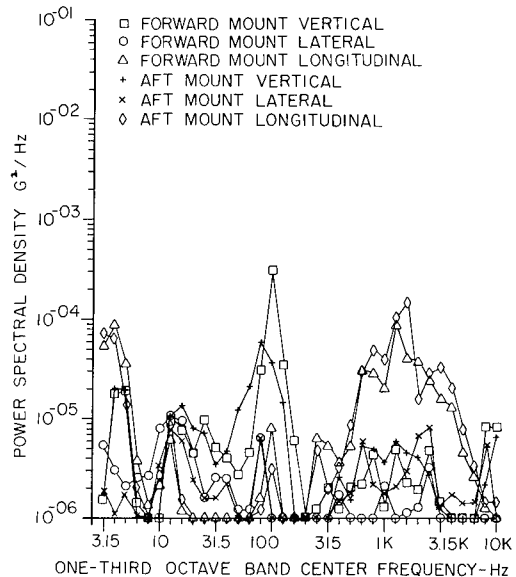


Fig. 5 - Equipment Mounting Point Responses at 35,000 Feet Altitude and 262 Knots.

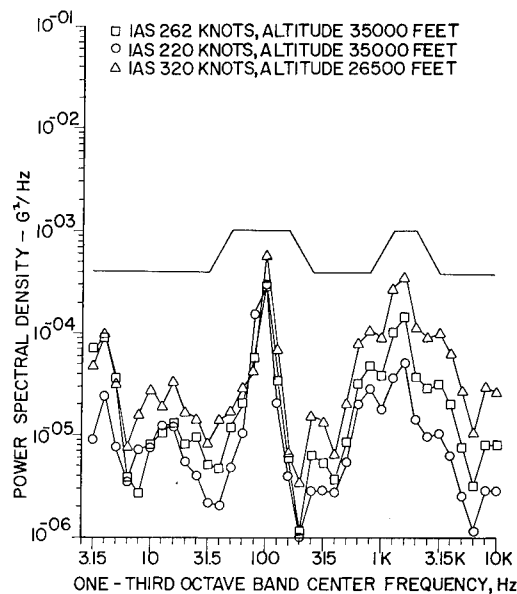


Fig. 7 - Maximum Responses of Equipment Mounting Points For Operating Conditions.

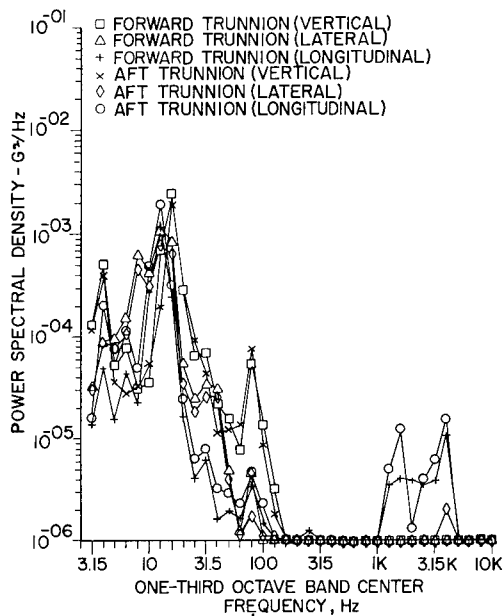


Fig. 8 - Equipment Mounting Point Responses During Takeoff.

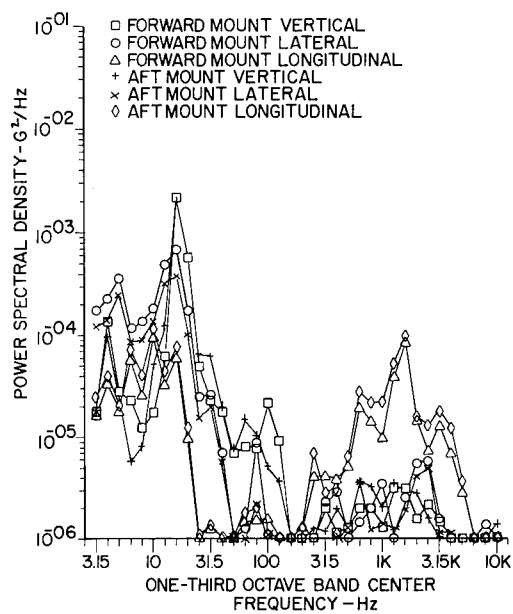


Fig. 10 - Equipment Mounting Point Responses During 2.2g Pullup From a Dive.

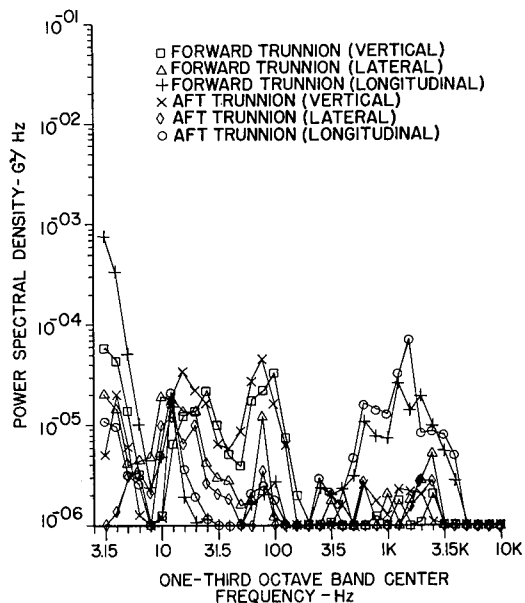


Fig. 9 - Equipment Mounting Point Responses at 26,500 Feet Altitude and 372 Knots.

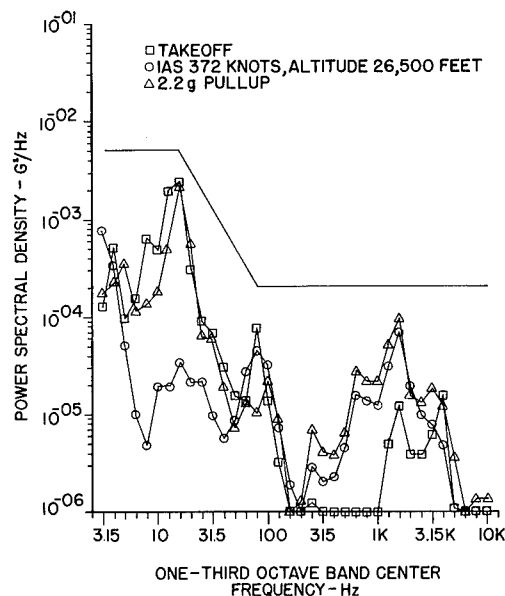


Fig. 11 - Maximum Responses of Equipment Mounting Points For Non-Operating Conditions.

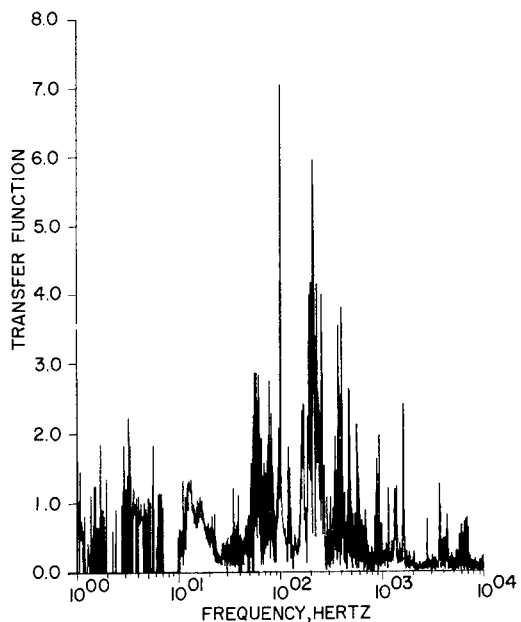


Fig. 12(a) - Vertical Transfer Function From Cargo Deck to Equipment Mounting Point.

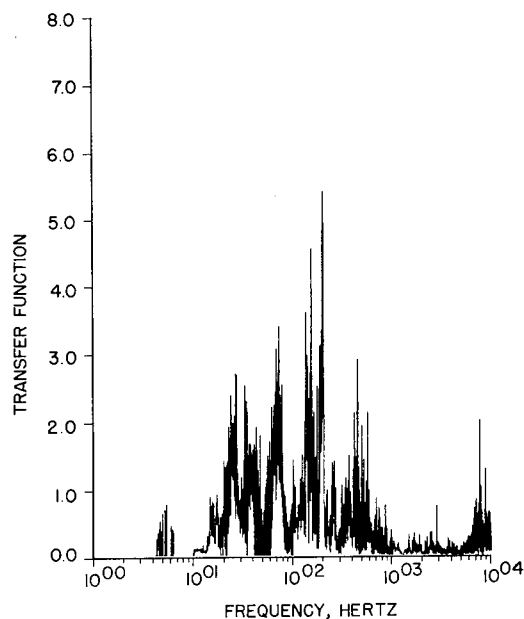


Fig. 12(c) - Longitudinal Transfer Function From Cargo Deck to Equipment Mounting Point.

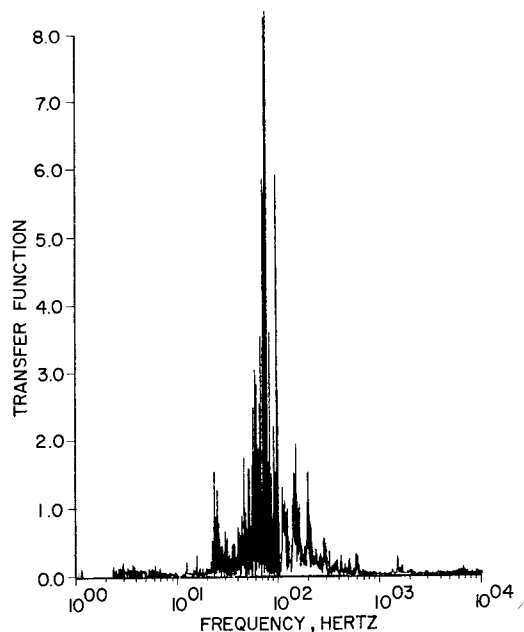


Fig. 12(b) - Lateral Transfer Function From Cargo Deck to Equipment Mounting Point.

conditions was drawn as shown, again allowing a safety factor to account for the short testing times. This envelope is dominated by the low frequency responses due to the landing gear/runway interaction. The envelopes of Figures 7 and 11 were used for the flight qualification testing of the equipment.

In addition to measuring the responses of the equipment mounting points, the responses of other points on the mount were measured. Figures 12a, b, and c show the transfer functions from the jackscrew attachment point to the equipment mounting points in third-octave bands for vertical, lateral and longitudinal accelerations, respectively. These results show that several resonances with large amplification factors occur in the lateral direction between 70 and 100 Hertz. The observed resonances are tabulated in the last column of Table I and, where possible, are correlated with the results of the laboratory vibration survey and the analysis. There is fair agreement between the frequencies observed in the flight test and those measured in the laboratory vibration survey.

The vibration envelope for the operating conditions is compared with previous data[4] from the KC-135A in Figure 13. The interaction of the system mass with the fuselage modification resulted in vibration levels distinctly lower than predicted. This was fortunate, since the high amplification factors of the mount shown by the laboratory vibration test, coupled with the flight environment which had been expected from the previous KC-135A data, would have prevented the equipment from operating.

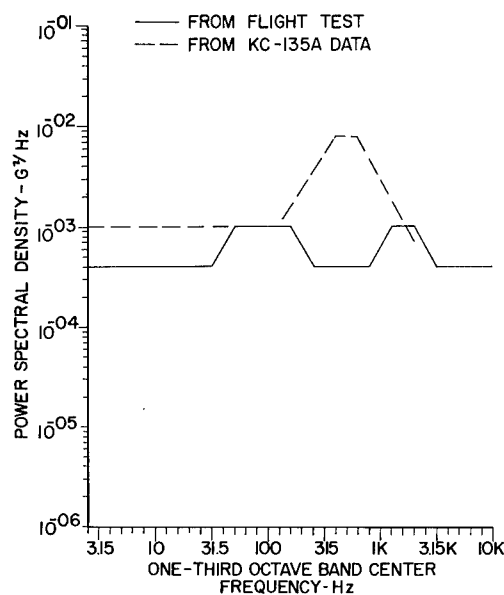


Fig. 13 - Comparison of Vibration Envelopes.

Figure 13 shows that the fuselage vibrations have been lowered over the entire frequency range, even though the envelopes are identical in the 50-160 Hz range. The reason is that the KC-135A data are the cargo deck vibrations, whereas the new flight test data include the amplification factors of the mount. These amplification factors, shown in Figure 12, indicate a reduction of 4 to 8 in the fuselage vibrations in the 50-160 Hz frequency range due to the mass loading.

CONCLUSIONS

The flight test showed resonant frequencies in the same range as the laboratory modal survey. The detailed resonances differed, however, because the flight tests measured the resonances of the equipment mounting points compared to the jackscrew attachment point, whereas the laboratory modal survey measured them compared to the carriage. Both of these tests differed from the generally higher frequencies predicted by the finite-element analysis.

The key information derived from the flight test was that both the analysis and the laboratory modal survey predicted vibration amplitudes and total vibrational energy significantly above those experienced in flight, due chiefly to the failure to accurately predict the effects of the added mass on the aircraft vibration levels. It should be emphasized that system mass interaction with the aircraft structure must be seriously considered in future analyses of airborne systems. For large and heavy systems such as the one in this test, in-flight vibration measurements are the key verification of the analysis and design.

REFERENCES

1. Magrath, H. A., Rogers, O. R., and Grimes, C. K.: "Shock and Vibration Handbook" (Harris and Crede, Editors.) Vol. 3, Chap. 47, McGraw-Hill, New York, 1961.
2. Harley, R. A.: "Impromptu Vibration Data Acquisition With The EL 1-31 Recorder." Institute of Environmental Sciences 13th Annual Technical Meeting Proceedings, Volume 1, April 1967, pp. 83-93.
3. Crede, C. E., and E. J. Lunney: "The Establishment of Vibration and Shock Tests For Airborne Electronics." WADC Technical Report 57-75, Wright Air Development Center, USAF, January 1958.
4. Kamm, A. J.: "Vibration Measurements on The KC-135A Airplane During Ground, Takeoff and Flight Conditions With The J57-P-43W Engines." Boeing Airplane Company Test Report No. T6-1255, 1958.

DISCUSSION

Mr. Wassman (Naval Ordnance Laboratory): How did you compute your transfer function? Was it done digitally or did you use analog equipment? If so it appeared to have very high variance. I was wondering if you had an estimate of how much averaging you had done.

Mr. Pearson: Yes, it was done digitally. I don't know how the averaging was done. Perhaps my co-author could help me on that.

Mr. Thaller: Unfortunately we didn't do enough averaging that's why we did not get as much smoothing. As the number of averages is increased you must decrease the size of your transforms to get that number of averages in the same amount of time. This means that the filter bandwidth increases. Hence you lose accuracy in defining the mode.

Dr. Allen Curtis (Hughes Aircraft): I'm not really sure what transfer function up through the gimbal system really means. The real question here was that the environment for the instrumentation had been predicted using the transfer function for the gimbal system from a math model and this gave some rather horrendous loads. The flight test revealed that because of the impedance effects plus the fact that the excitation was not merely a transmission up through the base, the actual environment was 10's of db below what had been predicted. I really think that the most important thing out of this exercise was a demonstration that, if you use math models, you have to be very careful to have the proper excitation of those math models before you rely too much on what they predict. You have to have some way of accounting for the loading or impedance match between, in this case, the base and where your driving function is. As you were talking you said we have a lot of energy here. If you looked at the ordinate scale, it was down in the 10^{-5} to 10^{-4} range. On most shakers it's pretty hard to control anything below 10^{-3} .

Mr. Pearson: Thank you for your comments. I agree with you that the problem of the direction of the input was a considerable problem. I didn't intend to say that the environment was driving a lot of energy into the equipment during the flight. Quite the contrary, we had a low amount of energy in the vibration modes during flight, lower than expected.

Mr. Gardner (Mechanics Research Incorporated): I was very interested in the comments by the gentlemen from Hughes, because I was also interested in the difficulties with the analytical prediction of the response. The only comparison you showed was not with excitation of the mathematical model, but simply with the mode shapes that were predicted.

I wondered, being primarily an analyst myself, where the problem was. I have rarely seen results that were that bad even for small pieces of hardware. The first response I had in trying to interpret the sketches that you showed was that there are quite a few nonlinearities in the gimbal system and in the hack screw system. Perhaps those were the difficulties. On the other hand the analytical model might have simply been too crude, as it often is in small pieces of hardware like that, to get some of the important interactions. Can you give us any information on that?

Mr. Pearson: Part of the problem was the jack screws and nonlinearities involved, but I don't really feel I can say too much more about the analysis because of the ground rules I was given from SAMSO for this discussion. If you want further information I have a contact at SAMSO that you can talk to. Perhaps he can provide you with more information.

Dr. Curtis: It seems to me that one of the problems we get into in modeling, if you compare flight data, and I don't think it was unique to this case at all, was that we very rarely install anything in anything with one attachment point. If you take a look for instance at the bottom of that sketch showing the accelerometer locations, there were several down at the base. It didn't really matter how far apart those were but there is sort of some general scale like the bigger the equipment the further apart the attachment points are. If you looked at the psd's measured at those various attachment points they are certainly not all identical in level. I certainly didn't attempt to look at the phase, but I think we could probably all agree that they weren't all in phase. With few exceptions when we model things and excite them, if we have several attachment points the common technique is to use a spider which is in effect a infinitely rigid element that joins all the attachment points together. So we put in a perfectly correlated equal amplitude at all attachment points of most any model we drive. Now that is a very severe and unrealistic constraint primarily imposed on us, because (1) we don't know the differences and (2) there aren't many software packages that would allow us to take into account even if we knew what they were. Yet that will drive a system in a much different way than you find out it will actually behave in the airplane. I think that probably accounts for a lot of difference between the reality and modeling. Which attachment point did you select for your transfer function or, perhaps a second part of the question was, did you try doing it from different attachment points to see if you got more or less the same results?

Mr. Pearson: Thank you for your additional comments. I'm glad you were here to add some detail to the talk. We used the worst case we could find on this thing and it turned out to be the forward mounting point of the equipment

and the forward location on the jack screw and floor attachment.

Dr. Curtis: Worst in what sense?

Mr. Pearson: Worst in the highest values of transfer function measurement.

THE USE OF LISSAJOUS FIGURES
IN VIBRATION TESTING

John D. Ray
Department of Mechanical Engineering
Memphis State University
Memphis, Tennessee

and

Charles W. Bert
School of Aerospace, Mechanical and Nuclear Engineering
University of Oklahoma
Norman, Oklahoma

Lissajous figures have been used quite extensively by engineers to study the relationship between two electrical signals. With the advent of electronic instrumentation, the vibration engineer has been using the Lissajous pattern to study the resonant frequencies and phase relationship between two input signals. Introduced in this paper is an extension to the information that can be obtained from the Lissajous pattern. A method is described for obtaining the spring constant and damping factor for a simple harmonically excited, single-degree-of-freedom system and extended to a specific form of non-harmonic excitation. Simple single-degree-of-freedom experimental results for harmonic excitation are presented to exemplify the method described.

INTRODUCTION

Lissajous figures are means of comparing two waves. The waves are introduced at right angles to each other on a common time plane. The resulting figure traced by the combination is referred to as a Lissajous figure. The first formal mention of this type of comparison was made by Julius A. Lissajous in 1857 at the Academy of Science of France. In 1815, Whittaker anticipated this method of wave comparison, but did not formulate his ideas as did Lissajous.

Lissajous did his work without the use of electronics as known today. The method he used was to compare the waves from two tuning forks. The trace was made by mechanical attachments to the tuning forks oriented at right angles to each other. When the forks were excited, the resulting trace was what we know as the Lissajous figure.

Probably the most useful and convenient means today for comparing two waves, using Lissajous figures, is the cathode ray oscilloscope [1]*. The oscilloscope is a device for directing a stream of electrons toward a fluo-

rescent screen within an evacuated tube. When the waves that are to be compared are applied to the plates at right angles, corresponding to the Cartesian axes, x and y , the trace on the screen will be a Lissajous figure. There are other methods for displaying the Lissajous figure such as an x - y automatic plotter or manual plotting. When the x - y plotter is used (manual or automatic), the two signals are introduced on perpendicular axes on a common time basis, and the resulting figures studied. If the frequency of the signals is below 5 to 10 cycles per second (Hz), the method can be effective, but since most of the present-day signals are above this range, the cathode ray oscilloscope is the most popular method for displaying the Lissajous figure.

For some time scientists and engineers have used the Lissajous figure quite extensively for the comparison of two waves. When a standard known signal is applied to one axis of the oscilloscope and the unknown or comparing signal is applied to the other axis, the resulting Lissajous pattern can be used to determine the relative frequency, phase angle, and distortion between the two signals [2], [3], [4].

*The number in brackets indicates the reference at the end of the text.

Electronic engineers make good use of this method, since most of their waves are in the form of electrical signals. In structural dynamic testing, the electrical signals are not as easily obtained. However, since the introduction of more sophisticated instrumentation (transducers and amplifiers), most of the wave forms in the field of data acquisition are in the form of electrical signals. This has made the use of Lissajous figures increasingly popular in vibration testing to determine resonant frequency, relative damping and distortion of vibratory structures.

In vibration testing the known signal is applied to one axis of the oscilloscope; this signal is usually the reference signal coming from the generator that is used to excite the vibrating structure. The unknown or comparing signal is applied to the other axis; this signal is usually the output of a vibration transducer located on the structure. By observing the Lissajous pattern, one can determine the relative phase relationship of the two signals, which information in turn can be used to determine the resonant frequency and relative damping of the structure.

More information can be obtained on the vibrating structure by a closer study of the Lissajous pattern. It is the purpose of this paper to develop some information that can be obtained from the Lissajous pattern in vibration tests. The procedure that is followed is to develop the method analytically, and then to apply the method in a simple experiment on a single-degree-of-freedom system.

TECHNOLOGY

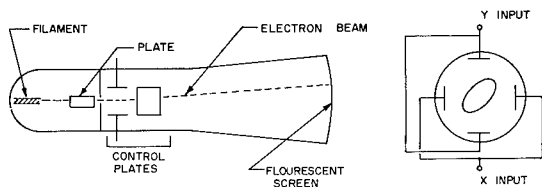


Fig. 1 Oscilloscope setup for displaying Lissajous patterns

An oscilloscope setup for displaying a Lissajous pattern is shown in Figure 1. The equations for the input to the x and y axes are:

$$x = X \sin \omega t \quad (1)$$

$$y = Y \sin (\omega t - \phi) \quad (2)$$

where X and Y are maximum amplitudes of the signals on the oscilloscope screen (these in turn are functions of the input signal voltages, the oscilloscope amplification and characteristics), ω is the frequency of the signals, and ϕ

is the phase difference between the two signals. The shape of the Lissajous figure that will be described on the oscilloscope screen will be in the form of an ellipse. Appendix A gives a formal proof that the combination of the signals described by equations (1) and (2) is an ellipse. For a simplified case, when time (t) is eliminated between equations (1) and (2), the following equation is obtained:

$$y = Y(\sin \omega t \cos \phi - \cos \omega t \sin \phi)$$

$$= Y \left[\frac{x}{X} \cos \phi - \left(1 - \frac{x^2}{X^2} \right)^{\frac{1}{2}} \sin \phi \right]$$

or

$$\frac{x^2}{X^2} + \frac{y^2}{Y^2} = 2 \frac{x^2}{X^2} \cos^2 \phi + \sin^2 \phi - 2 \frac{x}{X} \left(1 - \frac{x^2}{X^2} \right)^{\frac{1}{2}} \sin \phi \cos \phi \quad (3)$$

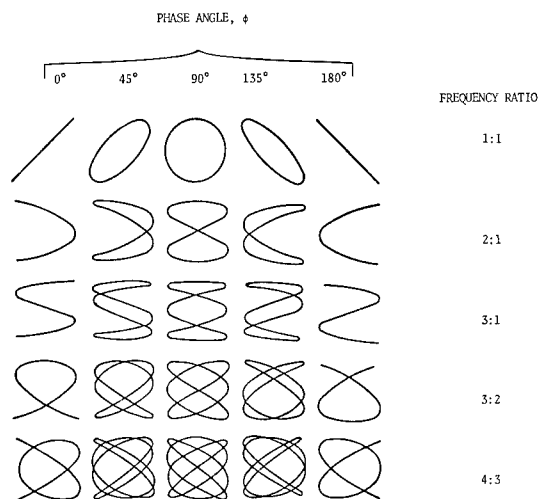


Fig. 2 Lissajous patterns for various frequency ratios and phase angles

This is not the standard form of the equation of an ellipse with its major and minor axes coinciding with the x and y axes. However, since the major and minor axes of the ellipse rotates about the center 0 as the phase angle (ϕ) changes (see Figure 2), a transformation of axes through a rotation angle will give the standard equation of an ellipse. Equation (3) can be quite useful in studying some simple forms of Lissajous figures. The equations simplify further if the input signals have equal amplitudes, $X = Y$. If further, the phase angle, ϕ , is 90° , equation (3) reduces to the equation of a circle (see Figure 3),

$$x^2 + y^2 = c \quad (4)$$

When the phase angle, ϕ , is 0° , equation (3) reduces to a straight line at 45° to the x axis (see Figure 3),

$$x = y$$

(5)

known wave form is a cosine function.

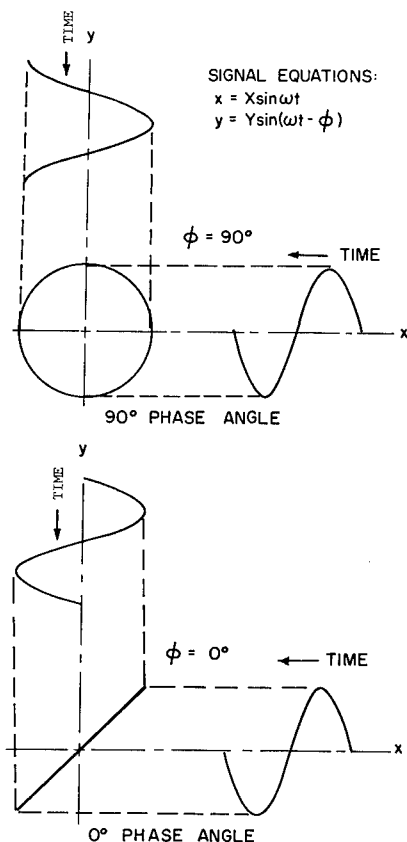


Fig. 3 Lissajous pattern displays for 0 and 90 degree phase angles

The above simple examples are based on the assumption that the amplitudes X and Y are equal. This is the usual case in forming the Lissajous figure on an oscilloscope; however, it is not mandatory. If the amplitudes are not equal, the figure will not be a circle, but will become an ellipse with the major and minor axes lying along the x and y axes. Which axes are major and which are minor will depend on which axis the larger signal is applied.

PHASE RELATIONS

The most frequently and easily used method for obtaining the phase relationship, ϕ , between two single-frequency wave forms using the Lissajous figure is:

$$\sin \phi = P/Q \quad (6)$$

where P is the intersection of the figure with x axis, and Q is the maximum amplitude of the figure as shown in Figure 4. Another method for measuring phase using the Lissajous was advanced by Ward [4]. In his method the areas of the Lissajous patterns that are displayed on the oscilloscope are measured, first when the known signal is a sine function, and then when the

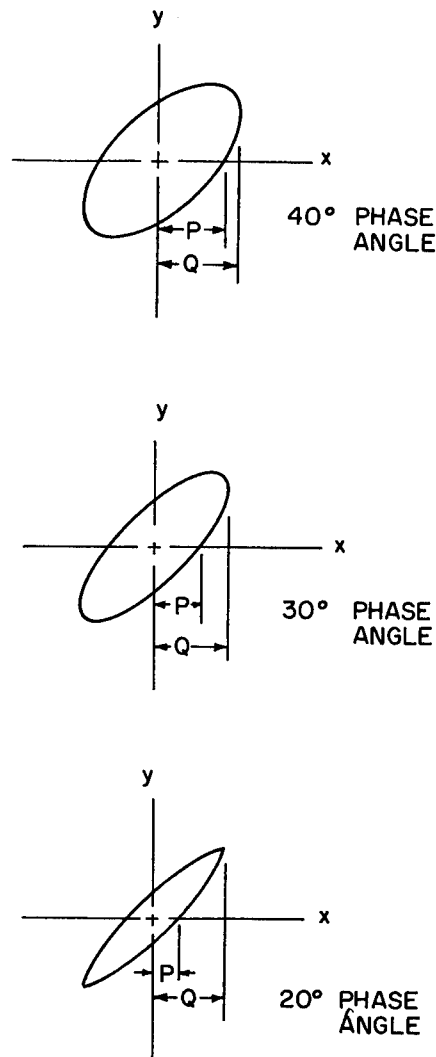


Fig. 4 Lissajous patterns for various phase angles

The relation for the phase angle is

$$\tan \phi = s_1/s_2 \quad (7)$$

where s_1 is the area when the known wave form is the sine function, and s_2 is the area when the cosine function is the known wave form. The proof of this procedure is given in Appendix B.

FREQUENCY RELATIONS

In the cases where the frequencies of the two input waves are different, there will be a multi-pattern Lissajous figure. If a comparison is made of two waves having equal amplitudes but

different frequencies, equations (1) and (2) become:

$$x = X \sin \omega_1 t \quad (8)$$

$$y = Y \sin (\omega_2 t - \phi) \quad (9)$$

If the frequency ratio is an integer (i.e. 1, 2, 3, ..., n), then the complex Lissajous figure will be stationary on the oscilloscope screen. By counting the number of times the Lissajous figure crosses the axis and then subtracting 1 (to account for the end crossing), one can determine the frequency ratio of the two signals. Figure 3 shows some examples of Lissajous patterns for various frequency ratios and phase angles. Reference 5 presents an example where a multi-frequency Lissajous figure was expanded in terms of a Fourier series with Bessel functions as coefficients.

If the ratio is a non-integer, the Lissajous figure will spin about an imaginary space axis. The rate of spinning is the frequency difference between the two input signals [3].

APPLICATION TO VIBRATING SYSTEMS

The Lissajous figure is directly applicable to a vibrating system since there will be a phase relation due to damping between the exciting motion and the system's motion. If the exciting motion and the system motion are measured, and a Lissajous plot of these values is displayed, the pattern can be used to study the structural transfer function, frequency distortion and other characteristics of the system. In the cases discussed in the following section, only a single-degree-of-freedom system is considered; later a multi-degree-of-freedom system is covered, since with modifications most of the single-degree information is applicable to a multi-degree system.

In most present-day vibration tests, the input force is applied to the system by means of an exciter and a reference input transducer is used to monitor the input level. The motion of the system is measured by a vibration transducer mounted on the effective mass. The Lissajous pattern is formed by using the reference input level into the system as the known signal, x , and the system's transducer output as the unknown or complex wave, y .

SINGLE-DEGREE-OF-FREEDOM SYSTEM

In a single-degree system as shown in Figure 5, f denotes the instantaneous input force defined by

$$f = F \sin (\omega t - \phi) \quad (10)$$

and x is the instantaneous displacement defined by

$$x = X \sin \omega t \quad (11)$$

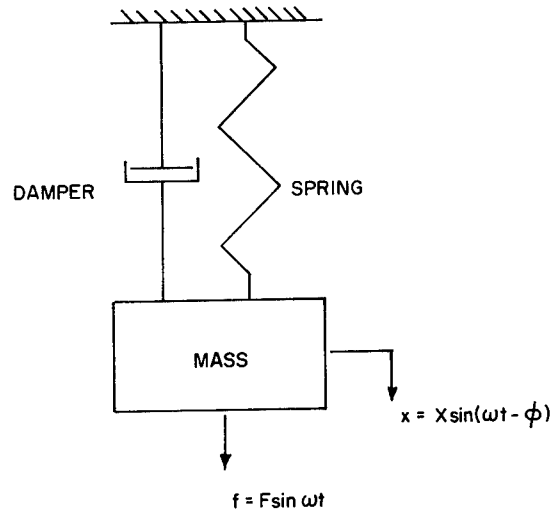


Fig. 5 Schematic of single-degree-of-freedom vibrating system

Assuming constant linear parameters, m , k , and c , independent of time and displacement, the equation of motion is:

$$m\ddot{x} + c\dot{x} + kx = f \quad (12)$$

where m , c , and k are defined in Figure 5, \dot{x} is dx/dt and \ddot{x} is d^2x/dt^2 . Applying the sinusoidal displacement, x , as given by equation (11), to equation (12), the resulting equation becomes

$$f = (-m\omega^2 X + kX) \sin \omega t + c\omega X \cos \omega t \quad (13)$$

As pointed out, the Lissajous figure is a representation of the displacement x applied on one axis and the force f applied on the other axis. The area of the ellipse will be:

$$\text{Area} = \int f dx = \int_0^{2\pi} f \frac{dx}{dt} dt \quad (14)$$

When x is defined by equation (11), $\dot{x} = \omega X \cos \omega t$, and f is defined by equation (13), the area becomes,

$$\begin{aligned} \text{Area} = \int_0^{2\pi} & (-m\omega^2 X + kX) X \sin \omega t \cos \omega t d(\omega t) \\ & + c\omega X^2 \cos^2 \omega t d(\omega t), \end{aligned}$$

$$(\text{Area})_1 = \pi c\omega X^2 \quad (15)$$

If the displacement is shifted by -90° , we obtain:

$$x = -X \cos \omega t, \quad (16)$$

$$\dot{x} = \omega X \sin \omega t \quad (17)$$

and the area becomes:

$$\begin{aligned}
 (\text{Area})_2 &= \int_0^{2\pi} [(-m\omega^2 X + k) X \sin \omega t \\
 &\quad + c\omega X \cos \omega t] X \omega \sin \omega t \, dt \\
 &= \pi(k - m\omega^2) X^2
 \end{aligned} \quad (18)$$

From equation (15), one obtains

$$c = \frac{(\text{Area})_1}{\pi X^2 \omega} \quad (19)$$

and from equation (18)

$$1 - (\omega/\omega_n)^2 = \frac{(\text{Area})_2}{\pi k X^2} \quad (20)$$

or

$$k - m\omega^2 = \frac{(\text{Area})_2}{\pi X^2} \quad (21)$$

Sometimes the above equation of motion is not strictly valid for the system, since some systems will have other than the assumed type of viscous damping. When this occurs, the damping coefficient can be made into an equivalent damping term. By plotting the equivalent damping term as a function of exciting frequency, a constant may be determined that will be a function of some known type of damping. Reference 6 gives the following equivalent viscous damping terms:

For Coulomb damping:

$$c_{eq} = (8/3\pi) X \alpha \omega \quad (22)$$

where α is a constant for Coulomb damping, ω is exciting frequency and X is maximum damper displacement.

For structural damping:

$$c_{eq} = \beta/\pi\omega \quad (23)$$

where β is constant for structural damping.

For friction damping:

$$c_{eq} = (4\alpha)/(\pi\omega X) \quad (24)$$

where α is the frictional force.

Sometimes the case may arise where the equivalent damper is not any of the above but may be a combination of any or all of the damping. By measuring the area of the Lissajous figure when force excitation is applied on one axis and displacement is applied on the other axis, one finds that the area of the figure will be the work done per cycle on the system. By using this value in the following equation, an equivalent viscous damping coefficient can be determined by

$$c_{eq} = \text{Work}/(\pi\omega X^2) \quad (25)$$

where Work is the work done per cycle.

NON-HARMONIC EXCITATION

The Lissajous figure can also be used to analyze a system with non-harmonic excitation motion. The complex motion of the system can be defined by superimposing the various system components in the form of a Fourier series.

$$x = \sum_n a_n \sin(\omega_n t - \phi_n) \quad (26)$$

As seen in Appendix B, n does not necessarily be an integer, but it does have to meet the requirements that

$$\left. \begin{aligned} \omega_i - \omega_k &= \text{integer } (i, k=1, 2, 3, \dots, n) \\ \text{and} \\ \omega_i + \omega_k &= \text{integer.} \end{aligned} \right\} \quad (27)$$

The Lissajous presentation can be used to investigate the wave equation by applying the complex wave to one axis of the oscilloscope and a known wave to the other axis, and analyzing the areas. The Lissajous areas are measured when the known wave is alternately defined by:

$$y = b_m \cos \omega_m t \quad (28)$$

or

$$y = b_m \sin \omega_m t \quad (29)$$

When $m = n$, the Lissajous pattern will become stationary, and the area will be a function of a_n , b_n . However, when the requirements of equation (27) are not met, the areas will also contain other components, and the method can not be used with simplicity.

From Appendix B, equations (B-7), (B-8) and (B-9) give

$$(\text{Area})_s = \pi a_n b_n \sin \phi_n \quad (30)$$

$$(\text{Area})_c = \pi a_n b_n \cos \phi_n$$

and

$$\tan \phi_n = \frac{(\text{Area})_s}{(\text{Area})_c} \quad (31)$$

where $(\text{Area})_s$ is defined as the Lissajous area when the known wave is a sine wave, and $(\text{Area})_c$ when the known wave is a cosine wave. As an example of this procedure for analyzing a complex wave, Figure 6 shows the Lissajous patterns for the form of equation (26):

$$x = a_1 \sin(\omega_1 t - \phi_1) + a_2 \sin(\omega_2 t - \phi_2)$$

The Lissajous patterns were drawn using the following values:

$$\omega_2 = 3\omega_1 ; a_2 = (2/3) a_1 ; \phi_1 = 10^\circ ; \phi_2 = 30^\circ$$

and for equations (28) and (29),

$$b_1 = b_2 = a_1$$

$$y = A \sin(\omega t - 10^\circ) + (2A/3) \sin(3\omega t - 30^\circ)$$

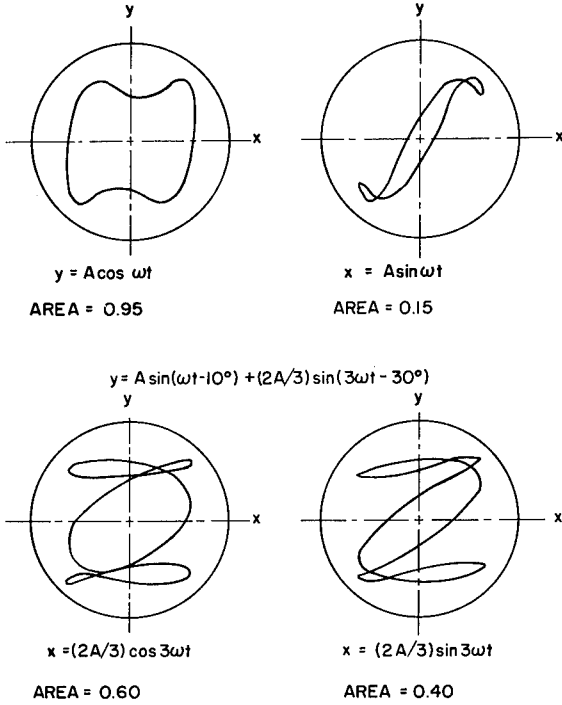


Fig. 6 Lissajous patterns for complex wave as a function of various known waves

Figure 6 shows the areas measured for each figure. Substituting the measured areas into equations (30) and (31), one finds

$$\tan \phi_1 = \frac{0.15}{0.95} = 0.16 \text{ or } \phi_1 = 9^\circ 5'$$

$$\tan \phi_2 = \frac{0.40}{0.60} = 0.667 \text{ or } \phi_2 = 33^\circ 42'$$

$$a_1 = \frac{(\text{Area})_{s_1}}{\pi b_1 \cos \phi_1} = \frac{0.95}{\pi b_1 (0.98)} = \frac{0.97}{\pi b_1}$$

$$a_2 = \frac{(\text{Area})_{s_2}}{\pi b_2 \cos \phi_2} = \frac{0.60}{\pi b_2 (0.83)} = \frac{0.73}{\pi b_2}$$

$$a_1 = 1.3a_2$$

The errors in the values of a_1 , a_2 , ϕ_1 , and ϕ_2 are due to the measuring procedure used for the areas. This method can be applied to a vibrating system, by applying the unknown complex wave to one axis of an oscilloscope and the output from a sine-cosine signal generator to the other axis. When a frequency range of interest is swept on the signal generator, the Lissajous pattern will

become stationary at each frequency component of the equation.

Measuring the areas at each frequency component, one can obtain the parameters a_n and b_n of equation (26) for the complex wave using the equations in Appendix B. A few precautions on using this method for absolute values are: the scale factors for the oscilloscope, transducers, etc., must be maintained; when measuring the areas, always follow the lines of the figure continuously counterclockwise in the same direction. This is important because some areas will be negative.

EXPERIMENTAL STUDY

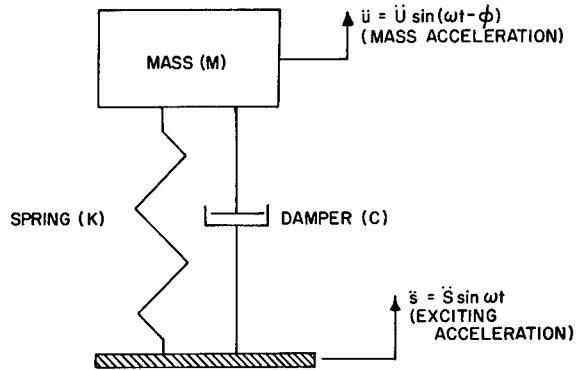


Fig. 7 Schematic of vibrating system used in experimental study

An experimental study was made on a single-degree-of-freedom base-excited system shown schematically in Figure 7. This experiment was to demonstrate the procedure outlined in the previous discussions. The equation of motion for the system shown in Figure 7 is

$$m\ddot{u} + c\dot{y} + ky = 0 \quad (32)$$

where c and k are equivalent values of damping coefficient and spring stiffness that are not functions of displacement y or time t , and m is defined on Figure 7 and previously; $y = u - s$, where from Figure 7,

$$u = U \sin(\omega t - \phi) \quad (33)$$

$$s = S \sin \omega t \quad (34)$$

Equation (32) becomes

$$\ddot{u} = \frac{c}{m} (\dot{s} - \dot{u}) + \frac{k}{m} (s - u); \quad (35)$$

applying equations (33) and (34)

$$u = \frac{c}{m} \omega S \cos \omega t + \frac{k}{m} S \sin \omega t - \frac{c}{m} \omega U \cos(\omega t - \phi) - \frac{k}{m} U \sin(\omega t - \phi) \quad (36)$$

The unknown wave was taken as the motion of the mass, m , and was applied to the vertical axis of the oscilloscope; the known wave was taken as the motion of the base, s , and was applied to the horizontal axis of the oscilloscope.

Using the method described above to obtain a relation between the area of the Lissajous pattern and known parameters, the area becomes:

$$\text{Area} = \int \ddot{u} \frac{ds}{dt} dt \quad (37)$$

$$\text{or Area} = \int_0^{2\pi} \ddot{u} \frac{ds}{d(\omega t)} d(\omega t) \quad (38)$$

When the base motion is described by equation (34), the area becomes

$$\frac{(\text{Area})_1}{\pi S} = \frac{c\omega}{m} (S - U \cos \phi) + \frac{k}{m} U \sin \phi \quad (39)$$

When the base motion is shifted 90° , the area becomes

$$\frac{(\text{Area})_2}{\pi S} = \frac{c\omega}{m} (U \sin \phi) + \frac{k}{m} (S - U \cos \phi) \quad (40)$$

Introducing

$$l = \frac{c\omega}{m}; \quad \omega_n^2 = \frac{k}{m}; \quad A_1 = \frac{(\text{Area})_1}{\pi S}, \quad A_2 = \frac{(\text{Area})_2}{\pi S},$$

one can rewrite equations (39) and (40) as

$$\left. \begin{aligned} A_1 &= l(S - U \cos \phi) + \omega_n^2 (U \sin \phi) \\ A_2 &= -l(U \sin \phi) + \omega_n^2 (S - U \cos \phi) \end{aligned} \right\} \quad (41)$$

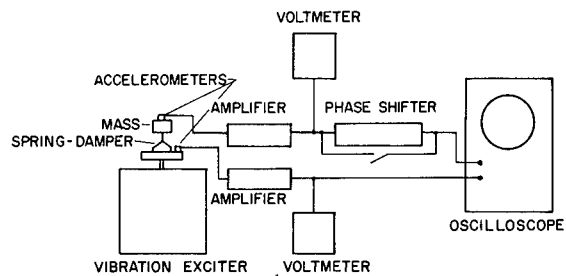
The experimental setup used to study the equations is shown schematically in Figure 8. The outputs from the two accelerometers, one located on the mass and one located on the base, were applied to the axes of the oscilloscope through matching amplifiers.

For the quadrature area, a 90° -phase-shifting network was introduced into the signal from the mass accelerometer before going into the oscilloscope.

The areas were measured, with and without the phase shift, by taking pictures of the patterns and measuring the areas from the pictures. These areas were converted to absolute values by applying the appropriate scale factors for the transducers, amplifiers, and oscilloscope. The phase angle between the two input signals was also measured from the Lissajous patterns.

The values for the maximum displacements of the mass (U) and the base (S) were obtained from the accelerometer outputs.

The Lissajous pictures were taken at excitation frequencies of 32, 50, and 60 cycles



EXCITER:	MB C-1D Electrodynamic Vibration Exciter
ACCELEROMETERS:	Endevco Model 2217, Serial No. JA08 (Mass) and Serial No. FA73 (Base)
AMPLIFIERS:	Endevco Model 2607, Serial No. FA45 (Mass) and Serial No. FA48 (Base)
VOLTMETERS:	EICO Model 250, Serial No. 4215 (Mass) and Serial No. 4213 (Base)
PHASE SHIFTER:	-90° , 1:1 Amplification, L-C Network
OSCILLOSCOPE:	Tektronix Model 503, with Series 125 Camera Attachment

Fig. 8 Schematic of experimental setup and instrumentation

per seconds (Hz). These frequencies were selected at random and were used only to demonstrate the procedure. The undamped natural frequency of the system as determined from the manufacturer's data on the spring-damper was set at approximately 28 Hz. by applying a weight of 2.84 pounds.

Copies of the observed Lissajous patterns during the test are shown in Figure 9. From these copies the phase angle, ϕ , the maximum amplitudes, S and U , and the areas were measured to be used in the calculation for the equivalent spring stiffness, k , and damping factor, c . Once the values were measured they were applied to equations (41), which gave two equations with two unknowns.

Table I summarizes the results of measured and calculated values. As can be seen from this table, the value of spring stiffness as applied to the linearized equations of motion was a function of exciting frequency, but the damping coefficient was independent of frequency. The spring stiffness, as used in the equation of motion, equation (32), could be considered as a frequency-dependent effective spring stiffness. A plot of the values of k , k/ω and c , as used in equation (32), is shown in Figure 10 along with the manufacturer's values. Since k/ω remains independent of amplitude (and thus of frequency), equation (32) can be rewritten as follows:

$$m\ddot{u} + c\dot{y} + (k/\omega)y = 0$$

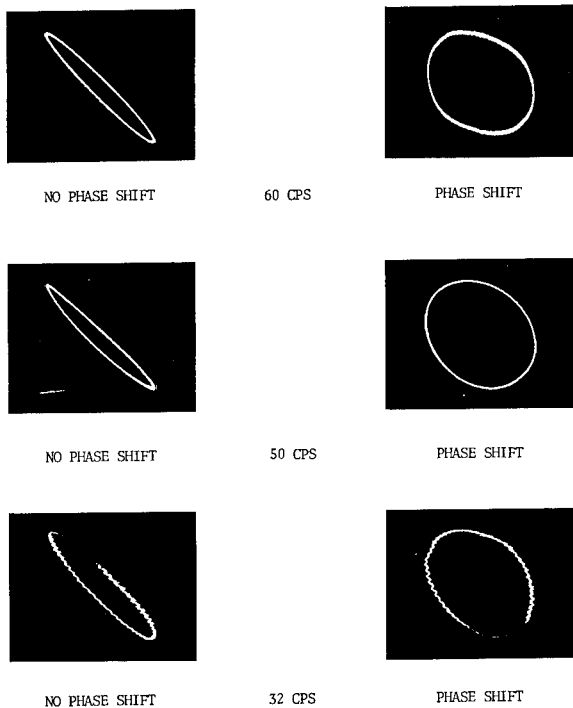


Fig. 9 Lissajous pattern photographs from oscilloscope camera during experiments

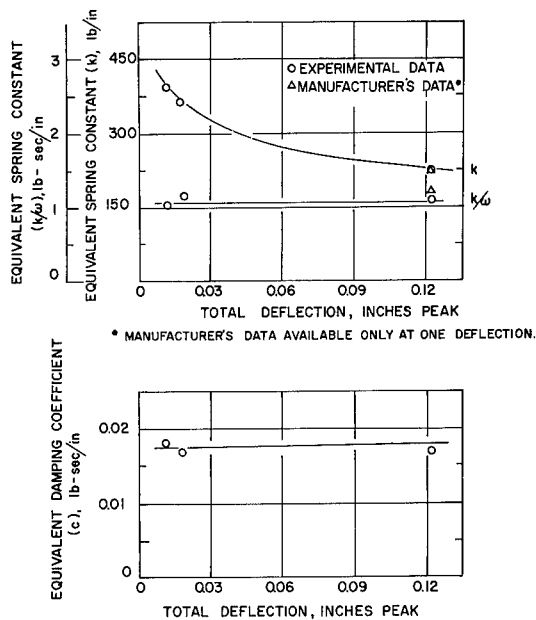


Fig. 10 Spring stiffness and equivalent damping coefficient from experiments

CONCLUSIONS

Although Lissajous patterns have been used for some time to measure the relative phase angle and frequency ratio between two electrical signals, they have not been used to any great extent by vibration engineers for measuring system parameters. The Lissajous figure can be used to obtain extensive information on a vibrating structure when a sine and cosine are alternately applied to one axis of the oscilloscope; proportional values can be obtained for the quadrature and in-phase components of an unknown wave form. The Lissajous is readily adaptable to a linear single-degree-of-freedom system to obtain an equivalent spring stiffness and damping coefficient, and in special cases can be applied to non-harmonic excited systems. An example of non-harmonic excitation would be random excitation. There are many more cases that could be examined such as multi-degree-of-freedom systems with and without harmonic excitation and further non-linear systems.

REFERENCES

1. W.A. Marrison, "Electrical Measurements, Frequency Measurements", Section 11 in Electrical Engineering Handbook, 4th Ed., Vol. 2, Electrical Communications and Electronics, H. Pender and K. McIlwain, editors, John Wiley and Sons, Inc., New York, 1950.
2. W. DuBois, "Structural Vibration--an Oscilloscope Tells the Story in Pictures", Product Engineering, Vol. 30, No. 5, pp. 52-53, Feb. 2, 1959.
3. Tien-Wei Chu, "Determination of Harmonics from Lissajous Figures", Master's thesis, Department of Electrical Engineering, West Virginia University, Morgantown, W. Va., 1959.
4. T.L. Ward, "How to Measure Phase Angle During Distortion and Noise", Control Engineering, Vol. 13, No. 2, pp. 57-59, Feb. 1966.
5. F.E. Relton, Applied Bessel Functions, Dover Publications, Inc., New York, 1965, p. 159.
6. W.T. Thomson, Vibration Theory and Applications, Prentice-Hall, Inc., Englewood Cliffs, N.J., 1965, pp. 70-73.

Table I. Experimental Results

TEST	1	2	3
Frequency (Hz)	32	50	60
Mass Acceleration (in/sec ²)	3971.2	1360.9	713.7
Base Acceleration (in/sec ²)	1037.7	1190.0	992.0
Mass Displacement (in) S.A.	0.098	0.014	0.005
Base Displacement (in) S.A.	0.026	0.012	0.007
Measured Area #1, (Area) ₁	0.14	0.095	0.075
Measured Area #2, (Area) ₂	0.30	0.325	0.31
Phase Angle, ϕ , (degrees)	170.5	177.8	178.0
Total Deflection (in) S.A.	0.122	0.016	0.012
Equivalent Stiffness, k/ω (lb-sec/in)	1.10	1.16	1.05
Equivalent Damping (lb-sec/in)	0.018	0.018	0.016
Calibration for Base Accelerometer		253 mv/pg	
Calibration for Mass Accelerometer		86.5 mv/pg	

APPENDIX A

FORMAL PROOF THAT A COMBINATION OF TWO SIGNALS OF SAME FREQUENCY AND DIFFERING PHASE YIELD AN ELLIPTICAL LISSAJOUS FIGURE.

To be proved: A plot of the equations

$$x = A \cos \theta, \quad (A-1)$$

and

$$y = B \sin (\theta - \Psi) \quad (A-2)$$

is an equation of a general ellipse.

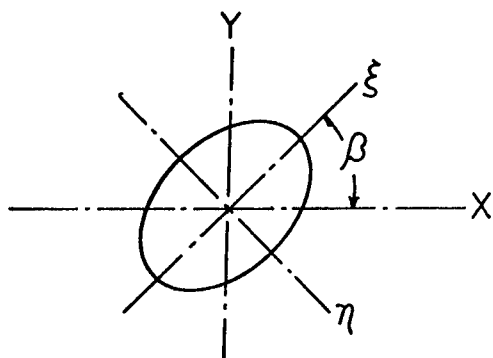


Fig. 11 Elliptic Lissajous figure

Proof: Introducing a new angle

$$\phi = \theta + \alpha, \quad (A-3)$$

where α is a constant angle;

from Figure 11,

$$\xi = x \cos \beta + y \sin \beta \quad (A-4)$$

$$\eta = -x \sin \beta + y \cos \beta \quad (A-5)$$

Substituting equations (A-1) and (A-2) into equation (A-4), one obtains

$$\xi = A \cos \theta \cos \beta + B \cos (\theta - \Psi) \sin \beta \quad (A-6)$$

and substituting equation (A-3) into equation (A-6), one finds

$$\begin{aligned} \xi &= A \cos (\theta - \alpha) \cos \beta + B \sin \beta \cos (\theta - \Psi) \\ &= A \cos \beta [\cos \phi \cos \alpha + \sin \alpha] + \\ &\quad B \sin \beta [\cos (\alpha + \Psi) \cos \phi + \sin (\alpha + \Psi) \sin \phi] \\ &= A \cos \beta \cos \alpha \cos \phi + A \cos \beta \sin \alpha \sin \phi + \\ &\quad B \sin \beta \cos (\alpha + \Psi) \cos \phi \\ &\quad + B \sin \beta \sin (\alpha + \Psi) \sin \phi \end{aligned}$$

When α and β satisfy this equation,

$$[A \cos \beta \sin \alpha + B \sin \beta \sin (\alpha + \Psi)] = 0 \quad (A-7)$$

Therefore;

$$\xi = \cos \phi [A \cos \beta \cos \alpha + B \sin \beta \cos (\alpha + \psi)] \quad (\text{A-8})$$

If the same analysis is applied to equation (A-5)

$$\eta = [-A \sin \beta \sin \alpha + B \cos \beta \sin (\alpha + \psi)] \sin \phi \quad (\text{A-9})$$

When

$$-A \sin \beta \cos \alpha + B \cos (\alpha + \psi) = 0 \quad (\text{A-10})$$

To determine the values of α and β , the solution of equations (A-7) and (A-10) becomes:

$$\tan \beta = \frac{-A \sin \alpha}{B \sin (\alpha + \psi)} = \frac{B \cos (\alpha + \psi)}{A \cos \alpha} \quad (\text{A-11})$$

and

$$\tan 2\alpha = \frac{\sin 2\alpha}{\cos 2\alpha} = \frac{-B^2 \sin 2\psi}{A^2 + B^2 \cos 2\psi} \quad (\text{A-12})$$

Multiplying equation (A-7) through by

$$(\cos \beta) / (\sin \beta)$$

and simplifying, one obtains

$$B \cos \beta \sin (\alpha + \psi) = \frac{-A \cos^2 \beta}{\sin \beta} \sin \alpha \quad (\text{A-13})$$

Using equation (A-10) and multiplying by $(\sin \beta) / (\cos \beta)$ and simplifying, one finds

$$B \sin \beta \cos (\alpha + \psi) = A \frac{\sin^2 \beta}{\cos \beta} \cos \alpha \quad (\text{A-14})$$

Substituting equation (A-14) into equation (A-8),

$$\xi = \cos \phi [A \cos \beta \cos \alpha + A \frac{\sin^2 \beta}{\cos \beta} \cos \alpha]$$

This equation simplifies to:

$$\xi = A \frac{\cos \alpha \cos \phi}{\cos \beta} \quad (\text{A-15})$$

Letting $\lambda = A \frac{\cos \alpha}{\cos \beta}$, we can reduce equation (A-15) to

$$\xi = \lambda \cos \phi \quad (\text{A-16})$$

Substituting equation (A-13) into equation (A-9), one obtains

$$\eta = \sin \phi (-A \sin \beta \sin \alpha - A \frac{\cos^2 \beta}{\sin \beta} \sin \alpha)$$

Which simplifies to,

$$\eta = \frac{-A \sin \alpha}{\sin \beta} \sin \phi \quad (\text{A-17})$$

Letting

$$\mu = -A \frac{\sin \alpha}{\sin \beta} \quad (\text{A-18})$$

equation (A-17) becomes

$$\eta = \mu \sin \phi \quad (\text{A-19})$$

Squaring equations (A-16) and (A-19) and adding

$$\frac{\xi^2}{\lambda^2} + \frac{\eta^2}{\mu^2} = \cos^2 \phi + \sin^2 \phi$$

or

$$\frac{\xi^2}{\lambda^2} + \frac{\eta^2}{\mu^2} = 1 \quad (\text{A-20})$$

This is the general equation for an ellipse. Q.E.D.

APPENDIX B

The area of the Lissajous figure is

$$s = \int_c y \, dx = \int_c y \frac{dx}{dt} \, dt \quad (\text{B-1})$$

where s = area of the figure, c = integrating curve, x = instantaneous displacement along the x axis, y = instantaneous displacement of the signal along the y axis.

The complex wave is described by superimposing the various frequency components and phase relations:

$$y = a_1 \sin(\omega_1 t - \phi_1) + a_2 \sin(\omega_2 t - \phi_2) + \dots + a_n \sin(\omega_n t - \phi_n) \quad (\text{B-2})$$

When a sine wave is applied along the y axis, then

$$x = b_1 \sin \omega_1 t$$

or

$$dx = b_1 \cos \omega_1 t \, d(\omega_1 t) \quad (\text{B-3})$$

Rewriting equation (B-2) using a trigonometric identity,

$$y = a_1 [\sin \omega_1 t \cos \phi_1 - \cos \omega_1 t \sin \phi_1] + a_2 [\sin \omega_2 t \cos \phi_2 - \cos \omega_2 t \sin \phi_2] + \dots + a_n [\sin \omega_n t \cos \phi_n - \cos \omega_n t \sin \phi_n] \quad (\text{B-4})$$

Substituting equations (B-3) and (B-4) into equation (B-1) and integrating over a period, one obtains the following area expression:

$$s_1 = \int_0^{2\pi} a_1 b_1 \cos \phi_1 (\sin \omega_1 t \cos \omega_1 t) \, d(\omega_1 t) - \int_0^{2\pi} a_1 b_1 \sin \phi_1 (\cos \omega_1 t \cos \omega_1 t) \, d(\omega_1 t) + \int_0^{2\pi} a_2 b_1 \cos \phi_2 (\sin \omega_2 t \cos \omega_1 t) \, d(\omega_1 t)$$

$$\begin{aligned}
& - \int_0^{2\pi} a_2 b_i \sin \phi_2 (\cos \omega_2 t \cos \omega_i t) d(\omega_i t) + \dots \\
& + \int_0^{2\pi} a_n b_i \cos \phi_n (\sin \omega_n t \cos \omega_i t) d(\omega_i t) \\
& - \int_0^{2\pi} a_n b_i \sin \phi_n (\cos \omega_n t \cos \omega_i t) d(\omega_i t)
\end{aligned}
\tag{B-5}$$

For the case when the signal applied along the y axis is

$$x = b_i \cos \omega_i t,$$

and

$$\frac{dx}{dt} = -b_i \sin \omega_i t,$$

the area becomes,

$$\begin{aligned}
s_2 = & - \int_0^{2\pi} a_1 b_i \cos \phi_1 (\sin \omega_1 t \sin \omega_i t) d(\omega_i t) \\
& + \int_0^{2\pi} a_1 b_i \sin \phi_1 (\cos \omega_1 t \sin \omega_i t) d(\omega_i t) \\
& - \int_0^{2\pi} a_2 b_i \cos \phi_2 (\sin \omega_2 t \sin \omega_i t) d(\omega_i t) \\
& + \int_0^{2\pi} a_2 b_i \sin \phi_2 (\cos \omega_2 t \sin \omega_i t) d(\omega_i t) + \dots \\
& - \int_0^{2\pi} a_n b_i \cos \phi_n (\sin \omega_n t \sin \omega_i t) d(\omega_i t) \\
& + \int_0^{2\pi} a_n b_i \sin \phi_n (\cos \omega_n t \sin \omega_i t) d(\omega_i t).
\end{aligned}
\tag{B-6}$$

Considering the integrals of equations (B-5) and (B-6) when n and i are integers, one finds that then all the terms are zero except the (n,n) terms and equations (B-5) and (B-6) reduce to:

$$\begin{aligned}
s_1 &= - \int_0^{2\pi} a_n b_n \sin \phi_n (\cos \omega_n t) d(\omega_n t) \\
&= -\pi a_n b_n \sin \phi_n
\end{aligned}
\tag{B-7}$$

and

$$s_2 = \pi a_n b_n \cos \phi_n. \tag{B-8}$$

Dividing equation (B-8) by equation (B-7), we get

$$\tan \phi_n = s_1/s_2 \tag{B-9}$$

There are some cases when n and i are not integers that will make all the cross-product terms equal to zero. These cases are when the

combination of $(n - i) = \text{integer}$, and $(n + i) = \text{integer}$.

As an example of this is when n and i are half integers, for instance, when $n + i = 3/2$, then $i = 1/2$, $n - i = 1$, and $n + i = 2$.

STRUCTURAL DYNAMIC RESPONSE ANALYSIS OF ROCKET TEST SLEDS*

Terry N. Gardner
Mechanics Research, Inc.
Los Angeles, California 90045

The structural dynamic response of dual rail and monorail rocket sleds is investigated, first by study of a limited amount of test data and then by a specially developed computer simulation. It is found that the principal source of excitation is rail roughness interacting with the gap between the slippers and the rail. Amplification is caused by rough burning of on-board motors and by unsteady aerodynamics. A simple parameter is identified for predicting maximum slipper forces in dual rail sleds and the nonlinear computer simulation is shown to be reliable for internal loads prediction for all sleds.

FOREWARD

The work reported in this paper was performed under the sponsorship of the Air Force Special Weapons Center's 6585th Test Group, Holloman Air Force Base, New Mexico. The Air Force project engineer, Dr. L. C. Mixon, substantially assisted the effort through his guidance and direction.

INTRODUCTION

The Air Force Special Weapons Center's 6585th Test Group runs a variety of test sleds over the 50,000-foot track at Holloman Air Force Base, New Mexico. Dual rail sleds run at speeds between Mach .4 and Mach 2.5 and weigh up to 30,000 pounds. Depending on trajectory requirements, they may be arranged in trains with as many as three stages. Monorail sleds generally weigh less than 1,000 pounds and have approached Mach 9.0.

Over the years, the structural design of sleds has been a success in that, excepting instances where high temperatures caused material degradation, structural failures have been very rare. Implicit in this success, however, is the possibility that the design criteria have been overly conservative. Since structure often comprises the major portion of the sled weight,

reduction of structural weight without loss of integrity offers a significant payoff in sled performance. This is especially true for high speed sleds which are designed primarily to dynamic response loads.

Current design practice calls for the combination of quasi-steady and dynamic loads. Quasi-steady loads are comprised of thrust, acceleration, weight, and aerodynamic forces. Experience and wind tunnel testing has led to fairly high reliability in prediction of these forces. Dynamic loads are accounted for by a multiplication factor applied to the dead-weight load distribution. The multiplication factor employed is specified as a function of the maximum velocity at which the sled is to be operated.

A number of studies has been performed (References [1]-[6]) into the nature and causes of dynamic excitation of sleds. Although several of the studies have shown perceptive analytical approaches, there have been insufficient substantiating data to permit their extension to a reliable design procedure. Data acquired recently at the Holloman test track offered the promise of fresh interpretation leading to a reliable method for more accurate prediction of design dynamic loads. Study of the data and development of new design

* This work was supported by Contract F29601-72-A-0113-006 for the Air Force Special Weapons Center, Kirtland AFB, New Mexico

procedures was undertaken by MRI under the sponsorship of the Air Force. Results of that work are reported in Reference [7] and summarized in this paper.

INTERPRETATION OF SLED TEST DATA

Two categories of data were available during the study. The first was a result of a survey made of a 400-foot section of the Holloman test track. Height measurements were taken every ten inches. A portion of the data is shown in Figure 1. A least-square-fit straight line was drawn through the data to remove the average height and slope. What remains is the rail roughness having peaks of about .030 inches. A spectral analysis of the data failed to reveal any significant frequency content.

The second category of data comprises strain gage measurements taken from the slipper support structure of various sleds. A sample of such data for a dual rail sled is shown in Figure 2. The four traces are strain gage measurements calibrated as vertical force acting on each of the four slippers. The subject of this test was a sled called the "Single Mod." The Single Mod is a pusher sled, that is, it is used to boost a forebody. It consists simply of a propellant tank mounted on two transverse slipper beams. Propulsion comes from an Aerojet AJ60 liquid engine which develops 150,000 pounds of thrust. The width of the sled between slippers is 84 inches; the length between slipper beams is 240 inches. At the time the data in Figure 2 was taken, the sled was travelling at maximum velocity of 1,762 fps and weighed 9,400 pounds. The high amplitude oscillations at the center were determined to result from engine burn-out transient forces associated with nozzle flow instabilities. The oscillations occurring subsequent to the engine burn-out were due to rail roughness. In addition to these excitation sources, rail roughness and rough engine burning, analyses of other data showed that oscillating aerodynamic loads are also a source of dynamic excitation when a dual rail sled accelerates through the transonic velocity range. Unfortunately, there are no data which measure directly the engine forces or the aerodynamic pressures acting on the sled.

It should be noted here the nonlinear nature of the dynamic phenomenon being observed. Sleds ride the rails on steel slippers with replaceable liners. Reasonable life of the liners requires that a gap be left between them and the rail surface. A standard value of .125 inches is used for all size sleds. The variation in natural frequency observed in Figure 2 is attributable to the presence of this gap. It is a predictable function of peak amplitude, as shown in Figure 3 where a curve was developed for the characteristics of the Single Mod sled. This phenomenon is commonly associated with the simple harmonic oscillator having a gap.

Data from two other dual rail sleds (one of which is shown in Figure 4) were similarly examined. More or less fortuitously, a parameter was found that correlates linearly with peak slipper forces. The parameter, designated a Sled Impact Parameter (SIMP), contains only physical parameters of the sled. SIMP, and its associated correlation with the peak slipper forces, are shown in Figure 5. Peak dynamic forces measured during coast are due to rail roughness alone. Those taken during the thrust period include the excitation of rough engine burning.

Monorail sleds, by comparison with dual rail sleds, are lighter, faster, travelling at least twice the speed, and perhaps most importantly from the structural dynamics viewpoint, a great deal stiffer. Whereas the slippers of dual rail sleds are in contact with the rails most of the time, monorail sleds spend most of their time flying in the gap. Contacts with the rail are brief and severe impacts. Furthermore, whereas dual rail sleds bounce almost exclusively in the vertical plane, monorail sleds have a significant component of roll motion.

The modular monorail sled shown in Figure 6 weighs 616 pounds and measured 62.2 inches between its slippers. During one run it reached a velocity of 3,500 fps. During that run, vertical force measurements were taken from a force transducer mounted above the forward slipper. A sample of those data is shown in Figure 7. Because of the high frequency nature of the force history, it is more meaningful to consider the average value of peaks at various velocities rather than individual peak values. By this method it was possible to construct the graph of Figure 8. Again, it is seen that the presence of an on-board thruster increases the amplitude of the slipper forces. The dependence of the forces on velocity seems to result, at least partially, from the increased aerodynamic lift associated with higher velocity.

DEVELOPMENT OF A MATHEMATICAL SIMULATION

Study of the test track data seemed to indicate that rail roughness is the principal source of sled dynamic excitation. Although rough engine burning and unsteady aerodynamics seem to contribute also, there are no direct data by which these sources can be quantified. Given the availability of a rail profile, the philosophy was adopted that if a mathematical simulation would successfully predict dynamic response to rail roughness excitation, design factors could be added to account for the other sources. Since linear, finite-element computer codes are already widely used in sled design, it was necessary that the dynamic response analysis method to be developed would be compatible. The presence of the slipper gap precluded the direct application of such linear methods as modal response, random and frequency domain analyses. Time domain simulation was selected as the only reliable approach.

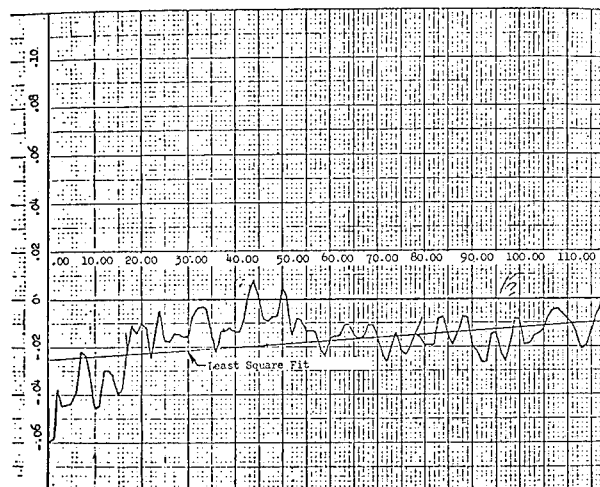


FIGURE 1. SECTION OF SAMPLE RAIL HEIGHT MEASUREMENTS
(BOTH SCALES INCHES)

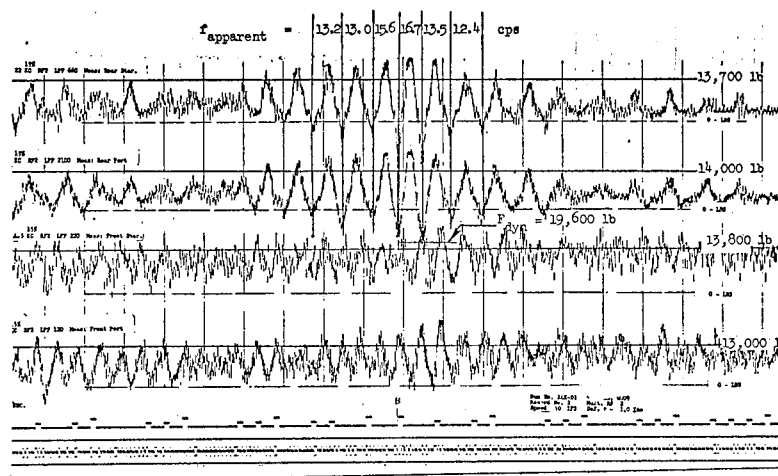


FIGURE 2. SINGLE MOD SLED, SLIPPER FORCE MEASUREMENTS
AT BURNOUT, RUN 24X-D1

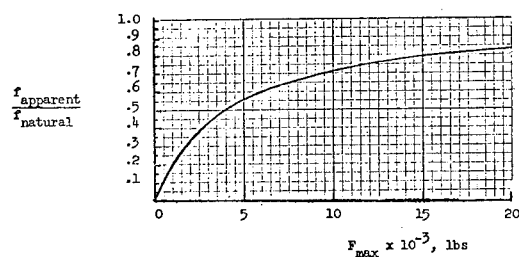


FIGURE 3. EFFECT OF SLIPPER GAP ON SINGLE MOD
SLED APPARENT NATURAL FREQUENCY

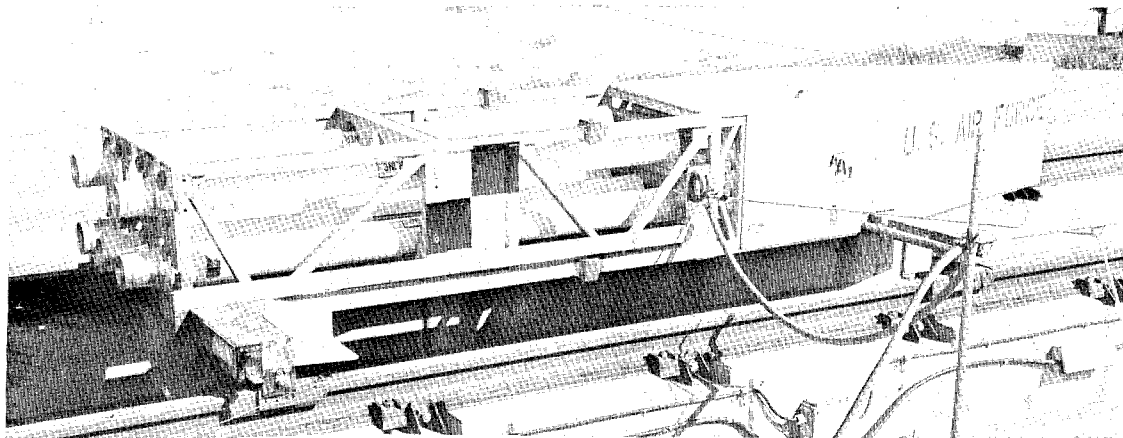


FIGURE 4. GNU (6208) DUAL RAIL SLED

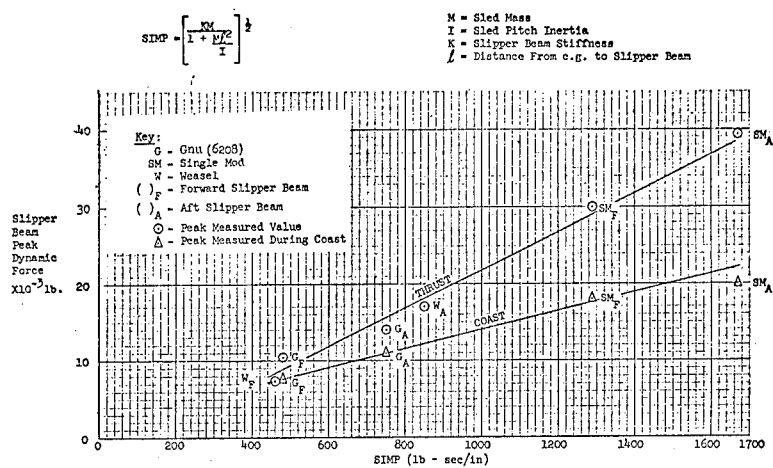


FIGURE 5. DUAL RAIL TEST TRACK DATA VS. SIMP

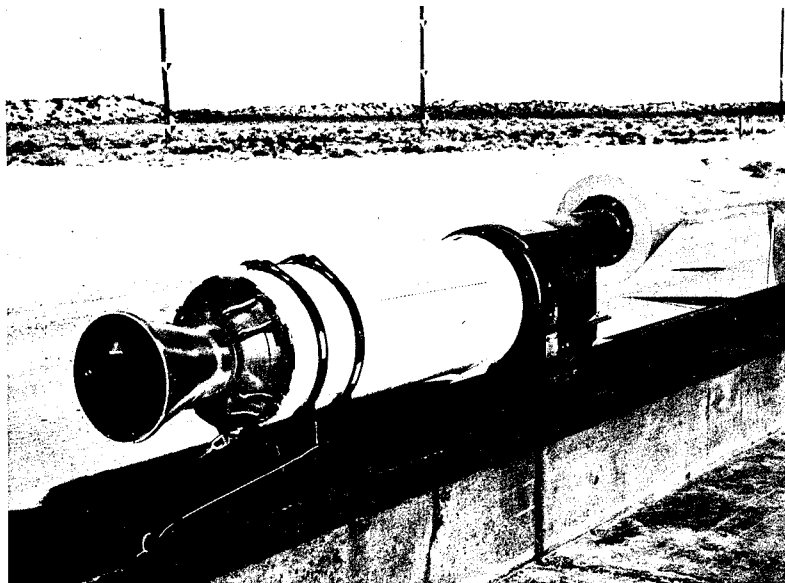


FIGURE 6. MODULAR MONORAIL SLED

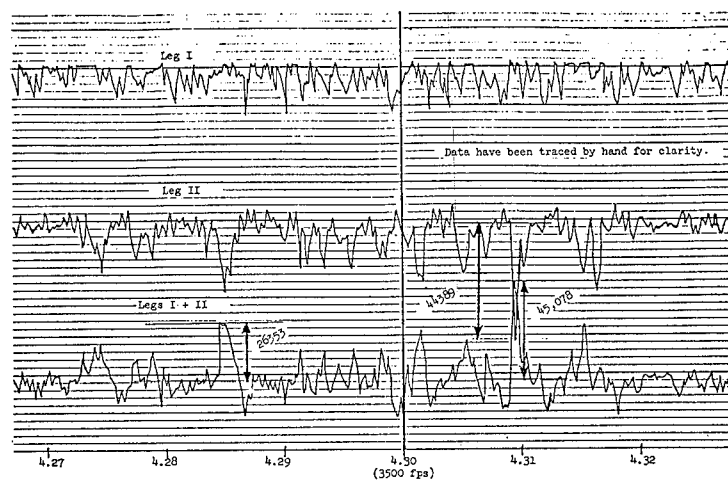


FIGURE 7. MODULAR MONORAIL, 53X-B2, FRONT SLIPPER FORCE MEASUREMENTS AT BURNOUT

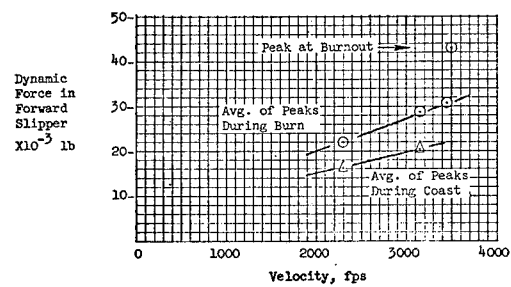


FIGURE 8. MODULAR MONORAIL, 53X-B2, MEASURED FORWARD SLIPPER DYNAMIC FORCES

Since time simulations would require longer stretches of track than the 400 feet of data which were available, a random generation scheme was developed. The 400-foot sample was broken into ten pieces, each having zero height for the first and last values. A random integer generator is employed to produce a sequence, and the corresponding segments of track are laid one after the other until there is enough track for the simulation.

Lumped parameter representations of sleds are rather complex. It is not economically feasible to integrate in time the entire set of equations of motion associated with the lumped mass model. Such a difficulty is usually solved through the use of the modal method. In fact, even in the related problem of recontact during staging of rocket launch vehicles, the modal method is employed. In that case, three sets of modes must be used; one set each for the two stages and one set for the combined vehicle. At each separation or recontact a new set of modes must be initialized. This is obviously not a practical solution when the contacts are as frequent as the sled impacting the rail.

The method adopted for analysis of sleds involves the assumption that there is a portion of the sled structure, immediately adjacent to each slipper, which can be considered a one-dimensional, weightless spring. The four such springs are designated the slipper springs and the points at which they attach to the sled become restraint points for a set of displacement functions which define the deformation of the rest of the sled structure. The essential feature is that the structure bounded by restraint points is linear and can now be condensed in representation to a set of normal modes of vibration.

The front view of a dual rail sled showing the placement of the restraints is shown in Figure 9. Figure 10 illustrates the resulting mode shapes and, in addition, shows the two rigid body modes which are added. Since it is only the rigid body modes which contain motion at the points of attachment of the springs, only they are involved in the nonlinear interaction with the rail.

Development of Simulation Equations

The motion of the sled in the vertical direction is defined as the sum of a set of displacement functions. The first two of these are a pure vertical translation (z) and a rotation of the rigid sled about its cg (θ). The rest of the set is comprised of the normal modes of vibration (orthogonal to each other but not to the rigid body functions) of the sled restrained against translation at the slipper support points. So the vertical displacement, w , of the sled, at time t and station x along its longitudinal axis is:

$$w(x,t) = z + (x - x_{cg}) \theta + \sum_i \varphi_i(x) q_i(t) \quad (1)$$

The $\varphi_i(x)$ are the normal modes of the sled pinned at the slipper supports and $q_i(t)$ are their instantaneous amplitudes.

We will, for the moment, ignore the stiffness of the slippers (and the associated nonlinear gap effect) while we derive the equations of motion. We start with Lagrange's equation:

$$\frac{d}{dt} \left(\frac{\partial T}{\partial \dot{\eta}_i} \right) + \frac{\partial U}{\partial \eta_i} - \frac{\partial W}{\partial \eta_i} = 0 \quad (2)$$

where T , U and W are the kinetic energy, the strain energy and the work. The η_i are the independent variables of motion which in this case include z , θ , and the q_i .

At this point we must more fully define the structure. In fact, since the structure of the sled will be idealized as a finite-element model, we convert our symbology to that of lumped parameter systems.

In matrix notation, Equation (1) becomes:

$$\{w\} = \{1.0\} z + \begin{Bmatrix} x_j \\ \vdots \\ x_{cg} \end{Bmatrix} \theta + \sum_i \{\varphi_i\} q_i \quad (3)$$

The kinetic energy is:

$$T = \frac{1}{2} \langle \dot{w} \rangle [m] \{\dot{w}\} \quad (4)$$

We substitute Equation (3) into (4)

$$T = \frac{1}{2} \langle \dot{\eta} \rangle [M] \{\dot{\eta}\} \quad (5)$$

Where we have defined

$$\eta = \begin{Bmatrix} z \\ \theta \\ q_1 \\ \vdots \\ q_i \end{Bmatrix}$$

We will make some observations about the elements of $[M]$

$M_{11} = m$, the mass of the sled

$M_{22} = I$, the pitch inertia of the sled

$M_{12} = M_{21} = 0$

because we took the rotation about the sled cg.

$$M_{1i} = M_{i1} = \langle 1.0 \rangle [m] \{\varphi_i^n\} \quad i > 2$$

$$= \sum_j m_j \varphi_j^n \quad n = i - 2$$

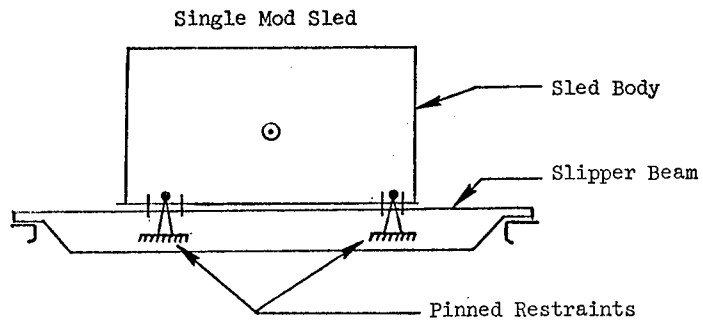
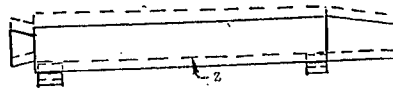
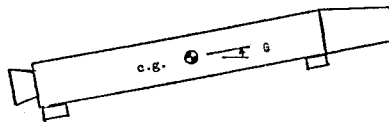


FIGURE 9. RESTRAINTS APPLIED TO DUAL RAIL SLED FOR CALCULATION OF SLEDYNE MODES

Rigid
Translation



Rigid
Rotation
About c.g.



Vibration
Modes of
Pinned-Pinned
Sled Structure

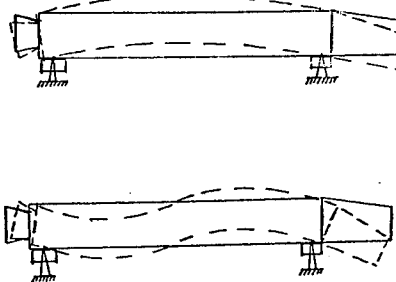


FIGURE 10. DISPLACEMENT FUNCTIONS USED IN NONLINEAR DYNAMIC RESPONSE SIMULATION

Where m_j is the lumped mass at the j th node and φ_j^n is the vertical deflection at that node in the n th mode.

$$M_{2i} = M_{i2} = \langle \dots x_j - x_{cg} \dots \rangle [\varphi_j^n] \quad i > 2$$

$$= \sum_j (x_j - x_{cg}) m_j \varphi_j^n \quad n = i - 2$$

$$M_{ii} = \sum_j m_j (\varphi_j^n)^2 \quad i > 2, n = i - 2$$

is the generalized mass of the n th mode.

$$M_{ij} = 0 \quad i \neq j; i, j > 2$$

because of the orthogonality of the modes.

The strain energy

$$U = \frac{1}{2} \langle w \rangle [k] \{w\} \quad (6)$$

where $[k]$ is the sled's stiffness matrix. Substituting Equation (3)

$$U = \frac{1}{2} \langle \eta \rangle [K] \{\eta\}$$

Due to the absence of strain energy in the rigid body functions and the orthogonality of the modes:

$$K_{11} = K_{22} = 0$$

$$K_{ij} = K_{ji} = 0 \quad i \neq j$$

$$K_{ii} = \langle \varphi^n \rangle [k] \{\varphi^n\} \quad i > 2, n = i - 2$$

$$= M_{ii} \omega_n^2$$

where ω_n is the natural frequency of the n th mode.

In order to define the work, we must now do business with the slipper springs. The work is a product of the force in those springs and the displacement of the attached structure. However, the attached structure was pinned in all the modes so the springs do work only on the rigid displacements, z and θ . The forward slipper force is:

$$F_F = -k_F \delta \left(Z + \ell_F \theta, \frac{\epsilon}{2} + y_r(x + \ell) \right) - D_F$$

where $\delta(u, v) = u - v, u > v$

$$= 0, |u| < v$$

$$= u + v, u < -v$$

ϵ is the slipper gap and y_r is the local rail height. The aft slipper force is

$$F_A = -k_A \delta \left(Z + \ell_A \theta, \frac{\epsilon}{2} + y_r(x) \right) - D_A$$

k_F and k_A are the slipper support stiffnesses and ℓ_F and ℓ_A are distances from the sled cg to the slipper supports.

D_F and D_A are the damping forces and act only when the slippers are in contact.

$$D_F = C_F \left(\dot{Z} + \ell_F \dot{\theta} - V y_r'(x + \ell) \right)$$

$$D_A = C_A \left(\dot{Z} - \ell_A \dot{\theta} - V y_r'(x) \right)$$

V is the sled downtrack velocity, and $y_r'(x)$ is the local slope of the rail head.

The equations may now be written out by making the appropriate substitutions into Equation (2).

$$\begin{bmatrix} m & 0 & M_{13} & M_{14} & \dots \\ & I & M_{23} & M_{24} & \dots \\ & & M_{33} & 0 & \dots \\ & & & M_{44} & \dots \\ \text{Symmetric} & & & & \end{bmatrix} \begin{Bmatrix} z \\ \theta \\ q_1 \\ q_2 \\ \vdots \end{Bmatrix} + \begin{bmatrix} 0 & 0 & 0 & 0 & \dots \\ & 0 & 0 & 0 & \dots \\ & & 2\zeta_1 M_{33} \omega_1 & 0 & \dots \\ & & & 2\zeta_2 M_{44} \omega_2 & \dots \\ \text{Symmetric} & & & & \end{bmatrix} \begin{Bmatrix} z \\ \theta \\ q_1 \\ q_2 \\ \vdots \end{Bmatrix} \quad (7)$$

$$+ \begin{bmatrix} 0 & 0 & 0 & 0 & \dots \\ & 0 & 0 & 0 & \dots \\ & & M_{33} \omega_1^2 & 0 & \dots \\ & & & M_{44} \omega_2^2 & \dots \\ \text{Symmetric} & & & & \end{bmatrix} \begin{Bmatrix} z \\ \theta \\ q_1 \\ q_2 \\ \vdots \end{Bmatrix} = \begin{Bmatrix} F_F + F_A + F_S \\ F_F \ell_F - F_A \ell_A + M_S \\ 0 \\ 0 \\ \vdots \end{Bmatrix}$$

A few terms have been added which were not yet discussed. Modal damping is included where ζ_n is the proportion of critical damping.

F_S and M_S are the quasi-steady forces and moments such as lift, drag and thrust. Exception might be taken to their being excluded from the modal equations since they do act over the whole sled body and, hence, do work on the modes. The response is:

- The modal deflections are small compared to those of the rigid body and so the work done on them by the quasi-steady loads will be as well.
- The quasi-steady loads are very low frequency (generally zero) and so are matched to the rigid body motion which is either low or zero frequency depending on whether or not the slippers are in contact.

- The output of the program is inertial load vectors

$$\{\ddot{\mathbf{r}}_I\} = -[\mathbf{m}] \left(\{1.0\} \ddot{\mathbf{z}} + \{x_j - x_{cg}\} \ddot{\theta} + \{\phi^n\} \ddot{q}_n \right)$$

which are unaffected by the quasi-steady forces except indirectly.

Verification of the Method

The random rail generation scheme and the nonlinear equations of motion were implemented in a computer code called SLEDYNE. An Adams-Moulton predictor-corrector numerical integration technique is used. The program searches for maximum dynamic displacements and stresses (computed on a modal summation basis) and also outputs inertial load vectors associated with peak values of each of the four slipper forces. The overall flow diagram for SLEDYNE is shown in Figure 11.

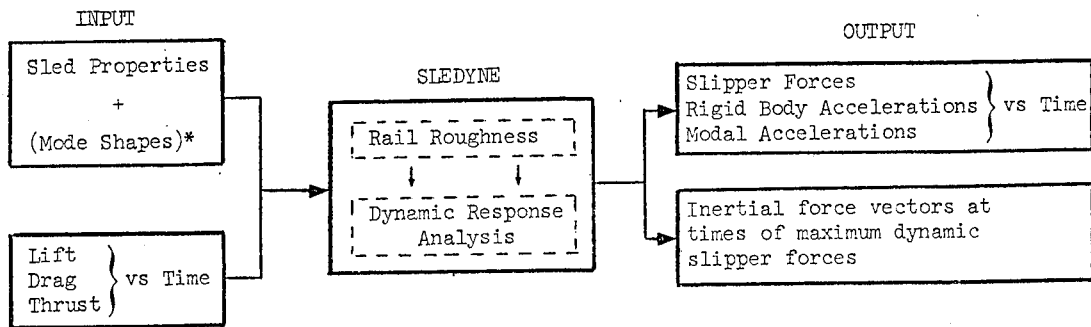
In considering the validity of the method described in the last section, it might be asked if the representation of the structure truly captures its dynamic characteristics. In order to verify this, a mathematical experiment was performed using a 300 DOF finite element model of the Single Mod sled. Two sets of vibration modes were calculated using MRI/STARDYNE. One set was calculated with the slippers restrained at the rail, the other set with all four slippers released, i.e., a free-free model. For comparison, two sets of eigenvalues were computed for the mass and two stiffness matrices from the simulation program corresponding to the same two boundary conditions. The comparison is shown in Table 1 and indicates the success with which the simulation functions represent the original model.

Comparisons of the simulation predictions of peak vertical slipper forces are shown in Figure 12 for dual rail sleds and Table 2 for monorail sleds. The dual rail data, Figure 12, are presented in terms of SIMP, the sled impact parameter. Peak forces are shown for the forward and aft slipper beams of three sleds. Superimposed on the experimental data are the SLEDYNE simulation results. They agree with the experimental points from the coast phase, but, as expected, lie below the peaks measured during the thrust periods.

Table 2 shows the comparison of monorail test track data with SLEDYNE simulations for two sleds at various velocities. Because of the very high frequency nature of the data (see Figure 7) and large number of impacts, the data and SLEDYNE results were smoothed by an averaging technique (as in Figure 8). The smoothed data agree very well. The SLEDYNE results contained greater scatter than the track data and hence the peaks were higher.

REFERENCES

1. Mixon, Larry C., Sled Design Techniques, AFSWC-TR-71-3, 6585th Test Group, Holloman AFB, New Mexico, February 1971.
2. Fisher, Gary K., and Stronge, W. J., Analytical Investigations of Rocket Sled Vibrations Excited by Random Forces, U. S. Naval Ordnance Test Station, China Lake, California, July 1964.
3. Oliver, R. E., and Wu, T. Y., Final Report: Sled Track Interactions and a Rapid Method for Track-Alignment Measurements, Aeronautical Engineering Research, Pasadena, California, June 30, 1958.
4. Hasse, Hans O., Provisional Summary of a Sled Vibration Study Report, WP-MDS, 66-1, AFMDC, Holloman AFB, New Mexico, February 1966.
5. Braun, Gerhard W., and Melkus, Harold A., On the Nonlinear Motion of a Rocket Sled, AFOSR/DRA-62-13, AFMDC, Holloman AFB, New Mexico, July 1972.
6. McIntyre, K. L., "Linear Aeroelastic Stability Analysis of USNOTS 8,000 FPS Third Stage Sled," General Dynamics Technical Memorandum No. 348-44, 3-2, 23 February 1967.
7. Greenbaum, G. A., Gardner, T. N. and Platus, D. L., Development of Sled Structural Design Procedures, MRI-2544-TR-2, Mechanics Research, Inc., April 20, 1973.



*Optional

FIGURE 11. SLEDYNE PROGRAM FLOW

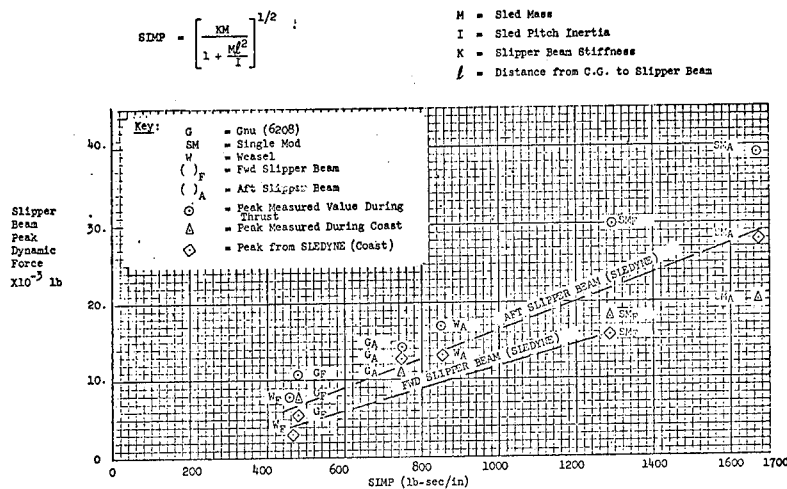


FIGURE 12. COMPARISON OF SLEDYNE RESULTS WITH
TEST TRACK DATA DUAL RAIL SLEDS

TABLE 1.

COMPARISON OF SLEDYNE MODAL REPRESENTATION
WITH "EXACT" STARDYNE MODES

	STARDYNE Modal Calculation	SLEDYNE* Equations
Fixed-Fixed	20.2	20.6
(Slippers in Contact with Rail)	27.6	27.9
	56.2	55.4
	125.1	124.6
	193.3	192.0
Free-Free	0.	0.
(Slippers in Gap)	0.	0.
	51.1	51.2
	121.7	122.9
	186.2	189.4
Single Mod Natural Frequencies - cps		

*Based on two rigid plus five pinned-pinned vibration modes

TABLE 2.

COMPARISON OF SLEDYNE RESULTS WITH TEST TRACK DATA, MONORAIL SLEDS -
VERTICAL FORCE DURING COAST (LBS)

Vehicle	Velocity (fps)	Average of Peaks*		Peak	
		SLEDYNE**	Test	SLEDYNE**	Test
Modular Monorail (fwd)	3400	21,800	22,280	34,900	30,240
Modular Monorail (fwd)	2300	18,430	17,700	29,000	23,720
Instrumented Monorail (fwd)	4000	16,610	16,000	20,680	16,000
Instrumented Monorail (fwd)	2900	13,270	12,500	19,860	14,000
Instrumented Monorail (aft)	4000	16,520	17,000	23,280	19,000
Instrumented Monorail (aft)	2900	13,400	13,600	17,820	12,000
* Average of peaks measured in .1 second intervals					
**Three percent damping, six vibration modes					

CONSIDERATION OF THE RESPONSE OF A
SLED BORNE MISSILE

Alva R. Glaser
Missile System Division
Rockwell International Corporation
Columbus, Ohio

and

Larry C. Mixon
6585th Test Group, AFSWC
Holloman Air Force Base, New Mexico

Discussed are the results obtained during a recently completed study which demonstrated the feasibility of conducting non-destructive tests of advanced propulsive concepts aboard high speed test sleds. This study required that an existing flight test missile and an existing high speed test sled both be structurally modified to attain test speeds of 2800 ft/sec. The considerations which governed the required missile and sled modifications are presented.

The missile was instrumented with several strain gage bending circuits and accelerometers, and was mounted to the carriage sled by force transducers. This instrumentation was continuously monitored during the several track tests which were conducted. Successive track tests involved changes in missile configuration and/or an increase in the maximum attained velocity. Thus measured responses were obtained as a function of the test configuration and velocity. These responses are discussed from both a design requirement and an analysis viewpoint.

The analysis method used to support the initial missile/sled modification and changes in this analysis method required to produce favorable comparisons between predicted and measured Power Spectral Densities are discussed. Based on the resulting method of analysis and the experimental results obtained, a means of estimating the design requirements for a different flight configured missile for carriage aboard a high speed sled is recommended.

INTRODUCTION

A program has been recently completed which demonstrated the feasibility of performing captive tests of ramjet engines at supersonic velocities aboard rocket sleds. The track tests were tailored toward simulation of low level flight in the Mach 2.5 regime and provided duplication of both Mach number and Reynolds number for a modified full size missile at 0° and -4° angles of attack. References 1 and 2 provide details of the program described herein.

The program required significant modification of the existing outrigger rocket sled and ramjet missile as shown in Figure 1. The structural modifications to the sled included the removal of the top one-third of the semimonocoque structure, introduction of missile support structures, and replacement of the original rocket sustainer subsystem with a less expensive rocket motor package. The flight test ramjet

hardware required modification of the nose cone, new structure at the sled interface joints, and repositioning of the ramjet fuel system.

The basic sled system had been previously track tested with a different payload in the Mach 2.5 to 3.0 velocity regime; however, this program placed new stringent requirements on the final stage configuration. The layout of the rocket sled/ramjet was controlled by the necessity that the ramjet's aft mounted inlets be unaffected by reflected shock waves and other ground interference effects as shown in Figure 2. In compliance with these aerodynamic considerations, ten feet of the missile was cantilevered forward of the sled structure.

The overall final system configuration is

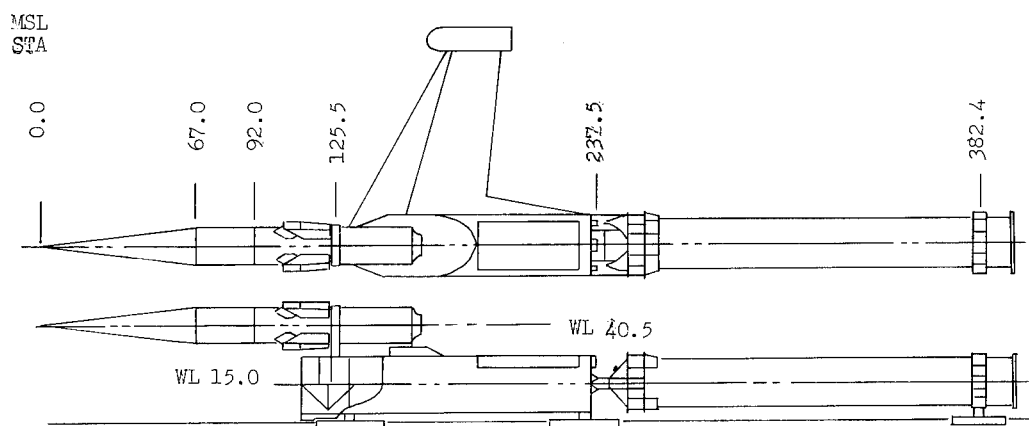
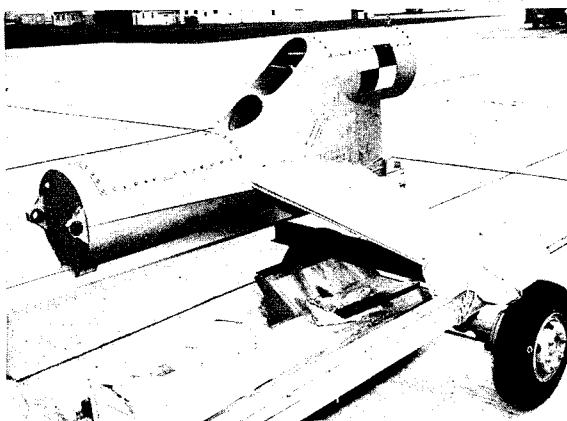


Figure 1
Unmodified Missile and Sled with Integration Concept

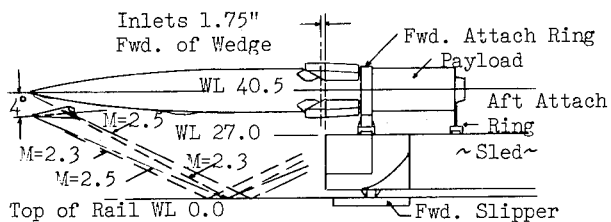


Figure 2
Reflected Shock and Inlet Design Consideration

shown in Figure 3. The complete sled system consisted of two outrigger pusher sleds and a final stage which provided the test bed for the ramjet missile and incorporated three sustainer rocket motors.

The uniqueness of this configuration directed the extensive use of mathematical models and environmental test techniques in order to satisfy program objectives. The purpose of the initial mathematical models was to provide internal loads information for the

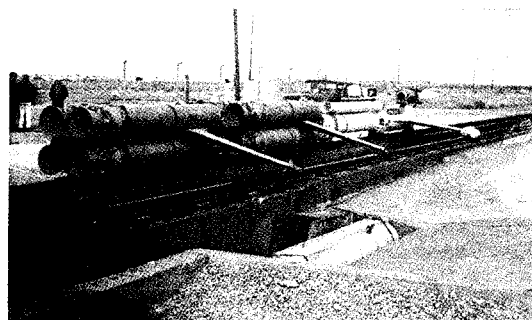
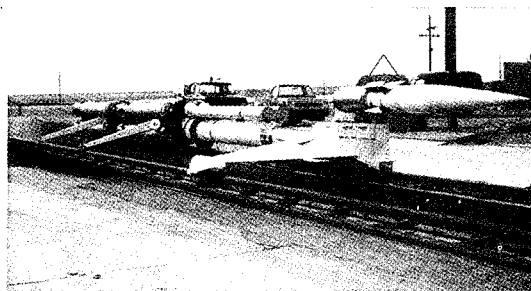


Figure 3
Final System Configuration

structural changes and to provide system loads estimates for the impending track tests. Once the track tests were initiated, the modeling emphasis was directed at the interface of the ramjet with the sled test bed and the resultant response of the long ramjet nose cone.

FORMULATION OF MATHEMATICAL MODELS

The sled system was separated into ten physical components, or subassemblies. These are the missile payload, the sled, the outrigger, sustainer, two interface elements, and four slippers. The payload, sustainer, and sled components are represented as beam-rods, thus each of these components are simulated as two analytical components. One analytical component provides vertical bending degrees of freedom, while the other provides lateral bending and torsional degrees of freedom. The outrigger is modeled as a single beam-rod having vertical bending and torsional degrees of freedom.

The sled system is simulated by 52 mass points as shown in Figure 4. Each of these

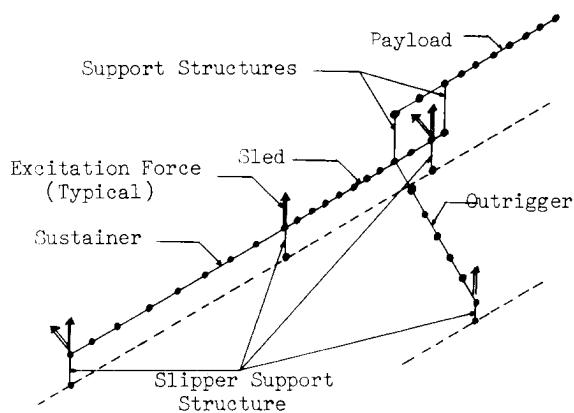


Figure 4
Vibration Math Model Lumped Parameter Representation

mass points is allowed to move in six degrees of freedom, giving 312 possible degrees of freedom. Those components which are simulated as beam-rod structures are considered rigid along their structural axes, however, and the outrigger was assumed rigid in fore-and-aft bending. Also, rotary inertia in bending was not included for the various components. Therefore, the sled system is actually permitted to have approximately 150 independent degrees of freedom.

VIBRATION ANALYSIS

The vibration analyses were accomplished by using the component coupling technique described in Reference 3. Briefly, this method involves determining the vibration characteristics for each component of the sled system and then coupling these results

together by enforcing compatibility at the various component attach points.

Two configurations were analyzed with two different slipper boundary conditions per configuration for a total of four vibration analyses. The two configurations differed in that one was for a long-nosed payload, while the other was for a short-nosed payload. One set of boundary conditions provided each slipper with its prescribed load carrying capability in the vertical and lateral directions, but each slipper was unrestrained in the longitudinal direction. This set of boundary conditions is a linear representation of the sled system as it moves down the track. The results of vibration analyses utilizing these boundary conditions were used in the preliminary random loads analysis. The second set of boundary conditions again provided each slipper with its proper load carrying capability in the vertical and lateral directions, but in addition, the forward sled slipper and the sustainer slipper were fixed in the longitudinal direction. This set of boundary conditions simulated the sled system as restrained during ground vibration tests. The results of vibration analyses incorporating the second set of boundary conditions was compared with the results of the ground vibration tests to verify the analytical model of the sled system.

Ground vibration testing was accomplished prior to the track tests to establish the adequacy of the mathematical models and to provide the opportunity to modify the models based on experimental data. Two configurations were tested; however, only the results of the more critical long-nosed configuration will be discussed in the interest of brevity. The basic laboratory experiment is shown in Figure 5. Approximately 100 acceleration measurement locations were monitored for each test configuration and were selected to coincide with the mass points in the mathematical models. A dual-beam oscilloscope was used for quick visual examination of wave forms and phasing relationships, and then a frequency synthesizer was used in place of the sweep oscillator for the final mode shape measurements. A 50-pound exciter was used for the basic excitation force, and an auxiliary matched shaker phased with the primary was used for excitation of some modes.

The primary variable that controlled the correlation of the mathematical model predictions and the measured response was slipper fixity. Special fixtures were used to restrain the lower slippers as shown in Figure 6. The first series of laboratory tests showed that the forward slipper may be supplying a yaw restraint to the system (see Figure 7), a restraint which had not been included in the model. This resulted in a predicted lower mode of vibration which could not be correlated. A yaw slipper spring was introduced into the

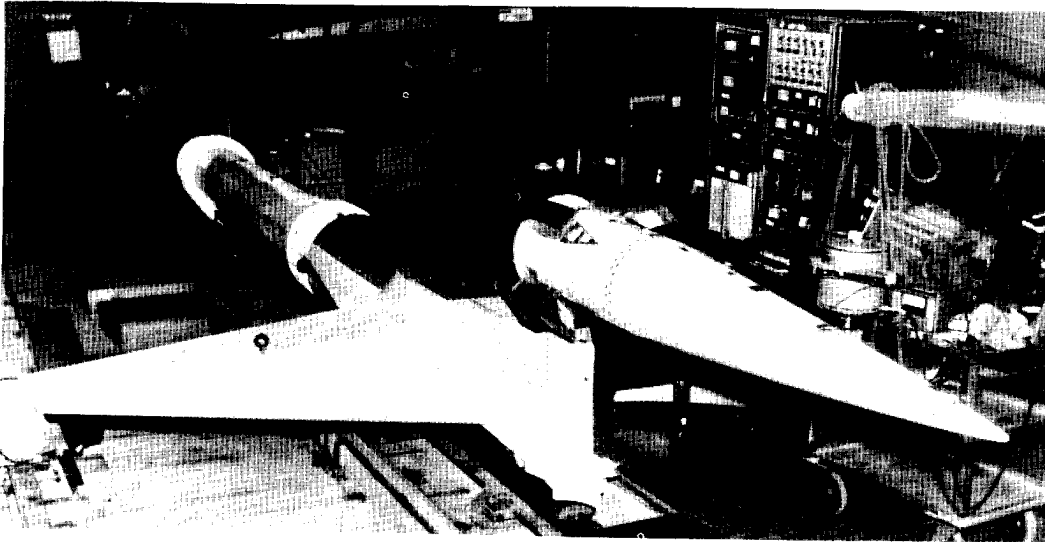


Figure 5
Ground Vibration Test Setup

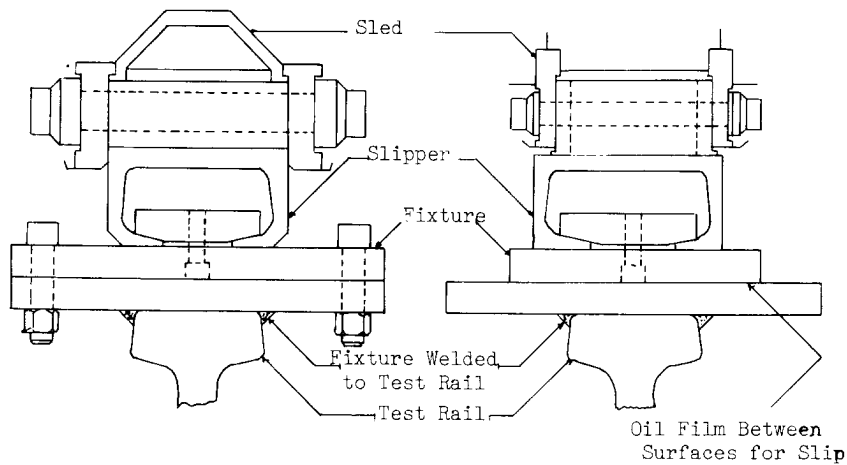


Figure 6
Ground Vibration Test Slipper Fixtures

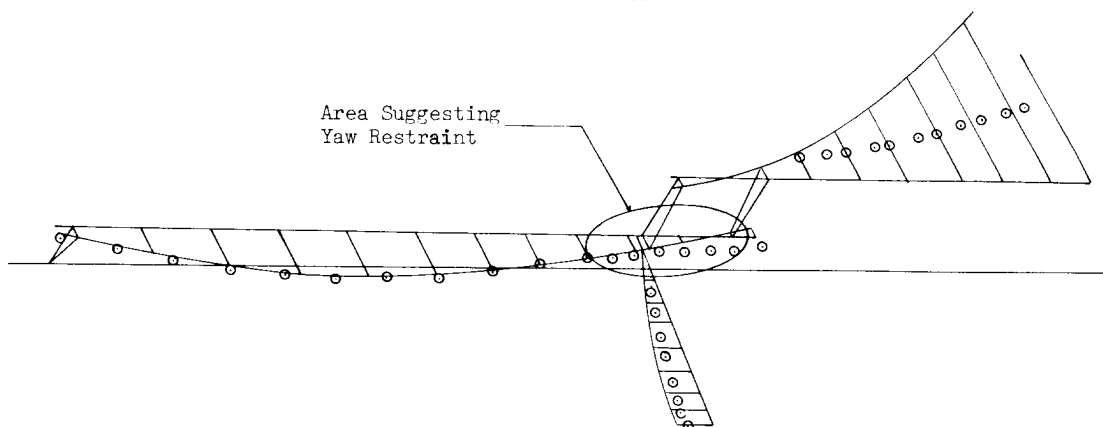


Figure 7
Measured Mode Shape Suggesting Yaw Restraint

model to simulate the observed restraint and several analyses were performed to study the effect of the yaw spring stiffness on predicted modal response. A spring rate was established which provided correlation for the troublesome mode without significantly affecting the correlation of the other modes of vibration. The first six frequencies were correlated with excellent results while the mode shape correlation was considered as very good. These results are characterized in Figure 8. Reasonable frequency agreement was obtained for modes above the first six, but mode shape correlation was not good.

* This mode not obtained for long-nosed missile configuration; however, this mode is outrigger torsion which by analysis is shown not to be sensitive to payload configuration.

MODE	Long-Nosed Configuration			
	Original Analysis Freq. (Hz)	Experimental Freq. (Hz)	Experimental Dmp Ratio c/c _c	*Revised Analysis Freq. (Hz)
1	14.1	26.4	.030	26.1
2	20.2	19.6	.035	19.6
3	33.9	28.8	.030	31.0
4	35.8	36.9	.015	36.5
5	46.1	43.5	.015	47.3
6	68.8	*	*	68.8
7	70.4	76.4	.010	70.5
8	94.1	94.2	.035	94.5

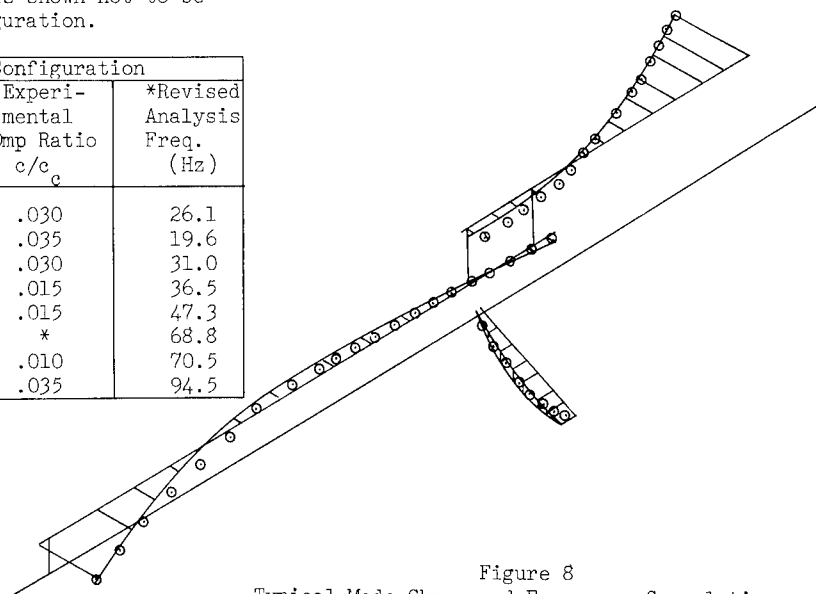


Figure 8
Typical Mode Shape and Frequency Correlation

FORCING FUNCTIONS

The forcing functions were derived in two formats. The first type was the relatively slow time varying quasi-steady state forces that result from thrust, aerodynamic forces, braking forces, and inertia. These data were obtained from manufacturers' data for the thrust curves, wind tunnel data for the aerodynamic forces, computer simulation of water braking forces, and a computer program used to calculate the system inertia and the complete velocity/time history for the trajectory. The derivation of these forces is straightforward and will not be discussed herein.

The more predominant forcing functions result from the interaction of the slippers with the rails. These forces are a function of the quasi-steady state forces, the slipper gap (a clearance of approximately 1/8 inch is

allowed between the guide surfaces and the railhead), the rail roughness, and the oscillatory aerodynamic and thrust forces[4]. The time constraints of this program did not allow for a complete examination or simulation of the non-linear multi-degree of freedom problem. Consequently, random forcing functions were derived from available measured data.

In an earlier program, the lateral forces transmitted to the original rocket sled from the front slipper had been measured for the same relative velocities. These measurements provided estimates of the shape of the random response reactions, and the magnitude of one slipper force. Based on this force data,

acceleration data, and scaled force data from other rocket sleds, a histogram (see Figure 9) was derived and assumed applicable for each of the six internal slipper forces. Estimates of the internal RMS slipper force levels expected at maximum velocity (3000 ft/sec) are given in Figure 9. Indications from previous sled programs led to the assumption that these slipper forces were proportional to sled velocity.

DESIGN LOAD LEVELS

The resonant frequencies and mode shapes calculated during the vibration analysis were used in the random analysis of the sled system. The random slipper forces were applied to the vibration model at the sled slippers in order to excite the model. Rational assumptions were made concerning correlation and phasing of the applied slipper forces which allowed the

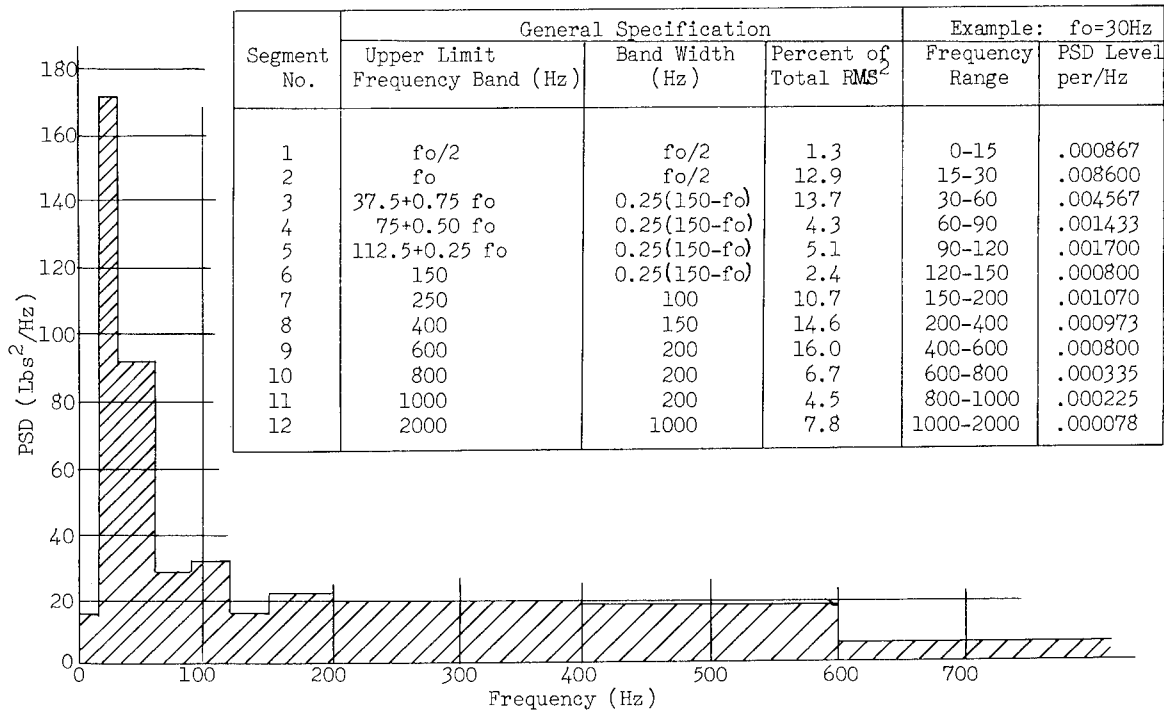


Figure 9
Power Spectral Density Histogram

RMS modal participation factors to be determined. These RMS modal participation factors were used in conjunction with associated mode shapes and resonant frequencies and with the geometry and distributed mass of the sled system to determine the internal load distributions and the missile support forces. The RMS slipper deflections and internal forces were also determined.

Comparison of the internal slipper forces thus calculated to the expected internal slipper forces and consideration of the distributed internal loads coupled with repeated analytical studies led to the following observations:

- If the specified slipper forces were interpreted as applied forces, then the resulting loads were so high as to be declared unreasonable and maximum response was found to occur with an energy concentration at unrealistically high frequencies.
- If the specified slipper forces were interpreted as resulting internal forces, then resulting load magnitudes and the frequency of energy concentration became reasonable, but the specified set of internal forces appeared to be mathematically incompatible

within the framework of the assumptions made.

The basic problem therefore appeared to be twofold:

- Determine a set of specified internal slipper forces which were mathematically compatible.
- Determine a set of applied forces which resulted in these specified internal slipper forces.

An iteration scheme was devised which adjusted the magnitude of the applied slipper forces with each iteration in an attempt to converge, in some sense, to specified internal slipper forces for selected slippers. In this scheme, the applied slipper force for each iteration was obtained by multiplying the previous applied force by the ratio of the desired internal slipper force to the internal slipper force previously obtained. Generally, "convergence" in some sense was achieved after ten such iterations. A numerical study was then performed wherein selected internal slipper forces were considered to be invariant. It was concluded on the basis of this study that the most meaningful mathematically consistent analysis was obtained when the forward

internal slipper forces were considered invariant.

This iteration procedure was repeated with the forward internal slipper forces held invariant while the reference PSD frequency was varied over the first ten structural frequencies. The results showed that maximum response occurred generally in a low frequency region and that the response was generally independent of the reference Power Spectral Density frequency.

Structural modification was guided by the internal loads thus calculated.

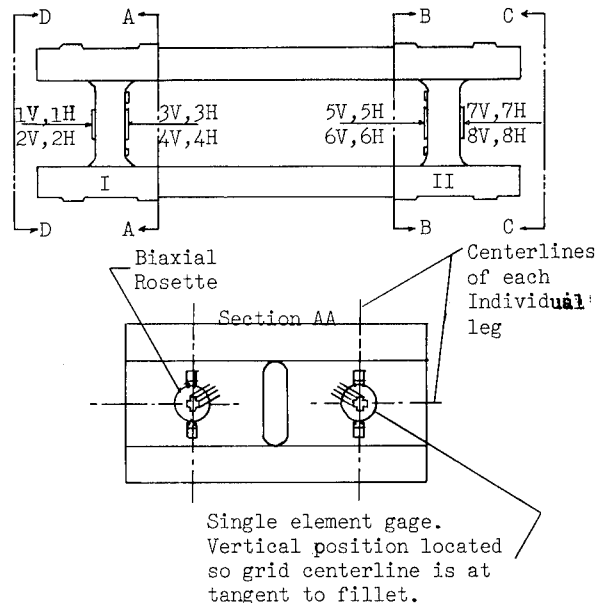
SLED INSTRUMENTATION

A unique facet of the design of the rocket sled/ramjet interface was the incorporation of force transducers. The capability of the outrigger rocket sled to carry a payload of similar size and weight to Mach 2.5 had been previously established in an earlier program. However, the task of propelling a low frequency cantilevered missile to these velocities were a more formidable problem. Consequently, the interface force transducer measurements, together with the bending moment and acceleration measurements provided the means to study the missile subsystem during each track test.

The forward support force transducer is shown in Figure 10. The configuration was a post or frame design with 16 strain gages applied to the vertical legs to measure the vertical forces and roll moments and 8 strain gages were applied in the corners of the unit to measure the lateral or cross-track forces. The unit was developed by the University of New Mexico and was subjected to numerous calibration tests and static combined load tests.

Bending moment strain measurement locations are shown in Figure 11. A total of eight bending moments were measured along the missile, four locations in each of the pitch and yaw planes. The strain gages were applied to the internal surfaces of the nose cone and to the external surfaces of the ramjet combustion chamber. Static force tests were performed in the laboratory for system calibration. These bending moments coupled with six force transducer measurements and 14 acceleration measurements provided 28 structural response measurements for each track test.

Throughout each track test a variety of data was monitored. This data defined the actual trajectory and provided response time histories of payload bending moments, accelerations and support loads. The structural data thus obtained from lower velocity less severe missile configurations were correlated with model or scaled predictions and scaled to the next plateau of testing. This scaled data was used to define structural modifications and instrumentation requirements necessary to



Notes:

1. Section BB is similar to section AA except for gage numbers.
2. View CC and DD are similar to section aa except the single element gages are not present, and gage numbers are different.
3. Identification numbers are shown by gages. For the rosettes, V indicates a vertical grid and H a horizontal grid.

Figure 10
Forward Force Transducer
and Instrumentation

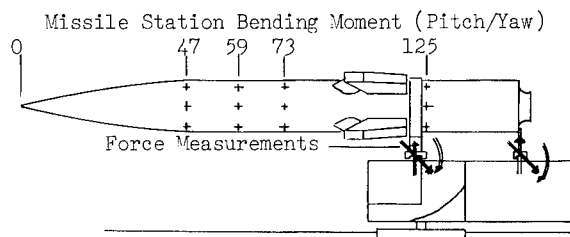


Figure 11
Bending Strain Gage Circuit Locations

insure the success of the next track test. This method of system development provided the means to carefully construct each test configuration and perform structural modifications before actually performing the track tests. The structural data was also used to substantiate or direct changes to a math model intended to aid in the determination of design criteria of future systems. Accelerometer data was used principally to substantiate the structural

data. Trajectory data was used to define the propulsion necessary to obtain the performance levels required in subsequent tests.

Peak amplitudes of the critical parameters were obtained from the response time history (quasi-steady plus oscillatory) data. Decisions regarding structural integrity and necessary structural modifications were based on these peak amplitudes. A comparison of measured peak bending moments obtained from the first low speed track test to predicted maximums along the missile body is shown in Figure 12. Comparisons in the lateral plane are not as good although the loads are considerably lower than those in the vertical plane.

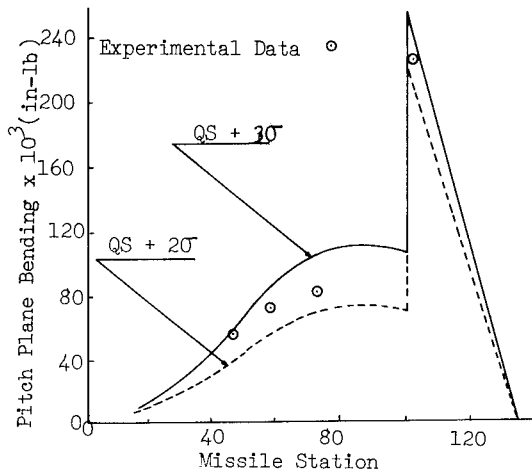


Figure 12
Predicted Vs Measured Maximum
Bending Moments

The analog records for these structural response measurements were digitized for each test and processed through a series of random analysis computer programs. The digitized records provide amplitude-time histories while RMS versus time plots were used to study the velocity dependence of the functions. Amplitude Probability Density and Power Spectral Density graphs were analyzed from selected time slices for correlation with model predictions. Typical variations found for the more significant functions monitored are shown in Figures 13 and 14.

MATH MODEL REVISIONS

An objective of this program was to modify and correct the mathematical models and forcing functions to accurately predict the critical system responses measured during track tests. The modifications to the mathematical

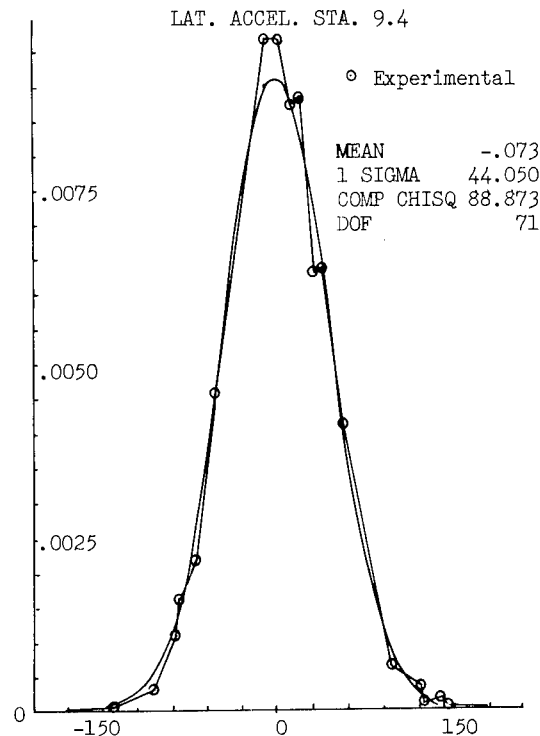


Figure 13
Sample Amplitude Probability Density

model was to be based on comparisons between model predictions and track test measured modes of vibration, internal forces (measured by the transducers between the sled test bed and the payload), and payload response (measured by accelerometers and strain gages).

The existing model shown in Figure 15 would be excited by applying power spectra distributions measured with the payload supporting transducers to the junctions of the supporting structure and the payload. The applied forcing spectra would then be varied until correlation was obtained for both the transducer measurements and bending moments.

Among the first problems considered was the differences between the math model representation and the data available. The math model representation must be driven by net vertical and lateral forces and torques at the forward and aft payload support points. Measured are vertical forces in each of two legs of the transducers and lateral transducer forces. Additionally, data for one leg of both transducers were not obtained. Thus considerable judgment had to be exercised in estimating the power spectral density of the measured torque and vertical force for the

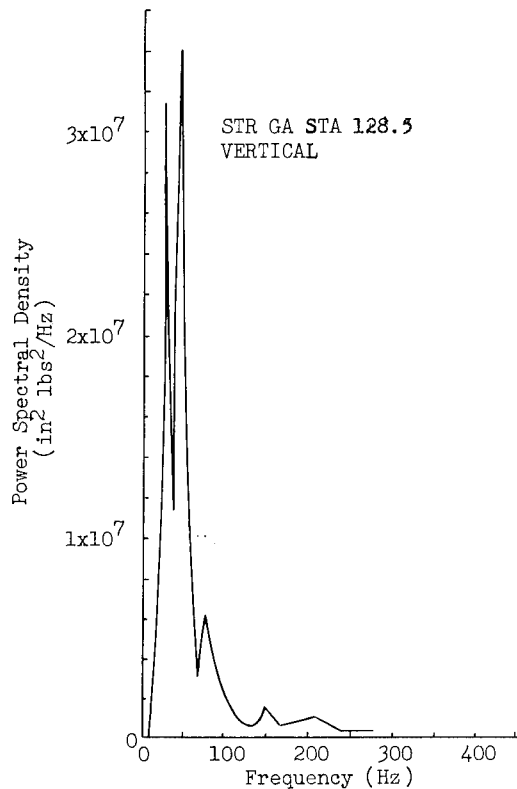


Figure 14
Sample Power Spectral Density

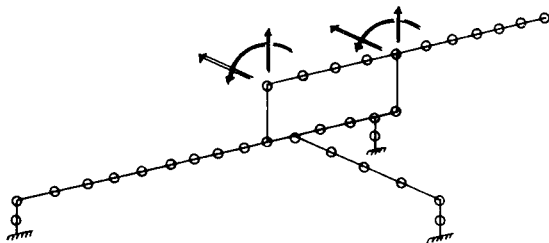


Figure 15
Random Analysis Math Model

two transducers.

The problem ultimately resolved to the determination of the RMS forces and torques associated with each transducer and the determination of each of their energy spectra and phasing as a function of frequency. A trial and error approach was too weak a method for such a formidable task.

Since all measurements had been analyzed

for the same time interval, the measured responses of the vehicle must be considered to be fully correlated. Consequently the forcing functions were also considered to be fully correlated. Implicit in this approach is the necessity to assume or calculate the degree of correlation and the associated phasing of the applied forces.

Several iteration schemes were devised and used to modify the applied forces by an amount based on the calculated response. These iteration schemes resulted in either numerical divergence, convergence to negative RMS values, or stabilized RMS levels with oscillatory power spectral density distributions. The iteration approach was then abandoned and further mathematical inquiry initiated. This inquiry led to the following conjectures.

- . The tendency of convergence towards a negative root which resulted in oscillatory behavior probably indicates a phasing relationship between the applied force frequency distributions which varies with the frequency. The math model, as implemented, could not recognize such phasing.
- . If phasing of the applied forces is important, then the phasing of the modal participation factors must also be important.
- . The system is modeled with ten degrees of freedom (i.e., ten flexible modes), however only six response functions are used as control functions. Thus the system model under consideration consisted of six equations with ten unknowns, a model for which a direct unique solution does not exist.
- . If the modal participation factors could be determined, then the system model would consist of ten equations with six unknowns. A unique solution to such a system can be obtained in a least square error sense.

The phasing problem suggested that the analysis be temporarily removed from a random response context and placed in a frequency response context. This change is easily accomplished by interpreting the power spectral density functions as the square of the frequency response curves. Four additional control functions were selected to be combined with the six transducer functions in the determination of the spectral distribution of the modal participation parameters. Chosen were the vertical and lateral bending functions at payload station 128.5 and the vertical and lateral accelerations in the nose of the payload.

It was realized that acceptance or rejection was based not on the error in modal participation but on the error in the calculated response as compared to the measured response. Thus the modal participation factors were determined from the control functions and the applied driving forces were determined so as to minimize the above error in a "least square error" sense.

The results of this procedure proved to be satisfactory. Several resulting predicted responses are compared to the measured responses in Figure 16.

CONCLUSIONS

A structurally sound test configuration was developed and tested which provided the velocity/time requirements necessary to perform propulsion testing of ramjets on the Holloman Test Track. Examination of the load variation with velocity indicated that a linear relationship between load and velocity for this system did not exist. It was recommended that a non-linear model of the system which considers only slipper flexibility as in Reference 4 be implemented to investigate the nature of the dependency of load on velocity. The Power Spectral

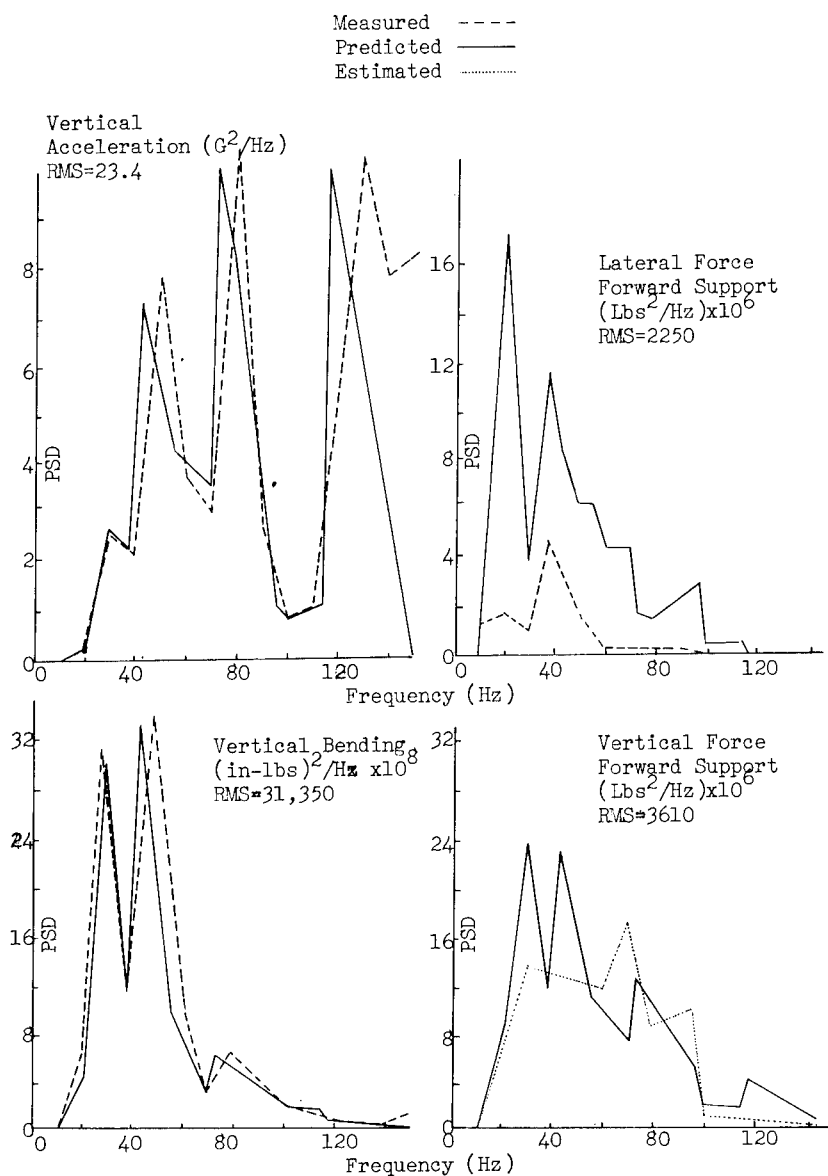


Figure 16
Measured Vs Predicted Power Spectral Densities

Densities of a set of driving forces were found which resulted in response predictions that agree in a "least square error" sense with corresponding measured data. It was found that for this system the Power Spectral Densities of the driving forces were in no way similar to the resulting internal forces. The results discussed herein are dependent on the basic approach taken in developing the mathematical representation of the physical system modeled. The basic approach taken herein resulted in unrealistically high slipper forces. It was recommended that a Ground Acceleration approach as described in Reference 5 be implemented and investigated for application to systems of the type investigated herein.

REFERENCES

1. Technical Report AFSWC 72-6, "Final Report on Pilot Model for Aeropropulsion Test Sled", 6585 Test Group, Holloman Air Force Base, New Mexico, August 1972.
2. Technical Report AFSWC 73-6, "Final Report on Environmental Investigation of Pilot Propulsion Test Sled", 6585 Test Group, Holloman Air Force Base, New Mexico, March 1973.
3. JPL Technical Report No. 32-530, "Dynamic Analysis of Structural Systems by Component Mode Synthesis", January, 1964.
4. Mixon, L. C., "Sled Design Techniques", AFSWC-TR-71-3, Test Track Division, 6586th Test Group, Holloman Air Force Base, New Mexico, February 1971.
5. Hurty, W.C. and Rubinstein, M. F., "Dynamics of Structures", Prentice-Hall, Inc., May 1965.

DISCUSSION

Mr. Glaser: Concluded with a motion picture.

Voice: What changes were made in the properties of the Vehicle?

Mr. Glaser: The length was increased by two feet the over hand was increased by two feet and the velocity was changed from 1500 feet per second to about 2000 feet per second.

Voice: Was there any increase in weight?

Mr. Glaser: Just slightly. This configuration weighed about 3000 lbs.

Voice: Did the bending moments go up?

Mr. Glaser: They did that's right.

FLOW-INDUCED VIBRATIONS OF A GLASS-REINFORCED PLASTIC SONAR DOME

Douglas A. King
Rockwell International Corporation
Anaheim, California

A comparison is made between applicable theory and experimental results of dome wall vibrations and boundary layer pressure fluctuations occurring in tests of a large buoyancy-propelled underwater vehicle. The vehicle had a body of laminar flow shape, 14 feet in diameter and 35 feet long, with tail fins on a boom, and a sonar dome on vibration mounts. The local velocity, wall thickness and boundary layer characteristics varied along the body. A method is described for incorporating the effects of these variations into the theoretical response of a flat infinite plate acted upon by pressure fluctuations of a uniform boundary layer. Effects of operating parameters on the vibration power spectral densities are shown.

INTRODUCTION

In 1970 a project was initiated by the Autonetics Division of Rockwell International Corporation, under the sponsorship of the Applied Physics Laboratory of Johns Hopkins University, to study some sonar flow noise problems at essentially full-scale conditions. A test vehicle was designed and built to house a 10-ft. -diameter acoustic Luneburg lens in a sonar dome. The dome, of fiberglass reinforced plastic construction, comprised the forward half of a laminar-flow shaped body of revolution. Tail fins on a boom assured hydrodynamic stability. To attain optimum quiet conditions, the vehicle was propelled by buoyancy and tested in vertical runs at the Naval Ship Research and Development Center (NSRDC) range at Lake Pend Oreille, Idaho. The laminar-flow shape allowed a minimum extent of turbulent boundary layer flow over the dome, and a very small hydrodynamic drag coefficient. When desired, the extent of turbulence was extended by tripping the boundary layer with a wire around the body near the nose.

During the tests, measurements were made of boundary layer pressure fluctuations and dome wall vibrations. The data were converted to power spectral density form, at

several speeds, by means of a fast Fourier transform computer algorithm for analysis. The pressure spectrums were of familiar form; that is, zero slope below a roll-off frequency, and merging into a fixed downward slope above roll-off when expressed in log-log form. The vibration spectra had a downward slope at both extremes, and the frequency range over which merging occurred was much greater than that of the pressure spectra. Vibration occurred at forward positions of the dome even when the boundary layer was laminar there. The shapes of the vibration spectra suggested a modification to a theory for plate vibrations which allows taking into account the variation of boundary layer excitation over the body surface. This modified theory shows satisfactory agreement with the experimental results, and thus, allows better analysis of the effects of various operating conditions.

TEST VEHICLE

The general structural assembly and configuration of the vehicle is shown in Fig. 1. Basically, it is a body of revolution, 35 ft. long and 14 ft. maximum diameter, with an NACA 63040 laminar-flow contour, fitted with four stabilizing fins on a tail boom.

PL-22704
ADD 420 193

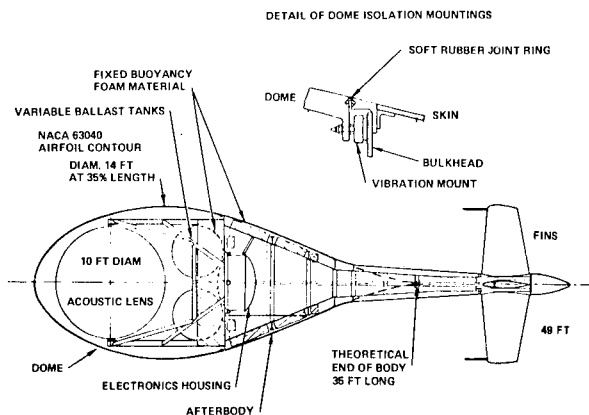


Fig. 1. Internal Structure of Test Vehicle

The structure of the vehicle is of aluminum alloy rings and longerons. The skin of the afterbody and tail fins is of fiberglass epoxy, and the tail boom skin is aluminum.

Fixed buoyancy blocks around the variable ballast tanks are of polyurethane covered with polymer-backed neoprene sheeting cemented in place to inhibit water seepage. The blocks in the afterbody are of syntactic foam with plastic spheres. Densities in air are 25 and 23 lb./cu. ft., respectively.

Two pressure-proof aluminum spheres and associated plumbing provided for varying the net buoyancy through a range of 6120 lb., from a minimum of 900 lb. to a maximum of 7000 lb. in the configuration tested.

The acoustic lens is an array of hollow plastic compliant tubing dispersed in such a manner that the sonic speed in the mixture of tubes and water provides focusing of the incident sound waves to points at the lens surface opposite to the sound source. The tubes are supported by fiberglass netting held by hoops, 12 meridional ribs, and a metal polar tube. It weighs 800 lb. in air and 80 lb. in water. The lens is isolated from the I-beam structure by means of six commercial vibration isolators

The fiberglass-epoxy sonar dome extends over 49 percent of the basic body length, and is supported at its base by means of 56 commercial vibration isolation mounts, as shown in the inset to Fig. 1. The isolation could be locked out by means of threaded rods located between the mounts and held to the dome base ring and the body structure by nuts. The mounts are Barry Series 2000 type, with a working load range of 100 lb. each, and stiffnesses of 5000 lb./in. lengthwise and 3000

lb./in. laterally. Taking into consideration the internal water and the hydrodynamic added mass, it was estimated that natural frequencies would be 5 Hz longitudinally and 6 and 0.7 Hz in lateral rocking motion. The dome weighs 4400 lb. in air and 2000 lb. immersed in water.

The dome is a laminate of woven roving faced with two layers of 181 cloth on the interior and exterior, plus an additional layer of 120 cloth on a gelcoat to provide additional smoothness on the exterior surface. Thickness of the dome wall was based somewhat on existing domes, and is 0.5 in. from the nose to abreast the lens, increasing smoothly to 0.8 in. at maximum diameter, 1 in. in way of the tanks, and 2 in. at the base. Under a design load condition at 1000 lb./sq. ft. applied laterally, stresses were less than 1000 psi, and the thickness distribution was adequate to prevent buckling.

Measurements of dome wall samples 0.6 in. thick showed the following material properties:

Ultimate strength in bending	44,300 psi
Ultimate strength in tension	23,700 psi
Interlaminar shear strength	1,500 psi
Modulus of elasticity in bending	1.92×10^6 psi
Modulus of elasticity in tension	1.86×10^6 psi
Specific gravity	1.57
Resin content	49%

The afterbody skin is of the same laminate construction, 0.5 in. thick, and held to the interior structure by flush-head screws. Both the dome and the afterbody skin were laid up by hand inside accurate fiberglass-epoxy molds, and air cured. Especial care was taken with surface smoothness, and surface waviness was held to less than 1/1000 height to length in order to achieve a contour conducive to preventing premature boundary layer transition.

The whole vehicle, including the lens, is flooded with water during operation. In air the vehicle weighs 23,600 lb.; in water the total mass to be accelerated is 200,000 lb., of which about 26,000 lb. is the hydrodynamic added mass. The vehicle is so massive that only about 75 to 80 percent of terminal velocity is attained in vertical pop-up runs from reasonable depth (currently limited to 600 ft. by the strength of the electronic housing) with the

available buoyancy. It was found safe to operate the vehicle without brakes up to an emergence speed of about 25 ft./sec. At this speed, about 70 percent of the body length, or 50 percent of the total length, is above water. The loss of buoyancy caused by progressive emergence of the water-filled dome provides large braking force.

VEHICLE HYDRODYNAMICS

The shape of the basic body was chosen to be a laminar-flow airfoil section on the basis of having a position of minimum pressure (maximum superelectricity) far aft to promote the greatest extent of laminar boundary layer flow, but not so far as to incur the possibility of flow separation at the rear for the low fineness ratio of 2.5. This small fineness ratio produces about the smallest hydrodynamic drag on a frontal area basis. The section chosen was the NACA 63040, and the body has a small volume and a center of volume well forward, relative to bodies based on other shape distributions. This gives a relatively low mass to be accelerated, and a relatively forward position of this center of gravity immersed and filled with water. The body diameter was chosen as the smallest that would allow the dome to be removable in one unit over the 10-ft. lens and its supports.

Hydrodynamic stability was assured by designing fins to produce a restoring pitching moment 55 percent greater than the unstable moment of the body. The fin span was kept equal to the maximum body diameter.

The combination of extensive laminar boundary layer and good pressure recovery aft coupled with smooth skin and avoidance of joints and discontinuities results in very low drag, about half that ordinarily obtained on bodies of the same fineness ratio. However, the greatest practical advantage of the body shape in this project was the ability to extend the turbulent layer artificially by tripping at a forward location when desired.

Two flow parameters of most interest to the investigation were the local superelectricity and the boundary layer thickness. These were calculated by the Douglas-Neumann computer program [1] and the results are shown in Figs. 2 and 3. The program automatically calculates the position of boundary layer transition, or transition can be ordered to occur where desired. At a speed of 10 fps, the Reynolds number based on body length is 25×10^6 .

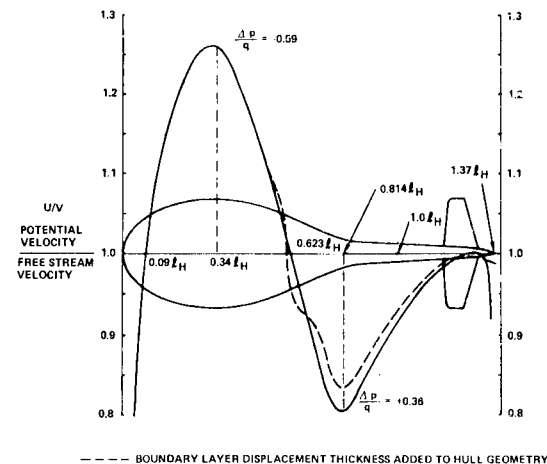


Fig. 2. Velocity Distribution About 63040 Hull Calculated by Neumann Method

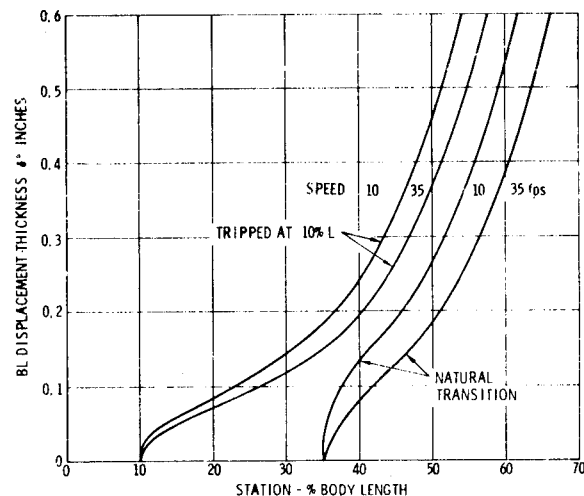


Figure 3. Calculated Boundary Layer Characteristics

Design calculations were checked by means of wind tunnel tests of a 1/14-size model. Drag, side force, pitching moment, and boundary layer transition measurements were made with and without tail fins. Other tests of a dynamic model the same size were made in the Autonetics Sonar Pool to check steadiness of running under various conditions, and to examine vehicle behavior at emergence. Both of the model tests indicated that no hydrodynamic problems should be expected in the full-scale test experiments.

The choice of a laminar-flow body of revolution and the successful hydrodynamic

design was based on extensive study of such shapes conducted by Autonetics for the purpose of attaining low-drag underwater bodies with extensive laminar boundary layer flow.

Performance characteristics of the vehicle are shown in Figure 4 as curves of speed attained at various run lengths as a function of buoyant thrust.

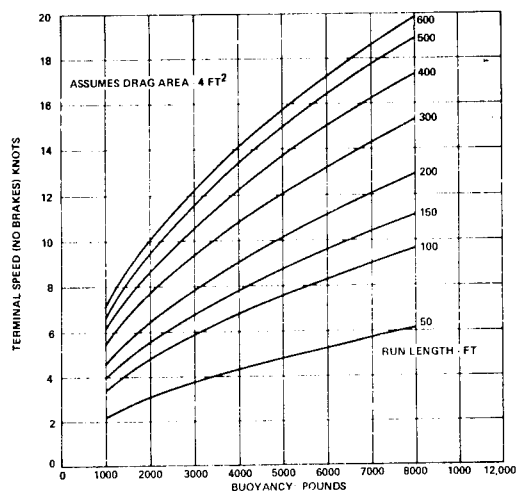


Fig. 4. Vehicle Speed Performance

INSTRUMENTATION

Instrumentation on the vehicle consisted of sensors located at desired points, amplifying and signal conditioning electronics in a pressure-proof housing, and batteries to supply power.

Locations of the boundary layer pressure hydrophones (mounted flush with the outer surface) and of the wall vibration accelerometers (mounted inside the skin in still water) are shown in Fig. 5. The flush hydro-

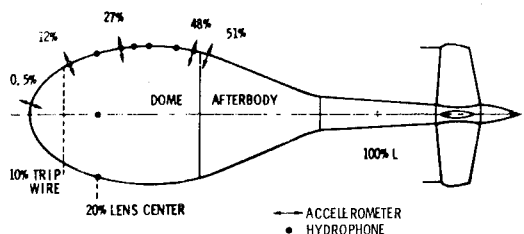


Fig. 5. Locations of Pressure Hydrophones and Vibration Accelerometers

phones were of the smallest size available consistent with adequate sensitivity in order to minimize the correction needed at large values of face diameter to convection wavelength. [2] They were Atlantic Research type LD-107, ² having an effective acoustic area of 0.0028 in. (diameter of 0.06 in.), a sensitivity of -119 dB rel. 1 volt/ μ bar, and a resonant frequency of 200 kHz. The dynamic accelerometers were Wilcoxon Research type 722, having a sensitivity of 125 mV/g, a nominal resonant frequency of 12 kHz, and a depth capability of 2500 ft. of water. With sufficient amplification, vibrations as small as 0.5×10^{-6} g could be measured. Other hydrophones were positioned on the lens and elsewhere inside the dome. The outputs, amplified as needed, were recorded in frequency modulation form on two tape recorders. Two of the 14 channels of each recorder were taken by a time code and vehicle velocity (really square-wave pulses denoting revolutions of a propeller speed meter at a calibrated rate of 12 revolutions for 10 ft. of travel), and the remainder used for selected sensors. Some sensors were used in all runs, and others selected as desired.

Items of vehicle performance recorded in amplitude analog form on the oscillograph included: time code, vehicle velocity, roll rate, pitch and yaw, strains at critical location on electronics case, and strains measuring lift force and torsion on one fin. These were used to monitor the steadiness of running.

Some measurements of strain in the dome wall due to vibrations were attempted, but no useful results were obtained.

TESTS AND DATA REDUCTION

The tests were conducted at the NSRDC Field Station at Lake Pend Oreille, Idaho. In the first half of November 1971, a series of 11 runs were made at gradually increasing buoyancies and start depths to investigate vehicle hydrodynamic characteristics. In May 1972, a series of 32 runs (in 11 test days) were made to obtain data under relatively standard conditions with various configurations. Ordinarily, the runs were made in pairs, the first with the boundary layer trip wire in place and the second with natural layer transition.

Data reduction was done after return to Autonetics. Particular runs were selected which contained the desired information. The time histories of the magnetic tape data were

duplicated in amplitude analog form on oscillograph tapes for examination of extraneous disturbances. Sections of clean data, 0.4 sec. long, were copied onto magnetic tape at nominally constant vehicle speeds of 0, 10, 14, 18, 22, and 24 ft/sec. These segments were transformed to power spectral density form by a fast Fourier transform computer algorithm and plotted to log-log scales by the computer, using calibration factors determined for each day's running at the test site. These graphs were then used for analysis.

BOUNDARY LAYER PRESSURE FLUCTUATIONS

Boundary layer theory indicates that transition from laminar to turbulent flow tends to occur at a constant Reynolds number (defined as $R = Ux/\nu$) which is a function of lengthwise pressure gradient, surface roughness, ambient turbulence level, and the like. Time history records of wall pressure at various stations along the dome bear this out. As the speed increases throughout a run, the position of transition is seen to move progressively further forward on the dome. The progression is modified by the pressure gradient along the hull, which as shown in Fig. 2, is adverse aft of the maximum diameter station (tending to promote earlier transition), and favorable forward of there (tending to delay transition to higher Reynolds number). Natural transition generally does not occur suddenly, but starts as isolated or intermittent bursts that coalesce into continuous turbulence as the speed continues to increase.

When the boundary layer was artificially tripped at 10 percent station, it was, of course, turbulent aft of there at all speeds throughout the run.

The motion of fluid particles in a boundary layer may be thought of as that caused by the passage of eddies of various sizes along the wall, at some speed less than that of the free stream. The smaller eddies cause high-frequency pressure fluctuations, and the larger ones low-frequency pressures. There is a balance of energy transfer from the larger to the smaller eddies as they break up, so that one would expect a gradually decreasing energy content with increasing frequency (decreasing eddy size). However, the largest size of eddies present, or lowest frequency, is limited by the thickness of the boundary layer. One would thus expect that the preceding increase in pressure fluctuations with decreasing frequency, from the

energy transfer between eddies of different sizes, to reach a limit below some frequency that is determined by boundary layer thickness. The power spectral density of the turbulent boundary layer pressure fluctuations may thus be given, in log-log plot form, by two straight lines of different slope joined at a roll-off frequency. Below and above roll-off, $p^2 \propto f^0$ and $p^2 \propto f^{-3}$, so slopes are 0 and -30 dB/decade. In actuality, there is a blend between the two extremes that can be considered a second-order corner, so that the pressure PSD can be expressed as:

$$P(f) = 3.16 \times 10^{-5} \rho^2 \delta^* U^3 [1 + (f/f_0)^2]^{-3/2} \quad (1)$$

The roll-off frequency is:

$$f_0 = U/\pi \delta^* \quad (2)$$

The nondimensional constants are valid for the case of a smooth flat plate in uniform flow with zero lengthwise pressure gradient and non-turbulent exterior flow. Little information on the effects of pressure gradient exist beyond the experiments of Schloemer (1967) [3].

For correlation with acoustics, in general the $P(f)$ is expressed in units of $(\text{dyne}/\text{cm}^2)^2/\text{Hz}$ equal to $(\mu\text{bar})^2/\text{Hz}$.

The preceding discussion is illustrated in Figure 6, which shows typical pressure PSDs measured at various speeds during two runs, one with boundary layer tripped at 10 %L and the other with natural transition. The dome was fixed to the after body in these runs.

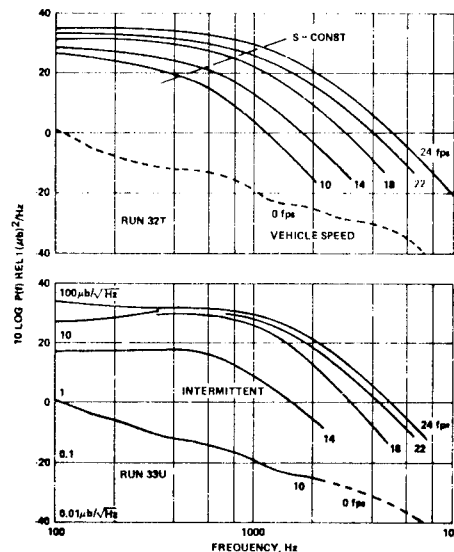


Fig. 6. Pressure Power Spectral Density Hydrophone FM5 at 27 %L

In the tripped run 32T, the shapes and variation with speed are as expected. The slanting line $S = f\delta^*/U = \text{constant}$ is drawn through the roll-off frequencies calculated from the values of U and δ^* from the computer solutions of Figs. 2 and 3. In the untripped run 33U, the boundary layer was laminar at 10 fps, intermittent turbulence was present at 14 fps with a turbulent burst of about 0.15 sec. occurring in the 0.4-sec. time interval, and the layer was fully turbulent at above 16 or 17 fps. Compared with the turbulent run, the roll-off frequencies are higher, consistent with the thinner boundary layer in the untripped run. In this run, the boundary layer measured at 20 %L showed some isolated bursts at 22 and 24 fps vehicle speed.

In both the tripped and untripped runs, the boundary layer pressure PSDs at locations along the dome follow the trends of Eqs. (1) and (2); that is, the roll-off frequencies tend to decrease as with increasing distance aft along the surface and increasing boundary layer thickness. In the untripped runs, the boundary layer was turbulent at the aft end of the dome.

DOMES VIBRATION RESULTS

Some typical dome vibration PSDs are given in Fig. 7, measured at the same location and during the same runs as the pressures of Fig. 6. The unit of acceleration used is cm/sec^2 (called the gal in terrestrial gravimetry) which is convenient and easily related to the μbar pressure unit by the relation:

$$1 \mu\text{bar} = 1 \text{ dyne/cm}^2 = 1 \text{ gram/cm}^2 \times 1 \text{ cm/sec}^2 \quad (3)$$

Results of measurements taken on the after-body skin just aft of the dome (fixed in these runs) during the same runs are given in Fig. 8, and show a better separation with speed.

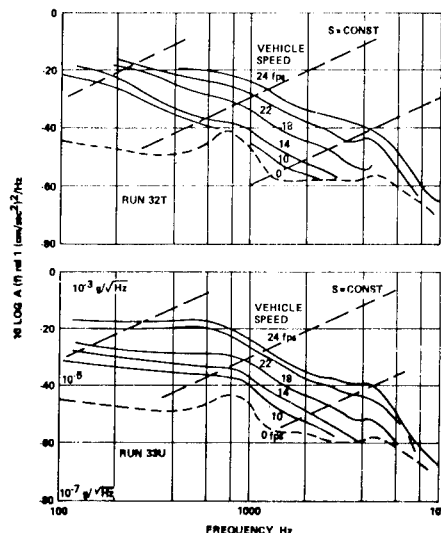


Fig. 8. Acceleration Power Spectral Density Accelerometer A13 at 51 %L on Afterbody

Aspects in which the vibration PSDs differ from the local pressure PSDs are noted as follows:

There is a general overall decrease in level with increasing frequency, similar to that occurring in a mass-controlled oscillator.

There is a difference in slope at the extreme high and low frequency ends of the spectra much like that at the extremes of the pressure PSDs.

The band of frequencies between which the extremes blend is much greater.

There is little or no overall frequency shift of "roll-off" at different locations.

The variation in level with vehicle speed is greater than that of pressure, and in the untripped run at 27 %L vibrations occur at 10 and 14 fps speed, even though the boundary layer is laminar there, or has isolated

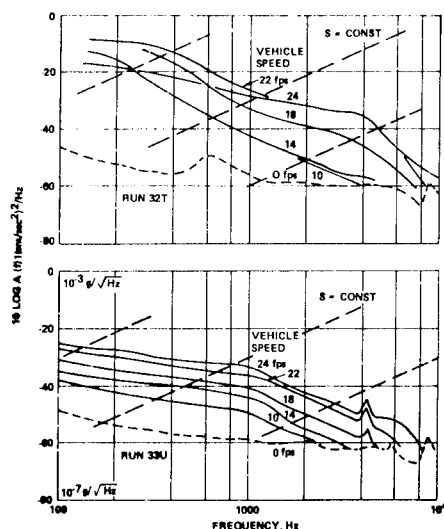


Fig. 7. Acceleration Power Spectral Density Accelerometer A5 at 27 %L

turbulent bursts. This last observation is explainable when one considers that the dome is a continuous body so that excitation anywhere will cause vibration elsewhere.

No strong resonances appear, except near 4000 Hz in untripped run at 27 %L, which also appeared at 12 %L data, but is either not present or is strongly damped out at the afterbody station. This appeared similarly in several other untripped runs.

THEORY OF TURBULENCE-INDUCED VIBRATION

The fluctuating pressures experienced at points on a wall under a turbulent boundary layer are equivalent to those resulting from pressure waves, correlated over some area, that are convected along the wall in the streamwise direction. When the wall is flexible, it will vibrate in the form of free bending waves. Such turbulence-induced vibrations have been studied extensively. When the plate is immersed in water, the plate vibrations produce pressure waves travelling at sonic speed, which add additional pressures to those of the turbulence. This occurs in air also, but the net effect is much smaller.

The most recent and most applicable theory of plate vibrations with fluid loading is that of Strawderman and Christman [4]. It seems rather complex, and only the end results that were used will be given here.

Consider a thin, flat plate lying in the x, y plane. Under static conditions, the normal deflection w in the z direction caused by pressure $p(x, y)$ acting on the plate surface is given by:

$$\nabla^4 w = \frac{\partial^4 w}{\partial x^4} + 2 \frac{\partial^4 w}{\partial x^2 \partial y^2} + \frac{\partial^4 w}{\partial y^4} = \frac{p(x, y)}{D} \quad (4)$$

with appropriate boundary conditions. The velocity of compressional waves in the plate is:

$$C_\ell = \sqrt{E/\rho_p(1 - \sigma^2)} \quad (5)$$

and the velocity of flexural bending waves without ambient fluid loading is:

$$C_f = \sqrt{C_\ell \omega h \sqrt{12}} \quad (6)$$

The normal deflection $w(x, y, t)$ of a plate, immersed in a fluid and acted on by a

turbulent pressure field $p(x, y, t)$ on one side, is:

$$D \nabla^4 w + r \frac{\partial w}{\partial t} + \mu \frac{\partial^2 w}{\partial t^2} = p(x, y, t) + p_a(x, y, 0+, t) + p_a(x, y, 0-, t) \quad (7)$$

Using results of their previous papers and taking into account appropriate lengthwise and lateral correlation factors of turbulent pressures, Strawderman and Christman derive expressions for all parts of this equation in spectral density form. They show that a finite plate exhibits the basic features of an infinite plate, plus resonances, but the finite case will not be considered here. Their final expression, with slight change in symbols, for the local velocity power spectral density with ambient fluid loading is:

$$V(\omega) = P(\omega) \left(\frac{8.05 \times 10^{-2} \omega^4}{\pi^2 U_c^2} \right) \times \left\{ \int_{|k| \leq |k_0|} \left[(Dk^4 - \omega^2)^2 + \left(r + \frac{2 \omega^2}{k_0^2 (1 - (\omega/k_0)^2)^{1/2}} \right)^2 \right] \left[\left(\frac{0.115 \omega}{U_c} \right)^2 + \left(\frac{\omega}{U_c} - k_1 \right)^2 \right] \left[\left(\frac{0.7 \omega}{U_c} \right)^2 + k_2^2 \right] \right\} + \int_{|k| > |k_0|} \left[(Dk^4 - \omega^2)^2 + \left(r + \frac{2 \omega^2}{k_0^2 (1 - (\omega/k_0)^2)^{1/2}} \right)^2 \right] \left[\left(\frac{0.115 \omega}{U_c} \right)^2 + \left(\frac{\omega}{U_c} - k_1 \right)^2 \right] \left[\left(\frac{0.7 \omega}{U_c} \right)^2 + k_2^2 \right] \right\} \quad (8)$$

In a vacuum, this reduces to:

$$V(\omega) = P(\omega) \left(\frac{8.05 \times 10^{-2} \omega^4}{\pi^2 U_c^2} \right) \int_{-\infty}^{\infty} \frac{dk}{(Dk^4 - \omega^2)^2 + (r\omega)^2} \left[\left(\frac{0.115 \omega}{U_c} \right)^2 + \left(\frac{\omega}{U_c} - k_1 \right)^2 \right] \left[\left(\frac{0.7 \omega}{U_c} \right)^2 + k_2^2 \right] \quad (9)$$

Acceleration spectral density, for a more direct comparison with our data, is obtained by merely multiplying velocity spectral density by ω^2 , so that

$$A(\omega) = \omega^2 V(\omega) - P(\omega) \times \frac{8.05 \times 10^{-2} \omega^6}{\pi^2 U_c^2} \times \int_{\text{plate and turbulence parameters}} dk \quad (10)$$

The ratio of $A(\omega)/P(\omega) = A(f)/P(f)$ is $1/(\text{mass per unit area})^2$ or μ^{-2} . It was calculated at various frequencies and free stream speeds for fiberglass plastic plates, using measured values of dome material modulus of elasticity and density. The integration of Eq. (8) is a little tricky, since the integrand rises to a very sharp peak that is dependent

on the damping coefficient r at the fluid loaded free wavenumber for which the first bracketed expression in the denominator reaches a minimum. This is the wavenumber for hydrodynamic coincidence. The accuracy of integration was checked by first doing it for the steel plate used as an illustration in the reference [4]. The results for the fiberglass-epoxy plate were found to be with water loading:

$$A(f) = P(f) \times 4.9 \times 10^{-7} U^2 / (f h^2) \quad (11)$$

The constant has units of $\text{cm}^4 \text{sec}/\text{gram}^2$.

For the plastic plate vibrating in vacuum, without fluid mass loading, the equation becomes:

$$A(f) = P(f) \times 9.5 \times 10^{-5} U^2 / (f^{1.5} h^{2.5}) \quad (12)$$

The effect of water mass loading is more pronounced at low frequency than at high. This loading effect is that of the p_a terms in Eq. 7.

The acceleration PSD of an unloaded plate is greater than that of a water loaded one at frequencies less than about 5×10^4 Hz, at which other effects may enter to vitiate the assumption of simple plate bending.

The constant in these equations seems to be proportional to the ratio $(\rho_M/E)^2$, since a few similar calculations for a steel plate in water give a value of 5×10^{-8} . These calculations give results agreeing with those used for illustrative purposes by Strawderman and Christman.

The pressure PSD for a flat plate with zero pressure gradient is given by:

$$P(f) = \frac{3.16 \times 10^{-5} \rho \delta^2 U^5}{[1 + (\pi \delta f / U)^2]^{3/2}} \quad (13)$$

When this is inserted into Eq. (9), there results the following expression for acceleration PSD, in $(\text{cm}/\text{sec}^2)^2/\text{Hz}$:

$$A(f) = \frac{1.55 \times 10^{-12} \rho \delta^2 U^5}{f h^2 [1 + (\pi \delta f / U)^2]^{3/2}} \quad (14)$$

Again, the constant is dimensional and valid when all dimensions are in the cgs system of units, and the plate is fiberglass plastic in water.

The plate is considered to be flat, unsupported, and acted upon by uniform turbu-

lence all over. In this case where the excitation has a single spectrum and has a single roll-off frequency, then the resulting vibration spectrum has the same single roll-off frequency. This is perhaps shown more clearly in Eq. (10).

APPLICATION OF THEORY TO VEHICLE

Conditions on the test vehicle differ in many respects from those for which the theory was developed, notably in the variation of local velocity and boundary layer thickness along the body, the variation of dome wall thickness, and the two-way curvature of the dome which adds additional stiffness not present in a flexing flat plate. As was shown previously, the effect of the varying boundary layer characteristics is to create various roll-off frequencies and varying pressure spectra at different locations, but the acceleration spectra do not seem to show frequency shifts at the different locations.

Considering all this and the continuous shell geometry of the dome and skin, a method has been devised of taking into account the variations of flow conditions assuming that the acceleration at any point of the dome is the sum of the incremental accelerations caused by pressure variations at all other points. This is illustrated by Fig. 9. The incremental acceleration caused by conditions at the shaded area is:

$$\left(\frac{\text{Area involved}}{\text{Total area}} \right) \left[A(f) \text{ with local conditions of Equation (14)} \right]^{1/2}$$

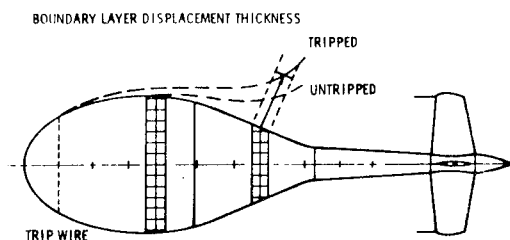


Fig. 9. Illustrating Calculation of Incremental Vibration Levels

These increments are summed over the area covered by turbulent boundary layer, and squared to obtain the resultant acceleration PSD. For the configuration of dome fixed, the summation was over the entire vehicle

plus tail fins, but did not include the tail boom since the very large boundary layer thickness there causes very low roll-off frequencies and adds very little pressure spectral components in the range of interest.

Calculated results for the condition of dome fixed are shown in Fig. 10, for the tripped and untripped boundary layer. It can be seen that tripping the boundary layer at 10 %L increases acceleration spectral levels, and that the increase is greater at the lower frequencies. The tripped boundary layer extends farther over the body and is thicker.

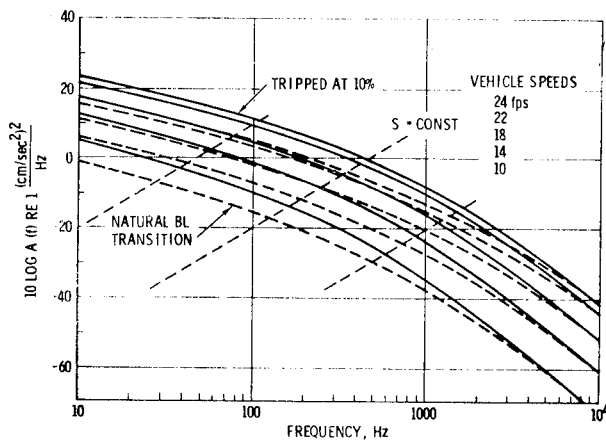


Fig. 10. Effect of Boundary Layer Tripping on Calculated Acceleration Power Spectra, SHAMU, Dome Fixed

Figure 11 shows the same comparison for the case assuming the dome to be fully isolated. Here, tripping the boundary layer causes a greater increase in acceleration power level since the calculations were carried out over the dome only, and the relative change in area excited by boundary layer turbulence was greater than for the other cases which included the afterbody and tail fins.

A comparison of Figs. 10 and 11 shows the effect of isolating the dome to be a reduction of acceleration power levels by an amount somewhat less than the difference between untripped and tripped boundary layers. The decrease at the highest frequencies is caused by the elimination of accelerations caused by excitation of the tail fins.

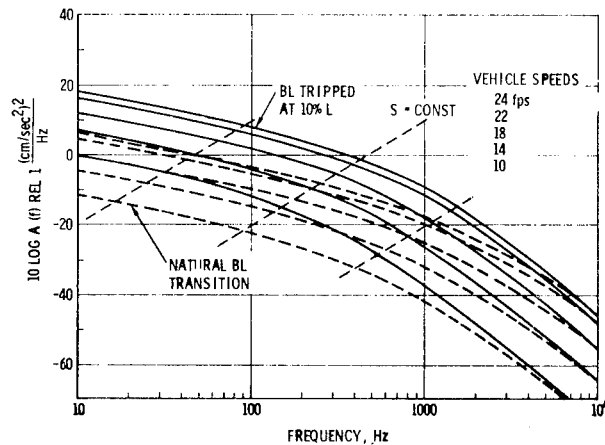


Fig. 11. Effect of Boundary Layer Tripping on Calculated Acceleration Power Spectra, SHAMU, with Dome Isolated

NORMALIZING OF ACCELERATION POWER SPECTRAL DENSITY

The preceding Eq. (14) can be used to determine normalized results; that is, to obtain factors that collapse acceleration PSDs at several speeds to one relationship of non-dimensional PSD as a function of Strouhal number $S = f \delta^* / U$ or $S = f \delta^* / V$. It is desired to obtain the slope of lines joining conditions of constant Strouhal number.

A trivial case is that for which δ^* is independent of speed, such as would occur at infinite Reynolds number. Then, $S = \text{const.}$ implies $f/U = \text{const.}$, and $f_2/f_1 = U_2/U_1$, so that:

$$\frac{A_2}{A_1} = \left(\frac{U_2}{U_1} \right)^5 \left(\frac{f_1}{f_2} \right) = \left(\frac{U_2}{U_1} \right)^4 = \left(\frac{f_2}{f_1} \right)^4 \quad (15)$$

Lines of constant S run upward diagonally at the rate of 40 dB per decade of frequency.

A more practical case occurs at Reynolds numbers in the range experienced. In this case, $\delta^* \propto U^{-1/5}$ about, at a fixed location on the body, and $S = \text{const.}$ implies

$$\frac{f_2}{f_1} = \left(\frac{U_2}{U_1} \right)^{6/5} \quad (16)$$

and

$$\frac{A_2}{A_1} = \left(\frac{U_2}{U_1}\right)^5 \left(\frac{\delta_2^*}{\delta_1^*}\right) \left(\frac{f_1}{f_2}\right) = \left(\frac{U_2}{U_1}\right)^{18/5} = \left(\frac{f_2}{f_1}\right)^3$$

Lines of constant S run upward diagonally at the rate of 30 dB per decade of frequency, as shown in Figs. 10 and 11. Unfortunately, it is not clear just what value of δ^* is to be used to obtain numerical values of S for the test vehicle, since it varies considerably with position along the body. The value of local velocity U/V also varies with position. But it is possible to normalize to arbitrary conditions, and this has been done to a reference $A(f)$ of $1 \text{ (cm/sec}^2\text{)}^2/\text{Hz}$ at a frequency of 1000 Hz and a vehicle speed of 24 fps. Fig. 12 shows the data from Fig. 7 normalized in this fashion. To show the different vehicle speeds more easily, the data are given in the form of coded points selected along the experimental traces.

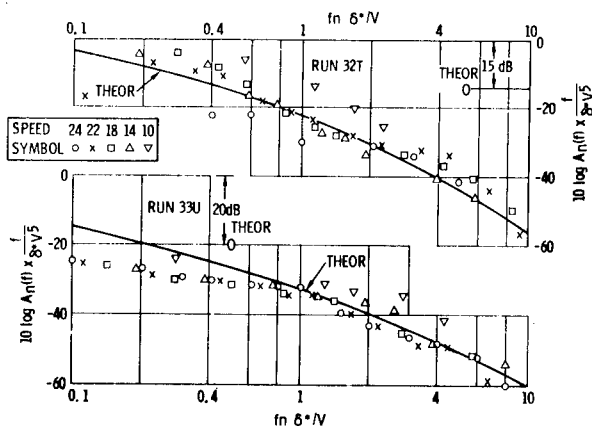


Fig. 12. Normalized Data Compared with Theoretical Calculation Accelerometer A5 at 27 %L

The data collapse well within a band about 2 to 4 dB wide. Also shown are curves of normalized theoretical vibration spectra calculated for the conditions of layer tripped at 10 %L and untripped assuming transition at 35 %L. They have been shifted up or down along the acceleration axis until the lines pass through the experimental data. The spectral shapes of the data agree with the theoretical, and the difference in amplitudes is probably due to the extra stiffening effect of the dome wall double curvature.

The difference between the ratio of $A(f)_{\text{theor}}/A(f)_{\text{exper}}$ for the two conditions of boundary layer tripping, on these runs, was

greater than would be expected, even though other data indicate that the natural transition was further forward than that used in the calculations. Experimental effects of tripping were in better agreement with the theoretical predictions for some other configurations.

SOME NORMALIZED VIBRATION RESULTS

Figure 13 shows normalized vibration spectra measured at all instrumented locations during these runs made in the vehicle configuration of lens in place and dome fixed. Theoretical curves were calculated for one wall thickness of 1/2 in., and would give lower accelerations for increased thickness. In the tripped run the experimental and theoretical spectral shapes are in good agreement. In the untripped run there is a tendency for the experimental vibration on the dome to be less than the theoretical trend at low Strouhal numbers, with the tendency being more pronounced for the stations further aft along the dome. This may be associated with increasing bending stiffness caused by increased wall thickness, or by the attachment to the vehicle structure at the dome base. In these runs the dome was fixed to the afterbody structure, and the lens was present.

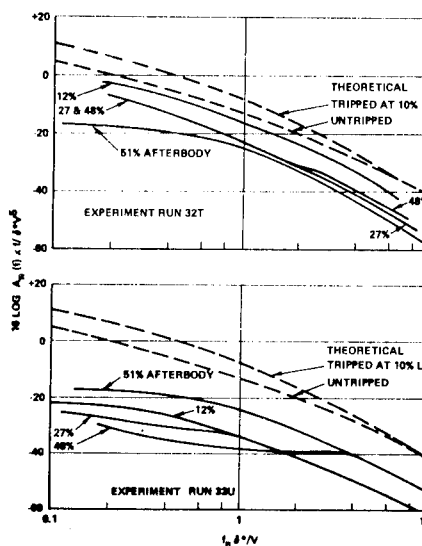


Fig. 13. Comparison of Vibration Data with Theory Configuration Dome Fixed, Lens in

A similar comparison of theory and experiment is given in Fig. 14 for the configuration of dome isolated and lens out. Here,

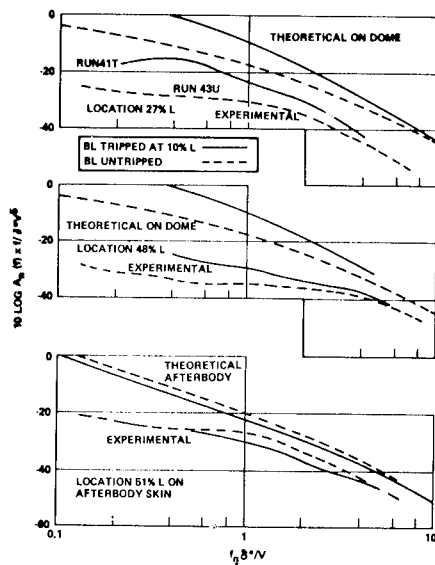


Fig. 14. Normalized Vibration PSD Dome Isolated, Lens Out

on the dome the effect of tripping the boundary layer at 10 %L, and thus extending the turbulent area covered by the turbulence, was an increase in acceleration levels more in agreement with the theoretical prediction than was the case for the runs of Fig. 13. On the afterbody, the area exposed to turbulence remains constant and boundary layer tripping thickens the layer there and reduces roll-off frequencies and the summed acceleration PSD, as shown by both the theoretical and experimental curves. This effect is present on the isolated dome also but is more than overcome by the relatively much greater increase in area excited by turbulent boundary layer.

A direct comparison of Figs. 13 and 14 shows that in the tripped boundary layer condition, the vibration levels in the configuration of dome isolated and lens out were lower in the dome base and at the afterbody skin. The theoretically calculated difference due to dome isolation is a 3-dB reduction. Unfortunately, not enough data was analyzed to separate the two effects of isolation and lens presence, but it is difficult to see why removing the lens should affect the vibrations.

In the untripped condition, little or no difference was noted between the vibration levels of the two configurations, although a reduction of 5 dB would be expected theoretically from dome isolation.

The distribution over the dome and afterbody skin of the vibration power intensity is shown in Fig. 15 for the two boundary layer conditions. The points plotted are the normalized acceleration PSD at a normalized frequency of 1.0, and thus, the values on the scale correspond directly to values of $10 \log A(f) \text{ rel. } 1 \text{ (cm/sec}^2\text{)}^2/\text{Hz}$ at a frequency of 1000 Hz and a vehicle speed of 24 fps. In the tripped condition the vibration level at the extreme nose of the dome is higher than that further aft, and at the dome base the vibrations are essentially the same as those on the afterbody skin whether or not the dome was isolated.

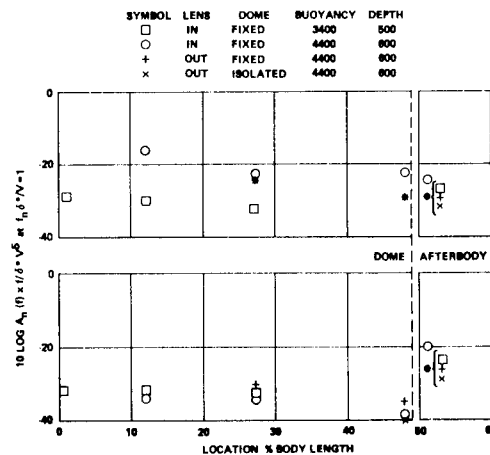


Fig. 15. Distribution of Vibration Power Intensity Over Vehicle

CONCLUDING REMARKS

Experimental vibration spectra agree with those calculated theoretically, in both frequency and vehicle speed dependence. This indicates that the concept of considering the vibration to be the summation of incremental vibrations caused by excitations from all the turbulent pressure spectra on the affected areas on the body is valid.

The differences in magnitude between experimental and theoretical are considered to be brought about by increased wall stiffness due to dome double curvature, and possibly by the end restraints at the dome base. Presumably, a similar theory developed for a cylindrical shell would give results more in agreement with these experimental ones.

In some cases, the effects of boundary layer tripping are predicted correctly by

theory, but this is not always so. The general intermittent nature of transition to turbulent flow makes it difficult to assess the area over which turbulence exists with its excitation. Then too, our vehicle was continually accelerating upward in a barostatic pressure field, never attaining steady state conditions in its flight. This caused dynamic lengthwise pressure gradients, which could bring about flow conditions different from those for which the basic boundary layer thickness and transition calculations were made.

The boundary layer pressure measurements are in agreement with other experiments and theory, though more investigation of the effects of pressure gradient is needed.

If one wishes a sonar dome free of vibration, it must be well isolated from vibrations originating elsewhere, and it must have laminar flow entirely over it. An alternative is to have a dome incapable of transmitting flexural vibrations.

REFERENCES

1. A. Smith and J. Pierce, "Exact Solution of the Neumann Problem. Calculation of Noncirculatory Plane and Axially Symmetric Flow About or With Arbitrary Boundaries," Douglas Aircraft E. S. Report 26988, 25 April 1958.
2. G. M. Corcos, "Resolution of Pressure in Turbulence," J. Acous. Soc. Am., Vol. 35, 1963, p. 192.
3. H. H. Schloemer, "Effects of Pressure Gradients on Turbulent Boundary Layer Wall-Pressure Fluctuations," J. Acous. Soc. Am., Vol. 42, 1967, p. 93.
4. W. A. Strawderman and R. A. Christman, "Turbulence-Induced Plate Vibrations: Some Effects of Fluid Loading on Finite and Infinite Plates," J. Acous. Soc. Am., Vol. 52, 1972, p. 1537.

BIBLIOGRAPHY

1. J. O. Hinze, Turbulence, McGraw Hill, New York, 1959.
2. H. Schlichting, Boundary Layer Theory, McGraw Hill, New York, 1960.
3. H. Tennekes and J. L. Lumley, A First Course in Turbulence, MIT Press, Cambridge, 1972.

SYMBOLS

$A(f), A(\omega)$	Vibratory acceleration power spectral density
c	Sonic speed in fluid
C_f	Plate flexural wave speed
C_ℓ	Speed of compression waves in plate
$D = E h^3 / 12(1 - \sigma^2)$	Plate bending stiffness
E	Young's modulus of elasticity
f	Frequency, Hz
f_0	Pressure fluctuation roll-off frequency
h	Plate thickness
\vec{k}	Vector wavenumber of plate flexure
k_1, k_2	Lengthwise and transverse components of \vec{k}
$k_0 = \omega_c$	Wavenumber in ambient fluid
L	Length of basic body in vehicle
$P(f), P(\omega)$	Turbulent boundary layer pressure fluctuation PSD
p	Pressure
p_a	Acoustic pressure generated in fluid by plate vibratory motion
$q = 0.5 \rho V^2$	Dynamic pressure in fluid
R	Reynolds number
r	Plate internal damping per unit area
S	Strouhal number
t	Time
U	Local free stream speed
U_c	Convection speed of eddies in boundary layer $U_c \approx 0.65 U$
u	Mean speed in boundary layer at distance z up from surface
V	Vehicle speed
$V(f), V(\omega)$	Vibratory velocity PSD
w	Normal deflection of plate
x	Streamwise distance along plate
y	Lateral distance across plate
z	Distance normal to plate
$\delta^* = \int (1 - u/U) dz$	Displacement thickness of boundary layer
μ	Mass per unit area of plate
ν	Kinematic viscosity of fluid
ρ	Mass density of fluid
ρ_p	Mass density of plate material
σ	Poisson's ratio
ω	Radian frequency, radian per second

ACKNOWLEDGEMENT

The results reported were obtained in the course of an investigation supported by the Applied Physics Laboratory of Johns Hopkins University, under Contract 372178.

AERO-ACOUSTIC ENVIRONMENT OF A RECTANGULAR CAVITY
WITH A LENGTH TO DEPTH RATIO OF FOUR

L. L. Shaw and D. L. Smith
Air Force Flight Dynamics Laboratory
Wright-Patterson Air Force Base, Ohio

This paper presents the results from a flight test where the aero-acoustic pressure environment was measured in an open rectangular cavity. The cavity tested was 9 inches wide, 10 inches deep, and 40 inches long, giving a length to depth (L/D) ratio of 4. It was instrumented with both static and dynamic pressure transducers as well as an accelerometer. The resulting data were correlated with empirical wind tunnel aero-acoustic predictions and formed the basis for a modified prediction method. This prediction scheme enables aircraft designers to predict the fluctuating pressure amplitudes for three resonant frequencies as well as the broadband levels for a rectangular cavity with an L/D ratio near 4 in the Mach number range of 0.6 to 1.3. The prediction scheme considers the longitudinal variation of the amplitude due to the standing waves that were observed to occur for each resonant frequency. A step by step procedure for estimating the aero-acoustic environment in a cavity is presented. In addition, an example is included and compared with results obtained from a prediction scheme presented in the literature.

INTRODUCTION

The aero-acoustic phenomena associated with pressure oscillations excited by flow over open cavities has been studied during the past twenty years by several investigators (References 1 - 7). Some knowledge has been gained about the phenomena but due to the complex nature of the problem, it is not completely understood. Methods to predict the pressure oscillations occurring in cavities have been reported in Reference 2 as determined from wind tunnel tests. The objective of this test program was to verify/modify these prediction methods with flight data. This paper briefly presents the flight test results for an open rectangular cavity with a length to depth (L/D) ratio of 4 for Mach numbers from 0.6 to 1.3. A prediction technique for determining the amplitude and frequency content of the oscillating pressure is also presented and compared to results obtained in Reference 2. The complete results from the flight test of the L/D = 4 cavity are reported in Reference 8.

DESCRIPTION OF TEST ARTICLE

The cavity was 40 inches long, 10 inches deep and 9 inches wide resulting in an L/D ratio of 4. It was constructed of 0.250 inch thick aluminum (6061 - T6). It was mounted in a modified SUU-41 munitions dispenser pod. The modified pod with the cavity mounted in it is shown in Figure 1. The pod was carried on the triple ejection rack (TER) of the left pylon of a RF-4C aircraft. The mounting is schematically illustrated in Figure 2.

INSTRUMENTATION AND DATA REDUCTION PROCEDURES

The cavity was instrumented with nine microphones, one accelerometer, one thermocouple, and three static pressure ports. The location of the instrumentation is shown in Figure 3 with the type and models presented in Reference 8 along with the data acquisition instrumentation. All data were continuously recorded on two fourteen channel tape recorders. The magnetic tapes recorded in flight were analyzed on a Hewlett Packard (5450)

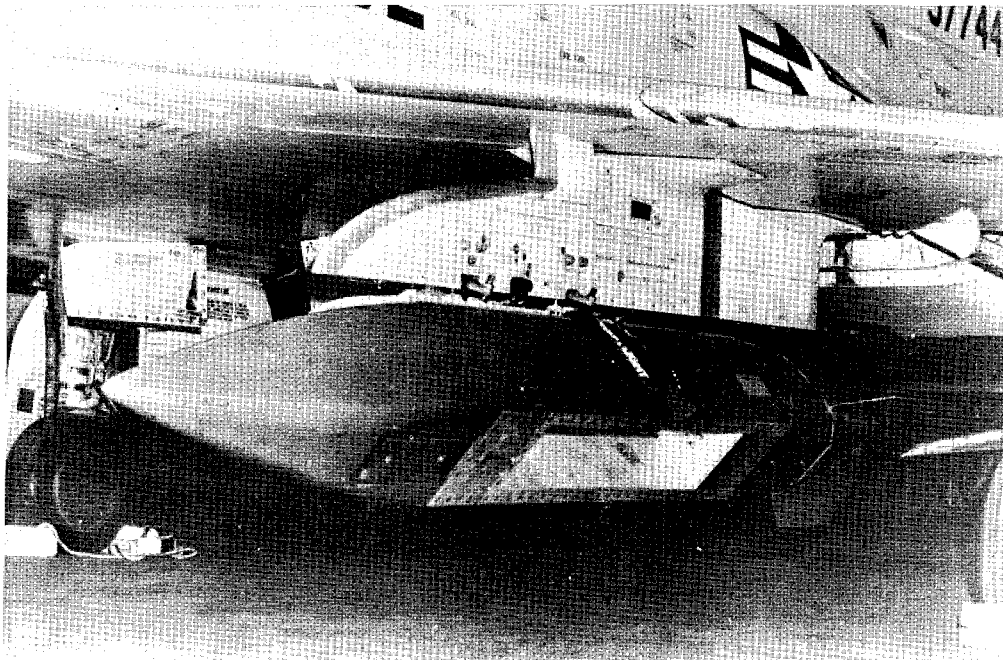


Fig. 1 - Ten Inch Cavity Mounted in a Modified SUU-41 Pod

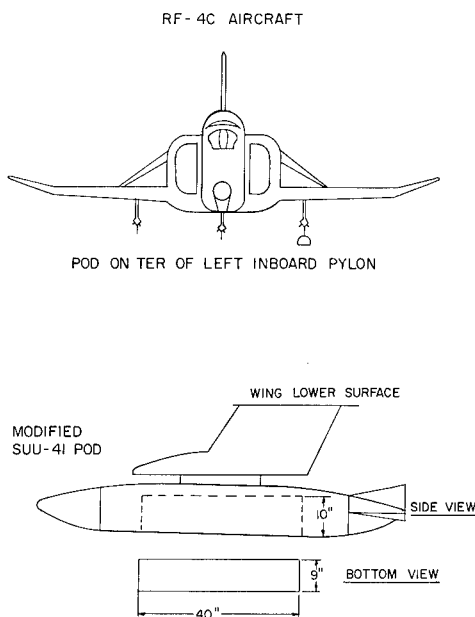


Fig. 2 - Modified SUU-41 Pod Mounted on RF-4C Test Aircraft

Fourier analyzer. Overall time histories, one-third octave band, and narrow band (2 Hz) analyses were performed for selected microphones and flight conditions. Further details of the calibration and data reduction procedures are given in Reference 8.

TEST PROCEDURES

Data were obtained at altitudes of 3,000 ft, 20,000 ft, and 30,000 ft. The aircraft, while at a constant altitude, was slowly accelerated (approximately 2 to 3 minutes) over a Mach number range with data being recorded continuously. The Mach number ranges covered were 0.61 to 0.93 for 3,000 ft and 0.61 to 1.30 for 20,000 ft, and 30,000 ft. Flights requiring speeds in excess of $M = 0.9$ below 30,000 ft were flown over Lake Huron with the remaining flights being flown over Washington Courthouse, Ohio.

TEST RESULTS

a. Static Pressures

The longitudinal variation of the static pressure along the cavity floor is shown in Figure 4 for an altitude of 30,000 ft. The data are presented as the difference between the cavity static pressure P_c and the free-stream static pressure P_∞ normalized with the free-stream static pressures. The static

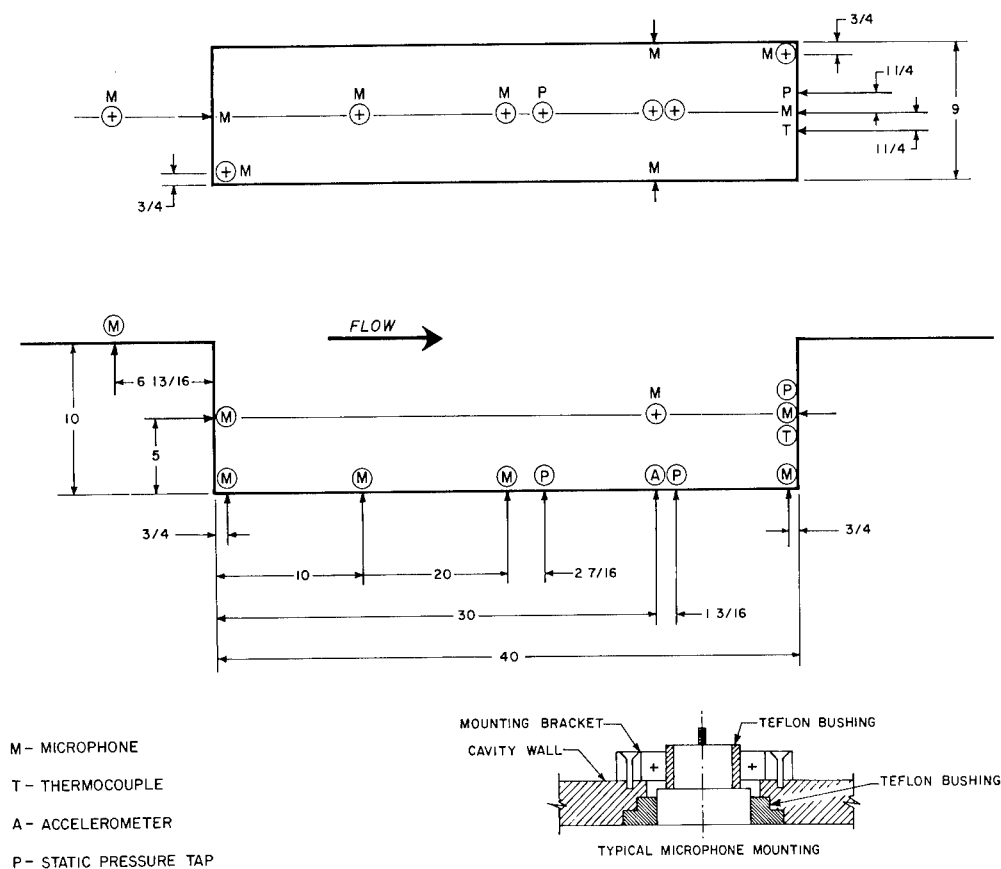


Fig. 3 - Open Cavity Instrumentation Location

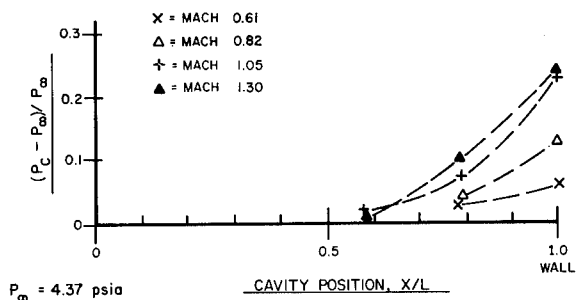


Fig. 4 - Longitudinal Variation of Static Pressure Along Cavity Floor for an Altitude of 30,000 Feet

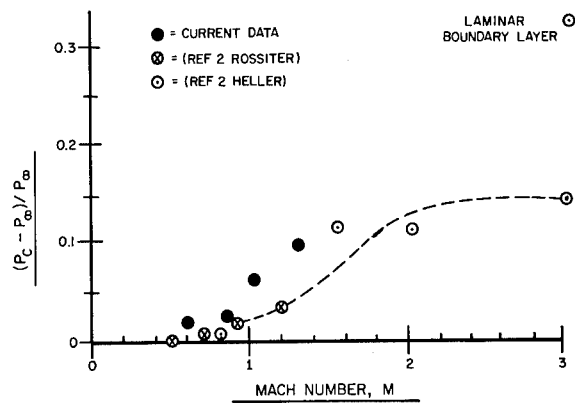


Fig. 5 - Variation of Static Pressure with Mach Number

pressure increased towards the rear of the cavity as was observed in wind tunnel investigations (Reference 2, 5, and 7). The static pressure at each location also showed a tendency to increase with Mach number. This Mach number effect was also observed in References 2 and 7, however, this trend did not continue above Mach 2 in these references. In Figure 5 the average of the static pressure measured at each location is plotted as a function of Mach number and compared to previously obtained wind tunnel data. This figure clearly shows an increase in cavity static pressure with Mach number. The flight data tends to be above the wind tunnel results which can be explained from the fact that from the flight data only pressures in the rear half of the cavity were available whereas in the wind tunnel static pressures were measured over the entire cavity length. Consequently, since the static pressure increased at the rear of the cavity the average flight test static pressure would be greater than the average static pressure determined from the wind tunnel tests.

b. Vibration

An accelerometer was installed in the cavity to insure that the vibration input did not significantly affect the microphone output. The vibration sensitivity of the Gulton microphones was reported to be 90 dB/lg, i.e., 1g of acceleration of the microphones would produce not more than a 90 dB reading. The maximum one-third octave band acceleration level measured at any flight condition was 30 gs. In all cases the measured fluctuating pressure level was at least 30 dB greater than the vibration induced level, thus it was assumed that the vibration of the cavity walls had no significant effect on the microphone outputs.

c. Fluctuating Pressures

The fluctuating pressure levels were obtained from the nine microphones. The overall time histories from the fore end of the cavity for 3,000 ft, 20,000 ft, and 30,000 ft altitudes are shown in Figure 6. The overall fluctuating pressure level is seen to increase with Mach number at all altitudes and at any Mach number the highest level occurs at the lowest altitude. These time histories are typical of all test results. However, the results from other longitudinal locations showed greater differences between the levels measured at the three altitudes resulting in a lack of free-stream dynamic pressure (q) scaling. In Reference 2 it was assumed that the flow induced cavity oscillations scaled with free-stream dynamic pressure, however, the flight test data show that the fluctuating pressure levels do not scale at certain longitudinal locations as will be illustrated in Figure 11.

A typical narrow band spectrum from the front of the cavity for the 20,000 ft alti-

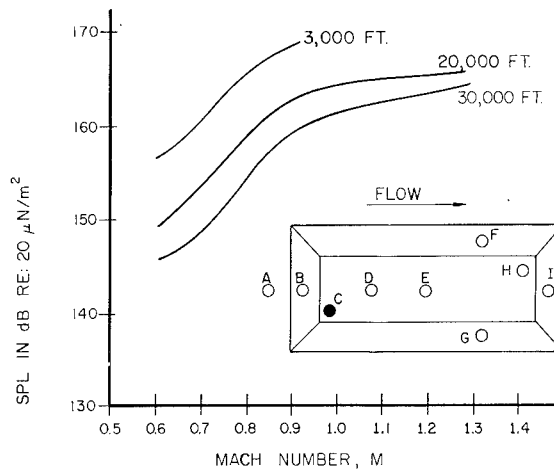


Fig. 6 - Overall Fluctuating Pressure Time Histories from the Front of the Cavity

tude and a Mach number of 1.30 is shown in Figure 7. The resonant frequencies are clearly evident and agree with the resonant frequencies determined from the modified Rossiter equation (Reference 2):

$$S = \frac{f L}{V} = \frac{m - 0.25}{\frac{M}{(1 + \frac{K-1}{2} M^2)^{1/2}} + 1.75} \quad (1) \quad m = 1, 2, 3$$

where the $m = 1$ frequency is referred to as the mode one frequency, etc. The nondimensional resonant frequencies calculated for all observed resonances are shown in Figure 8 along with data from Reference 2 and compared to the modified Rossiter equation. The agreement is quite good.

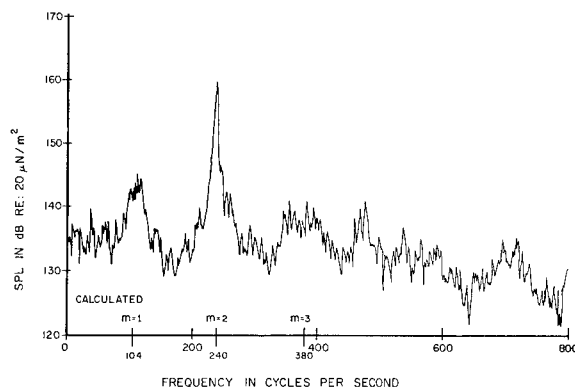


Fig. 7 - Two Hz Narrowband Spectrum from the Front of the Cavity at 20,000 Foot Altitude at Mach Number 1.30

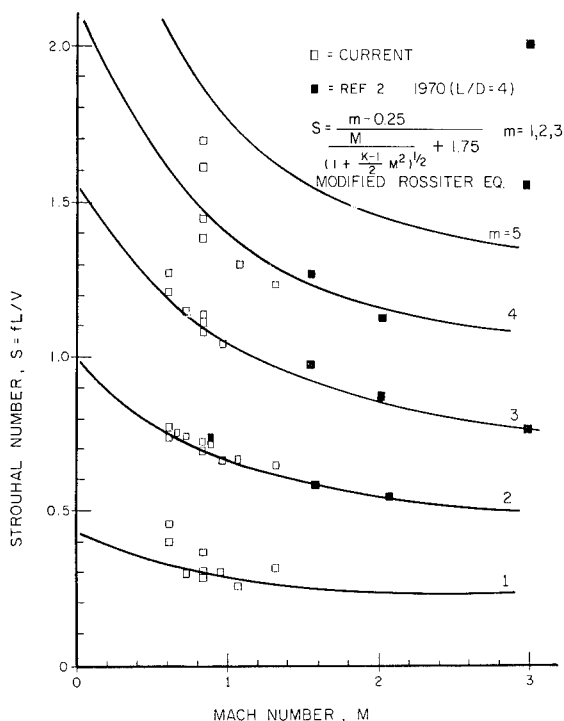


Fig. 8 - Comparison of the Nondimensional Resonant Frequencies with the Modified Rossiter Formula

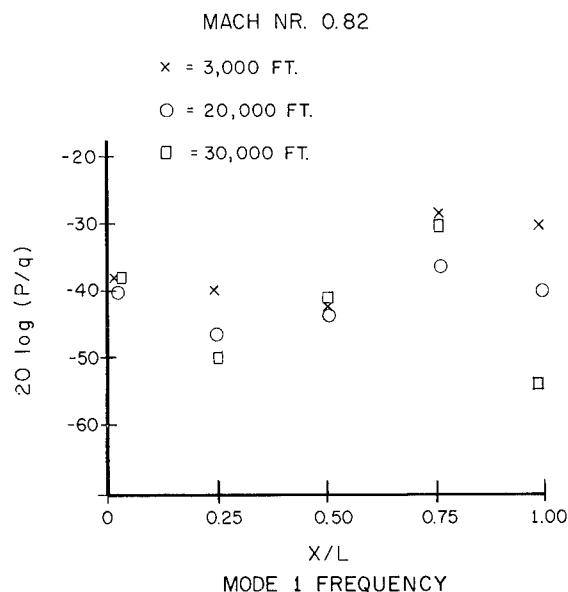


Fig. 10 - Longitudinal Variation of Peak One-Third Octave Band Referenced to Free Stream Dynamic Pressure Depicting Mode Shapes for Mach Number 0.82

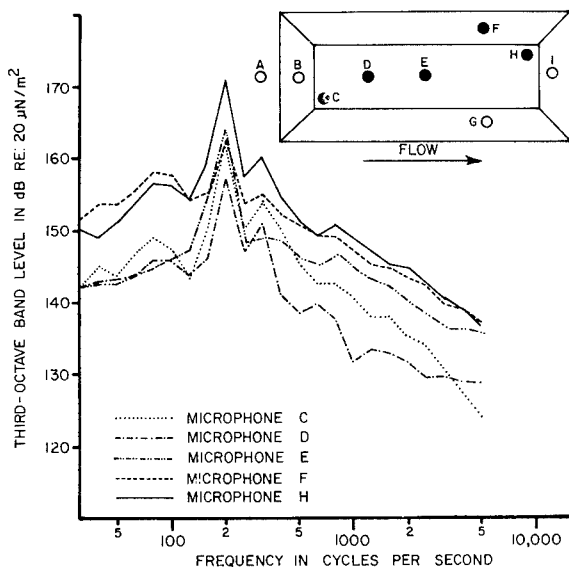


Fig. 9 - One-Third Octave Spectra for 3,000 Foot Altitude at Mach 0.82 Displaying Longitudinal Effect on Broadband Level

The longitudinal variation of the one-third octave band spectra are shown in Figure 9 for an altitude of 3,000 ft and a Mach number of 0.82. This variation is also shown in Figure 10 for the mode one frequency at Mach 0.82 for all altitudes. The measured one-third octave band level containing this frequency is normalized with the free-stream dynamic pressure and plotted against the non-dimensional cavity location. The lack of dynamic pressure scaling is evident at a number of cavity locations and only scales at $X/L = 0$ and $X/L = 0.5$.

In Reference 2, mode shapes were presented for the first three mode frequencies and are shown in Figure 11. These mode shapes were obtained from microphone outputs on an axis near the center of the cavity and were used to determine mode shapes for the flight test data. It was assumed that flight test data followed similar variations and ramped sinusoidal equations were derived to fit the data. The resulting equations describing the variation in normalized sound pressure level, $20 \log (P_m/q)_{X/L}$, with normalized longitudinal distance, X/L , as determined from the 3,000 ft altitude data are:

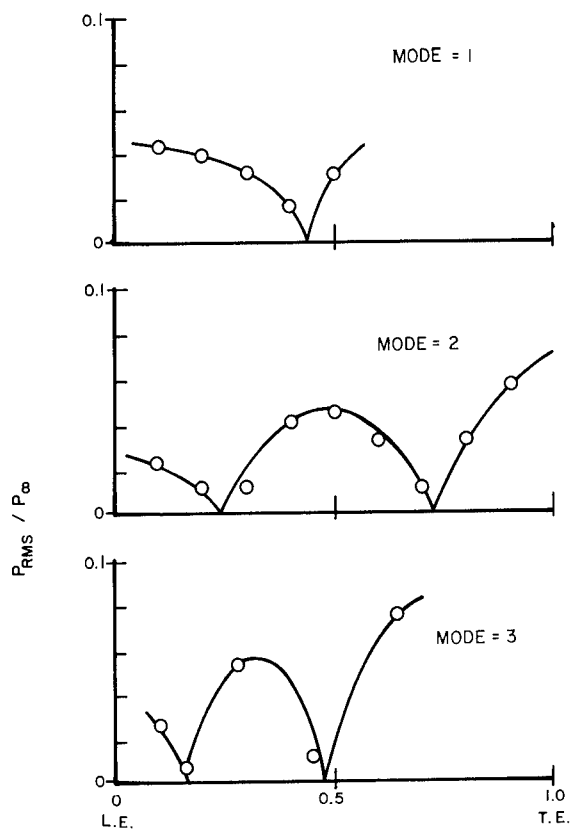


Fig. 11 - Suggested Shape for First, Second and Third Order Modes from Reference 2

$$20 \log (P_m/q)_{X/L} = 20 \log (P_m/q)_{\max} \quad (2)$$

$$-10(1.7 - 0.7 X/L - |\cos \alpha_m X/L|) \quad m=1,2,3$$

where: $20 \log (P_m/q)_{\max}$ = the normalized sound pressure level at $X/L = 1$

$$\alpha_1 = 3.5$$

$$\alpha_2 = 6.3$$

$$\alpha_3 = 10.0$$

These equations are plotted in Figure 12 for an altitude of 3,000 feet and a Mach number 0.82 where the fluctuating pressure has been normalized with the free-stream dynamic pressure.

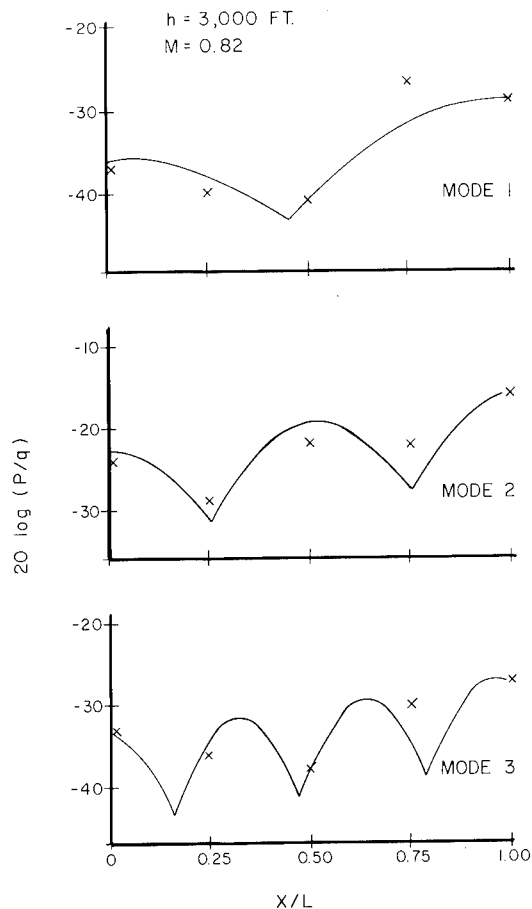


Fig. 12 - Comparison of Mode Shape Equations with the Measured Data for an Altitude of 3,000 Feet and Mach Number 0.82

The flight test data are also shown in Figure 12. The agreement is seen to be quite good except at $X/L = 0.75$ where the microphone was located on the center of the side wall rather than the floor, thus indicating variation in the depth direction. These equations, describing the longitudinal variation of the peak fluctuating pressure levels, are assumed to apply at all altitudes and Mach numbers for which data were obtained.

The solution of these equations requires the determination of $20 \log (P_m/q)_{\max}$ for each mode frequency. The normalized expression for $(SPL_2)_{\max}$ was determined from a second order least square curve which encompassed all measured data points as shown in Figure 13 and given by:

$$20 \log (P_{2\max}/q) = -4 + 20 \log (-M^2 + 2M - 0.7) \quad (3)$$

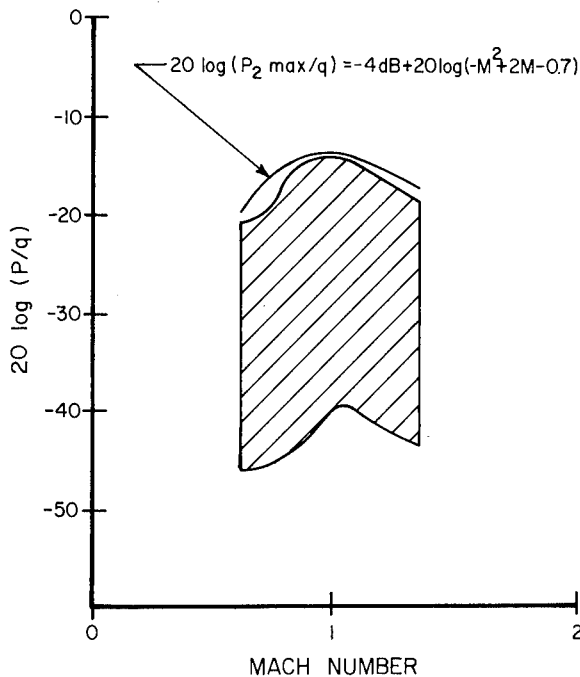


Fig. 13 - Prediction Curve for Peak One-Third Octave SPL at the Aft End of the Cavity

where: P_{2max} = mode 2 rms pressure
 q = free stream dynamic pressure
 M = Mach number

The values for the normalized fluctuating pressures corresponding to the other mode frequencies were observed to be

$$20 \log (P_{1max}/q) = 20 \log (P_{2max}/q) - 14 \quad (4)$$

$$20 \log (P_{3max}/q) = \begin{cases} 20 \log (P_{2max}/q) - 11 & M > 0.7 \\ 20 \log (P_{2max}/q) & M \leq 0.7 \end{cases} \quad (5)$$

The above expressions enable the estimation of the amplitude, frequency, and longitudinal distribution of the fluctuating pressures associated with cavity resonance. In order to predict the complete one-third octave band spectrum, broadband levels are also required.

The broadband levels were shown in Figure 9 to increase towards the aft end of the cavity, which was also observed in wind tunnel tests (References 2, 5, and 7). In general, this increase was approximately 10 dB from the front to the aft of the cavity. For prediction purposes a linear variation was assumed. Figure 14 presents one-third octave spectra from the front of the cavity for an altitude of 30,000 ft and for various Mach numbers with the data referenced to the free-stream dynamic pressure. The normalized broadband levels are seen to increase with increasing Mach number. For prediction purposes the shape of the broadband spectrum was assumed to follow the Strouhal relationship given in Figure 15. The maximum level is established by the Mode 2 resonant frequency peak and the longitudinal position. Note that this assumes that the broadband levels vary with Mach number as did the maximum value of the mode two rms pressure.

Equations 1 through 5 and Figure 15 can now be used to predict the complete one-third octave band spectrum and distribution of the fluctuating pressure in an open rectangular cavity with an L/D of 4 for a Mach number range of 0.6 to 1.3. For clarity an example of the application of this scheme is given below and results are compared to those obtained using the method presented in Reference 2.

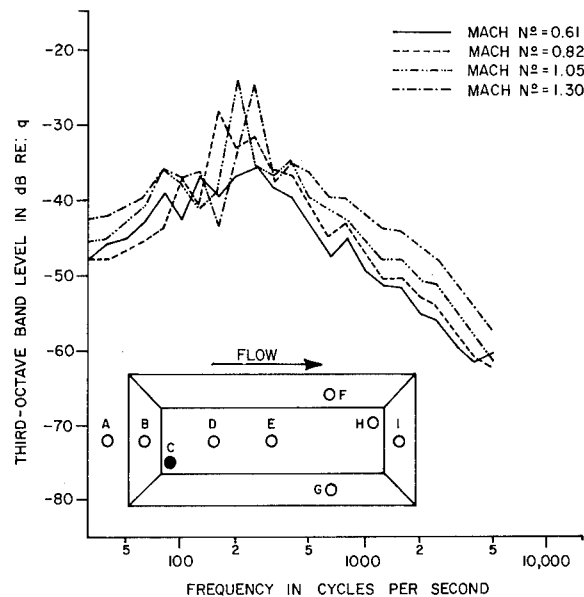


Fig. 14 - One-Third Octave Band Spectra from the Front of the Cavity at 30,000 Foot Altitude

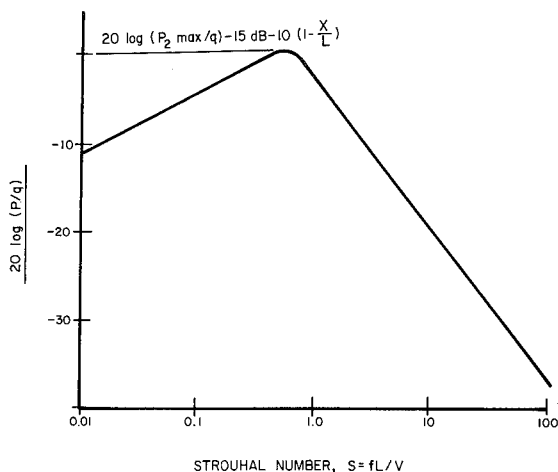


Fig. 15 - Broadband Level Versus Strouhal Number

d. Working Example

Consider the case of an aircraft flying at Mach 0.9 near sea level with an open nearly rectangular cavity 20 feet long and 5 feet deep. It is desired to predict the aero-acoustic environment at the center and at the rear of the cavity. The solution is obtained as follows:

Step I

The first step is to determine the resonant frequencies. This is accomplished using the modified Rossiter equation (Equation 1)

$$f_m = \frac{V}{L} \frac{\frac{m - 0.25}{M}}{\left(1 + \frac{K-1}{2} M^2\right)^{1/2}} + 1.75 \quad m=1,2,3$$

$$\begin{aligned} f_1 &= 15 \text{ Hz} \\ f_2 &= 34 \text{ Hz} \\ f_3 &= 54 \text{ Hz} \end{aligned}$$

Step II

The second step is to determine the maximum normalized amplitude for each mode frequency.

$$\begin{aligned} 20 \log (P_{2\max}/q) &= 20 \log (-M^2 + 2M - 0.7) \\ -4 \text{ dB} &= -15 \text{ dB} \end{aligned} \quad (\text{Eq 3})$$

$$\begin{aligned} 20 \log (P_{1\max}/q) &= 20 \log (P_{2\max}/q) \\ -14 \text{ dB} &= -29 \text{ dB} \end{aligned} \quad (\text{Eq 4})$$

$$\begin{aligned} 20 \log (P_{3\max}/q) &= 20 \log (P_{2\max}/q) \\ -11 \text{ dB} &= -26 \text{ dB} \end{aligned} \quad (\text{Eq 5})$$

Step III

The normalized fluctuating pressure amplitudes at the center of the cavity are now found for each mode frequency from Equation 2.

$$\begin{aligned} 20 \log (P_m/q)_{X/L} &= 20 \log (P_m/q)_{\max} \\ &- 10 (1.7 - 0.7 X/L - |\cos^{\alpha_m} X/L|) \\ &m=1,2,3 \end{aligned}$$

$$\begin{aligned} \alpha_1 &= 3.5 \\ \alpha_2 &= 6.3 \\ \alpha_3 &= 10.0 \end{aligned}$$

Thus at $X/L = 0.5$ the levels referenced to $20 \mu\text{N}/\text{m}^2$ are:

$$\begin{aligned} \text{SPL}_1 &= 148 \text{ dB} \\ \text{SPL}_2 &= 170 \text{ dB} \\ \text{SPL}_3 &= 152 \text{ dB} \end{aligned}$$

At $X/L = 1.0$ the levels obtained from Equations 3 to 5 are not altered by Equation 2 since this position is an antinode for each mode.

Thus, for $X/L = 1.0$

$$\begin{aligned} \text{SPL}_1 &= 160 \text{ dB} \\ \text{SPL}_2 &= 174 \text{ dB} \\ \text{SPL}_3 &= 163 \text{ dB} \end{aligned}$$

Step IV

The final step is to determine the broadband levels. This is done by entering Figure 15 with

$$\begin{aligned} 20 \log (P_{2\max}/q) &- 15 \text{ dB} - 10 (1 - X/L) \\ &= \begin{cases} -35 & \text{for } X/L = 0.5 \\ -30 & \text{for } X/L = 1.0 \end{cases} \end{aligned}$$

and reading other values.

The spectra obtained are shown in Figure 16 along with the spectrum one would predict using the scheme offered in Reference 2. The

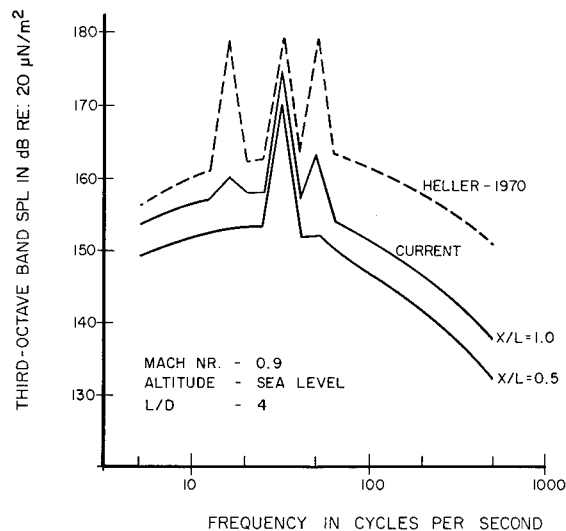


Fig. 16 - Comparison of Spectra from the Working Example for the Current Prediction Scheme and Heller's

current results show resonant modes 1 and 3 completely attenuated for the center position, this is due to the longitudinal mode shapes. The $X/L = 0.5$ position is seen in Figure 12 to be a node for the mode 1 and 3 frequencies while an antinode for mode 2.

CONCLUDING REMARKS

Based on the results of the investigation the following conclusions are made:

1. The resonant frequencies are accurately predicted by the modified Rossiter equation.
2. Free-stream dynamic pressure scaling appears to fail for certain locations in the cavity.
3. The longitudinal variation in the resonant amplitude shows a strong tendency to follow the mode shapes observed in Reference 2.
4. The current prediction scheme results in realistic levels while accounting for longitudinal variations in the resonant amplitudes and is recommended for application within the range of parameters of the test data.

REFERENCES

1. East, L. F., "Aerodynamical Induced Resonance in Rectangular Cavities", Journal of Vibration and Sound, May 1966.
2. Heller, H. H., Holmes, G. Covert, E. E., "Flow-Induced Pressure Oscillations in Shallow Cavities", AFFDL-TR-70-104, Dec 1970.
3. Krishnamurty, K., "Acoustic Radiation from Two-Dimensional Rectangular Cutouts in Aerodynamic Surfaces", NACA Tech Note 3487, August 1955.
4. Maull, D. J., and East, L. F., "Three-Dimensional Flow in Cavities", Journal of Fluid Mech 16, pp 620, 1963.
5. Plumblee, H. D., Gibson, J. S., and Lassiter, L. W., "A Theoretical and Experimental Investigation of the Acoustic Response of Cavities in Aerodynamic Flow", WADD-TR-61-75, 1962.
6. Roshko, A., "Some Measurements of Flow in a Rectangular Cutout", NACA Tech Note 3488, 1955.
7. Rossiter, J. E., "Wind Tunnel Experiments on the Flow Over Rectangular Cavities at Subsonic and Transonic Speeds", RAE Rep Nr 64037, R&M Nr 3438, 1966.
8. Shaw, L. L., et al, "Aero-Acoustic Environment of a Rectangular Cavity with a Length to Depth Ratio of Four", AFFDL-TM-73-130-FYA, to be published.

RESPONSE OF LINEAR DYNAMICAL SYSTEMS UNDER NONSTATIONARY RANDOM EXCITATIONS

T.S. Sankar and D. Doan
Department of Mechanical Engineering
Sir George Williams University
Montreal H3G 1M8, Canada

This paper presents an analytical investigation of single-degree-of-freedom linear dynamical systems subjected to nonstationary type of random excitations. Expressions for the corresponding nonstationary responses are derived using the impulse response characteristics of the system. The input excitation is modelled as a product of a modulating component and a stationary white noise stochastic component of zero mean. Under such representation, the autocorrelation of the input excitation is a delta function with a specified strength function. Purely harmonic, harmonic with exponential decay, and simple linear variations are considered for the strength function to simulate a wide variety of nonstationary forces. The variation of the maximum mean square amplitudes of the system responses and their phase angles against frequency ratios are presented in the form of plots for different values of the system parameters. From the results, the "resonance regions" are identified and conclusions are drawn on the behaviour of dynamical systems under nonstationary random excitations.

INTRODUCTION

Most of the random processes occurring in reality are essentially nonstationary in character. Examples of such physical random processes are forces due to explosions, shock, and earthquake; gust response; vibrations environment of vehicles; forces arising from rapid acceleration or deceleration; and similar transient phenomena. To a large extent, random excitations experienced by many mechanical systems are also of nonstationary type. The reason for this is, in most dynamical systems, the external forces contain random disturbances in addition to dynamically fluctuating deterministic forces. For example, mechanical systems such as connecting rods, suspensions, gear trains, etc. do experience random excitations, over and above the dynamic forces, that vary rapidly in magnitude during specific operating time intervals. Another justification for nonstationary excitation arises from the consideration that any measured excitation process may not be long enough to provide statistical properties independent of time. It is then important to have a knowledge of the response of linear systems under such random excitation environments.

The behaviour of linear dynamical systems under stationary random excitations has been extensively investigated by many [1, 2, 6].

However, similar investigations when the excitation is nonstationary are very few. In this paper, the nonstationary random excitation on the system is considered as the product of a modulating part and a stationary white noise process. This concept was introduced by Roberts [3, 4] and was also investigated by different methods by Barnoski and Maurer [7], and Bucciarrelli and Kuo [8] recently.

As mentioned, a nonstationary excitation $Z(t)$ is expressed in terms of a modulating part $Z_1(t)$ and a stationary white noise excitation $F(t)$ of zero mean in the form

$$Z(t) = Z_1(t) F(t) \quad (1)$$

Such a definition will yield an autocorrelation function of the form

$$R_{ZZ}(t_1, t_2) = I(t_1) \delta(t_1 - t_2) \quad (2)$$

where $\delta(\cdot)$ is a Dirac Delta function and $I(t_1)$ is known as a strength function [3] of the autocorrelation of the excitation force. When $I(t_1)$ is a constant, $Z(t)$ is the well-known stationary white noise excitation; on the other hand, if $I(t_1)$ is a function of time, $Z(t)$ yields a nonstationary white noise process [3].

In this investigation, following three

types of strength functions are considered:

i) harmonic with exponential decay; that is,

$$I(t_1) = Ae^{-\alpha p |t_1|} \cos pt_1 \quad (3)$$

ii) purely exponential decay for which

$$I(t_1) = Ae^{-\alpha |t_1|} \quad (4)$$

iii) simple linear decay for which

$$I(t_1) = A \left(1 - \frac{|t_1|}{T}\right), \text{ for } |t_1| < T \\ = 0 \text{ for } |t_1| > T \quad (5)$$

where A is a known amplitude, α and p are non-negative constants.

PRELIMINARIES

Consider a damped mass spring oscillator as shown in Figure 1. The equation of motion for the system is:

$$m\ddot{X}(t) + c\dot{X}(t) + kX(t) = F(t) \quad (6)$$

Here, m : mass of oscillator
c : constant of viscous damper
k : linear spring constant
F(t): nonstationary random excitation
X(t): displacement of mass m

Let $c/m = 2\zeta\omega_n$
 $k/m = \omega_n^2$
 $F(t)/m = Z(t)$

where ω_n : natural frequency of the system
 ζ : damping ratio

Eq.(6) now takes the form

$$\ddot{X}(t) + 2\zeta\omega_n\dot{X}(t) + \omega_n^2 X(t) = Z(t) \quad (7)$$

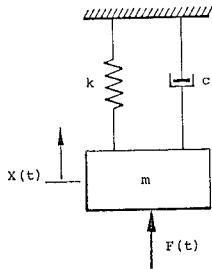


Fig.1: Idealized Dynamic System

The random excitation Z(t) in this equation is nonstationary taking the form expressed in Eq.(1), such that the strength function of its autocorrelation might take successively the form given in Eqs.(3), (4) and (5). The analysis described is conducted in the time domain to determine the corresponding mean square values of the response X(t).

SYSTEM RESPONSE UNDER HARMONICALLY VARYING STRENGTH FUNCTION WITH AN EXPONENTIAL DECAY

In this case, the autocorrelation of the input Z(t) has the form

$$R_{ZZ}(t_1, t_2) = Ae^{-\alpha p |t_1|} \cos pt_1 \delta(t_1 - t_2) \quad (8)$$

where A, α , p are positive constants. The physical nature of the excitation may be explained by evaluating the power spectral density of Z(t) which can be obtained by taking the double Fourier transform of $R_{ZZ}(t_1, t_2)$ [5],

$$S_{ZZ}(\omega_1, \omega_2) = \int_{-\infty}^{\infty} \int_{-\infty}^{\infty} R_{ZZ}(t_1, t_2) e^{-j(\omega_1 t_1 - \omega_2 t_2)} dt_1 dt_2 \quad (9)$$

It may be pointed out that, for delta-correlated processes such as those considered here, $S_{ZZ}(\omega_1, \omega_2)$ is always a function of $(\omega_1 - \omega_2)$ as derived by Mark [9]. Then, it follows directly that $S_{ZZ}(\omega_1 - \omega_2)$ is the complex conjugate of the Fourier transform of $I(t_1)$ and therefore describes the frequency content of the strength function $I(t_1)$.

For infinite operating time systems, the autocorrelation of the response X(t) is [1],

$$R_{XX}(t_1, t_2) = \int_0^{\infty} \int_0^{\infty} h(\xi_1) h(\xi_2) R_{ZZ}(t_1 - \xi_1, t_2 - \xi_2) d\xi_1 d\xi_2 \quad (10)$$

where $h(\xi) = \frac{1}{\omega_d} e^{-\zeta\omega_n t} \sin \omega_d t$, is the impulse response of the system. Here

$$\omega_d = \omega_n(1 - \zeta^2)^{1/2}$$

Substituting $R_{ZZ}(t_1, t_2)$ from Eq.(8) into Eq.(10) and integrating, the autocorrelation of the response X(t) of the system may be obtained as

$$R_{XX}(t_1, t_2) = \frac{Ae^{-\zeta\omega_n |t_2 - t_1| - \alpha p |t_1|}}{2\omega_d^2} \left[\frac{2a \cdot (2\zeta\omega_n - \alpha p)(2\omega_d)p + 2b \cdot (2\omega_d)[(2\zeta\omega_n - \alpha p)^2 + (2\omega_d)^2 + p^2]}{[(2\zeta\omega_n - \alpha p)^2 + (2\omega_d - p)^2][(2\zeta\omega_n - \alpha p)^2 + (2\omega_d + p)^2]} \right. \\ - \frac{c \cdot p(2\zeta\omega_n - \alpha p)^2 + p^2 - (2\omega_d)^2}{[(2\zeta\omega_n - \alpha p)^2 + (2\omega_d - p)^2][(2\zeta\omega_n - \alpha p)^2 + (2\omega_d + p)^2]} \\ - \frac{d \cdot (2\zeta\omega_n - \alpha p)[(2\zeta\omega_n - \alpha p)^2 + p^2 + (2\omega_d)^2]}{[(2\zeta\omega_n - \alpha p)^2 + (2\omega_d - p)^2][(2\zeta\omega_n - \alpha p)^2 + (2\omega_d + p)^2]} \\ \left. + \frac{c \cdot p + d \cdot (2\zeta\omega_n - \alpha p)}{[(2\zeta\omega_n - \alpha p)^2 + p^2]} \right] \quad (11)$$

$$\text{where, } \begin{cases} a = \sin \omega_d(t_2 - t_1) \sin pt_1 \\ b = \sin \omega_d(t_2 - t_1) \cos pt_1 \\ c = \cos \omega_d(t_2 - t_1) \sin pt_1 \\ d = \cos \omega_d(t_2 - t_1) \cos pt_1 \end{cases} \quad (12)$$

The mean value of $X(t)$ may be obtained by setting $t_1 = t_2 = t$ in Eq. (11),

$$\begin{aligned}
 E[X^2(t)] &= R_{XX}(t, t) \\
 &= \frac{Ae^{-\alpha p|t|}}{2\omega_n^3 \sqrt{1-\zeta^2}} \left\{ \left[\frac{p'}{(2\zeta - \alpha p')^2 + p'^2} \right. \right. \\
 &\quad - \frac{p'[(2\zeta - \alpha p')^2 + p'^2 - 4(1-\zeta^2)]}{[(2\zeta - \alpha p')^2 + (2\sqrt{1-\zeta^2} - p')^2][(2\zeta - \alpha p')^2 + (2\sqrt{1-\zeta^2} + p')^2]} \\
 &\quad \sin pt + \left[\frac{(2\zeta - \alpha p')}{(2\zeta - \alpha p')^2 + p'^2} \right. \\
 &\quad \left. \left. - \frac{(2\zeta - \alpha p')[(2\zeta - \alpha p')^2 + p'^2 + 4(1-\zeta^2)]}{[(2\zeta - \alpha p')^2 + (2\sqrt{1-\zeta^2} - p')^2][(2\zeta - \alpha p')^2 + (2\sqrt{1-\zeta^2} + p')^2]} \right] \right. \\
 &\quad \left. \cos pt \right\} \quad (13)
 \end{aligned}$$

where $p' = p/\omega_n$. Recognizing Eq. (13) in the form

$$E[X^2(t)] = \frac{A e^{-\alpha p|t|}}{\omega_n^3} (P \sin pt + Q \cos pt) \quad (14)$$

$$= \frac{A e^{-\alpha p|t|}}{\omega_n^3} R \cos(pt + \phi) \quad (15)$$

$$\text{where } R = (P^2 + Q^2)^{\frac{1}{2}} \quad (16a)$$

$$\phi = \tan^{-1} \left(\frac{P}{Q} \right). \quad (16b)$$

R and ϕ may be considered as the maximum amplitude and phase components of the mean square response of the system.

Figures 2 and 3 give the values of the quantities R and ϕ as functions of frequency ratio p/ω_n for different values of damping ratio ζ , when $\alpha = 0.2$. From Figure 2, it may be noted that large values for the maximum mean square amplitude R occur in the region $p/\omega_n \approx 0$ and $p/\omega_n \approx 2.0$. The peaks are more pronounced for small damping ratios, especially when $\zeta < 0.4$.

Similar plots for $\alpha = 1.0$ are given in Figures 4 and 5. The behaviour of the system is essentially the same as for $\alpha = 0.2$ except that the peak amplitudes are relatively closely spaced. Also, unlike the plots for $\alpha = 0.2$, there is only one dominant peak or "resonance region" in this case for every ζ value.

Figures 6 and 7 show the maximum mean square amplitude R of the response $X(t)$ as function of frequency ratio p/ω_n for different values of the decay parameter α of the strength function, for a given system with damping $\zeta = .25$ and $\zeta = .45$ respectively. From these figures, it may be seen that all the curves start at the same point when $p/\omega_n = 0$. This means that the maximum mean square response of the system is a constant regardless of the values of the decay parameter α when the correlation frequency of the excitation is zero.

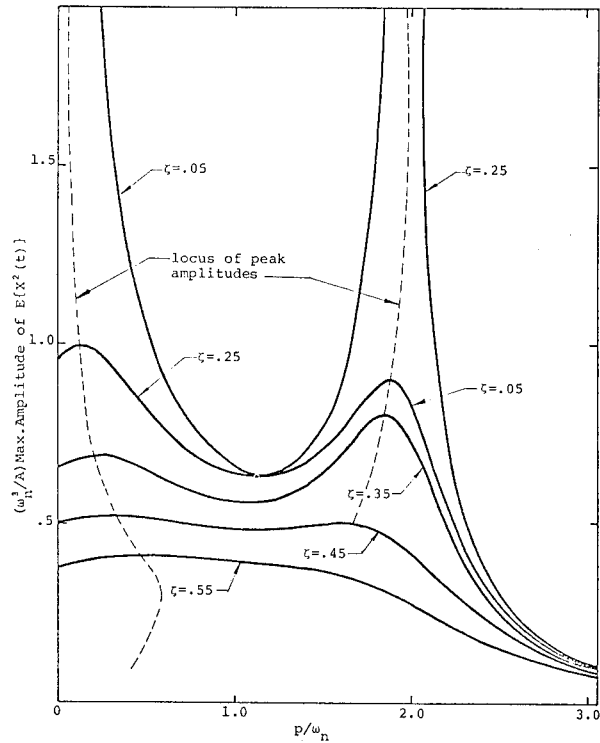


Fig.2: Maximum Amplitude $E[X^2(t)]$ against p/ω_n , $\alpha = 0.2$.

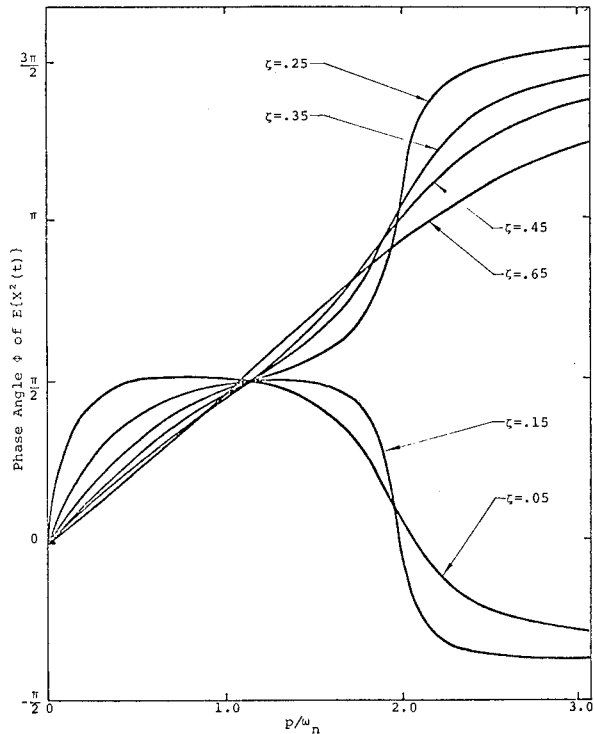


Fig.3: Phase Angle of $E[X^2(t)]$ against p/ω_n , $\alpha = 0.2$

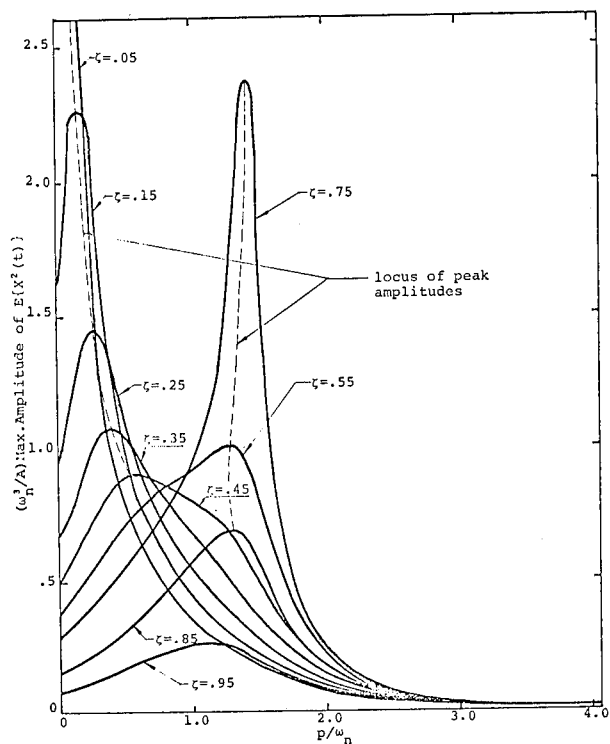


Fig.4: Maximum Amplitude $E[X^2(t)]$ against p/ω_n , $\alpha = 1.0$

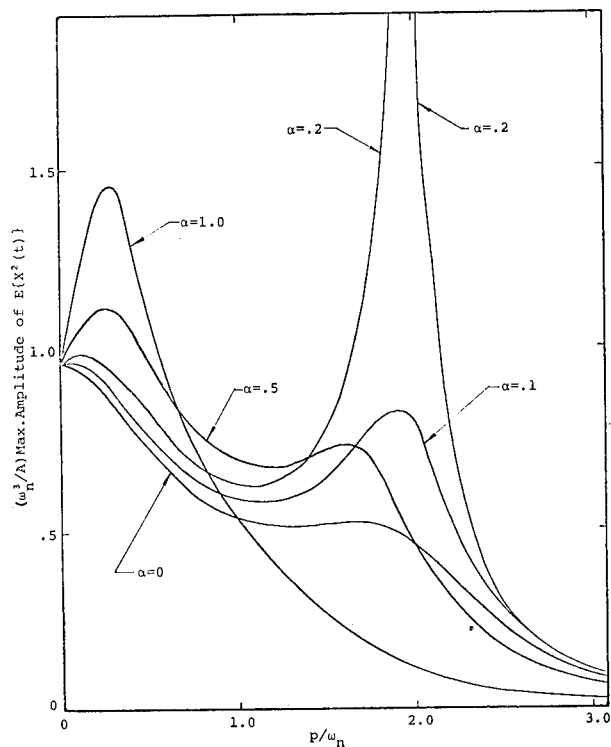


Fig.6: Maximum Amplitude $E[X^2(t)]$ against p/ω_n , $\zeta = 0.25$

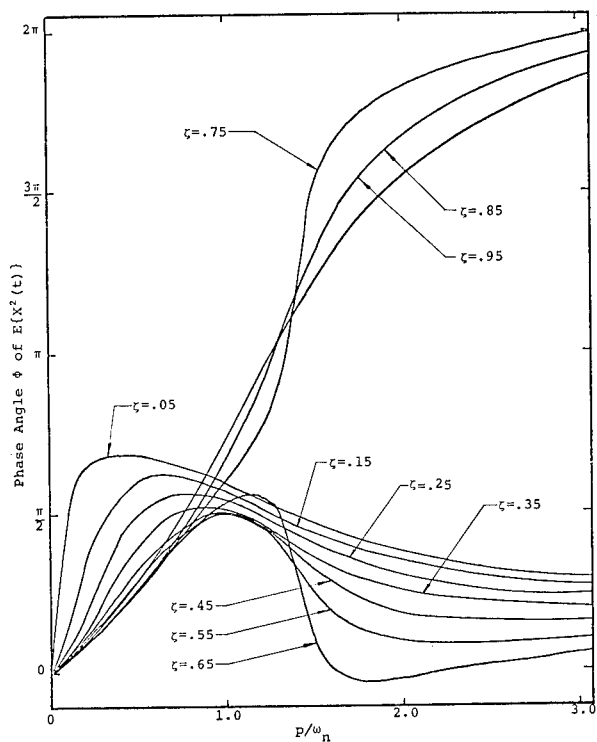


Fig.5: Phase Angle of $E[X^2(t)]$ against p/ω_n , $\alpha = 1.0$

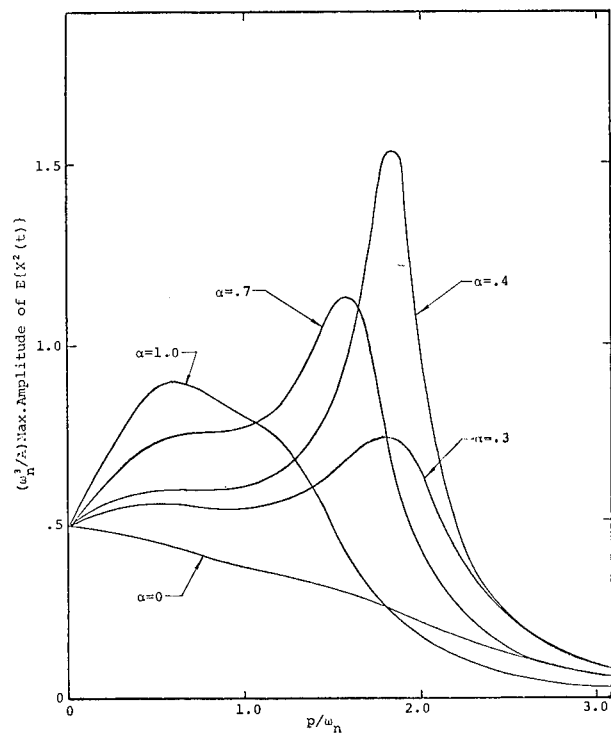


Fig.7: Maximum Amplitude $E[X^2(t)]$ against p/ω_n , $\zeta = 0.45$

Special Case 1 : $\alpha = 0$

When $\alpha = 0$, the input autocorrelation $R_{ZZ}(t_1, t_2)$ has a harmonically varying strength function $I(t_1)$, namely,

$$R_{ZZ}(t_1, t_2) = A \cos pt \delta(t_1 - t_2) \quad (17)$$

Setting $\alpha = 0$ in Eq.(11), the autocorrelation of the response $X(t)$ becomes

$$R_{XX}(t_1, t_2) = \frac{Ae^{-\zeta\omega_n |t_2 - t_1|}}{2\omega_d^2} \left[\frac{2a(2\zeta\omega_n)(2\omega_d)p + 2b(2\omega_d) [(2\zeta\omega_n)^2 + (2\omega_d)^2 + p^2]}{[(2\zeta\omega_n)^2 + (2\omega_d - p)^2][(2\zeta\omega_n)^2 + (2\omega_d + p)^2]} - \frac{cp[(2\zeta\omega_n)^2 + p^2 - (2\omega_d)^2]}{[(2\zeta\omega_n)^2 + (2\omega_d - p)^2][(2\zeta\omega_n)^2 + (2\omega_d + p)^2]} - \frac{d(2\zeta\omega_n)[(2\zeta\omega_n)^2 + p^2 + (2\omega_d)^2]}{[(2\zeta\omega_n)^2 + (2\omega_d - p)^2][(2\zeta\omega_n)^2 + (2\omega_d + p)^2]} + \frac{cp + d(2\zeta\omega_n)}{[(2\zeta\omega_n)^2 + p^2]} \right] \quad (18)$$

where the expressions for a , b , c and d are given under Eq.(12).

The mean square value of the response $X(t)$ is now obtained either by setting $\alpha = 0$ in Eq.(13) or by setting $t_1 = t_2 = t$ in Eq.(18). Then,

$$E[X^2(t)] = \frac{A}{2\omega_n^3 \sqrt{1-\zeta^2}} \left\{ \left[\frac{p'}{(2\zeta)^2 + p'^2} - \frac{p'[(2\zeta)^2 + p'^2 - 4(1-\zeta^2)]}{(4+p'^2)^2 - [4p'\sqrt{1-\zeta^2}]^2} \right] \sin pt + \left[\frac{2\zeta}{(2\zeta)^2 + p'^2} - \frac{2\zeta(4+p'^2)}{(4+p'^2)^2 - [4p'\sqrt{1-\zeta^2}]^2} \right] \cos pt \right\} \quad (19)$$

where $p' = p/\omega_n$.

This can also be written in the form

$$E[X^2(t)] = \frac{A}{\omega_n^3} [P_0 \sin pt + Q_0 \cos pt] \quad (20)$$

or

$$E[X^2(t)] = \frac{A}{\omega_n^3} R_0 \cos(pt + \phi_0) \quad (21)$$

$$\text{where } R_0 = (P_0^2 + Q_0^2)^{\frac{1}{2}} \quad (22a)$$

$$\phi_0 = \tan^{-1} \left(\frac{P_0}{Q_0} \right) \quad (22b)$$

The quantities R_0 and ϕ_0 are plotted against p/ω_n in Figures 8 and 9 for a range of values of damping ratio ζ . The results for this particular case are identical to those obtained

by Roberts [3,4].

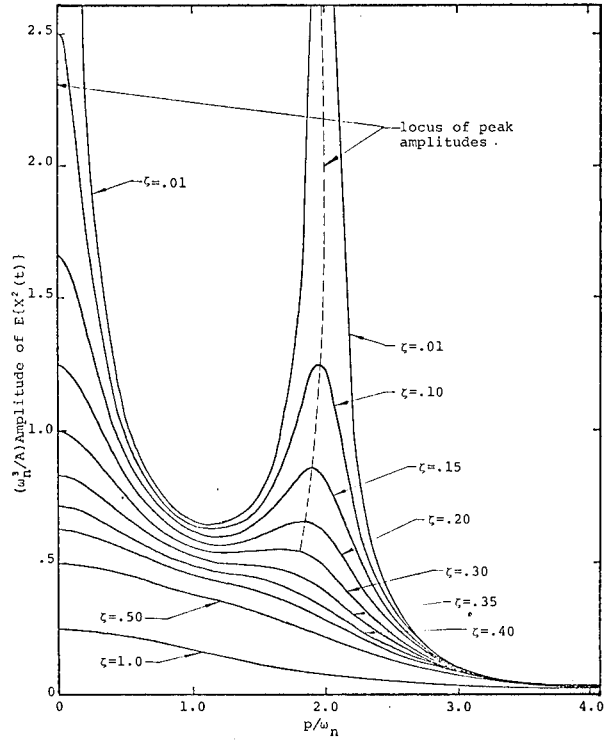


Fig.8: Amplitude $E[X^2(t)]$ against p/ω_n , $\alpha = 0$.

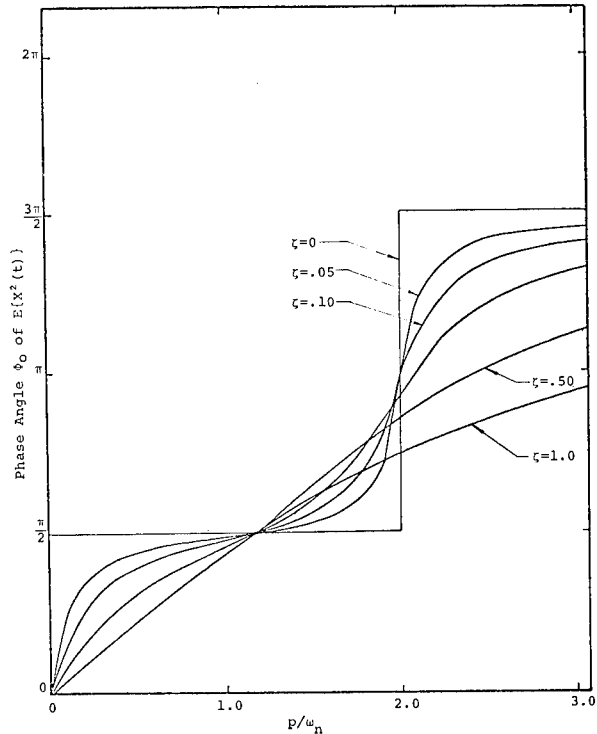


Fig.9: Phase Angle of $E[X^2(t)]$ against p/ω_n , $\alpha = 0$

Special Case 2 : $p = 0$

When $p = 0$, the autocorrelation of the input $Z(t)$ in Eq.(8) becomes

$$R_{ZZ}(t_1, t_2) = A \delta(t_1 - t_2) \quad (23)$$

or

$$R_{ZZ}(\tau) = A \delta(\tau) \quad (24)$$

where $\tau = |t_1 - t_2|$, and the input process $Z(t)$ in this case becomes a stationary white noise process with an intensity A .

From Eq.(11), when $p = 0$, the autocorrelation of the response $X(t)$ takes the form

$$R_{XX}(\tau) = \frac{Ae^{-\zeta\omega_n\tau}}{4\zeta\omega_n^3} \left[\frac{\zeta}{\sqrt{1-\zeta^2}} \sin\omega_d\tau + \cos\omega_d\tau \right] \quad (25)$$

Usually for stationary white noise excitation, the amplitude of strength function A is written in the form $A = 2\pi S_0$, where S_0 is the constant value of the spectral density of the excitation. Therefore, Eq.(25) may be rewritten as

$$R_{XX}(\tau) = \frac{\pi S_0 e^{-\zeta\omega_n\tau}}{2\zeta\omega_n^3} \left[\frac{\zeta}{\sqrt{1-\zeta^2}} \sin\omega_d\tau + \cos\omega_d\tau \right] \quad (26)$$

which is the standard expression as that obtained by Crandall and Mark [2] for a stationary case.

The mean square response of the system in this case may be obtained by setting $p = 0$ in Eq.(13) or by setting $\tau = 0$ in Eq.(26) and is

$$E[X^2] = \frac{\pi}{2} \frac{S_0}{\zeta\omega_n^3} \quad (27)$$

This value is independent of time and is the mean square response of an one-degree-of-freedom linear system subjected to a stationary white noise excitation [2].

RESPONSE UNDER AN EXPONENTIALLY DECAYING STRENGTH FUNCTION

In this case, the autocorrelation of the excitation is of exponentially decaying from,

$$R_{ZZ}(t_1, t_2) = A e^{-\alpha|t_1|} \delta(t_1 - t_2) \quad (28)$$

Substituting $R_{ZZ}(t_1, t_2)$ from Eq.(28) into Eq.(10) and integrating, the autocorrelation of the response $X(t)$ is obtained as

$$R_{XX}(t_1, t_2) = \frac{Ae^{-\zeta\omega_n|t_2-t_1|-\alpha|t_1|}}{(2\zeta\omega_n-\alpha)^2 + (2\omega_d)^2} \left[\frac{1}{\omega_d} \sin\omega_d(t_2-t_1) + \frac{2}{2\zeta\omega_n-\alpha} \cos\omega_d(t_2-t_1) \right] \quad (29)$$

By setting $t_1 = t_2 = t$ in the expression

for the autocorrelation $R_{XX}(t_1, t_2)$ in Eq.(29),

$$E[X^2(t)] = \frac{2A e^{-\alpha|t|}}{\omega_n^3 (2\zeta-\alpha') (\alpha'^2 - 4\zeta\alpha' + 4)} \quad (30)$$

where $\alpha' = \alpha/\omega_n$

Eq.(30) may also be written in the form

$$E[X^2(t)] = E[X^2(0)] e^{-\alpha|t|} \quad (31)$$

where

$$E[X^2(0)] = \frac{2A}{\omega_n^3 (2\zeta-\alpha') (2\zeta-\alpha'+2\sqrt{\zeta^2-1}) (2\zeta-\alpha'-2\sqrt{\zeta^2-1})} \quad (32)$$

The quantity $E[X^2(0)]$ is plotted in Figure 10 against α/ω_n for different value of $\zeta \leq 1.0$. This quantity has unbounded values when the denominator in Eq.(32) has a zero value. This happens when $\alpha'_1 = 2\zeta$, $\alpha'_2 = 2\zeta + (\zeta^2-1)^{1/2}$, and $\alpha'_3 = 2\zeta - (\zeta^2-1)^{1/2}$. The values of α'_2 and α'_3 will be complex if the damping ratio $\zeta < 1.0$. Therefore, for $\zeta < 1.0$ and for real values of α' , the quantity $E[X^2(0)]$ will approach infinite value only when $\alpha' = 2\zeta$ as may be deduced from the figure.

As a particular case, suppose $\alpha = 0$. The autocorrelation of the input process in Eq.(28) is exactly the same as in Eq.(23) giving a stationary white noise process. The mean square value of the response $X(t)$ of the system in this case will be same as in Eq.(27), namely

$$E[X^2] = \frac{\pi}{2} \frac{S_0}{\zeta\omega_n^3}$$

This can be directly obtained by setting $\alpha = 0$ and $A = 2\pi S_0$ in Eq.(32).

RESPONSE UNDER LINEARLY DECAYING STRENGTH FUNCTION

In this case the autocorrelation of the input process takes the form

$$R_{ZZ}(t_1, t_2) = A(1 - \frac{|t_1|}{T}) \delta(t_1 - t_2), |t_1| < T \quad (33)$$

where T is a certain constant value of time.

Substituting $R_{ZZ}(t_1, t_2)$ from Eq.(33) into Eq.(10) and integrating, the autocorrelation of the response for an infinite operating time system is given by the following expression

$$R_{XX}(t_1, t_2) = \frac{Ae^{-\zeta\omega_n|t_2-t_1|}}{4\zeta\omega_n^3} \left\{ \frac{\zeta}{(1-\zeta^2)^{1/2}} \left[1 - \frac{|t_1|}{T} + \frac{\zeta}{\omega_n T} \right] \sin\omega_d(t_2-t_1) + \left[1 - \frac{|t_1|}{T} + \frac{1+2\zeta^2}{2\zeta\omega_n T} \right] \cos\omega_d(t_2-t_1) \right\} \quad (34)$$

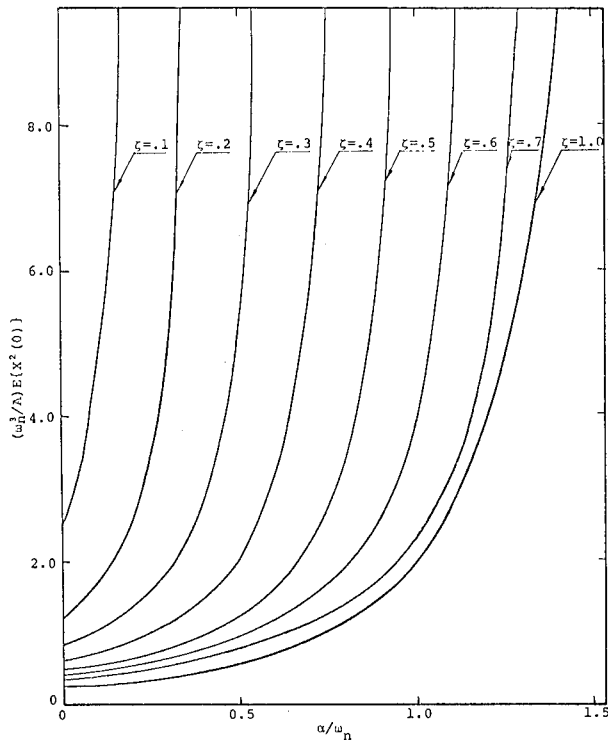


Fig.10: Amplitude $E[X^2(t)]$ against α/ω_n

The mean square value of the response $X(t)$ is obtained by setting $t_1 = t_2 = t$ in the expression for the autocorrelation in Eq.(34). Then

$$E[X^2(t)] = \frac{A}{4\zeta\omega_n^3} \left[1 + \frac{1+2\zeta^2}{2\zeta\omega_n T} - \frac{|t|}{T} \right] \quad (35)$$

which is essentially a linear function of time. By definition, this expression is valid only for $|t| < T$.

By assuming $T = \tau/n$, where τ is the natural period of the system and n is a proportional constant, Eq.(35) may be written as

$$E[X^2(t)] = \frac{A}{4\zeta\omega_n^3} \left[1 + \frac{n(1+2\zeta^2)}{4\pi\zeta} - n\left(\frac{|t|}{\tau}\right) \right] \quad (36)$$

For any given value of n , the mean square response of $X(t)$ may be evaluated in term of t/τ for different values of damping ratio ζ . Some of these results for $E[X^2(t)]$ are plotted against t/τ in Figure 11. By Eq.(5), the limiting value for $E[X^2(t)]$ is achieved when $|t|/\tau$ is equal to $1/n$. In Figure 11, n is taken as unity and therefore values of $E[X^2(t)]$ beyond $t/\tau = 1.0$ are purely hypothetical. It is noted that when $T \rightarrow \infty$, $n \rightarrow 0$, and the strength function of the input autocorrelation in Eq.(33) becomes a constant. Then the mean square value of the response $X(t)$ in Eq.(36) takes the form

$$E[X^2] = \frac{A}{4\zeta\omega_n^3} = \frac{\pi}{2} \frac{S_0}{\zeta\omega_n^3}$$

This is the standard mean square response of the system under stationary white noise excitation.

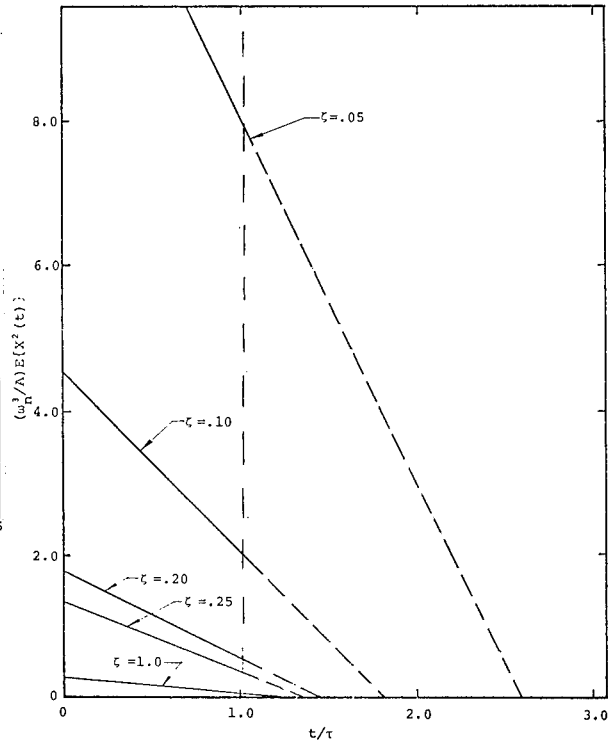


Fig.11: Amplitude $E[X^2(t)]$ against t/τ , $n = 1$.

ACKNOWLEDGEMENTS

The investigation presented in this paper was supported by National Research Council of Canada Grant No. A 7104 and Defence Research Board of Canada Grant 4701-07.

REFERENCES

1. T.K. Caughey, "Nonstationary Random Inputs and Responses", Chapter 3, Random Vibration, Vol. 2, Ed. S.H. Crandall, Massachusetts Institute of Technology Press, Cambridge, 1963.
2. S.H. Crandall and W.D. Mark, Random Vibration in Mechanical Systems, Academic Press, New York, 1963.
3. J.B. Roberts, "On the Harmonic Analysis of Evolutionary Random Vibration", Journal of Sound and Vibration, Vol. 2(3), pp.336-352, 1965.
4. J.B. Roberts, "The Response of Linear Vibratory Systems to Random Impulses", Journal of

Sound and Vibration, Vol. 2(4), pp. 375-390, 1965.

5. A. Papoulis, Probability, Random Variables and Stochastic Processes, McGraw-Hill, New York, 1965.
6. T.K. Caughey and H.J. Stumpf, "Transient Response of a Dynamic System Under Random Excitation", Journal of Applied Mechanics, Transactions of the ASME, Vol. 83, pp. 563-566, 1961.
7. R.L. Barnoski and J.R. Maurer, "Mean Square Response of Simple Mechanical Systems to Nonstationary Random Excitation", Journal of Applied Mechanics, Transactions of the ASME, Vol. 91, pp. 221-227, 1969.
8. L.L. Buciarelli, Jr. and C. Kuo, "Mean Square Response of a Second Order System to Nonstationary Random Excitation", Journal of Applied Mechanics, Transactions of the ASME, Vol. 92, pp. 612-616, 1970.
9. W.D. Mark, "Spectral Analysis of the Convolution and Filtering of Nonstationary Stochastic Processes", Journal of Sound and Vibration, Vol. 11 (1), pp. 19-63, 1970.

MEANS OF CONTROLLING THE DYNAMIC MOTION OF BOTTOM
MOORED MINE CASES EXPOSED TO HIGH CURRENT

J. J. O'Neill, J. Berezow, J. E. Goeller
Naval Ordnance Laboratory
Silver Spring, Maryland

An elastically supported right-circular cylinder that is exposed to steady fluid crossflow experiences rather high-tilt angles caused by hydrodynamic drag and the hydrodynamic alternating force due to vortex shedding. More than 200 scale-model and full-size tests were conducted at two Navy facilities to investigate means of stabilizing flow-induced vibrations on an elastically supported mine case exposed to steady fluid flow. Many configurations were tested for stabilizing effect and packaging capability. A hydrofoil configuration was the best design that could steady the mine case in the pitch and yaw planes and be successfully packaged and deployed. Scaling laws, test results and hydrofoil stabilizing theory are discussed.

INTRODUCTION

Naval systems sometimes involve the use of cylindrically shaped underwater mines which are anchored to the ocean bottom. The mine and tether comprise a vibrating system consisting of a buoyant cylinder and a flexible cable attached to the bottom of the cylinder. In the presence of steady fluid crossflow, the drag force on the mine case and tether causes the cylinder to dip in the pitch plane (in the direction of fluid flow) as seen in Fig. 1. Also, the vortex shedding around the cylinder induces hydrodynamic alternating forces which cause the case to oscillate in the yaw plane (perpendicular to the direction of fluid flow) as seen on the right side of Fig. 1.

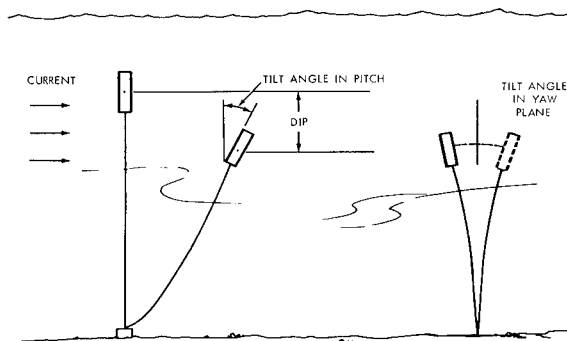


Fig. 1 - Illustration of Mine Motion

The case dip can become a problem for long cable systems, since the case could possibly dip to a depth where the pressure is sufficient to crush it. In specific types of mine systems, the resultant tilt angle due to drag (in the pitch plane) and vortex shedding can result in a significant degradation of system performance.

The problem of mine case motion induced by vortex shedding was investigated previously by Berezow and Sallet [1, 2, 3]. For a full-scale bare case, two basic modes of oscillation were observed as depicted in Fig. 2. The first mode is just a simple pendulum-type motion. The second mode involves oscillation about the center of total mass. If one assumes that the frequency of oscillation is given by the Strouhal equation

$$f = S \frac{V}{D} \quad (1)$$

where S is the Strouhal number, V is the current velocity, and D is the case diameter,

then the current at which resonance of the modes occurs can be reasonably well predicted. This involves considering the case/tether combination as a double pendulum, computing the natural frequencies and equating them to the Strouhal frequency. Berezow and Sallet also investigated ways of reducing the tilt angle in the yaw plane by applying various surface modifications to the

case. A splitter plate attached rigidly to a cylinder generator with a height equal to the length of the case and a length of three case diameters was found to be the most effective way of eliminating motion due to vortex shedding.

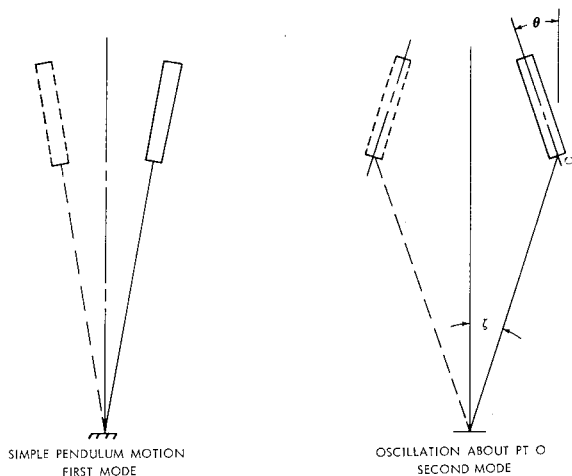


Fig. 2 - Vibration Modes

The dip angle experienced with the splitter plate configuration was not investigated in Ref. [1]. However, Sallet showed in Ref. [4] that the dip angle with this configuration can be stabilized by connecting the tether to a bridle which is attached to the cylinder at its center of drag (Fig. 3). Nevertheless, packaging the splitter plate in the application for which it was designed proved to be impractical. Therefore, a vigorous and extensive program was launched to find another means of controlling and minimizing the tilt angle of the mine case. The results of these tests are contained in this paper.

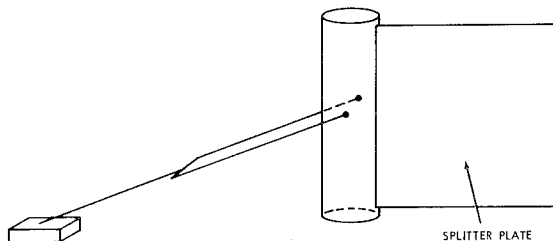


Fig. 3 - Cylinder with Stabilizing Splitter Plate

The full-scale mine case, which has a diameter of 21 inches and lengths of 106 inches and 116 inches, was used as the baseline prototype in all the experimental testing. Table 1 contains a summary of the important

characteristics of all the models tested. For convenience in this paper, the displacement and weight of models are quoted in terms of equivalent full-scale values. The net buoyancy is the most important parameter, which is defined as the displacement of the case (pounds) minus the weight of the case without cable weight. The values shown in Table 1 are considered baseline. In some cases, however, the net buoyancy, as shown in test results, was changed by varying the weight of the case. The equivalent full-scale tether length was generally 15 feet, 30 feet, or 95 feet, while the full-scale tether diameter was 0.5 inches. Nylon cord was used for tethers. However, a 12-conductor instrumentation cable was used as a tether for instrumented models.

Table 1

Summary of Model Characteristics

Config- uration No.	Scale Factor	Equivalent Full-Scale Values					
		d dia (in.)	L length (in.)	B displace- ment (lbs)	W weight (lbs)	B-W net buoyancy (lbs)	I Moment of inertia (slug-ft ²)
1	1.0	21	106.38	1318	1155	163	
2	.190	21	106.2	1318	1148	170	
3	.380	21	106.2	1318	1148	170	
4	1.0	21	116	1475	1267	208	360
5	.190	21	116	1475	1305	170	

TEST FACILITIES

The facilities at the Naval Ordnance Laboratory (NOL) and at the Naval Ship Research and Development Center (NSRDC) were used to conduct the tests. The NOL Hydroballistics Facility includes a stainless steel lined water tank which is 100 feet long, 75 feet deep, and 35 feet wide containing the excellent clarity water necessary for good photographic records (Fig. 4). In conducting the tow tests, the tether of the mine case was attached to a carriage on the rails at the bottom of the tank and was towed back and forth using a variable speed motor at various velocities (Fig. 5). Tests on full scale, .38 scale, and .19 scale were conducted and, because of the large water depth capability in the Hydroballistics Facility, different lengths of the mine tether were examined. Orthogonal photography was employed to record the motion of the mine case and measure its tilt and yaw angles. Instrumented mine case tests of the full scale and .38 scale consisted of free gyros and pendulum inclinometers used to measure the tilt angle and these results were checked with photographic records. The length of the test run was limited to about 60 feet which did not provide enough time in certain tests to reach steady-state conditions. A series of .38-scale instrumented model tests were conducted

at the NSRDC tow basin which is 22 feet deep and 1885 feet long in order to obtain the long test run necessary to insure steady-state conditions.

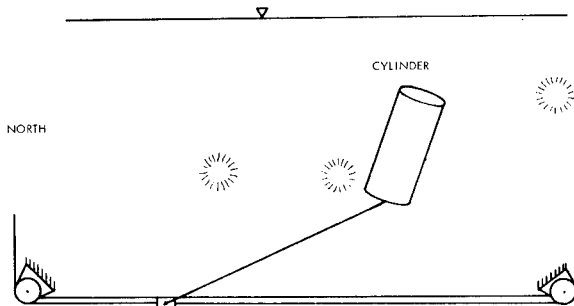
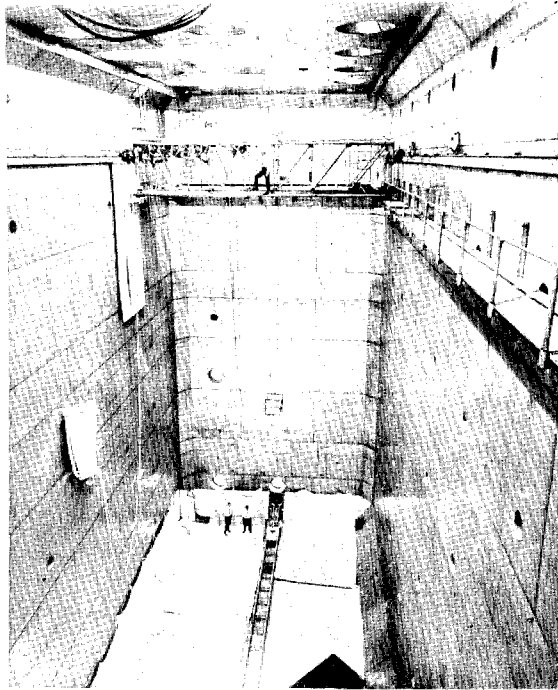


Fig. 5 - Test Arrangement in NOL Test Tank

Relatively long test times were obtained in the NSRDC circulating water channel where the water is continuously circulated around a loop. Fig. 6 is the test section of the facility which is 60 feet long, 22 feet wide, and up to 9 feet deep (Ref. 5). Viewing windows are located at the bottom of the channel as well as at both sides. Note the camera locations as used in the NSRDC tests. The motor that drives

the pump impeller can attain flow speeds of up to 10 knots. The water depth in the water channel was about 9 feet, which required small models of 0.19 scale or smaller and short tether lengths. In addition, the circulating pumps could not provide a steady current velocity of less than 0.3 knots in the channel. Tests at this facility were generally used as screening tests to check out various methods of case stabilization.

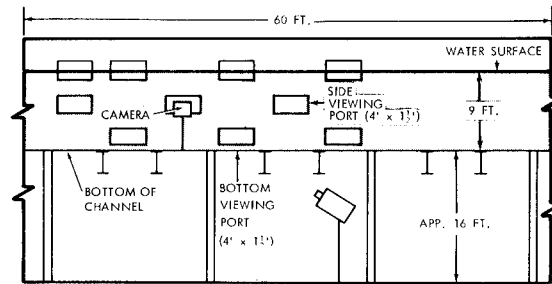


Fig. 6 - Test Section of NSRDC Circulating Water Channel

SCALING LAWS

The models were scaled geometrically. Therefore, if λ is the scale factor then

$$\lambda = \frac{L_M}{L_P}$$

The weight and moment of inertia then were scaled according to

$$W_M = \lambda^3 W_P$$

$$I_M = \lambda^5 I_P$$

Displacement is scaled the same as weight. Therefore, the characteristics of the models can be obtained from Table 1 by applying the appropriate multiplication factor.

The scaling considerations for the model tests are somewhat controversial because of the inability to scale Froude number and the Reynolds number simultaneously. The velocity of current was scaled with Froude scaling. Hence

$$\frac{V_M^2}{L_M} = \frac{V_P^2}{L_P}$$

or

$$V_M = \sqrt{\frac{L_M}{L_P}} V_P = \sqrt{\lambda} V_P$$

The last equation indicates that in order to get equal tilt angles for the model and prototype, the current velocity for the model must be $\sqrt{\lambda}$ times the full-scale current. A detailed

discussion of why Froude scaling is considered most representative is given in Appendix A.

Static tilt in the pitch plane (plane of current) and dynamic tilt due to vortex shedding are considered. It should be mentioned that the series of tests conducted were considered as screening tests to explore methods of case stabiliztion. The ultimate selection of the best stabilizing technique requires full-scale verification testing.

TEST RESULTS

The first series of tests was performed in the NOL Hydroballistics Facility with a full-scale model. The detailed geometry of the case is given in Fig. 7. The model was instrumented with free gyros to measure tilt angle in the pitch and yaw planes. The full-scale configurations shown in Fig. 8 were towed in the tank at many towing speeds. The tether of the first design was attached directly to the bottom of the case along the axis of the case. The second design utilized a bridle with the attachment at a trunnion located at the theoretical center of pressure of the case. The third design utilized a bail which consisted of a rail and roller system. The curvature of the bail was designed so that the direction of the tether force always passed through the center of pressure of the case. These latter two designs were intended to eliminate the tilt angle (in the pitch plane) induced by the drag on the case.

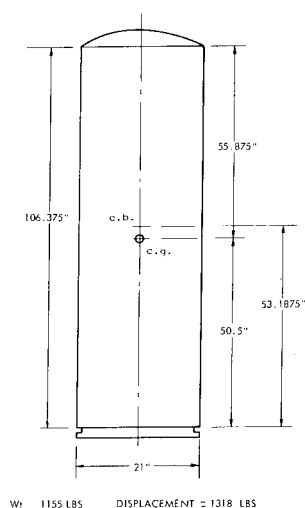


Fig. 7 - Schematic of Case Tested

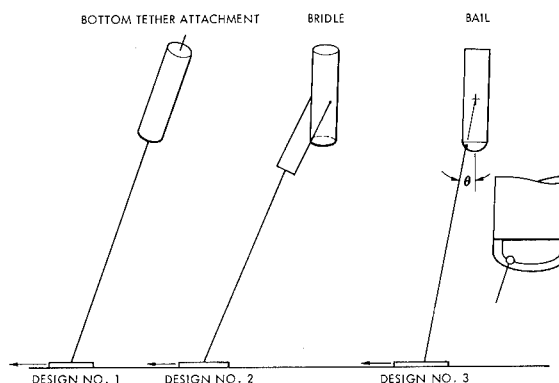


Fig. 8 - Test Configurations

Fig. 9 shows the maximum tilt angle from drag plus vortex shedding plotted against current speed for various cable lengths (design 1). The mooring line was attached to the bottom of the case. The data from tests in Ref.[1] were used to fair in the curve between the data points obtained in these tests. Note the maximum tilt angle of about 27 degrees that is generated when the smooth case is towed on a 15-foot tether. The scaled line shown in the figure labeled "tilt due to drag alone" is a theoretical curve of case tilt without the effect of vortex shedding. For small angles, the tilt angle can be estimated from

$$\theta = \frac{1/2 \rho C_D A V^2}{B - W \frac{L_{cg}}{L_{cp}}} \quad (1)$$

where ρ is the water density, C_D is the drag coefficient, A is the projected case area, V is the velocity, B is the displacement, W is the weight, L_{cp} is the distance to center of pressure from the bottom of the case, and L_{cg} is the distance to the center of gravity from the bottom of the case. This should represent the lower limit of the case tilt.

Vortex shedding causes the oscillatory motion. The data shown for the 100-foot cable were obtained from the .190-scale tests. For speeds up to 1 knot with a 100-foot cable, the case exhibited little motion due to vortex shedding. Above this speed, the second mode of vibration (yawing about center of mass) became more pronounced, but the major portion of the tilt angle was due to drag on the case causing tilt in the pitch plane.

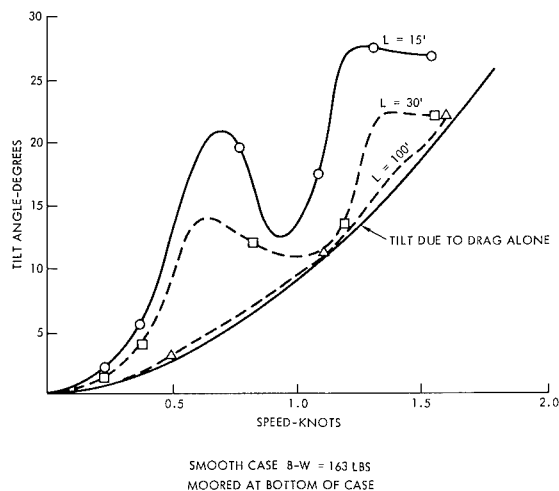


Fig. 9 - Resultant Tilt Angle from Drag Plus Vortex Shedding

Various configurations including the bridle, the bail, splitter plates, and streamers were investigated to reduce tilt. Fig. 10 shows the results of the tests. Although the splitter bridle combination resulted in the lowest tilt angle, this configuration was eliminated because of a difficult packaging problem for a practical mine system. The bridle unit yielded excessive tilt in field tests of a full-scale prototype.

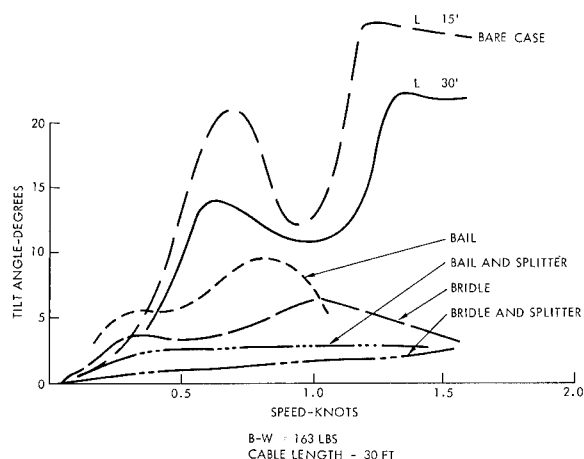


Fig. 10 - Comparison of Tilt Angle

TESTS AT NSRDC AND NOL

A model test program was initiated to investigate other possible solutions to the case-motion problem. The following summary contains the results of some of the tests which were conducted at NOL and NSRDC:

a. Bridle Tests. Small-scale (.190) models were tested in the

circulating water channel at NSRDC. A flexible bridle was attached to the case at the center of pressure, then at the c.g., then alternately above and below the c.p. The case motion was erratic in all instances and produced excessive tilt angles. A bail plus bridle unit (see Fig. 11) was statically unstable. Use of a rigid bridle provided some improvement. An eccentric bridge unit (Fig. 12) was the most stabilizing bridle configuration. Ref. [6] describes bridle tests in greater detail.

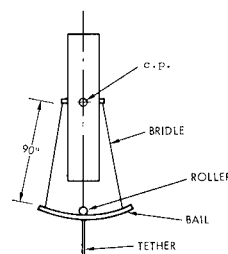


Fig. 11 - Schematic of Bail Plus Bridle

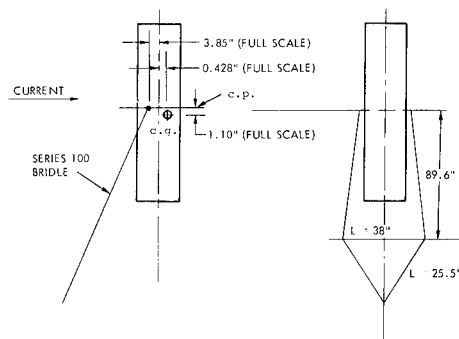


Fig. 12 - Schematic of Eccentric Bridle

b. Splitter Plates. A splitter plate with a height equal to the length of the case and extending out a length of three case diameters was rigidly attached to a case that was equipped with a bridle at the center of pressure. The angles in the yaw plane were quite small. Toward the end of the tests, the unit experienced large angles in the pitch plane, which was caused by poor balancing of the splitter plate. In addition, the water in the channel contained a considerable amount of entrained air. The splitter plate and the case were literally engulfed in air bubbles which could have affected the balancing. This exemplifies the problems of testing bridle units on a small scale, since there is very little static restoring moment. Nevertheless, the tests did indicate that the splitter plate is an effective means of minimizing the yaw oscillation.

The splitter plate was also tested on a case with a bail at the bottom. Fig. 13 shows a plot of the maximum resultant tilt angle as a function of equivalent full-scale current. Again, the splitter plate was effective in reducing the yaw angle. In general, the bail did a reasonably good job in reducing the pitch angle. Friction between the roller and the rail caused the roller to move sluggishly at times, thereby resulting in rather large pitch angles.

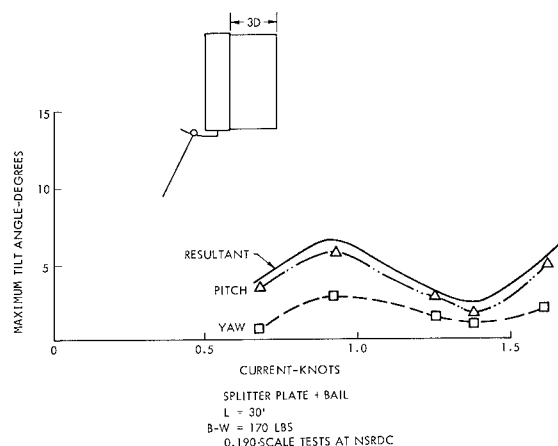


Fig. 13 - Maximum Tilt Angle vs. Current

c. Hydrofoil Stabilizing Units.

The Applied Research Laboratory of the University of Texas suggested the application of an extended hydrofoil to reduce tilt by generating a counter-balance moment, as seen in Fig. 14. The hydrofoil (Fig. 15) was a 90-degree sector of a cylinder 48 inches long and attached to a 95-inch arm. The cylinder concavity was directed up-stream. A small slit about 2 inches wide ran almost the entire length of the hydrofoil along the longitudinal centerline.

A plot of the maximum resultant tilt angle is also shown in Fig. 15. The plot is a little misleading, since the unit had about 2 to 3 degrees static tilt due to the weight of the hydrofoil. The unit gave encouraging results at the high speed, in that it did provide a significant righting effect. The unit did, however, exhibit significant yaw at about 1 knot due to a resonant condition (second mode type oscillation).

A hydrofoil without a slit was used with the concavity directed downstream, as shown in Fig. 16. Fig. 16 shows the .38-scale instrumented model being towed in the NOL Hydroballistics Facility with the 90-degree sector hydrofoil. The results of a .19-scale model are shown in Fig. 17. Again,

there was a slight amount of static tilt, which indicates that a properly balanced unit would yield even smaller angles. Moreover, the unit showed a slight yaw angle bias due probably to slight misalignment of the hydrofoil off the centerline of the case. At low speed (about .4 knot) the case oscillates as a simple pendulum due to vortex shedding. The hydrofoil is relatively ineffective in damping this type of motion, but is quite effective at the higher speeds.

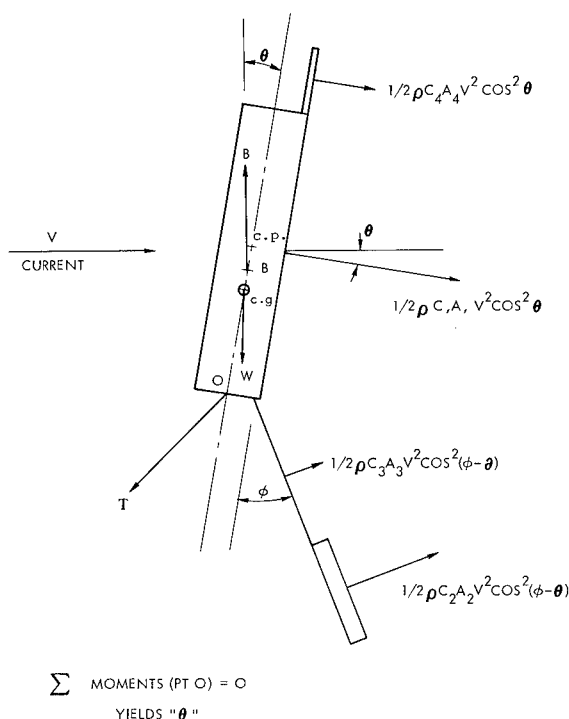


Fig. 14 - Hydrodynamic Forces

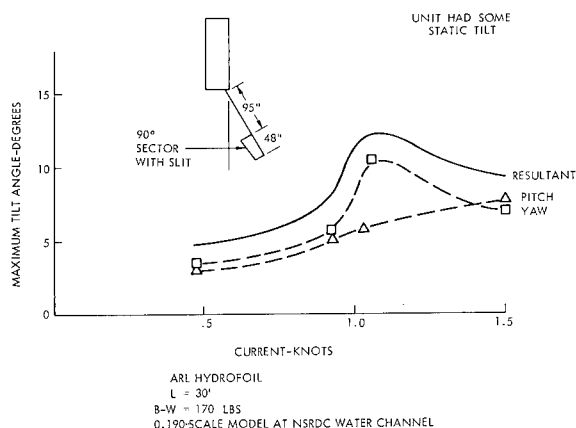


Fig 15 - Maximum Tilt Angle vs. Current

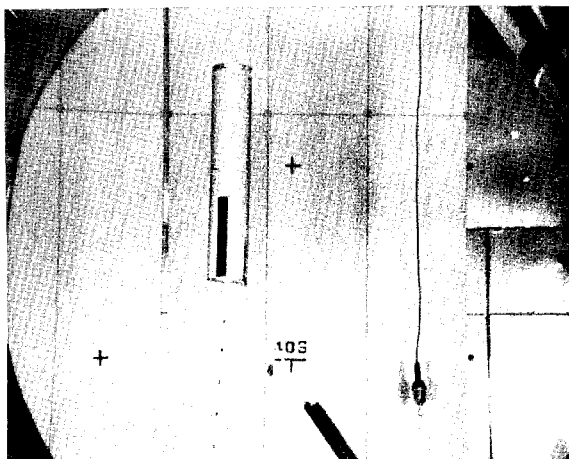


Fig. 16 - .38-Scale Instrumented Case with 90-degree Hydrofoil Sector

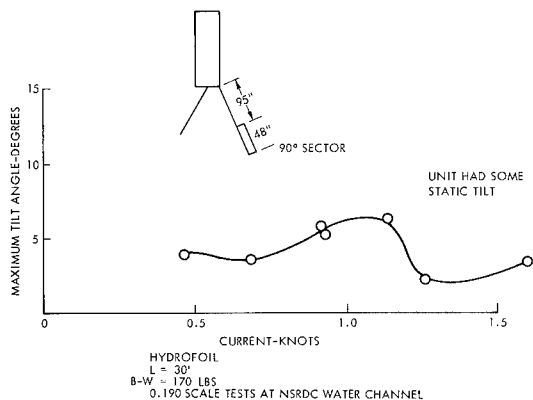


Fig. 17 - Maximum Tilt Angle vs. Current

In order to get information on scale effects, an instrumented .38-scale model was towed in NSRDC's tow channel, where long test runs could be made. These results are shown in Fig. 18.

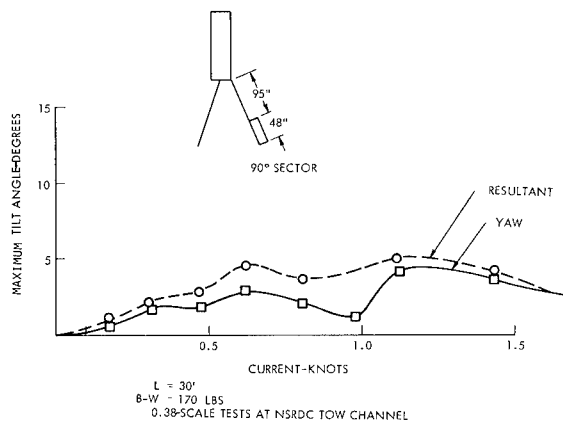


Fig. 18 - Maximum Tilt Angle vs. Current

Tests were performed with a 95-foot tether on a case with a hydrofoil in the NOL tank using a .38-scale instrumented model with an equivalent net buoyancy of 175 pounds. Fig. 19 shows the results. Comparison with Fig. 18 shows that the cable length helps to reduce the yaw angle significantly.

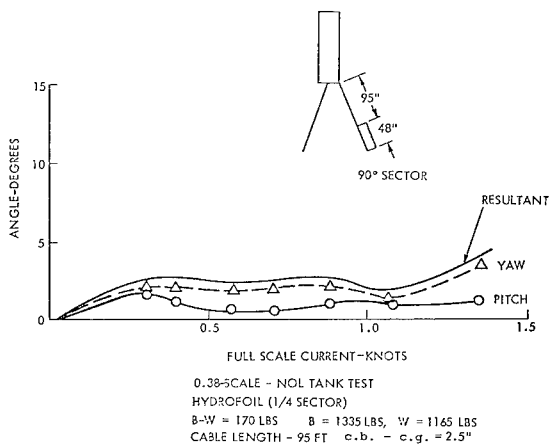


Fig. 19 - Maximum Tilt Angle vs. Current

Tests were made using a 60-inch arm (instead of a 95-inch arm) and a 54-inch-long hydrofoil with a 90-degree section to keep the total length (arm and hydrofoil) less than the case length in packaging. The net buoyancy was also increased to 215 pounds and the tether length was kept at 95 feet. The results shown in Fig. 20 again indicate tilt angles of less than 5 degrees for currents of up to 1.5 knots.

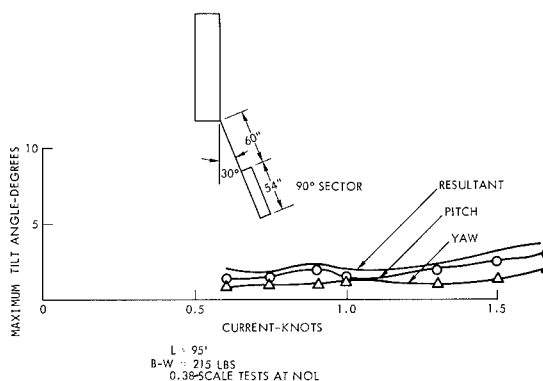


Fig. 20 - Maximum Tilt Angle vs. Current

The hydrofoil area of a 90-degree sector is not sufficient to completely counterbalance the moment (about the tether attachment point) due to the drag on the case. Note from Fig. 20 that while pitch angle is relatively small, it increases with current

velocity. Pitch angle of a hydrofoil configuration can be calculated with good accuracy using the method described in Appendix B. A 135-degree hydrofoil sector was also tested and found to have a greater stabilizing effect on the case motion than the 90-degree sector. Fig. 21 illustrates the results towing a 0.38-scale mine-case bottom moored to a 95-foot tether, using a 56-inch-long 135-degree sector hydrofoil attached to the case with a 60-inch arm. Note that the 135-degree sector was the only theoretical comparison that was made with a 90-degree sector by use of the computer program in Appendix B.

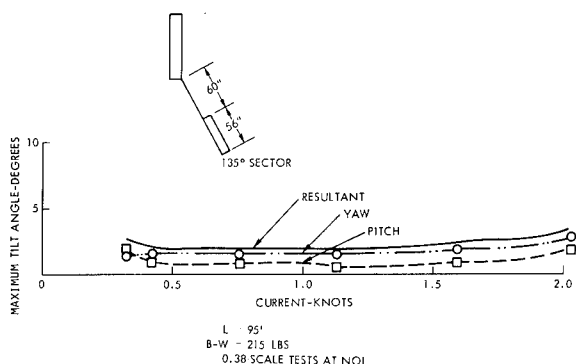


Fig. 21 - Maximum Tilt Angle vs. Current

Theoretical predictions of pitch angle were made using a drag coefficient of .85 for the case and 1.2 for the hydrofoil and arm. The theoretical pitch agrees quite well with the measured pitch except at low current, where transverse oscillations apparently induce pitch angle. The resultant angle was less than 3 degrees for current up to 1.5 knots.

FULL-SCALE HYDROFOIL TEST - NOL

A full-scale mine case with a 54-inch-long hydrofoil (90-degree sector) and 60-inch arm was tested in the NOL Hydroballistics Facility. The hydrofoil was deployed from a packaging position flush with the mine case when the case was in a rest position. The net positive buoyancy was 208 pounds. The initial tether length was 30 feet, but it stretched considerably. Fig. 22 shows a plot of the maximum tilt angle as a function of flow velocity. The initial tests were made with an antenna offset to the side. The antenna caused the case to roll slightly, thereby rotating the hydrofoil (similar to a rudder turning). This caused the case to yaw significantly to the side. The lower set of curves in Fig. 22 was obtained when the antenna was brought in line with the hydrofoil. There were

noticeable yaw oscillations at a current of .5 knot with resultant tilt angles approaching 5 degrees. However, the hydrofoil still maintained the resultant tilt angle below 5 degrees for current up to 1.5 knots. The full-scale mine equipped with a 90-degree sector hydrofoil, was deployed successfully from a plane at an NOL testing facility.

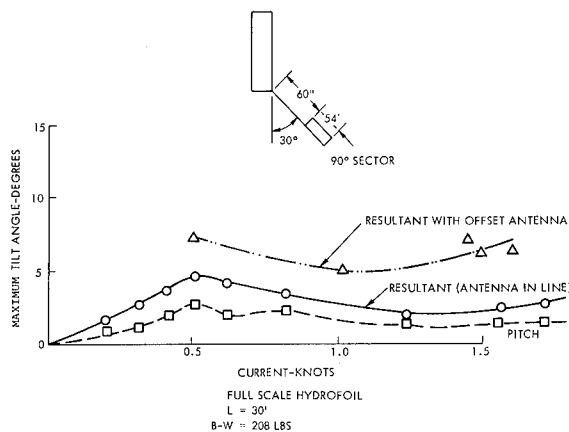


Fig. 22 - Maximum Tilt Angle vs. Current

The full-scale case goes through a critical Reynolds regime beginning at about .75 knot ($T = 70$ degrees Fahrenheit), where the drag coefficient drops significantly (see Fig. 23). The models do not go through this regime because of their smaller size. The hydrofoil does not go through a drag reduction, since it is essentially a flat plate with sharp edges. Therefore, it is possible for the hydrofoil to overcompensate and cause a high pitch angle at high current. Overcompensation did not occur for the size hydrofoil tested.

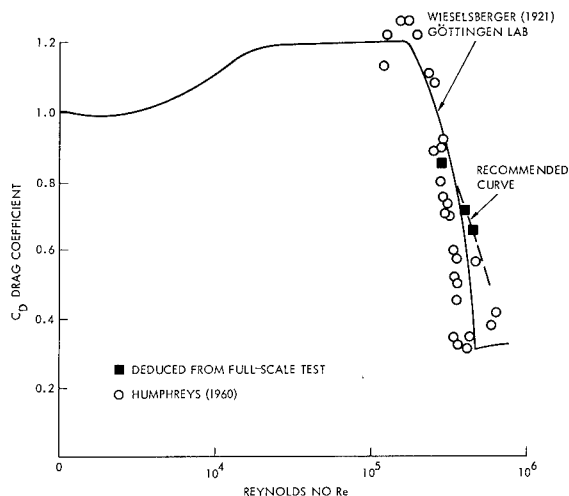


Fig. 23 - Drag Coefficient vs. Reynolds Number

The data were analyzed in an attempt to establish a curve for drag coefficient in the transition regime. Using the theoretical analysis of Appendix B for predicting pitch angle, the drag coefficient was computed to get a reasonable fit of the experimental pitch angle. Fig. 23 shows C_D versus Reynolds number for an infinite cylinder and three data points from the full-scale tests (the values in Fig. 23 must be ratioed by .705 because of finite length effects). These points fall within the data from the various investigators. A transition line has been drawn through the data and is recommended for future calculations.

Fig. 24 shows a plot of the experimental pitch angle compared to theoretical values using the recommended transition curve and a drag coefficient of 1.2 on the hydrofoil. It should be noted that the hydrofoil does not experience a transition because of its sharp edges. The experimental data are presented reasonably well. The effect of transition can be seen by comparison with the curve marked "no transition." Also shown in Fig. 24 is the effect of 40-degree fresh water. The pitch angle is larger in 40-degree fresh water because the higher viscosity causes transition to occur at a higher current velocity.

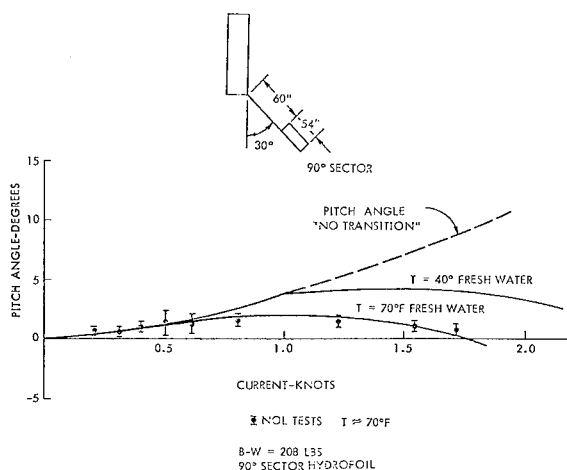


Fig. 24 - Pitch Angle vs. Current

In order to evaluate the effect of a larger hydrofoil, a theoretical calculation was made for a 135-degree sector hydrofoil 56 inches long (Fig. 25). The same transition curve of Fig. 23 was used. Overcompensation does appear to be high for currents approaching 2 knots in 70-degree sea water. If 40°F sea water is dominant in the application, the 135-degree sector appears to be the best choice.

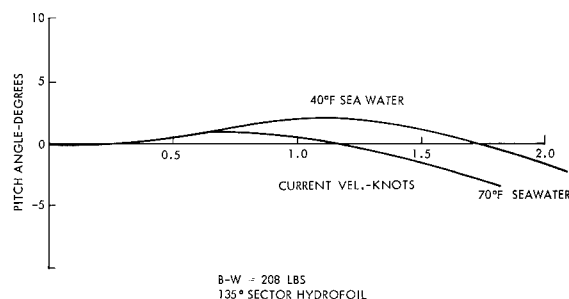


Fig. 25 - Theoretical Pitch Angle vs. Current

The effect of hydrofoil angle off the vertical was also investigated. The normal force coefficient C_N of the hydrofoil depends on the angle of attack α . A plot of C_N (from Ref. [7]) is shown in Fig. 26. The discontinuity at $\alpha = 40$ degrees occurs because of stall. It should be noted that the normal force is computed from

$$F_N = 1/2 \rho C_N A V_N^2$$

where V_N is the normal velocity component given by

$$V_N = V \cos (\phi - \theta)$$

and A is the projected planform area. The lift force then becomes

$$F_L = 1/2 \rho C_N A V^2 \cos^2 (\phi - \theta) \sin (\phi - \theta).$$

The drag force then becomes

$$F_D = 1/2 \rho C_N A V^2 \cos^3 (\phi - \theta).$$

Fig. 27 shows a plot of tilt angle in the pitch plane as a function of current velocity for various angles of hydrofoil angle ϕ . Fig. 28 shows a plot of lift force and drag force on the hydrofoil for a current of about 1 knot in 70°F sea water. Based on these plots, it appears that the preferred angle ϕ lies in the range of 30 to 50 degrees. Ideally, we would like to minimize the drag and maximize the lift so that the case dip is minimized.

CONCLUSIONS

Based on the tests performed to date, the following conclusions are made:

a. The standard bridle unit gives unacceptable tilt angles even for units with high buoyancy (250 pounds).

b. The eccentric bridle offers significant improvement.

c. The bare case with 30-foot tether gives excessive tilt angles.

d. The bare case with 95-foot tether gives tilt angles less than 5 degrees for currents below .75 knot.

e. A splitter plate attached rigidly to a cylinder generator with a height equal to the length of the case and a length of three case diameters, is effective in reducing yaw oscillations. A bridle or bail is needed to reduce the pitch oscillations.

f. A 56-inch long 135-degree sector hydrofoil attached with a 60-inch arm to the mine case that is bottom-moored to a 95-foot tether is the best solution thus far to the mine-case motion problem.

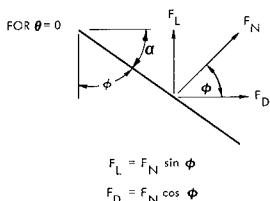
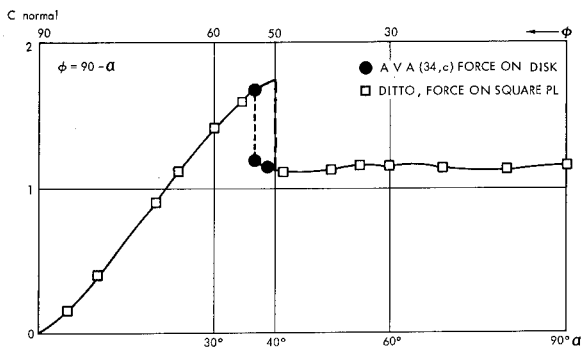


Fig. 26 - Normal Force Coefficient vs. Angle of Attack

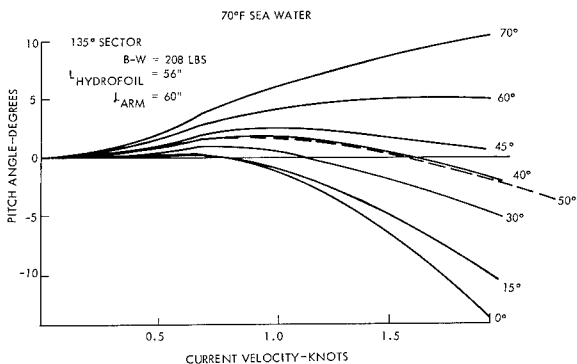


Fig. 27 - Tilt Angle in Pitch Plane vs. Current for Various Angles of Hydrofoil

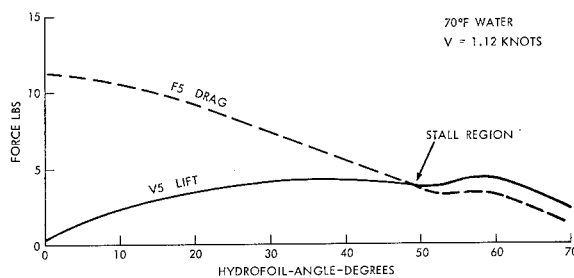


Fig. 28 - Hydrofoil Lift and Drag vs. Angle of Hydrofoil

ACKNOWLEDGEMENT

The authors would like to acknowledge the advice and suggestions of the following people: Dr. T. Peirce, Mr. F. Butler, and Mr. O. Seidman of the Naval Ordnance Systems Command; Dr. A. Seigel, Dr. V. Dawson, Mr. R. Schmied, and Mr. P. Fineran of NOL; and Mr. R. Grady and Mr. D. Cieslowski of NSRDC.

NOMENCLATURE

A	= Projected case area or planform area
B	= Displacement (pounds)
C_D	= Drag coefficient
C_k	= Von Karman lift coefficient
C_N	= Normal force coefficient
c.g.	= Center of gravity
c.p.	= Center of pressure
D	= Case diameter (inches)
F_D	= Drag force (pounds)
F_L	= Lift force (pounds)
f	= Frequency of oscillation
I	= Moment of inertia (slug-ft ²)
I_M	= Moment of inertia of model
I_P	= Moment of inertia of prototype
K	= Amplification factor
L_{cg}	= Distance to c.g. from bottom of case
L_{cp}	= Distance to c.p. from bottom of case
L_B	= Distance to center of buoyancy from bottom of case
L_M	= Length of model (inches)
L_P	= Length of prototype (inches)
M_e	= Virtual mass
S	= Strouhal number
V	= Current velocity
V_N	= Normal velocity component
	$V \cos (\phi - \theta)$
W	= Weight (pounds)
W_M	= Weight of model
W_P	= Weight of prototype
α	= Angle of attack
λ	= Scale factor
ρ	= Water density
θ	= Tilt angle
ϕ	= Angle between hydrofoil arm and cylinder generator

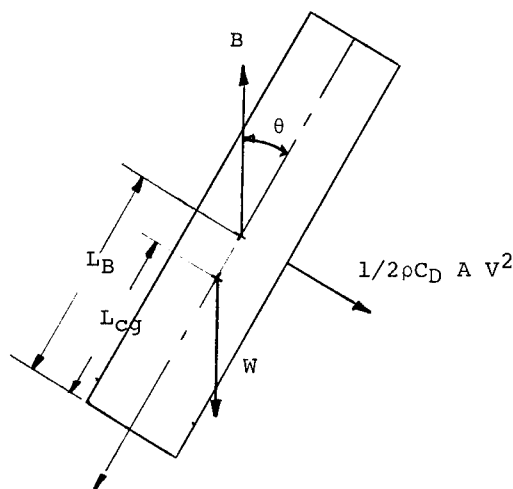
REFERENCES

1. J. Berezow and D. W. Sallet, "An Experimental Investigation of Means to Suppress the Flutter Motion of Elastically Suspended Cylinders Exposed to Uniform Crossflow," NOLTR 72-6, 28 Feb 1972
2. D. W. Sallet, "On the Self-Excited Vibrations of a Circular Cylinder in Uniform Flow," Shock and Vibration Bulletin, No. 40, Part 3, pp. 303-309, Dec 1969
3. D. W. Sallet and J. Berezow, "Suppression of Flow-Induced Vibrations by Means of Body Surface Modifications," Shock and Vibration Bulletin, No. 42, Part 4, pp. 215-228, Jan 1972
4. D. W. Sallet, "A Method of Stabilizing Cylinders in Fluid Flow," J. of Hydronautics, Vol. 4, No. 1, pp. 40-45, Jan 1970
5. "Principles of Naval Architecture," Society of Naval Architects and Marine Engineers, pp. 330, 1967
6. J. J. O'Neill, J. E. Goeller, and J. Berezow, "Dynamic Motion of Bottom-Moored Mine Cases Exposed to High Current," NOLTR 73-123, 7 Jun 1973
7. S. F. Hoerner, Fluid Dynamic Drag, 1965

APPENDIX A

The question of applicable scaling laws for model tests is controversial. The following is an attempt to justify Froude scaling as the most representative one for the major part of the velocity regime under consideration.

Consider first the tilt angle in the pitch plane due to drag on the case.



By taking moments about the cable attachment point, the tilt angle (for small angles) is

$$\theta = \frac{1/2 \rho C_D A V^2}{B-W \frac{L_{cg}}{L_B}} \quad (1)$$

Using subscript M for model and P for prototype, we get

$$\frac{\theta_M}{\theta_P} = \frac{(C_D A V^2)_M}{(C_D A V^2)_P} \frac{(B-W \frac{L_{cg}}{L_B})_P}{(B-W \frac{L_{cg}}{L_B})_M}$$

For geometric scaling let $\frac{L_M}{L_P} = \lambda$ (scale factor)

Then

$$\left. \begin{aligned} \frac{B_M}{B_P} &= \lambda^3 \\ \frac{A_M}{A_P} &= \lambda^2 \end{aligned} \right\}$$

Then

$$\frac{\theta_M}{\theta_P} = \frac{(C_D)_M}{(C_D)_P} \left(\frac{V_M^2}{V_P^2} \right) \left(\frac{A_M}{A_P} \right) \frac{(B-W \frac{L_{cg}}{L_B})_P}{(B-W \frac{L_{cg}}{L_B})_M} \quad (2)$$

$$\frac{\theta_M}{\theta_P} = \frac{C_{DM}}{C_{DP}} \left(\frac{V_M^2}{V_P^2} \right) (\lambda^2) \left(\frac{1}{\lambda^3} \right)$$

For equal tilt angle

$$\left(\frac{V_M}{V_P} \right)^2 = \left(\frac{C_{DP}}{C_{DM}} \right) \lambda \quad (3)$$

We know that, in general, the drag coefficient C_D depends on Reynolds number. This presents the usual problem that we cannot duplicate both Reynolds number and Froude number. However, for a rigid cylinder, C_D is relatively insensitive to Reynolds number over a range of about 10^2 to 2×10^5 . (See Fig. 23). Hence, over this range

$$\frac{C_{DP}}{C_{DM}} \approx 1.$$

Hence, Equation (3) becomes

$$V_M = \sqrt{\lambda} V_P$$

This is Froude scaling. At the critical Reynolds number of 2×10^5 , a transition range is experienced. This corresponds to a full-scale current of about .75 knot (70°F water). Hence, above .75 knot (full scale) the model tests should give higher angles than the prototype. The model tests are therefore conservative. One way to compensate for this is to roughen the model surface so that the critical Reynolds number is lowered.

Now consider dynamic loading from vortex shedding. If we consider the case as moored at the bottom, its natural frequency, considering a simple pendulum, is

$$f_n = \frac{1}{2\pi} \sqrt{\frac{B-W}{M_e l}}$$

where M_e is the virtual mass, l = cable length. Again, for a rigidly held cylinder, the frequency of vortex shedding is

$$f = S \frac{V}{D}$$

The Strouhal number is also relatively insensitive to Reynolds number over the range 10^2 to 2×10^5 . The forcing function on the case is frequently approximated by:

$$F_k = 1/2 \rho C_k A V^2 \sin(2\pi f t)$$

where C_k is the von Karman lift coefficient. The response of a simple undamped pendulum to the forcing function is

$$\theta = \frac{\frac{F_k}{B-W}}{\left(\frac{f}{f_n}\right)^2} = \frac{K \rho C_k A V^2}{2(B-W)}$$

$$\text{where } K = \frac{1}{1 - (f/f_n)^2}$$

This equation is the same form as Equation (1). The differences are the inclusion of the amplification factor K and the substitution of C_k for C_D . Let us first examine the frequency ratio.

$$\frac{f}{f_n} = 2\pi \frac{SV}{D} \sqrt{\frac{M_e l}{B-W}}$$

or

$$\begin{aligned} \left(\frac{f}{f_n}\right)_M &= \left(\frac{S_M}{S_P}\right) \left(\frac{V_M}{V_P}\right) \left(\frac{D_P}{D_M}\right) \sqrt{\frac{M_{eM}}{M_{eP}} \frac{(B-W)_P}{(B-W)_M} \left(\frac{l_M}{l_P}\right)} \\ &= \left(\frac{S_M}{S_P}\right) \left(\frac{V_M}{V_P}\right) \frac{1}{\lambda} \sqrt{\lambda} \\ &= \left(\frac{S_M}{S_P}\right) \left(\frac{V_M}{V_P}\right) \frac{1}{\sqrt{\lambda}} \end{aligned}$$

Since the Strouhal number is relatively insensitive to Reynolds number over a wide range, it is reasonable to take $S_M = S_P$. Therefore, for equal frequency ratio, and hence, equal amplification factor for model and prototype we get

$$V_M = \sqrt{\lambda} V_P$$

This is, again, Froude scaling. The same approach also applies to discrete systems with many degrees of freedom. Hence, the tilt angles of the model and prototype are nearly equal for Froude scaling if the lift coefficient C_k is nearly the same for the model and prototype. For a rigidly held cylinder, the lift coefficient is the same order of magnitude as the drag coefficient over a wide range of Reynolds number below the critical value. Again, the prototype goes through transition before the model. Hence, the model results should be conservative. Roughening the model case, as previously mentioned, should compensate for this.

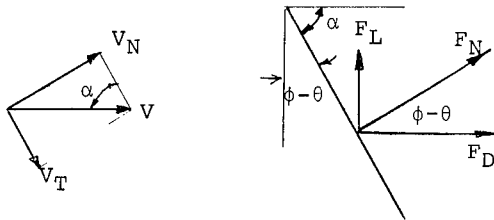
Practically all the reasoning given in the preceding is based on data from rigidly held cylinders. The effect of large case transverse oscillation on lift coefficient and Strouhal number is relatively unknown. An attempt is being made to develop such information. However, in the interim, it is believed that Froude scaling is the most representative, and should be used for all screening tests. The final selected design should be tested in the full scale.

APPENDIX B

This appendix contains a listing of the computer program employed to calculate the pitch angle of the mine case under the action of the various hydrodynamic forces. These forces are illustrated in the diagram. The mine case goes through a Reynolds number transition regime with its associated drop in drag coefficient in the velocity regime tested. There are no Reynolds number transition phenomena associated with the flow normal to the surface of flat plates with sharp edges. The hydrofoil sector used in the testing was analyzed as such a section and the normal force coefficient was obtained from Ref. [7]. The antenna on top of the case and the hydrofoil arm are in the Reynolds number regime where the drag coefficient has a constant value of 1.2.

The coefficients C_1 , C_2 , C_3 , and C_4 are actually normal force coefficients. The "crossflow principle" as described in Ref. [7] was used to compute the normal force. Hence, at an angle of attack α , flow pattern and the fluid-dynamic pressure forces only correspond to the velocity component in the direction normal to their axis. Therefore

$$F_N = 1/2 \rho V_N^2 A C_N$$



$$V_N = V \sin \alpha = V \cos (\phi - \theta)$$

$$F_N = 1/2 \rho C_N V^2 \cos^2 (\phi - \theta)$$

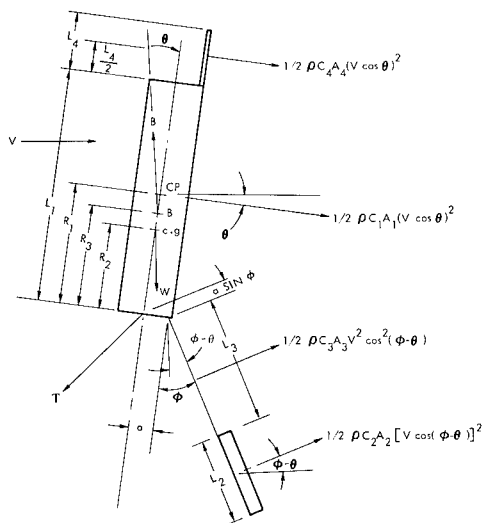
The lift force F_L is given by

$$F_L = F_N \sin (\phi - \theta)$$

and the drag force F_D

$$F_D = F_N \cos (\phi - \theta)$$

Knowing the normal forces on the various parts of the case and hydrofoil, the tilt angle θ can be computed by summation of moments about the mooring line attachment point to the case.



SUMMATION OF MOMENTS ABOUT MOORING PT

$$\frac{R_1}{2} \rho C_{A_1} V^2 \cos^2 \theta - \frac{(L_3 + a \sin \phi + .5 L_2)}{2} \rho C_{A_2} V^2 \cos^2 (\phi - \theta) + \frac{(L_1 + .5 L_4)}{2} \rho C_{A_4} V^2 \cos^2 \theta - \frac{.5 L_3 + a \sin \phi}{2} \rho C_{A_3} V^2 \cos^2 (\phi - \theta) - (B R_3 - W R_2) \sin \theta = 0$$

THIS CAN BE SOLVED BY ITERATION FOR TILT ANGLE θ .
THE REQUIRED HYDROFOIL DRAG FOR $\theta = 0$ IS

$$C_{A_2} = \frac{R_1 C_{A_1} - (.5 L_3 + a \sin \phi) C_{A_3} \cos^2 \phi + (L_1 + .5 L_4) C_{A_4}}{(L_3 + a \sin \phi + .5 L_2) \cos^2 \phi}$$

ILLUSTRATION OF TILT ANGLE AND HYDRO FORCES ON HYDROFOIL

```

1  REM THIS PROGRAM COMPUTES "CAPTOR CASE MOTION"
2  REM B=GROSS DISPLACEMENT (LBS)
3  REM W=DRY WEIGHT (LBS)
4  REM V=VELOCITY (KNOTS)
5  REM L1= LENGTH OF CASE (INCHES)
6  REM D1= DIA. OF CASE (INCHES)
7  REM C1= DRAG COEFFICIENT OF CASE
8  REM L2=LENGTH OF HYDROFOIL (INCHES)
9  REM C2=DRAG COEFFICIENT OF HYDROFOIL
10 REM D2=WIDTH OF HYDROFOIL (INCHES)
11 REM R0=DENSITY OF WATER
12 REM T=TILT ANGLE (DEGREE)
13 REM Q=ANGLE OF HYDROFOIL (DEGREE)
14 REM R9=REYNOLDS NUMBER
15 REM R1=LG TO CP(FROM BOTTOM) (INCHES)
16 REM R2=LG TO CG(FROM BOTTOM) (INCHES)
17 REM R3=LG TO CB(FROM BOTTOM) (INCHES)
18 REM Z=LENGTH OF HYDROFOIL ARM (INCHES)
19 REM A=RADIUS TO HYDROFOIL ATTACHMENT (INCHES)
20 REM R8=REYNOLDS NUMBER FULL SCALE
21 REM C3=DRAG COEFFICIENT OF ARM
22 REM D3=DIA. OF ARM (INCHES)
23 REM L3=LENGTH OF ARM (INCHES)
24 REM L4=LENGTH OF ANTENNA (INCHES)
25 REM D4=DIA. OF ANTENNA (INCHES)
26 REM D5=DRAG COEFFICIENT ON HYDROFOIL
27 REM L5=LIF COEFFICIENT OF HYDROFOIL
28 REM F5=DRAG FORCE
29 REM V5=LIFT FORCE
30
31 READ B,W,R1,R2,R3
32 READ L1,D1
33 READ L2,D2,Z,A
34 READ L3,D3,C3
35 READ L4,D4,C4
36 READ R0,Q
37 READ C2
38 PRINT
39 PRINT "C1=";
40 INPUT C1
41 INPUT V
42 IF V=0 THEN 9999
43 LET A1=L1*D1/144
44 LET A2=L2*D2/144
45 LET A3=L3*D3/144
46 LET A4=L4*D4/144
47 LET V=V*.69
48 LET F1=.5*R0*C1*A1*V+2/32.2
49 LET Q=Q/57.3
50 LET F2=.5*R0*C2*A2*V+2/32.2
51 LET F3=.5*R0*C3*A3*V+2/32.2
52 LET F4=.5*R0*C4*A4*V+2/32.2
53 LET B9=(B*R3-W*R2)/12
54 LET M1=F1*R1/12
55 LET M2=(Z+A*SIN(Q)+L2/2)*F2/12
56 LET M3=F3*(L3/2+A*SIN(Q))/12
57 LET M4=F4*(L1+.5*L4)/12
58 LET Q9=(M1+M4-(M2+M3)*(COS(Q))+2)/B9
59 LET R3=V*D1*.083E+5
60 LET V=V/1.69
61 IF V>.25 THEN 283
62 PRINT "B="B,"W="W,"L1="L1,"D1="D1,"C1="C1
63 PRINT "R0="R0
64 PRINT "L3="L3,"D3="D3,"C3="C3
65 PRINT "L2="L2,"D2="D2,"C2="C2,"A="A,"Z="Z
66 PRINT
67 PRINT "R1="R1,"R2="R2,"R3="R3,"R8="R8
68 PRINT "L4="L4,"D4="D4,"C4="C4
69 PRINT
70 LET T=Q9
71 IF Q-T<=.372 THEN 300
72 LET C2=1.8*(1.5708-(Q-T))/.697
73 LET F2=.5*R0*C2*A2*V+2/32.2
74 LET M2=(Z+A*SIN(Q)+L2/2)*F2/12
75 LET M9=((M1+M4)*(COS(T))+2-(M2+M3)*(COS(Q-T))+2)/B9
76 LET J=SQR(1-M9+2)
77 LET T9=ATN(M9/J)
78 IF ABS(T-T9)<=.0001 THEN 410
79 LET T=T+(T9-T)/20
80 GO TO 286
81 LET D5=C2*COS(Q-T)+3
82 LET L5=C2*COS(Q-T)+2*SIN(Q-T)
83 LET F5=.5*R0*D5*A2*V+2/32.2
84 LET V5=.5*R0*L5*A2*V+2/32.2
85 LET T=57.3*T
86 LET Q9=Q9*57.3
87 LET Q=Q*57.3
88 PRINT

```



```
540 PRINT "C2="C2
550 PRINT "T="T,"Q9="Q9,"V="V,"Q="Q
560 PRINT
566 PRINT "D5="D5,"LS="LS,"F5="F5,"VS="VS
567 GO TO 136
800 DATA 1475,1267,53.25,55.95,58.25
900 DATA 116.5,21
920 DATA 56,19.4,60,11
930 DATA 60,2.5,1.2
935 DATA 29,1.25,1.2
940 DATA 64,0
950 DATA 1.2
9999 END
**
```